UNIVERISTY OF CALIFORNIA SAN DIEGO

# Redox Dynamics of Nitrogenase

A dissertation submitted in partial satisfaction of the requirements for the degree Doctor of Philosophy

in

Chemistry

by

Hannah Leah Rutledge

Committee in charge:

Professor F. Akif Tezcan, Chair
Professor Michael Gilson
Professor Susan Golden
Professor Mark Herzik
Professor Michael Sailor
Professor Alina Schimpf

2022

The dissertation of Hannah Leah Rutledge is approved, and it is acceptable in quality and form for publication on microfilm and electronically.

University of California San Diego

2022

# DEDICATION

To all my friends and family that have encouraged me.

# EPIGRAPH

How you do anything is how you do everything.

TABLE OF CONTENTS

DISSERTATION APPROVAL PAGE ..... iii

DEDICATION ..... iv

EPIGRAPH ..... v

TABLE OF CONTENTS ..... vi

LIST OF ABBREVIATIONS ..... x

LIST OF FIGURES ..... xiv

LIST OF TABLES ..... xvii

ACKNOWLEDGMENTS ..... xviii

VITA ..... xxii

ABSTRACT OF THE DISSERTATION ..... xxiv

Chapter 1: Introduction to biological nitrogen fixation by molybdenum-nitrogenase ..... 1

1.1 Introduction to the nitrogen cycle and biological nitrogen fixation ..... 1

1.2 Structure and properties of the nitrogenase proteins ..... 3

1.2.1 Overview of Fe-protein and MoFe-protein ..... 3

1.2.2 Structure and properties of Fe-protein and the [4Fe-4S] cluster ..... 3

1.2.3 Structure and properties of MoFe-protein, the P-cluster, and FeMoco ..... 6

1.3 Electron transfer in nitrogenase is a dynamic process ..... 8

1.3.1 The Thorneley-Lowe model ..... 8

1.3.2 Nucleotide-dependent Fe-protein—MoFe-protein docking interactions ..... 10

1.3.3 The deficit spending model and conformational gating of electron transfer (ET) in nitrogenase ..... 13

1.3.4 Remaining questions about the nitrogenase catalytic mechanism ..... 16

1.4 Dissertation objectives ..... 16

1.5 Acknowledgements ..... 17

Chapter 2: Redox-metastability of the nitrogenase P-cluster ..... 18

2.1 Abstract ..... 18

2.2 Introduction ..... 18

2.2.1 Redox-dependent conformational changes of the nitrogenase P-cluster ..... 18

2.2.2 Conservation of oxygenic P-cluster ligand and implications for biological nitrogen fixation ..... 20

2.3 Results and discussion ..... 26

2.3.1 Structural characterization of *Azotobacter vinelandii* MoFe-protein P-cluster mutants ..... 26

2.3.2 Electron paramagnetic resonance (EPR) spectroscopy of *Azotobacter vinelandii* MoFe-protein P-cluster ligand mutants ..... 35

2.3.3 *In vitro* specific activity of *Azotobacter vinelandii* MoFe-protein P-cluster mutants 38

2.3.4 Growth rates of *Azotobacter vinelandii* MoFe-protein P-cluster ligand mutant strains ..... 39

2.4 Conclusions ..... 40

2.5 Future directions: Covariance analysis of nitrogenase MoFe-protein sequences ..... 41

2.6 Materials and methods ..... 44

2.6.1 Site-directed mutagenesis, expression, and purification of *Azotobacter vinelandii* MoFe-protein mutants ..... 44

2.6.2 Crystallography of MoFe-protein ..... 47

2.6.3 Electron paramagnetic resonance spectroscopy of MoFe-protein ..... 48

2.6.4 *In vitro* MoFe-protein $NH_3$, $H_2$, and $C_2H_4$ activity assays ..... 48

2.6.5 Covariance analysis of nitrogenase MoFe-protein sequences ..... 49

2.7 Acknowledgments ..... 50

Chapter 3: Probing the role of βSer188 in *Azotobacter vinelandii* MoFe-protein ..... 51

3.1 Abstract ..... 51

3.2 Introduction ..... 51

3.2.1 Comparing canonical electron transfer Fe-S clusters to the P-cluster ..... 51

3.2.2 Naturally occurring, interconverting [4Fe-4S] clusters and their unique properties . 52

3.3 Results and discussion ..... 53

3.3.1 *Azotobacter vinelandii* βSer188 protects the P-cluster from oxidative stress *in vivo* 53

3.3.2 *Azotobacter vinelandii* βSer188 is required for optimal diazotrophic growth of cells under Fe-limiting conditions ..... 55

3.3.3 RT-qPCR of *nifK* gene expression and activity of MoFe-protein *in vivo* ..... 56

3.3.4 Mössbauer spectroscopy of *Azotobacter vinelandii* $^{57}$Fe-reconstituted βSer188Ala P-cluster ..... 59

3.3.5 Structural characterization of mismetallated *Azotobacter vinelandii* βSer188Ala P-clusters ..... 61

3.3.6 Electron paramagnetic resonance spectroscopy of mismetallated *Azotobacter vinelandii* βSer188Ala MoFe-protein ..... 65

3.3.7 *Azotobacter vinelandii* βSer188Ala ΔnifB P-cluster behaves differently than its holo counterpart ..... 68

3.4 Conclusions ..... 69

3.5 Materials and methods ..... 70

3.5.1 Site-directed mutagenesis, expression, and purification of *Azotobacter vinelandii* MoFeP protein mutants ..... 70

3.5.2 Oxidative stress test of *Azotobacter vinelandii* cells ..... 71

3.5.3 Growth curves of *Azotobacter vinelandii* cells with different iron concentrations ..... 71

3.5.4 RT-qPCR of *nifK* gene ..... 71

3.5.5 Whole cell $C_2H_2$ reduction activity assays ..... 73

3.5.6 Preparation of reconstituted *Azotobacter vinelandii* βSer188Ala MoFe-protein P-cluster with different metals ..... 73

3.5.7 Mössbauer spectroscopy of *Azotobacter vinelandii* βSer188Ala MoFe-protein ..... 74

3.5.8 Crystallization of mismetallated βSer188Ala MoFe-protein ..... 74

3.5.9 Electron paramagnetic resonance spectroscopy of MoFe-protein ..... 74

3.6 Acknowledgements ..... 75

Chapter 4: CryoEM structures of the nitrogenase complex during catalytic turnover ..... 76

4.1 Abstract ..... 76

4.2 Introduction ..... 76

4.2.1 Structures of nitrogenase under non-resting state conditions ..... 76

4.2.2 Nitrogenase has not previously been structurally characterized during catalytic turnover ..... 82

4.3 Results and discussion ..... 82

4.3.1 CryoEM of the nitrogenase complex reveals an asymmetric 1:1 FeP:MoFeP complex ..... 82

4.3.2 Asymmetric nucleotide hydrolysis and MoFeP residue conformations in $^{t/o}$Complex-1 and $^{t/o}$Complex-2 ..... 100

4.4 Conclusions ..... 116

4.5 Future directions ..... 117

4.5.1 CryoEM of the nitrogenase complex under turnover with non-natural substrates ..... 117

4.5.2 Investigating the nitrogenase complex during low electron-flux $N_2$ catalytic turnover with cryoEM ..... 117

4.6 Materials and methods ..... 119

4.6.1 Protein expression and purification ..... 119

4.6.2 Sample preparation for EM analysis ..... 120

4.6.3 EM data acquisition and image processing ..... 121

4.7 Acknowledgements ..... 125

Chapter 5: Conclusions ..... 127

5.1 Introduction ..... 127

5.2 Redox-mediated dynamics and stabilization of the nitrogenase P-cluster ..... 127

5.3 Dynamics of the nitrogenase complex during catalytic reduction of $N_2$ ..... 129

References ..... 131

LIST OF ABBREVIATIONS

| | |
|---|---|
| Å | angstrom |
| ADP | adenosine diphosphate |
| *adp* | ADP bound nitrogenase complex |
| Ala | alanine |
| *alf* | ADP.$AlF_4^-$-inhibited nitrogenase complex |
| AMPPCP | adenosine-5'-[(β,γ)-methyleno]triphosphate |
| Asp | aspartic acid |
| ATP | adenosine triphosphate |
| *Av* | *Azotobacter vinelandii* |
| BM | Burke's media |
| BM- | Burke's media lacking a fixed source of nitrogen |
| bpy | 2,2-bipyridine |
| cDNA | complementary deoxyribonucleic acid |
| CfbD | methanogenic oxidoreductase |
| CODH | carbon monoxide dehydrogenase |
| cryoEM | cryogenic electron microscopy |
| Cys | cysteine |
| DEAE | dimethylaminoethanol |
| DG1 | docking geometry one |
| DG2 | docking geometry two |
| DG3 | docking geometry three |
| DNA | deoxyribonucleic acid |
| DPOR | dark-operative protochlorophyllide oxidoreductase |

| | |
|---|---|
| DT | dithionite |
| EPR | electron paramagnetic resonance |
| ET | electron transfer |
| Fd | ferredoxin |
| FeMoco | FeMo-cofactor (iron molybdenum-cofactor) |
| FeP | Fe-protein (iron-protein) |
| Fe-S | iron-sulfur |
| FID | flame ionization detector |
| FSC | Fourier shell correlation |
| *Gd* | *Gluconacetobacter diazotrophicus* |
| Gln | glutamine |
| Glu | glutamic acid |
| HAD | 2-hydroxyacyl-CoA |
| HEPES | 4-(2-hydroxyethyl)-1-piperazineethanesulfonic acid |
| HiPIP | high-potential iron-sulfur protein |
| His | histidine |
| ICP-MS | inductively coupled plasma mass spectrometry |
| IDS | indigo disulfonate |
| IS | proposed substrate channel named after authors Igarashi and Seefeldt |
| *Kp* | *Klebsiella pneumoniae* |
| LIP | labile iron pool |
| MoFeP | MoFe-protein (molybdenum iron-protein) |
| MOPS | 3-(N-morpholino)propanesulfonic acid |
| mRNA | messenger ribonucleic acid |

| | |
|---|---|
| MUSCLE | Multiple Sequence Comparison by Log-Expectation |
| MW | molecular weight |
| *nf* | nucleotide-free nitrogenase complex |
| nif- | diazotrophic strain that is unable to fix nitrogen |
| nif+ | diazotrophic strain that is capable of nitrogen fixation |
| *nifB* | gene coding for protein that is part of the FeMoco maturation pathway |
| *nifD* | gene coding for α-subunit of MoFeP |
| *nifH* | gene coding for γ-subunit of FeP |
| *nifK* | gene coding for β-subunit of MoFeP |
| NMA | normal mode analysis |
| $OD_{600}$ | optical density at 600 nm |
| OPA | *o*-phthaladehyde |
| $P^{1+}$ | one-electron oxidized state of the P-cluster |
| PCA | principal component analysis |
| *pcp* | AMPPCP bound nitrogenase complex |
| *pcp/adp* | AMPPCP and ADP bound nitrogenase complex |
| Phe | phenylalanine |
| $P_i$ | inorganic phosphate |
| $P^N$ | all ferrous, fully reduced state of the P-cluster |
| $P^{OX}$ | two-electron oxidized state of the P-cluster |
| Pro | proline |
| QM/MM | quantum mechanics/molecular mechanics |
| RMSD | root-mean-square-deviation |
| RNA | ribonucleic acid |

| | |
|---|---|
| rRNA | ribosomal ribonucleic acid |
| RT | reverse transcription |
| RT-qPCR | quantitative reverse transcription polymerase chain reaction |
| SDS-PAGE | sodium dodecyl sulfate polyacrylamide gel electrophoresis |
| Ser | serine |
| TCD | thermal conductivity detector |
| TL | Thorneley-Lowe |
| TRIS | tris(hydroxymethyl)aminomethane |
| Trp | tryptophan |
| Tyr | tyrosine |
| VFeco | VFe-cofactor (vanadium iron-cofactor) |
| VFeP | VFe-protein (vanadium iron-protein) |
| wt | wild-type |
| *Xa* | *Xanthobacter autotrophicus* |

LIST OF FIGURES

**Figure 1.1** The nitrogen cycle ..... 2

**Figure 1.2** The Mo-nitrogenase complex ..... 4

**Figure 1.3** MgADP bound FeP ..... 5

**Figure 1.4** The Thorneley-Lowe kinetic scheme ..... 9

**Figure 1.5** Docking geometries of the nitrogenase complex ..... 11

**Figure 1.6** Nucleotide-dependent conformational changes in FeP ..... 14

**Figure 1.7** MoFeP superpositions ..... 15

**Figure 2.1** Redox-dependent structural changes of the *Av* nitrogenase P-cluster ..... 19

**Figure 2.2** Redox-dependent structural changes of the *Gd* nitrogenase P-cluster ..... 20

**Figure 2.3** X-ray crystal structures of the P-cluster of *Av* βSer188Ala MoFeP ..... 27

**Figure 2.4** Maps demonstrating complete loss of Fe1 and Fe5 from the IDS-oxidized *Av* βSer188Ala MoFeP P-cluster ..... 27

**Figure 2.5** X-ray crystal structures of the P-cluster of *Av* βPhe99Tyr/βSer188Ala MoFeP ..... 31

**Figure 2.6** Structural alignment of oxidized P-clusters ..... 31

**Figure 2.7** Equilibrium conformational states of the IDS-oxidized [7Fe-7S] P-cluster of *Av* βPhe99Tyr/βSer188Ala MoFeP ..... 32

**Figure 2.8** X-ray crystal structures of the P-cluster of *Av* βPhe99Tyr MoFeP ..... 33

**Figure 2.9** $2F_O$-$F_C$ omit maps contoured at 5.0 σ corresponding to all atoms in residues β99 and β188 and the P-cluster ..... 34

**Figure 2.10** Structures of FeMoco demonstrate proper cluster incorporation into each of the *Av* MoFeP mutants ..... 35

**Figure 2.11** X-band EPR spectra of the *Av* MoFeP variants ..... 36

**Figure 2.12** Parallel-mode X-band EPR spectra of the DT-reduced *Av* MoFeP variants ..... 38

**Figure 2.13** Activity assays for wt, βSer188Ala, βPhe99Tyr/βSer188Ala, and βPhe99Tyr MoFeP ..... 39

**Figure 2.14** Diazotrophic growth curves of *Av* MoFeP variants and wt *Av* ..... 40

**Figure 2.15** Wt *Av* and *Gd* P-clusters with covarying residue (βTyr102 or βHis 101, respectively) ..... 42

**Figure 2.16** *NifK* sequencing results of mutations to *Av* chromosomal DNA ..... 45

**Figure 2.17** SDS-PAGE of various proteins studied in this work ..... 47

**Figure 3.1** Oxidative stress test of wt and βSer188Ala *Av* cells represented as cell survival ..... 54

**Figure 3.2** Diazotrophic growth curves of wt and βSer188Ala *Av* cells under varying concentrations of Fe in the medium ..... 56

**Figure 3.3** Relative diazotrophic *niK* expression rates determined using RT-qPCR ..... 57

**Figure 3.4** Whole-cell $C_2H_2$ reduction assay using the cultures used for RT-qPCR in Figure 3.3 ..... 58

**Figure 3.5** Mössbauer spectra of βSer188Ala after reconstitution with $^{57}Fe^{2+}$ and after subsequent reconstitution with natural abundance $Fe^{2+}$ ..... 60

**Figure 3.6** Crystal structures of *Av* βSer188Ala P-clusters with heterometals ..... 62

**Figure 3.7** X-band EPR spectra (4 K) of wt and βSer188Ala MoFeP after isotope labeling ($^{57}Fe^{2+}$) or soaking with heterometals ($Ga^{3+}$, $Ni^{2+}$, and $Co^{2+}$) ..... 67

**Figure 3.8** X-band EPR spectra collected of DT-reduced apo βSer188Ala MoFeP and IDS-oxidized apo βSer188Ala MoFeP soaked with various metals ($^{57}Fe^{2+}$, $Co^{2+}$, $Ni^{2+}$, $Ga^{3+}$) ..... 69

**Figure 3.9** 1% DNA agarose gel showing representative cDNA samples ..... 73

**Figure 4.1** Carbon monoxide (CO)-bound FeMoco ..... 78

**Figure 4.2** Carbon monoxide (CO)-bound FeVco ..... 78

**Figure 4.3** FeVco bound to a reaction intermediate, proposed to be a protonated N-species ..... 80

**Figure 4.4** $N_2$-species bound FeMoco ..... 81

**Figure 4.5** CryoEM maps of *Av* nitrogenase. ..... 84

**Figure 4.6** Data processing flowchart for the single-particle cryoEM analysis of nitrogenase complexes formed under turnover. ..... 85

**Figure 4.7** Improvements in map quality for the 1:1 FeP:MoFeP complexes formed under turnover. ..... 87

**Figure 4.8** Data processing flowchart for the single-particle cryo-EM analysis of free MoFeP ($^{rs}$MoFeP) 88

**Figure 4.9** Data processing flowchart for the single-particle cryo-EM analysis of the BeFx-trapped nitrogenase complex. ..... 95

**Figure 4.10** Comparison of $BeF_X$-bound cryoEM structure with $AlF_X$ crystal structure. ..... 97

**Figure 4.11** Structural details of nitrogenase complexes characterized under turnover conditions. ..... 101

**Figure 4.12** Principal component analysis (PCA) of FeP. ..... 103

**Figure 4.13** Structural comparison of MoFeP from the turnover complexes with MoFeP from crystal structures. ..... 105

**Figure 4.14** P-clusters of $^{rs}$MoFeP, $^{t/o}$Complex-1, and $^{t/o}$Complex-2. ..... 106

**Figure 4.15** Overlay of important residues between the P-cluster and FeMoco. ..... 107

**Figure 4.16** Diversion of the IS channel during turnover. ..... 109

**Figure 4.17** Overlay of αHis274, αPhe300 and αHis451 from pH 5.0 MoFeP crystal structure and cryoEM structures. ..... 110

**Figure 4.18** The FeMoco environment in the cryoEM structures. ..... 111

**Figure 4.19** Changes in the FeMoco environment observed during catalytic turnover. ..... 112

**Figure 4.20** $^{t/o}$Complex-1, and $^{t/o}$Complex-2 colored by B-factor and comparison of αIII density. ..... 114

**Figure 4.21** Low electron flux (i.e., high salt) turnover cryoEM structure of $\alpha^{1}$ FeMoco ..... 118

LIST OF TABLES

**Table 1.1** Reported potentials of the redox-active centers in *Av* nitrogenase FeP ..... 7

**Table 1.2** Nucleotide-dependent changes in the physical features of the FeP-MoFeP complex..... 12

**Table 2.1** Sequence alignments of the 95 classified nitrogenase sequences ..... 22

**Table 2.2** X-ray data collection and refinement statistics ..... 28

**Table 2.3** Group I MoFeP covariance analysis by identity of residues..... 43

**Table 3.1** Best fit resolution of Mössbauer spectra of $^{57}Fe^{2+}$-reconstituted βSer188Ala MoFeP..... 60

**Table 3.2**. X-ray data collection and refinement statistics ..... 63

**Table 4.1** CryoEM data collection and refinement statistics of *Azotobacter vinelandii* $^{t/o}$Complex-1 and $^{t/o}$Complex-2. ..... 90

**Table 4.2** CryoEM data collection and refinement statistics of *Azotobacter vinelandii* $^{rs}$MoFeP..... 92

**Table 4.3** CryoEM data collection and refinement statistics of *Azotobacter vinelandii* nitrogenase complex inhibited by $BeF_x$..... 98

**Table 4.4** RMSDs of MoFeP alignments ..... 108

**Table 4.5** Average B-factors for the MoFeP components and the αIII domains in various nitrogenase X-ray crystal structures. ..... 115

ACKNOWLEDGMENTS

I would like to thank my advisor, Akif Tezcan, for giving me the opportunity to conduct research in his lab. After leaving a different graduate program, I was worried that I wouldn't be able to join a top tier lab. Akif believed in me and welcomed me. What I accomplished in grad school would not have been possible without his support and enthusiasm. He has helped me develop into a better scientist by teaching me how to identify the big scientific questions, how to design experiments, and how to best convey my findings to a variety of audiences. The lab is very dynamic with people constantly moving on to new positions and new people joining, and Akif has found a way to keep it full of amazing people that are a joy to work with.

I would like to thank all of the amazing team nitro members that have supported and worked alongside me. The mentorship and friendship of Faith Katz was truly amazing. I barely even knew what a protein was when I joined the lab. She quickly taught me everything she knew about nitrogenase, and she was so much fun to work with. I would never have been able to produce results so early in grad school without her guidance. While I didn't overlap with Cedric Owens, he still helped me by answering the millions of questions I emailed him. All of the team nitro undergrads- Alkane, Laura, and Robin- have been so dedicated and excited about research, and they all have such amazing attitudes. Now, Sarah Narehood is taking the team nitro torch. It has been so great training her, and I am excited to see what she will accomplish during grad school.

I would also like to thank the non-nitro members of the Tezcan lab that have helped me along the way. Everyone in the lab has always been supportive. I am thankful that of all the people from my class, Albert is the one that joined the Tezcan lab with me. I admire his work ethic, sense of humor, and concern for others. I am grateful for all of the help JR provided me with during my first few years in the lab. I was initially intimidated by both his seriousness and his breadth of knowledge, but he was always willing to answer my questions and help me with experiments. After getting to know him better, I also realized that he has a non-serious side too. Rohit was the first friend that I made in San Diego, and I appreciate how he

made me feel so welcome. Rob and Rohit always let me bounce my ridiculous nitrogenase ideas off of them, they proofread about a hundred million drafts of my chem rev, and they kept me sane on all of the coffee breaks we'd take together. Just about everything I know about protein crystallography, I learned from Jake. I am grateful for Julian's help and support with many things, especially molecular biology. Jie, Derek, Eyal, Nicole, and Raymond taught me to stay calm even when things went wrong in addition to helping me with my research. Alex was forced to endure more of my crazy ideas than most due to his proximity to my desk, and I am grateful for the insights that he provided and his willingness to always listen. I enjoyed exchanging jokes with Lewis, and he always made Mondays exciting. I am thankful for the conversations with Kenneth about whatever crazy (mostly non-lab related) things we were interested in. I have really enjoyed having Yiying as a labmate- her motivation and amazing attitude are contagious.

I would also like to thank many other people at UCSD that have helped me during grad school. I am extremely grateful for the mentorship and cheerleading that I received from Betsy Komives. She is an amazing role-model, and I am lucky to have support from someone like her. I did not have the expertise needed to carry out cryoEM experiments on my own. Mark Herzik and Brian Cook have been instrumental in completing that project, and it has been incredibly fun working with them. Mark even went so far as to sacrifice the skin on his forearms for our project. I would like to thank Christine Morrison for teaching me how to do anaerobic crystallography. Ryan Lumpkin's quirkiness, excitement for everything, and amazing friendship were instrumental.

Thank you to the people at institutions outside of UCSD that have helped me throughout grad school. Mike Green and Mackenzie Field helped me with all things spectroscopy. Valerie Cash and Dennis Dean have helped me by providing many *Av* strains and answering questions about molecular biology with *Av*, making it possible for me to generate the many strains needed for my experiments.

I also need to thank all of my friends from outside the lab. My friendship with Adam has helped keep me sane, and I know we will be friends for life. All of our hikes and beach fires have been so great. I have really enjoyed hanging out with Lindsey and Mark, even when Lindsey helps Jeremy beat me at

board games. I never expected to become friends with a student that I TA'ed, but I ended up becoming good friends with Shay, who is such a genuine and hilarious person. Climbing has been a great outlet for me, and I appreciate all of the friends that I have made at the gym.

I would like to thank my family who have provided me with support. My mom and dad have always encouraged me in my interests, including science. I'd also like to thank my sister for all of the phone conversations and for visiting me during grad school. She's always willing to lend an ear, even when we have to play phone tag because my phone is perpetually on silent.

Importantly, I need to thank my husband, Jeremy, for his constant encouragement and love throughout all my iterations of grad school. He has supported me at my lowest lows and my highest highs, and I don't think I could have accomplished so much without him. We have done so many amazing things together since moving to San Diego, and I can't wait to move to Germany with him and begin the next chapter of our lives together.

This dissertation was funded in part by UCSD's Molecular Biophysics Training Grant (NIH).

Chapter 1 is reproduced, in part, with permission from H. Rutledge and F. A. Tezcan. Electron Transfer in Nitrogenase, *Chemical Reviews* **2020**, *12*, 5158-5193. The dissertation author is the primary author on all reprinted materials.

Chapter 2 is reproduced, in part, with permission from H. Rutledge, J. Rittle, L. M. Williamson, W. A. Xu, D. M. Gagnon, and F. A. Tezcan. Redox-Dependent Metastability of the Nitrogenase P-Cluster, *Journal of the American Chemical Society* **2019**, *141*, 10091-10098. The dissertation author is the primary author on all reprinted materials.

Chapter 3 is reproduced, in part, with permission from H. Rutledge, M. J. Field, J. Rittle, M. T. Green, and F. A. Tezcan. The Role of Serine Coordination in the Structural and Functional Protection of the Nitrogenase P-cluster. The dissertation author is the primary author on all reprinted materials.

Chapter 4 is reproduced, in part, with permission from H. Rutledge, B. Cook, H. Nguyen, M. Herzik, and F. A. Tezcan. CryoEM structures of nitrogenase complex during catalytic turnover. The dissertation author is the primary author on all reprinted materials.

# VITA

## EDUCATION

| | |
|---|---|
| 2012 | B.S., Chemistry, Rice University |
| 2014 | M.S., Chemistry, University of Chicago |
| 2022 | Ph.D., Chemistry, University of California San Diego |

## HONORS AND AWARDS

| | |
|---|---|
| 2021 | Distinguished Graduate Student Fellowship |
| 2020 | Teddy Traylor Award for Graduate Research in Chemistry |
| 2020 | Ford Foundation Dissertation Fellowship Honorable Mention |
| 2017 – 2019 | NIH Molecular Biophysics Training Grant Fellow |
| 2014 | Physical Sciences Division Teaching Award |
| 2013 – 2014 | Graduate Assistance in Areas of National Need (GAANN) Fellow |
| 2012 | Arthur L. Draper Award for Excellence in Undergraduate Chemistry |

## PUBLICATIONS

**Rutledge, H.**, Tezcan, F.; Electron Transfer in Nitrogenase. *Chem. Rev*. **2020**, 120(12).

**Rutledge, H.**, Rittle, J., Williamson, L., Xu, W., Gagnon, D, Tezcan, F.; Redox-Dependent Metastability of the Nitrogenase P-Cluster. *J. Am. Chem. Soc*. **2019**, 141(25).

**Rutledge, H.**, Oliva-Chatelain, B. L., Maguire-Boyle, S. J., Flood, D. L. & Barron, A. R. Imbedding Germanium Quantum Dots in Silica by a Modified Stöber Method. *Mater. Sci. Semicond. Process*. **2014**, 17.

## FIELDS OF STUDY

Major Field: Chemistry

Studies in Bioinorganic Chemistry, Biophysics
Professor F. Akif Tezcan

ABSTRACT OF THE DISSERTATION

Redox Dynamics of Nitrogenase

by

Hannah Leah Rutledge

Doctor of Philosophy in Chemistry

University of California San Diego, 2022

Professor F. Akif Tezcan, Chair

Nitrogen is an essential component of many biomolecules such as DNA and proteins. Biological nitrogen fixation is carried out by the enzyme nitrogenase. This multi-electron reduction requires the precise timing of electron and proton flow from the reductase, Fe-protein, through the [8Fe-7S] P-cluster to the catalytic site, FeMo-cofactor, located in the catalytic protein, MoFe-protein. Electron flow through nitrogenase is a dynamic process controlled by a conformational "gate" in which structural changes in MoFe-protein promote the accumulation of electrons at the FeMo-cofactor. Elucidating the mechanism thus requires a detailed understanding of structural changes that occur during catalysis. I have investigated the dynamics involved in nitrogenase catalysis, focusing on (1) the P-cluster's dynamic role in orchestrating electron transfer to FeMo-cofactor and (2) structural characterization of the nitrogenase complex during $N_2$ reduction.

The experimental results discussed in Chapters 2 and 3 of this dissertation describe how the P-cluster has evolved to rest on the brink of stability, and that mutations to the redox-switchable, O-based P-cluster ligand (serine or tyrosine) result in a cluster that can reversibly lose Fe atoms. Furthermore, the O-

based ligand protects the P-cluster from oxidative stress *in vivo*, is required for efficient diazotrophic growth under Fe-limiting conditions, and protects the P-cluster from metal exchange *in vitro*. These results indicate the native flexibility of the P-cluster are vital to its function in timing electron transfer to the active site.

In Chapter 4, I discuss structural characterization of the nitrogenase complex at high-resolution during catalytic $N_2$ reduction with cryoEM. Many structures were determined: structures of the complex during turnover at 2.6 Å and 2.7 Å, free MoFeP at 1.9 Å, and ADP.$AlF_4^-$-inhibited complexes at 2.4 Å and 2.8 Å. Taken together, these structures have provided valuable insights into the mechanism of biological nitrogen fixation. The complex formed during turnover has a 1:1 Fe-protein:MoFe-protein stoichiometry, implying that there is negative cooperativity between the two halves of the complex. Furthermore, conformational differences between the two halves of MoFe-protein reveal previously unobserved conformational changes, which may be a part of the conformational "gate". These observations provide critical insights into the dynamics required for nitrogenase function.

## Chapter 1: Introduction to biological nitrogen fixation by molybdenum-nitrogenase

### 1.1 Introduction to the nitrogen cycle and biological nitrogen fixation

Nitrogen is an essential element for all forms of life. It is required for the synthesis of many biomolecules including macromolecules such as proteins, deoxyribonucleic acid (DNA), and ribonucleic acid (RNA), as well as coenzymes and cofactors including chlorophyll, heme, adenosine triphosphate (ATP), and cobalamin. Despite the Earth's atmosphere being the largest reservoir of nitrogen (in the form of dinitrogen, $N_2$) on the surface of the planet, most organisms find this form of nitrogen to be metabolically unreactive. Instead, most organisms rely on bioavailable, or fixed forms of nitrogen. The nitrogen cycle describes the biogeochemical transformations of nitrogen (**Fig 1.1**). To increase the amount of fixed nitrogen in the cycle, atmospheric $N_2$ must be converted, either abiotically via production of $NO_X$ species by lightning, or biotically via the enzymatic production of ammonia ($NH_3$). The group of organisms that are capable of enzymatic production of ammonia are called diazotrophs, which includes some bacteria and archaea. Breaking and reducing the strong, non-polar triple bond of $N_2$ is arguably one of the most difficult and complex biochemical reactions. In an industry setting, this reaction is carried out by the Haber-Bosch process which requires extreme conditions (>450 ˚C, >250 atm) and is responsible for ~2% of global energy consumption.[1, 2] Biologically fixed nitrogen accounts for the majority of non-industrially produced fixed nitrogen in the nitrogen cycle. Nitrogenase is the enzyme that carries out biological fixation of atmospheric $N_2$ into $NH_3$. Unlike the harsh conditions of the Haber-Bosch process, biological nitrogen fixation must occur under physiological conditions (~20 ˚C, 1 atm). The most studied isoform of nitrogenase, molybdenum (Mo)-nitrogenase, reduces $N_2$ according to the equation:[3]

$$N_2 + 8e^- + 8H^+ + nATP \longrightarrow 2NH_3 + H_2 + nADP + nP_i \qquad \text{(Equation 1)}$$

where *n* is commonly believed to be 16, yielding a stoichiometry of two ATPs hydrolyzed per one electron and one proton transferred.[4-7] The complexity of tasks that nitrogenase must carry out in concert are evident from Equation 1. Nitrogenase must activate the extremely stable (both kinetically and

thermodynamically) $N_2$ triple bond by precisely orchestrating the sequential transfer of many electrons over a long distance.[8] These tasks are powered by ATP hydrolysis. Nitrogenase has evolved unique components to perform this reaction. There are three known classes of nitrogenases, Mo-, V- and Fe-only nitrogenases (named after the metal content of their catalytic clusters),[9, 10] with the Mo-containing isoform being the subject of this dissertation. V- and Fe-only nitrogenases are less efficient than their Mo-counterpart in that they require more ATP and evolve more $H_2$ per $N_2$ reduced.[11-14]

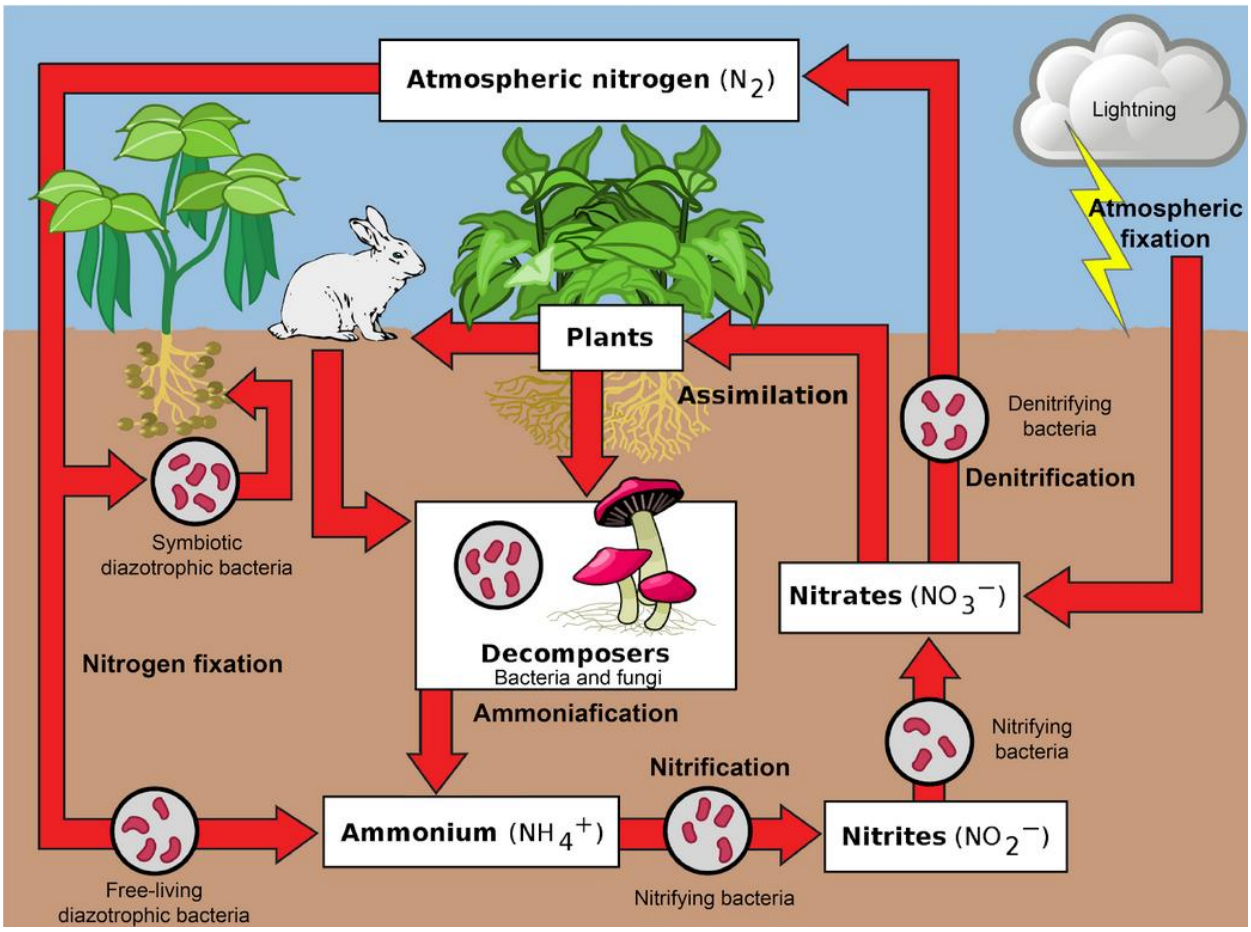


**Figure 1.1** The nitrogen cycle. The majority of biogeochemically produced nitrogen comes from nitrogen fixation by free-living and symbiotic diazotrophic bacteria (bottom left). Atmospheric fixation by lightning (top right) also produces bioavailable forms of nitrogen from $N_2$. This figure is adapted from the original version by Johann Dréo and is licensed under the Creative Commons Attribution-Share Alike 3.0 license.

## 1.2 Structure and properties of the nitrogenase proteins

### 1.2.1 Overview of Fe-protein and MoFe-protein

The Mo-nitrogenase enzyme is composed of two component proteins (**Fig 1.2**): the reductase and ATPase, termed Fe-protein (FeP), and the catalytic component, termed MoFe-protein (MoFeP).[10] FeP is a homodimer ($\gamma^1\gamma^2$ or $\gamma^3\gamma^4$)[15] that is coded for by the highly conserved *nifH* gene.[16] FeP contains a [4Fe-4S] cluster that is situated between the two γ-subunits and is ligated by four Cys residues (two from each γ-subunit), and each γ-subunit provides one nucleotide binding site.[15] MoFeP is a heterotetramer ($\alpha^1\beta^1\alpha^2\beta^2$) coded for by the *nifDK* genes for the α- and β-subunits, respectively.[17] Each αβ-dimer of MoFeP contains two unique superclusters: an [8Fe-7S] cluster and a [7Fe-1Mo-9S-1C-*R*-homocitrate] cluster termed the P-cluster and FeMo-cofactor (FeMoco), respectively.[17-21] The P-cluster serves as an intermediary electron relay site, and FeMoco is the site of catalysis.

### 1.2.2 Structure and properties of Fe-protein and the [4Fe-4S] cluster

FeP has many vital roles in nitrogenase function beyond providing reducing equivalents to MoFeP.[22] Here, I will focus only on the structure of FeP and its role as the electron donor to MoFeP. FeP is a $C_2$ symmetric protein (MW ~60 kDa).[15] Each γ-subunit contains an α/β domain consisting of an eight-stranded β-sheet surrounded by nine α-helices, and they are bridged by a [4Fe-4S] cluster (**Fig 1.3**). Each of the subunits contains a single nucleotide-binding site that consists of the canonical nucleotide binding motifs switch regions: the Walker A motif (also known as the P-loop), the Walker B motif,[23-25] Switch I, and Switch II.[26, 27] Nucleotide binding to FeP induces large scale conformational changes across the protein.[26, 27] The Switch regions interact with the terminal phosphate of ATP and undergo conformational changes during ATP hydrolysis.

FeP's architecture is distinctive from typical electron transfer (ET) proteins such as flavodoxins, ferredoxins, and cytochromes in many regards. Typical ET proteins are single-domain structures and are considerably smaller than FeP (MW < 20 kDa). Furthermore, [4Fe-4S] ferredoxins contain mostly buried

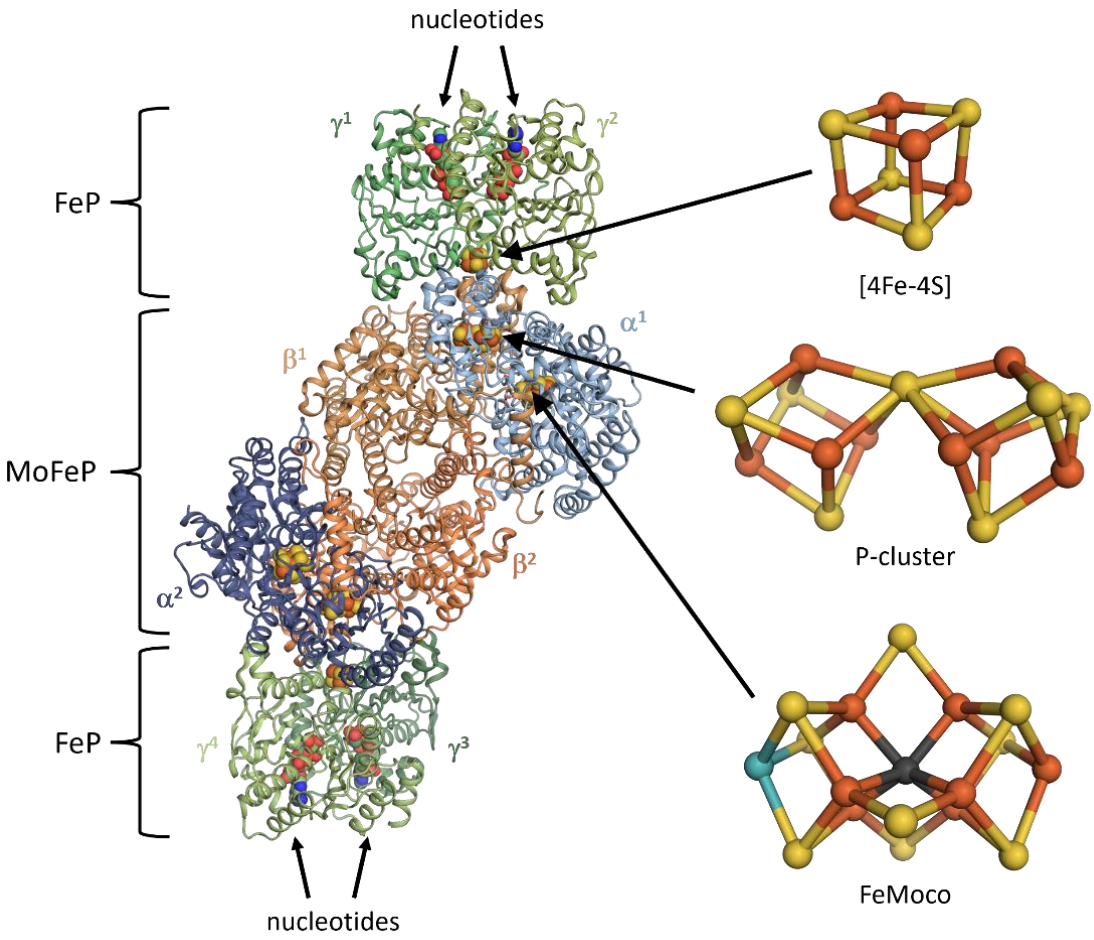


**Figure 1.2** The Mo-nitrogenase complex. FeP is depicted in green. MoFeP is depicted in orange and blue. Subunits of component proteins are labeled. Each MoFeP contains two P-clusters and two FeMocos, and each FeP contains one [4Fe-4S] cluster and two nucleotide binding sites. PDB ID: 4WZB

clusters, unlike FeP. The [4Fe-4S] cluster in FeP is highly solvent exposed, and the extent of the exposure is mediated by nucleotide-binding. Upon binding of ATP, solvent accessibility of the cluster increases considerably, as evidenced by fast Fe-removal kinetics by chelators (2,2'-bipyridine or bathophenanthroline disulfonate) only in the presence of MgATP.[28-33] The location of the [4Fe-4S] cluster in FeP is located in an unusual helix-cluster-helix motif where each subunit provides one helix, termed the γ100s helix (γ97-112, *Azotobacter vinelandii* (*Av*) numbering) (**Fig 1.3**). The N-terminal ends of the helices are located proximal to the cluster, which may provide a means to tune its midpoint potential by means of placing the positive ends of the helix dipoles next to the cluster. There are a handful of other

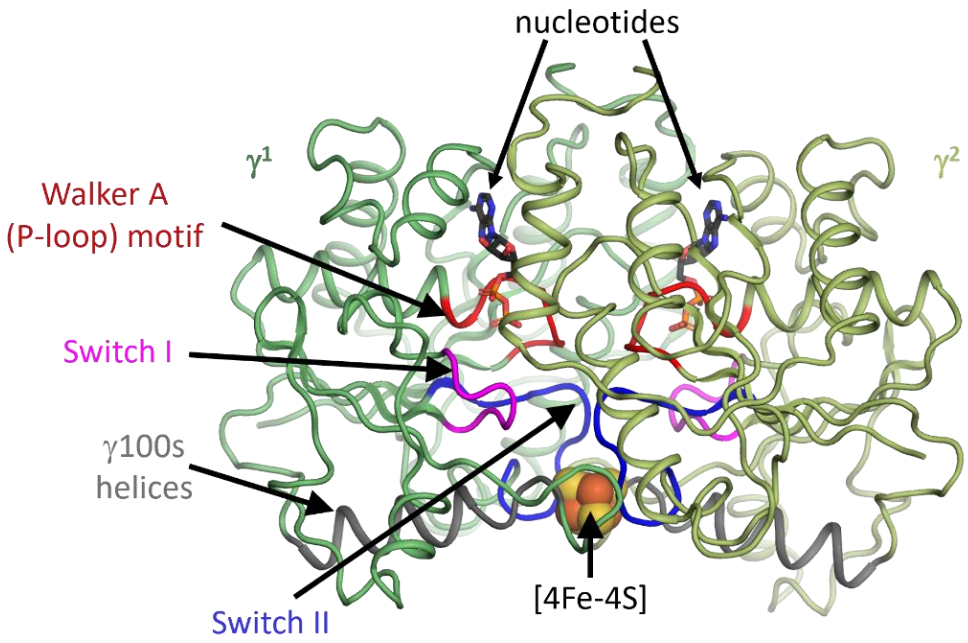


**Figure 1.3** MgADP bound FeP. Canonical motifs are shown: Walker A motif (red), Switch I (magenta), and Switch II (blue). Additionally, the nucleotides (sticks), the γ100s helices (gray), and the [4Fe-4S] cluster (orange and yellow spheres) are labeled. The two γ-subunits are colored dark and light green. PDB ID: 6N4L

[4Fe-4S] containing reductases that share these uncommon properties including the activators of 2-hydroxyacyl-CoA (HAD). This class of proteins has been termed "archerases" due to the geometry resembling an archer's bowstring.[34-36]

Additionally, the redox properties of FeP differ from canonical [4Fe-4S] ferredoxins, which can only access one redox couple under physiological conditions (approximately -1 V to +1 V), either $[4Fe\text{-}4S]^{2+}/[4Fe\text{-}4S]^{1+}$ or $[4Fe\text{-}4S]^{3+}/[4Fe\text{-}4S]^{2+}$ in the case of low-potential ferredoxins or high-potential iron-sulfur (Fe-S) proteins (HiPIPs), respectively.[37, 38] In contrast, the [4Fe-4S] cluster of FeP can access two redox couples, including the highly reduced, all ferrous state which is inaccessible to typical ferredoxins: $[4Fe\text{-}4S]^{2+}/[4Fe\text{-}4S]^{1+}$ and $[4Fe\text{-}4S]^{1+}/[4Fe\text{-}4S]^{0}$.[39-43] Aside from FeP, this redox state has only been reported in rare biological systems[36, 44] and model complexes.[45, 46] Low potential ferredoxins and HiPIPs modulate the midpoint potentials of their [4Fe-4S] clusters with the protein environment with values in the range of -150 to -700 mV and +100 to +400 mV, respectively.[38] The redox potentials of FeP's

[4Fe-4S] cluster is further modulated by binding of nucleotides.[30, 39, 47, 48] While there is general agreement upon the 2+/1+ potential in the literature,[30, 39, 47, 48] there is conflicting reports of the 1+/0 potential (**Table 1.1**).[39, 49] The unique structural and electronic properties of FeP and its [4Fe-4S] cluster underly its role as the unique reductase of MoFeP.

### 1.2.3 Structure and properties of MoFe-protein, the P-cluster, and FeMoco

The catalytic portion of Mo-nitrogenase, MoFeP, contains two α- and two β-subunits (MW ~240 kDa). The α- and β-subunits are similar in structure and likely arose from gene duplication events during the evolution of Mo-nitrogenase.[52] Each subunit consists of ~500 amino acids and contains three α/β-type domains.[53] The two αβ-dimers are roughly related by a $C_2$ rotation-axis, and each dimer houses one P-cluster and one FeMoco.[53] The P-cluster bridges the α- and β-subunits.[53] Upon FeP binding, the P-cluster is situated between FeP's [4Fe-4S] cluster and FeMoco, where it orchestrates ET upon FeP-MoFeP-association.[54-57] Its ability to precisely time electron flow to the active site is likely dependent on its dynamic nature, unlike canonical ET clusters.

The P-cluster is unique both in its composition, [8Fe-7S], and in its protein environment. It resembles two [4Fe-4S] clusters fused at a central, $\mu^6$ sulfide (**Fig 1.2**). In canonical Fe-S clusters, every Fe atom is coordinated to a terminal side chain residue (typically Cys or His), and the ligand set is stable. In contrast, the P-cluster is ligated by four terminal and two bridging Cys residues. Furthermore, one-electron oxidation from the dithionite (DT)-reduced state, termed $P^N$, to the $P^{1+}$ state results in one cubane opening as an Fe center dissociates from the central sulfide and coordinates to an oxygenic ligand (Ser or Tyr).[58] Oxidation by one more electron to the $P^{OX}$ state further opens the same cubane as another Fe moves away from the central sulfide and binds the backbone amidate of one of the bridging Cys ligands.[21, 59] The oxygenic and amidate ligands likely serve to stabilize the oxidized P-cluster in a redox-switchable manner. The midpoint potentials of $P^{OX}/P^{1+}$ and $P^{1+}/P^N$ couples are virtually indistinguishable at -310 mV.[51, 60-62] Whether both redox couples are relevant to catalysis has yet to be established, although

**Table 1.1** Reported potentials of the redox-active centers in *Av* nitrogenase FeP. This table is reproduced, in part, from ref 8.

| Redox couple | Nucleotides/ Metal | Potential (mV) vs NHE | pH | Type of Measurement | Reference |
|---|---|---|---|---|---|
| $[4Fe\text{-}4S]^{2+}/[4Fe\text{-}4S]^{1+}$ | Nucleotide-free | −300 | 7.0 - 9.0 | Controlled potential microcoulometry and spectroelectrochemistry | 47 |
| | | −280 | 8.0 | EPR potentiometric titration | 48 |
| | | −310 | 8.0 | Controlled potential microcoulometry | 39 |
| | | −290 | 8.0 | Controlled potential microcoulometry | 30 |
| $[4Fe\text{-}4S]^{2+}/[4Fe\text{-}4S]^{1+}$ | $MgCl_2$ | −393 | 7.0 | EPR potentiometric titration | 50 |
| | | −330 | 7.0 – 9.0 | Controlled potential microcoulometry and spectroelectrochemistry | 47 |
| $[4Fe\text{-}4S]^{2+}/[4Fe\text{-}4S]^{1+}$ | MgATP | −435 | 7.0 | EPR potentiometric titration | 50 |
| | | −430 | 7.0 – 9.0 | Controlled potential microcoulometry and spectroelectrochemistry | 47 |
| | | −430 | 8.0 | EPR potentiometric titration | 48 |
| | | −430 | 8.0 | Controlled potential microcoulometry | 30 |
| $[4Fe\text{-}4S]^{2+}/[4Fe\text{-}4S]^{1+}$ | MgAMPPCP | −385 | 7.0 – 9.0 | Controlled potential microcoulometry and spectroelectrochemistry | 47 |
| $[4Fe\text{-}4S]^{2+}/[4Fe\text{-}4S]^{1+}$ | MgADP | −473 | 7.0 | EPR potentiometric titration | 50 |
| | | −490 | 7.0 – 9.0 | Controlled potential microcoulometry and spectroelectrochemistry | 47 |
| | | −440 | 8.0 | Controlled potential microcoulometry | 30 |
| $[4Fe\text{-}4S]^{2+}/[4Fe\text{-}4S]^{1+}$ | ATP | −340 | 7.0 – 9.0 | Controlled potential microcoulometry and spectroelectrochemistry | 47 |
| $[4Fe\text{-}4S]^{1+}/[4Fe\text{-}4S]^{0}$ | Nucleotide-free | −460 | 7.0 - 8.0 | Controlled potential microcoulometry | 39 |
| | | −790 | 8.0 | Controlled potential microcoulometry | 49 |
| $[4Fe\text{-}4S]^{2+}/[4Fe\text{-}4S]^{1+}$ | Nucleotide-free ΔLeu127 FeP | −420 | 8.0 | EPR potentiometric titration | 51 |
| $[4Fe\text{-}4S]^{2+}/[4Fe\text{-}4S]^{1+}$ | Nucleotide-free ΔLeu127 FeP complexed with MoFeP | −620 | 8.0 | EPR potentiometric titration | 51 |

circumstantial evidence (both the [4Fe-4S] cluster of FeP and the P-cluster can reversibly access two redox couples) indicates that the [4Fe-4S] cluster may indeed transfer two electrons at a time to the P-cluster. In combination, the unique structural features and dynamics of the P-cluster suggest that the P-cluster is an active ET relay site that plays a key role in reducing $N_2$.

Similar to the P-cluster, FeMoco is unique in both its composition and dynamics. FeMoco is a large, highly symmetric [7Fe-1Mo-9S-1C-*R*-homocitrate][18-20] cluster (**Fig 1.2**) that serves as the active site where $N_2$ binds, is activated and reduced to two $NH_3$ molecules. FeMoco resembles two cubanes that are fused at the central (and biologically unprecedented) $\mu^6$ carbide. The Fe atoms in the cubanes are further connected by three sulfides, termed the "belt" sulfides. These sulfides provide the cluster with an unusual stoichiometry in which there is one more acid-labile sulfide than there are metal ions. FeMoco is bound to MoFeP through ligation of a terminal Cys to the terminal Fe and a terminal His to the Mo atom. Additionally, *R*-homocitrate is a bidentate ligand to the Mo atom. The geometry and ligands of FeMoco result in all the metals being coordinatively saturated: all Fe atoms are tetrahedrally coordinated and Mo is octahedrally coordinated. Thus, proposed binding modes of $N_2$ to FeMoco require structural rearrangements for catalysis. Such conformational changes are supported by displacement of one of the belt sulfides from FeMoco upon binding of the inhibitor carbon monoxide (CO)[63] and the (disputed) structures of nitrogen-species- bound FeMoco[64-66] and VFeco (the V-nitrogenase analog of FeMoco).[67, 68]

### 1.3 Electron transfer in nitrogenase is a dynamic process

#### 1.3.1 The Thorneley-Lowe model

In the 1970s, Thorneley and Lowe began detailed studies into the mechanism of nitrogenase catalysis that culminated in the proposed catalytic mechanism called the Thorneley-Lowe (TL) model (**Fig 1.4**).[69-81] Their model has impressively withstood the test of time, despite their work taking place long before any structures of the nitrogenase proteins had been determined. While many details have been

added to their model since their original publications, no major revisions have been necessary.[82] The TL model can be split into two cycles: the FeP cycle (**Fig 1.4a**) and the MoFeP cycle (**Fig 1.4b**).

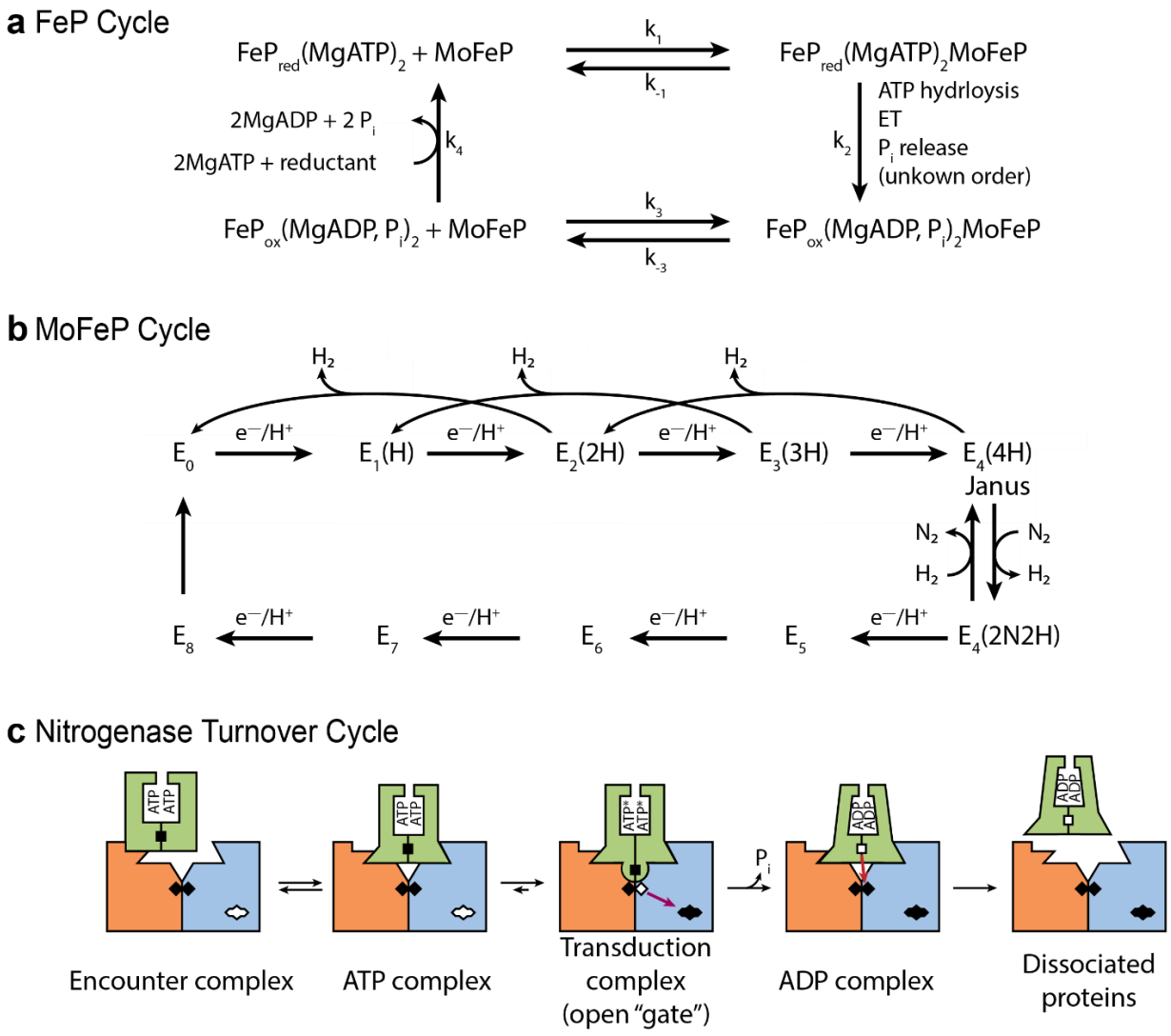


**Figure 1.4** The Thorneley-Lowe kinetic scheme. (a) The FeP cycle of the TL model. (b) The simplified MoFeP cycle of the TL model. (c) The nitrogenase turnover cycle including the proposed order of events where ATP hydrolysis occurs after the first ET event. Adapted from reference 8.

In the FeP cycle (**Fig 1.4a**), FeP binds two molecules of MgATP. The MgATP-FeP complex then associates with MoFeP, and many events occur including ATP hydrolysis, $P_i$ release, and ET from the [4Fe-4S] cluster to MoFeP, although the order of these events is still debated. MgADP-FeP then

dissociates from MoFeP, followed by reduction of the [4Fe-4S] cluster and exchange of MgADP for MgATP, completing the FeP cycle.[8, 83]

At least eight electrons must be transferred from FeP to MoFeP in order to reduce one molecule of $N_2$ and to produce the concomitant molecule of $H_2$ (Equation 1). Each FeP cycle delivers only one or two electrons (the number of electrons transferred per FeP cycle is still controversial), thus multiple (at least four) cycles of FeP-MoFeP association and dissociation are required for $NH_3$ production. With each ET event, FeMoco becomes more reduced, and this is depicted in the TL MoFeP cycle as $E_n$ ($0 \leq n \leq 8$) states where $n$ = the number of reducing equivalents FeMoco has received (**Fig 1.4b**). $N_2$ cannot bind to FeMoco until MoFeP has reached the $E_4$ state.[84, 85] After $N_2$ binds and undergoes the first reduction to a diazene state, the MoFeP cycle becomes committed to $NH_3$ production. Prior to this step, MoFeP can decay to a previous $E_{n-2}$ state via the reduction of two protons to form $H_2$. The $E_4$ state has been nicknamed the Janus intermediate after the Roman god of transitions because $E_4$ stands at a crossroads where MoFeP either reverts to a lower $E_n$ state via $H_2$ production or becomes committed to $N_2$ reduction.[84, 85]

The MoFeP cycle has been expanded upon in recent decades. Each FeP-MoFeP association event is coupled with many changes that take place within MoFeP (**Fig 1.4c**): (1) FeP forms an encounter complex with MoFeP.[86] (2) FeP forms a stable ATP complex with MoFeP.[55] (3) FeP transduces conformational changes in MoFeP, forming the transduction complex.[87] (4) ET proceeds from the P-cluster to FeMoco, ATP is hydrolyzed, and the P-cluster is reduced by FeP's [4Fe-4S] cluster, forming the ADP complex.[55, 56] (5) Finally, FeP dissociates from MoFeP. The precise order of the events in (4) is still not well understood. Characterization of the MoFeP $E_n$ states in the TL cycle is further complicated by the large ensemble of states in which MoFeP is reduced by FeP up to eight times and by the number of states the complex can form (encounter complex, ATP complex, transduction complex, ADP complex).

### 1.3.2 Nucleotide-dependent Fe-protein—MoFe-protein docking interactions

It is evident that FeP must form specific interactions with MoFeP to induce ET based on the observations that FeP is the only reductase that can activate MoFeP for $N_2$ reduction, that FeP requires ATP hydrolysis for ET to occur, and that ATP hydrolysis by FeP only occurs in the presence of MoFeP.[23, 88] Crystal structures of the nitrogenase complex from the organism *Azotobacter vinelandii* (*Av*) were solved in the presence of ADP.$AlF_4^-$ (an inhibitor[54] that traps the complex in a state similar to the ATP hydrolysis transition-state,[89, 90] hereafter referred to as *alf*), AMPPCP (a non-hydrolyzable ATP analog, hereafter referred to as *pcp*)[55], ADP (hereafter referred to as *adp*),[55] and in the presence of no nucleotides (hereafter referred to as *nf*)[55] (**Fig 1.5**). These structures demonstrated that FeP can occupy three distinct, nucleotide-dependent docking sites on the surface of MoFeP (referred to as DG1, DG2, and DG3).

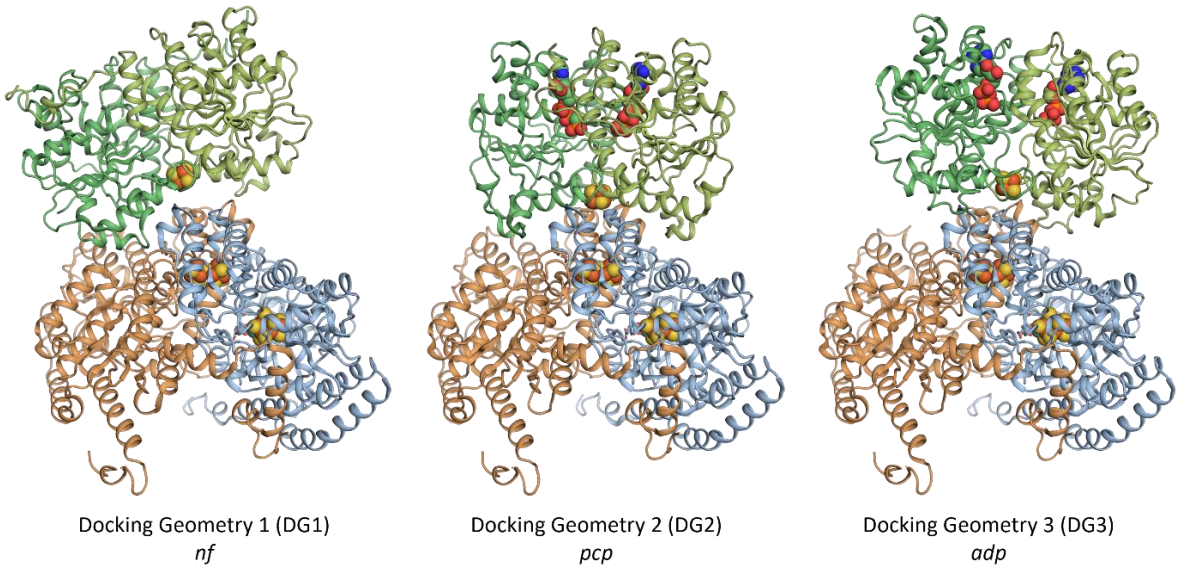


**Figure 1.5** Docking geometries of the nitrogenase complex. Only one half of MoFeP (one αβ-dimer) and one FeP dimer is shown. Nucleotides and Fe-S clusters are shown as spheres, colored by element. FeP is shown in green. MoFeP is shown in blue and orange for the α- and β-subunits, respectively. Left: Docking geometry 1 (DG1) is occupied by *nf* (PDB ID: 2AFH). The ratio of this complex is 1:1 FeP:MoFeP, unlike the other complexes which crystallized in a 2:1 FeP:MoFeP stoichiometry. Middle: DG2 is *pcp* (PDB ID: 4WZB). This DG places the P-cluster in closest proximity to the [4Fe-4S] cluster (ET-active state). Right: DG3 is occupied by *adp* (PDB ID: 2AFI).

DG1 is observed in *nf*, in which FeP is situated primarily over the β-subunit of MoFeP.[55] This interaction contains a large hydrogen-bonding network between a negatively-charged patch on FeP and a

positively-charged patch on MoFeP. Mutagenesis studies in which these electrostatic interactions were altered indicated that this DG is mechanistically relevant, and it has been termed the "encounter complex".[86] DG2 is occupied by *alf* and *pcp*.[54, 55] In DG2, FeP is situated over both the α- and β-subunits of MoFeP such that the pseudo-2-fold symmetry axis of the αβ-dimer is aligned with the 2-fold symmetry axis of FeP. DG2 has the largest buried surface area and places the [4Fe-4S] cluster of FeP in closest proximity to the P-cluster of MoFeP (**Table 1.2**). Thus, DG2 is the most likely to be the "activated" complex in which ET occurs. DG3 is occupied by *adp*.[55] In DG3, FeP rests primarily over the α-subunit of MoFeP. Taken together, these crystal structures represent snapshots of the nucleotide-dependent FeP-MoFeP interactions that occur during catalysis. Despite FeP being a homodimer, the motion of FeP appears to be steered unidirectionally across the MoFeP surface, driven by a combination of ATP hydrolysis and specific interactions between FeP and MoFeP.

**Table 1.2** Nucleotide-dependent changes in the physical features of the FeP-MoFeP complex. This table is reproduced, in part, from ref 8.

| **Complex (DG)** | **Buried surface area (Å$^2$)** | **γ100s helices angle, ϕ (0° is coplanar)** | **Center-to-center distance from P-cluster to [4Fe-4S] (Å)** |
|---|---|---|---|
| *nf* (DG1) | 2800 | 30 | 23.2 |
| *pcp* (DG2) | 3700 | 21 | 17.8 |
| *adp* (DG3) | 1600-2000 | 26-33 | 22.6-23.7 |
| *alf* (DG2) | 3400-3600 | 12-13 | 17.5-17.6 |
| *pcp/adp* (DG2) | 3600 | 11 | 17.9 |

Recently, the structure of the nitrogenase complex was co-crystallized in the presence of both MgADP and MgAMPPCP.[56] Interestingly, the complex that formed (hereafter referred to as *pcp/adp*) had selectively bound MgAMPPCP to the $\gamma^1$-subunit (located above the β-subunit of MoFeP) and MgADP to the $\gamma^2$-subunit (located above the α-subunit of MoFeP). The preference of FeP, which is a symmetric

homodimer, to asymmetrically bind ADP and AMPPCP suggests that the interactions between FeP and MoFeP influence the selectivity of nucleotide-binding. Furthermore, this asymmetry implies that the firing of nucleotide hydrolysis in the nitrogenase complex occurs sequentially rather than simultaneously.

In addition to the large differences in overall complex geometry in the DGs, there are also large, nucleotide-dependent conformational changes within FeP.[8, 55, 56] The motions in FeP involve orientation differences between the two γ-subunits that can be visualized by observing the γ-100s helices (**Fig 1.6**). The two γ-subunits undergo (1) a hinge-like motion in which the γ-100s helices flatten (**Table 1.2**) and the [4Fe-4S] cluster becomes more surface exposed and (2) a twisting motion. DG2 has the flattest γ-100s helices' angle, contributing to the shortening of the distance between the P-cluster and the [4Fe-4S] cluster (**Fig 1.6a,c**). Furthermore, residues involved in ATP hydrolysis are in different rotameric conformations in the various DGs, with the conformations in DG2 being poised for ATP hydrolysis (**Fig 1.6b**). In contrast, aligning the MoFeP structures from the nitrogenase complex crystal structures does not reveal any conformational changes within MoFeP (**Fig 1.7**), indicating that the dynamic states of MoFeP are too transient to crystallize.[8]

### 1.3.3 The deficit spending model and conformational gating of electron transfer (ET) in nitrogenase

ET in nitrogenase occurs through a molecular wire consisting of the [4Fe-4S] cluster in FeP, and the P-cluster and FeMoco in MoFeP (**Fig 1.2**). There are thus two possible mechanisms for ET in the nitrogenase complex: a "sequential model" in which the [4Fe-4S] cluster first reduces the P-cluster, followed by reduction of FeMoco by the reduced P-cluster, or a "deficit spending model" in which FeMoco is first reduced by the P-cluster, followed by backfilling the P-cluster via reduction by the [4Fe-4S] cluster. Experimental evidence indicates that the deficit spending model is the correct model.[91] The P-cluster, which is the obligatory electron relay to FeMoco, is all ferrous ($Fe^{2+}$) in the as-isolated, DT-reduced resting state. There is no biological precedent for an Fe-S cluster to be reduced beyond the

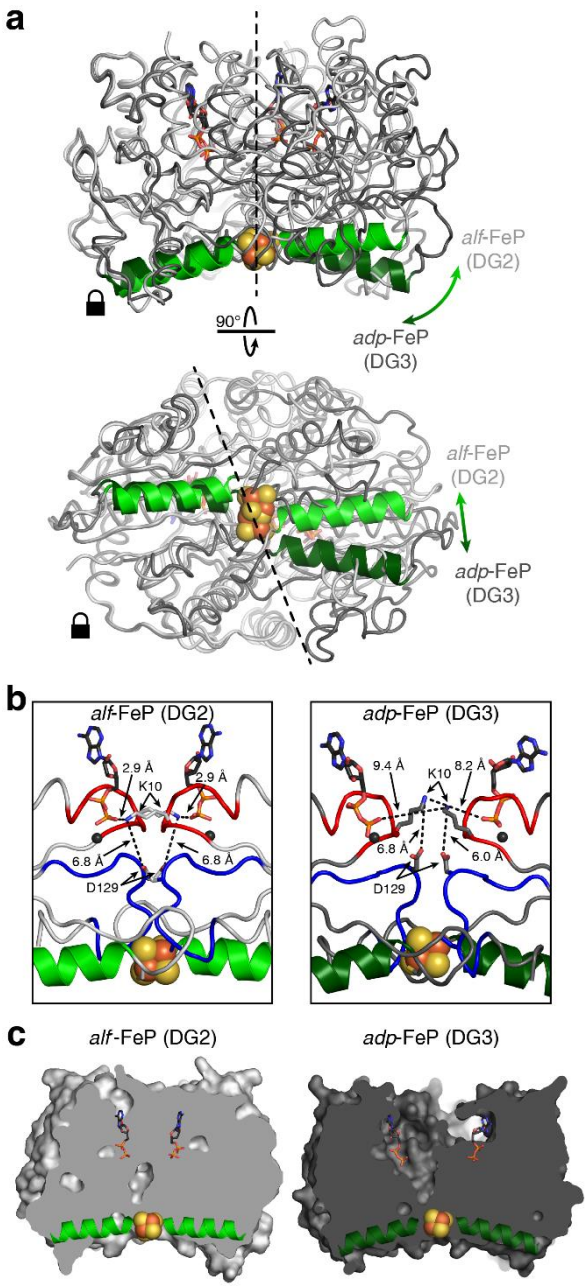


**Figure 1.6** Nucleotide-dependent conformational changes in FeP. Proteins are depicted in shades of gray with an emphasis on the γ100s helices shown in green. A comparison of FeP from *alf* (PDB ID: 1M34, light gray and light green) and FeP from *adp* (PDB ID: 2AFI, dark gray and dark green) are shown. The [4Fe-4S] cluster is shown as yellow and orange spheres, and nucleotides are represented as sticks. (a) The left subunit of FeP from both structures is structurally aligned. The hinge-like motion about a pivot point near the [4Fe-4S] cluster (top) and sliding motion between the γ-subunits (bottom) is evident when comparing the γ100s helices (green). These motions result in the flattening of the binding surface in DG2. (b) DG2 *alf* has residues γLys10 and γAsp129 poised for ATP hydrolysis. (c) Cross sections of FeP demonstrate that the [4Fe-4S] cluster of *alf* is more surface exposed than in *adp*. This figure is reproduced from ref 8.

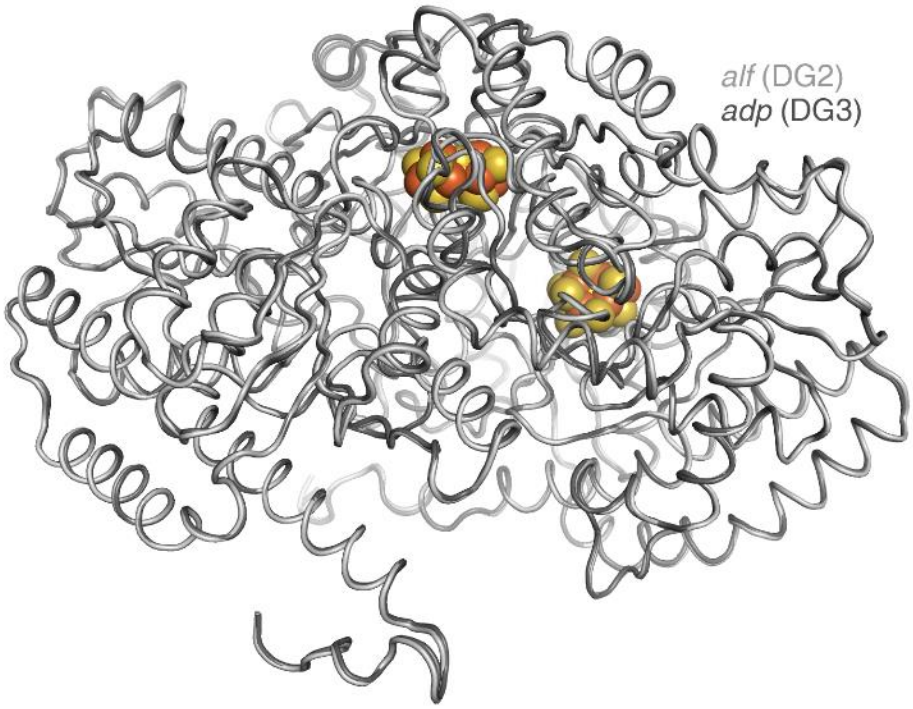


**Figure 1.7** MoFeP superpositions. Overlay of αβ-dimer from *alf* (light gray, PDB ID:1M34) and *adp* (dark gray, PDB ID: 2AFI) nitrogenase complex crystal structures. The P-cluster and FeMoco are depicted as spheres, colored by element. The RMSD over all αCs is only 0.317 Å, demonstrating the structure similarity in MoFeP across different DGs. This figure is reproduced from reference 8.

all-ferrous state, suggesting that the P-cluster must be oxidized before ET from the [4Fe-4S] occurs. Additionally, studies of a nitrogenase variant (*Av* βSer188Cys MoFeP) was used in stopped-flow measurements, demonstrating that the first ET event is a slow ($k_{obs} \approx 170\ s^{-1}$), intramolecular ET from the P-cluster to FeMoco, followed by a fast ET ($k_{obs} \geq 1700\ s^{-1}$) from the [4Fe-4S] cluster to the P-cluster.[91]

The first, intramolecular ET from the P-cluster to FeMoco only occurs in the presence of ATP-FeP (AMPPCP is not sufficient), suggesting that ATP hydrolysis by FeP is a requirement for this ET event.[91] This can be explained by a model in which ATP-FeP induces transformational changes in MoFeP opening an ET "gate". Conformational gating of ET in MoFeP is well supported by the literature. Experiments that measured the temperature-dependence of ET from FeP to MoFeP found that the derived Marcus parameters were well outside of the theoretical range that would be expected for a process strictly limited by electron tunneling kinetics,[92] indicating that conformational changes accompany the ET event.

More evidence for conformational gating was provided by examining how viscosity and osmotic pressure affect ET between FeP and MoFeP. The results demonstrated that ET kinetics were independent of viscosity but decreased exponentially with osmotic pressure, indicating that ET in nitrogenase was limited by an energy-requiring conformational gating event (rather than a diffusion process).[87]

### 1.3.4 Remaining questions about the nitrogenase catalytic mechanism

Despite decades of research into the catalytic mechanism of nitrogenase, many key questions remain regarding the mechanism of biological nitrogen fixation. Some of these questions include: How does the P-cluster function as a dynamic electron relay to FeMoco? What conformational changes does FeP induce in MoFeP to open the conformational gate, and what role does ATP play in this process? Where is the substrate binding site on FeMoco, and what structural rearrangements of the cluster and surrounding protein environment must occur to accommodate catalysis?

Answering these questions is difficult for a variety of reasons: (1) Nitrogenase must be expressed from its native organism, which means that mutagenesis of nitrogenase proteins requires altering the genome of the diazotroph. (2) Structural studies of nitrogenase have relied on protein X-ray crystallography, which can only provide static snapshots of the component proteins and their clusters. (3) Isolating a single $E_n$ state of MoFeP remains challenging due to the heterogeneity of nitrogenase solutions during catalytic turnover.

## 1.4 Dissertation objectives

The primary objective of this dissertation is to gain a detailed understanding of the dynamics of the nitrogenase relevant to catalysis:

- Small (Å)-scale dynamics of the nitrogenase P-cluster: understand how the redox-mediated conformational changes of the P-cluster are stabilized and what role these P-cluster dynamics play in physiological nitrogen fixation, with a focus on the oxygenic P-cluster ligand (Ser or Tyr).

- Large (nm)-scale dynamics of the nitrogenase complex *during* catalysis: solve the structure of the entire Fe-protein—MoFe-protein complex *during* $N_2$ reduction to provide insights into the mechanistic role of ATP-mediated structural changes.

**1.5 Acknowledgements**

Chapter 1 is reproduced, in part, with permission from H. Rutledge and F. A. Tezcan. Electron Transfer in Nitrogenase, *Chemical Reviews* **2020**, *12*, 5158-5193. The dissertation author is the primary author on all reprinted materials.

Chapter 2 is reproduced, in part, with permission from H. Rutledge, J. Rittle, L. M. Williamson, W. A. Xu, D. M. Gagnon, and F. A. Tezcan. Redox-Dependent Metastability of the Nitrogenase P-Cluster, *Journal of the American Chemical Society* **2019**, *141*, 10091-10098. The dissertation author is the primary author on all reprinted materials.

Chapter 3 is reproduced, in part, with permission from H. Rutledge, M. J. Field, J. Rittle, M. T. Green, and F. A. Tezcan. The Role of Serine Coordination in the Structural and Functional Protection of the Nitrogenase P-cluster. The dissertation author is the primary author on all reprinted materials.

Chapter 4 is reproduced, in part, with permission from H. Rutledge, B. Cook, H. Nguyen, M. Herzik, and F. A. Tezcan. CryoEM structures of the nitrogenase complex during catalytic turnover. The dissertation author is the primary author on all reprinted materials.

## Chapter 2: Redox-metastability of the nitrogenase P-cluster

### 2.1 Abstract

Biological nitrogen fixation by Mo-nitrogenase requires the coordinated transfer of eight electrons per molecule of reduced $N_2$. ET proceeds from the reductase, FeP, to the catalytic MoFeP through the intermediary site, the P-cluster, and culminates in the accumulation of electrons at the active site cofactor, FeMoco. Structural studies of MoFeP from two organisms, *Azotobacter vinelandii* (*Av*) and *Gluconacetobacter diazotrophicus* (*Gd*), have revealed that the P-cluster is dynamic and undergoes redox-mediated conformational changes upon two-electron oxidation from the DT-reduced $P^N$ state to the $P^{2+}$ ($P^{OX}$) state. The $P^{OX}$ state is stabilized by changes in coordination, including the ligation of a backbone amidate and an oxygenic residue (Ser or Tyr). These conformational changes have been implicated in the conformational gating of ET in nitrogenase. Here, I investigated the role of the native oxygenic ligand (βSer188) in *Av* MoFeP by generating and characterizing three MoFeP variants in which (1) the oxygenic ligand was removed (βSer188Ala), (2) the primary coordination sphere and oxygenic ligand were converted to that of *Gd* (βPhe99Tyr/βSer188Ala), and (3) both oxygenic ligands were present (βPhe99Tyr). The findings demonstrate that the *Av* P-cluster requires the native, oxygenic ligand (βSer188) to maintain its compositional stability. Removal or swapping of βSer188 results in a redox-labile P-cluster in which one or two Fe centers are lost upon oxidation to $P^{OX}$. Furthermore, these studies revealed that the *Gd* P-cluster is further stabilized by residues outside of the primary coordination sphere, which are not present in *Av* MoFeP. The P-cluster is thus inherently labile, and its compositional instability may be a key component to the multielectron transfer that occurs during $N_2$ reduction.

### 2.2 Introduction

#### 2.2.1 Redox-dependent conformational changes of the nitrogenase P-cluster

The intermediary ET relay site in nitrogenase is an [8Fe-7S] cluster, termed the P-cluster, located in MoFeP.[57] The P-cluster is unique compared to other ET Fe-S clusters in both its composition and

ligating residues. In nitrogenase homologs such as dark-operative protochlorophyllide oxidoreductase (DPOR) and the methanogenic oxidoreductase CfbD, there is a [4Fe-4S] cluster in place of the nitrogenase P-cluster.[93, 94] Canonical ET clusters are smaller than the P-cluster (such as [2Fe-s2] or [4Fe-4s] clusters), and they are bound to the protein via terminal residues, most often via Cys or His residues. In contrast, the dithionite (DT)-reduced resting state P-cluster resembles two [4Fe-4S] clusters bridged at a central, $\mu^6$ sulfide, and it is ligated by four terminal and two bridging Cys residues (**Fig. 2.1a**).[21] This ligation scheme reduces the overall negative charge of the P-cluster and likely serves to help stabilize the cluster in its DT-reduced, all-ferrous resting state ($P^N$). Additionally, canonical ET Fe-S clusters can only access one redox couple under physiological conditions. In contrast, the P-cluster can reversibly access two redox-couples: the reduced/one-electron oxidized couple ($P^N/P^{1+}$) and the one-electron oxidized/two-electron oxidized ($P^{1+}/P^{OX}$) couple.[51, 60-62]

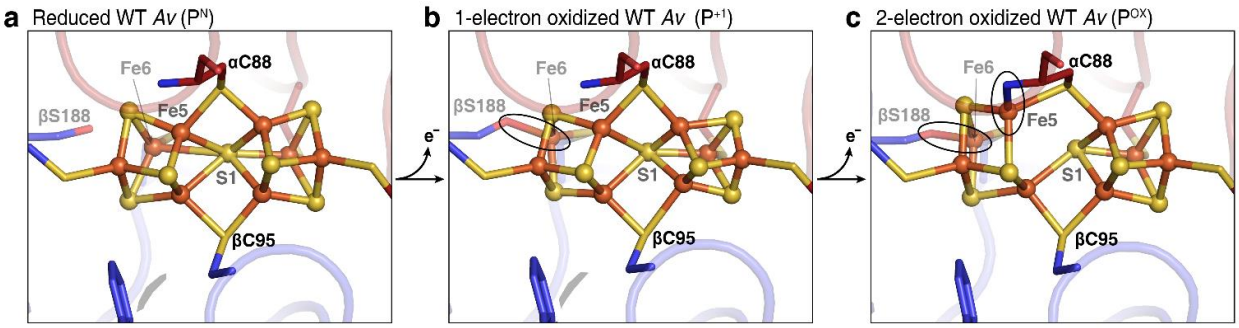


**Figure 2.1** Redox-dependent structural changes of the *Av* nitrogenase P-cluster. (a) The DT-reduced resting state of the *Av* P-cluster ($P^N$) resembles two [4Fe-4S] clusters fused at the central sulfide (S1) and is ligated by four terminal and two bridging Cys residues. (PDB ID: 3MIN) (b) One-electron oxidation of the *Av* P-cluster to $P^{1+}$ is accompanied by ligation of βSer188 to Fe6. Fe6 dissociates from S1, opening one cubane. (PDB ID: 6CDK) (c) Two-electron, IDS-oxidation of the *Av* P-cluster to $P^{OX}$ results in ligation of the backbone amidate of bridging ligand αCys88 to Fe5, which dissociates from S1. (PDB ID: 2MIN)

Upon oxidation, the P-cluster undergoes conformational changes (**Fig. 2.1**). In *Av* MoFeP, oxidation to $P^{1+}$ results in opening of one cubane such that Fe6 dissociates from the $\mu^6$ sulfide (S1) and coordinates to the side chain of βSer188 (**Fig. 2.1b**).[58] Oxidation by one more electron to $P^{OX}$ opens the cubane even more as Fe5 moves out of bonding distance of S1 and coordinates to the backbone amidate of the bridging αCys88 ligand (**Fig. 2.1c**).[21] These conformational changes are accompanied by changes

in the electron paramagnetic resonance (EPR) spectra of *Av* MoFeP. In $P^N$, the P-cluster is all ferrous and thus EPR silent. $P^{OX}$ exhibits an integer-spin ($S \geq 3$) with a feature visible in the parallel-mode spectrum at $g \approx 12$.[51, 95, 96]

Surprisingly, βSer188 (*Av* numbering will be used hereafter unless otherwise noted) is not strictly conserved among all nitrogenases: many MoFePs contain Ala in position β188, which cannot ligate Fe-S clusters.[59] Recently, MoFeP from *Gluconacetobacter diazotrophicus* (*Gd*), an organism whose MoFeP lacks βSer188, was crystallized in both the DT-reduced state and the indigo disulfonate (IDS)- oxidized state. *Gd* MoFeP was found to contain a Tyr residue in a different location (βTyr99) that ligates the P-cluster in $P^{OX}$, analogous to the *Av* P-cluster (**Fig. 2.2**). The parallel-mode EPR spectrum of $P^{OX}$ of *Gd* MoFeP contains a feature at $g \approx 16$.[59]

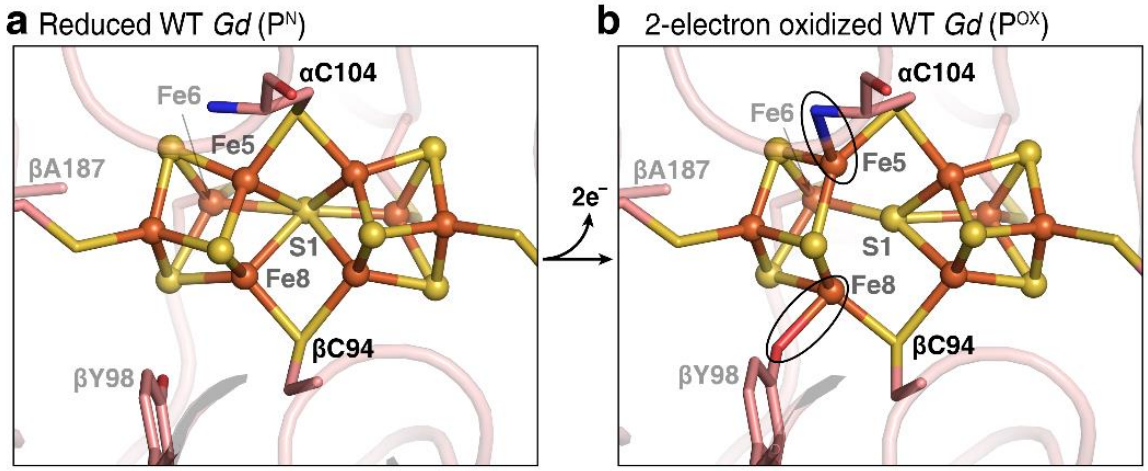


**Figure 2.2** Redox-dependent structural changes of the *Gd* nitrogenase P-cluster. (a) $P^N$ of *Gd* resembles two [4Fe-4S] clusters fused at the central sulfide (S1) and is bound by four terminal and two bridging cysteine residues. (PDB ID: 5KOH) (b) $P^{OX}$ of *Gd* is ligated by the backbone amidate of αCys104 (α88 *Av* numbering) and βTyr 98 (β99 *Av* numbering) and the cubane opens. (PDB ID: 5KOJ)

### 2.2.2 Conservation of oxygenic P-cluster ligand and implications for biological nitrogen fixation

Sequence alignments and covariance analysis revealed that the ligating residue (Ser or Tyr) is covariant (such that the sequence contained either βTyr99 or βSer188 and a non-coordinating residue in the other position) in 92 of the 95 MoFeP sequences (**Table 2.1**).[97] Two of the sequences contained both

βTyr99 and βSer188, and only one sequence contained neither. The conservation of a hard, oxygenic P-cluster ligand implied that it is functionally relevant to ET in nitrogenase.

Combined, all the unique features of the P-cluster indicate that it plays a critical and specific role as a dynamic ET-relay site to FeMoco. Biological nitrogen fixation requires multielectron ET, unlike the less complex redox reactions carried out by the nitrogenase homologs DPOR and CfbD.[94, 99] Nitrogenase has to precisely time each ET event in order to preferentially reduce $N_2$ over $H^+$. ET from the P-cluster to FeMoco is likely gated by conformational changes that occur in MoFeP as a result of FeP binding and ATP hydrolysis.[87, 92] Despite the evidence for gating, very few conformational changes within MoFeP have been directly observed. The redox-dependent conformational changes of the P-cluster may play a role in conformational gating of ET. Thus, studying the dynamics of the P-cluster is vital to elucidating the mechanism of biological nitrogen fixation by nitrogenase.

To investigate the role and necessity of the redox-switchable oxygenic ligand, I made, purified, and characterized three *Av* MoFeP mutants in which the primary coordination sphere of the P-cluster was altered: (1) a mutant which contained no oxygenic ligand (βSer188Ala), (2) a *Gd*-like mutant which contained only a coordinating Tyr residue (βPhe99Tyr/βSer188Ala), and (3) a mutant which contains both oxygenic ligands (βPhe99Tyr).[97]

**Table 2.1** Sequence alignments of the 95 classified nitrogenase sequences (including *nifK* (MoFeP), *vnfK* (VFeP), and *anfK* (FeFeP) α-subunit genes) demonstrating the highly conserved oxygenic ligand (βY99 or βSer188) in all but one nitrogenase (*Methanococcus aeolicus* Nankai).

| Organism | Nitrogenase group[98] | K geneID (*nifK, vnfK, anfK*) | Tyrosine region (β95-β100 *Av* numbering) | Serine region (β185-β190 *Av* numbering) |
|---|---|---|---|---|
| *Acidithiobacillus ferrooxidans* | I | WP_012536579.1 | CVAY**Y**R | HTPAFV |
| *Azoarcus sp.* | I | WP_011764275.1 | CVAYFR | HTP**S**FV |
| *Azospirillum brasilense Sp245* | I | CCC97490.1 | CVAY**Y**R | HTPAFV |
| *Azotobacter vinelandii* | I | WP_012698833.1 | CVAYFR | HTP**S**FV |
| *Bradyrhizobium japonicum* | I | AAG60730.1 | CVAY**Y**R | HTPAFV |
| *Calothrix desertica PCC 7102* | I | ACA61792.1 | CVAYFR | HTP**S**FV |
| *Chlorogloeopsis fritschii PCC 6912* | I | ACA61793.1 | CVAYFR | HTP**S**FV |
| *Cyanothece sp. ATCC 51142* | I | AAB61284.1 | CVAYFR | HTP**S**FV |
| *Desulfitobacterium hafniense DCB-2* | I | ACL19111.1 | CTAYFR | NTP**S**FK |
| *Desulfosporosinus sp. OT* | I | EGW39328.1 | CAAYFR | NTP**S**FK |
| *Fischerella muscicola PCC 7414* | I | ACA61795.1 | CVAYFR | HTP**S**FV |
| *Frankia alni* | I | WP_011607845.1 | CVAYFR | HTP**S**FV |
| *Geobacter sulfurreducens PCA*[1] | I | NP_953863.1 | CASY**Y**R | NTP**S**FN |
| *Gluconacetobacter diazotrophicus* | I | WP_012222816.1 | CVAY**Y**R | HTPAFV |
| *Halorhodospira halophila* | I | WP_011813089.1 | CVAYFR | HTP**S**FV |
| *Heliobacterium modesticaldum* | I | WP_012282220.1 | CAAYFR | QTP**S**FV |
| *Klebsiella spp.* | I | WP_008804133.1 | CVAYFR | HTP**S**FI |
| *Magnetococcus marinus* | I | WP_011712866.1 | CVAYFR | HTP**S**FV |
| *Mesorhizobium japonicum loti MAFF303099* | I | BAB52277.1 | CVAY**Y**R | HTPAFV |
| *Methylobacterium sp. 4-46* | I | WP_012333318.1 | CVAY**Y**R | HTPAFV |
| *Methylococcus capsulatus* | I | WP_010959596.1 | CVAY**Y**R | HTPAFV |
| *Methylocystis sp. ATCC 49242* | I | WP_036285696.1 | CVAY**Y**R | HTPAFV |
| *Nodularia spumigena CCY9414* | I | EAW47004.1 | CVAYFR | HTP**S**FV |
| *Nostoc sp. PCC 7120* | I | WP_010995612.1 | CVAYFR | HTP**S**FV |

**Table 2.1** Sequence alignments of the 95 classified nitrogenase sequences, continued.

| | | | | |
|---|---|---|---|---|
| *Paraburkholderia xenovorans* | I | WP_011491822.1 | CVAY**Y**R | HTPAFV |
| *Pectobacterium atrosepticum* | I | WP_011094485.1 | CVAYFR | HTP**S**FI |
| *Pelobacter carbinolicus DSM 2380*[1] | I | ABA89340.1 | CASY**Y**R | NTP**S**FN |
| *Polaromonas naphthalenivorans* | I | WP_011801728.1 | CVAY**Y**R | HTPAFV |
| *Pseudomonas stutzeri* | I | WP_011912506.1 | CVAYFR | HTP**S**FV |
| *Rhodobacter capsulatus* | I | WP_013066314.1 | CVAY**Y**R | HTPAFV |
| *Rhodobacter sphaeroides 2.4.1* | I | YP_353612.1 | CVAY**Y**R | HTPAFV |
| *Rhodomicrobium vannielii* | I | WP_013419577.1 | CVAY**Y**R | HTPAFV |
| *Rhodopseudomonas palustris CGA009* | I | CAE30058.1 | CVAY**Y**R | HTPAFV |
| *Rhodospirillum rubrum ATCC 11170* | I | YP_426100.1 | CAAYFR | HTP**S**FV |
| *Scytonema sp. PCC 7814* | I | ACA61802.1 | CVAYFR | HTP**S**FV |
| *Sinorhizobium fredii NGR234* | I | NP_444138.1 | CVAY**Y**R | HTPAFV |
| *Sinorhizobium medicae WSM419* | I | YP_001314760.1 | CVAY**Y**R | HTPAFV |
| *Synechococcus sp. JA-2-3B'a(2-13)* | I | WP_011432083.1 | CVAYFR | HTP**S**FV |
| *Syntrophobotulus glycolicus* | I | WP_013625929.1 | CAAYFR | NTP**S**FV |
| *Thermodesulfovibrio yellowstonii DSM 11347* | I | ACI20660.1 | CVAYFR | NTP**S**FT |
| *Trichodesmium erythraeum IMS101* | I | AAF82639.1 | CVAYFR | HTP**S**FV |
| *Trichormus variabilis* | I | WP_011320929.1 | CVAYFR | HTP**S**FV |
| *Wolinella succinogenes* | I | CAE10457.1 | CVAYFR | NTP**S**FK |
| *Xanthobacter autotrophicus* | I | WP_011995768.1 | CVAY**Y**R | HTPAFV |
| *Zymomonas mobilis* | I | WP_011241558.1 | CVAY**Y**R | HTPAFV |
| *Alkaliphilus metalliredigens* | II | WP_012064610.1 | CCSFHR | NTP**S**YA |
| *Methanoregula boonei* | II | WP_012106692.1 | CCAYHR | NTP**S**YV |
| *Chlorobaculum tepidum TLS* | II | NP_662421.1 | CCAYHR | STP**S**YV |
| *Chlorobium phaeobacteroides DSM 266* | II | ABL64793.1 | CCSYHR | STP**S**FV |
| *Clostridium kluyveri DSM 555* | II | EDK35085.1 | CCSYHR | NTP**S**YV |

**Table 2.1** Sequence alignments of the 95 classified nitrogenase sequences, continued.

| | | | | |
|---|---|---|---|---|
| *Clostridium pasteurianum* | II | WP_003447875.1 | CCSYHR | NTP**S**YV |
| *Clostridium spp.* | II | WP_012058234.1 | CCSYHR | NTP**S**YV |
| *Dehalococcoides mccartyi* | II | WP_010936846.1 | CCAYHR | NTP**S**YA |
| *Desulfonatronospira thiodismutans* | II | WP_008868629.1 | CCSYHR | STP**S**YV |
| *Desulfotomaculum reducens* | II | WP_011879116.1 | CCSYHR | NTP**S**YQ |
| *Desulfovibrio vulgaris str. Hildenborough* | II | YP_009051.1 | CCSYHR | NTP**S**YV |
| *Ethanoligenens harbinense* | II | WP_013485454.1 | CCSYHR | HTP**S**YV |
| *Methanosarcina acetivorans* | II | WP_011023795.1 | CLSYLR | STP**S**YV |
| *Methanosarcina barkeri* | II | WP_011305207.1 | CLSYLR | STP**S**YV |
| *Methanosphaerula palustris E1-9c* | II | ACL15930.1 | CCAYHR | NTP**S**YV |
| *Opitutaceae bacterium TAV5* | II | AHF89133.1 | CCSYHR | NTP**S**FI |
| *Paludibacter propionicigenes* | II | WP_013444942.1 | CCSYHR | NTP**S**YV |
| *Thermoanaerobacterium thermosaccharolyticum DSM 571* | II | ADL69353.1 | CTSYLR | STP**S**YV |
| *Caldicellulosiruptor saccharolyticus*[5] | III | WP_011917960.1 | CCTYVR | HTP**S**YA |
| *Candidatus Desulforudis audaxviator*[3,5] | III | WP_012301309.1 | CTTYVR | STP**S**FA |
| *Desulfofundulus kuznetsovii*[3,5] | III | AEG16826.1 | CTTYVR | NTP**S**FA |
| *Methanocaldococcus sp. FS406-22*[5] | III | WP_012979651.1 | CCTYVR | HCP**S**YQ |
| *Methanococcus aeolicus Nankai-3*[2] | III | ABR57006.1 | CTTYAR | HCPAYK |
| *Methanococcus maripaludis* | III | WP_011868427.1 | CSTFVR | NTP**S**FV |
| *Methanothermobacter thermautotrophicus* | III | WP_010877173.1 | CSTFVR | STP**S**FV |
| *Thermodesulfatator indicus*[3,5] | III | WP_013907667.1 | CTTYVR | NTP**S**FA |
| *Oscillochloris trichoides*[4,5] | IV | WP_044199137.1 | CATYPR | KTP**S**YI |
| *Roseiflexus castenholzii*[4,5] | IV | WP_012122494.1 | CATYPR | KTP**S**YI |
| *Roseiflexus sp. RS-1*[4,5] | IV | ABQ89605.1 | CATYPR | KTP**S**YI |
| *Trichormus variabilis ATCC 29413* | Vnf | ABA23632.1 | CSMFVR | HTP**S**YR |
| *Azospirillum brasilense* | Vnf | WP_014199516.1 | CSMFVR | HTP**S**FK |

**Table 2.1** Sequence alignments of the 95 classified nitrogenase sequences, continued.

| | | | | |
|---|---|---|---|---|
| *Azotobacter vinelandii* | Vnf | WP_012698948.1 | CTMFVR | HTP**S**FK |
| *Clostridium kluyveri* | Vnf | WP_012102137.1 | CSMFVR | HTP**S**YS |
| *Ethanoligenens harbinense* | Vnf | WP_013486174.1 | CCTFVR | HTP**S**YS |
| *Methanosarcina acetivorans* | Vnf | WP_011021239.1 | CSMFVR | HTP**S**YS |
| *Methanosarcina barkeri str. Fusaro* | Vnf | AAZ71201.1 | CSMFVR | HTP**S**YS |
| *Rhodomicrobium vannielii ATCC 17100* | Vnf | ADP69798.1 | CTMFVR | HTP**S**FK |
| *Rhodopseudomonas palustris CGA009* | Vnf | NP_946730.1 | CTMFVR | HTP**S**KF |
| *Azotobacter vinelandii* | Anf | WP_012703359.1 | CVMFVR | HTP**S**FV |
| *Clostridium kluyveri* | Anf | WP_011988941.1 | CVMFVR | HTP**S**FT |
| *Desulfosporosinus sp. OT* | Anf | EGW37580.1 | CVMFVR | HTP**S**FK |
| *Geminisphaera colitermitum* | Anf | WP_043589561.1 | CVMFVR | HTP**S**FV |
| *Methanosarcina acetivorans* | Anf | WP_011021230.1 | CVMFVR | HTP**S**FK |
| *Methanosarcina barkeri str. Fusaro* | Anf | AAZ70498.1 | CVMFVR | HTP**S**FK |
| *Paludibacter propionicigenes WB4* | Anf | ADQ79507.1 | CVMFVR | HTP**S**FK |
| *Rhodobacter capsulatus SB 1003* | Anf | ADE84353.1 | CVMFVR | HCP**S**FV |
| *Rhodomicrobium vannielii ATCC 17100* | Anf | WP_013420903.1 | CVMFVR | HQP**S**FV |
| *Rhodopseudomonas palustris CGA009* | Anf | WP_011156998.1 | CVMFVR | HCP**S**FV |
| *Rhodospirillum rubrum ATCC 11170* | Anf | YP_426480.1 | CVMFVR | HTP**S**FV |
| *Syntrophobotulus glycolicus DSM 8271* | Anf | ADY57118.1 | CVMFVR | HTP**S**FK |

1. Sequence contains both βY99 and βS188, *Av* numbering
2. Sequence contains neither βY99 nor βS188, *Av* numbering
3. Selenocysteine at αU62, *Av* numbering (αC62 in all other nitrogenase sequences) (ref)
4. Organism lacks nifE gene
5. Organism lacks nifN gene

## 2.3 Results and discussion

### 2.3.1 Structural characterization of *Azotobacter vinelandii* MoFe-protein P-cluster mutants

To determine what, if any, redox-dependent reorganization occurs at the P-cluster in the mutants, each MoFeP variant was crystallized in both $P^N$ and $P^{OX}$ with DT as the reductant and IDS as the oxidant, respectively (**Table 2.2**). The P-cluster of *Av* βSer188Ala MoFeP in $P^N$ (PDB ID: 6O7L, 2.3 Å) resembled the wild-type (wt) *Av* and *Gd* P-clusters' geometry (two cubanes fused at the central S1 sulfide, ligated by four terminal and two bridging Cys residues) (**Fig. 2.3a**). Upon two-electron oxidation with IDS, the *Av* βSer188Ala MoFeP P-cluster (PDB ID: 6O7S, 2.3 Å) demonstrated complete loss of two Fe centers (Fe1 and Fe5), yielding a structure that resembled two [3Fe-4S] clusters joined at S1 (**Fig 2.3b**). There was electron density in the $2F_O$-$F_C$ map at the Fe5 position but not any corresponding anomalous density, indicating that the atom at position Fe5 was *not* an Fe center (**Fig. 2.4**). This density was tentatively modeled as a Na ion. The anomalous electron density map was carefully inspected, revealing no novel Fe-binding sites on or within MoFeP, indicating complete loss of the two Fe atoms. Interestingly, neither of the unoccupied Fe sites corresponded to the site that coordinates the Ser residue in wt *Av* MoFeP (Fe6). The loss of Fe1 and Fe5 likely stabilized the [6Fe-7S] cluster by converting both bridging Cys residues (αCys88 and βCys95) to terminal ligands, a conformation in which all Fe centers are tetra-coordinate to terminal Cys sidechains, closely resembling canonical Fe-S clusters. After learning that βSer188 is necessary to both stabilize $P^{OX}$ and maintain its composition, I investigated whether the [6Fe-7S] P-cluster could be converted back to the [8Fe-7S] P-cluster by solving the crystal structure of re-reduced *Av* βSer188Ala MoFeP (PDB ID: 6O7Q, 2.0 Å). Upon re-reduction with DT, the P-cluster of *Av* βSer188Ala MoFeP returned to the wt-like [8Fe-7S] cluster with full occupancy of all Fe-sites (**Fig 2.3c**).[97] The lability of the two Fe centers in the *Av* βSer188Ala MoFeP P-cluster is similar to the compositionally labile Fe-S clusters of aconitase,[100] biotin synthase,[101] lipoyl synthase,[102] carbon monoxide dehydrogenase (CODH),[103] and even FeMoco.[63, 64, 104]

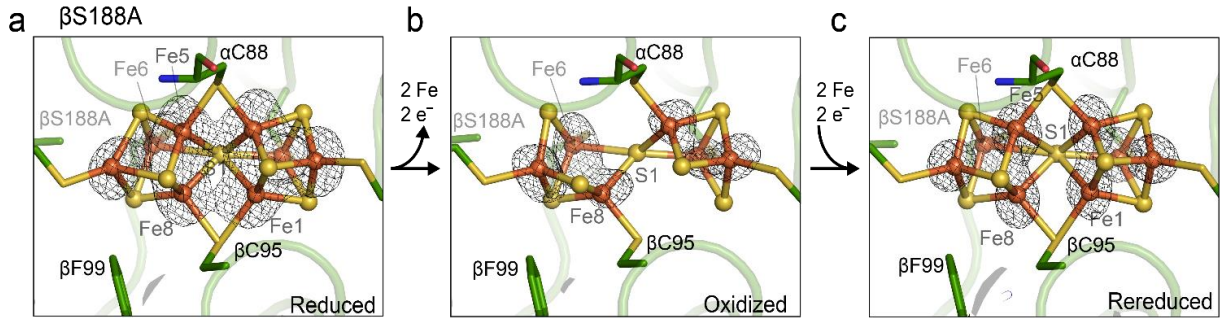


**Figure 2.3** X-ray crystal structures of the P-cluster of *Av* βSer188Ala MoFeP. Anomalous electron density difference maps determined using X-ray diffraction data collected near the Fe K-edge are shown in black mesh. (a) The DT-reduced state of the βSer188Ala P-cluster. Map is contoured at 8.0 σ. (7.13 keV, Fe f" = 3.93) (PDB ID: 6O7L) (b) The IDS-oxidized state of the βSer188Ala P-cluster. Fe1 and Fe5 are not present in the IDS-oxidized P-cluster. Map is contoured at 3.5 σ. (12.0 keV, Fe f" = 1.64) (PDB ID: 6O7S) (c) The DT-re-reduced state of the βSer188Ala P-cluster after one cycle of IDS oxidation. Fe1 and Fe5 are both present at full occupancy. Map is contoured at 8.0 σ. (7.13 keV, Fe f" = 3.93) (PDB ID: 6O7Q)

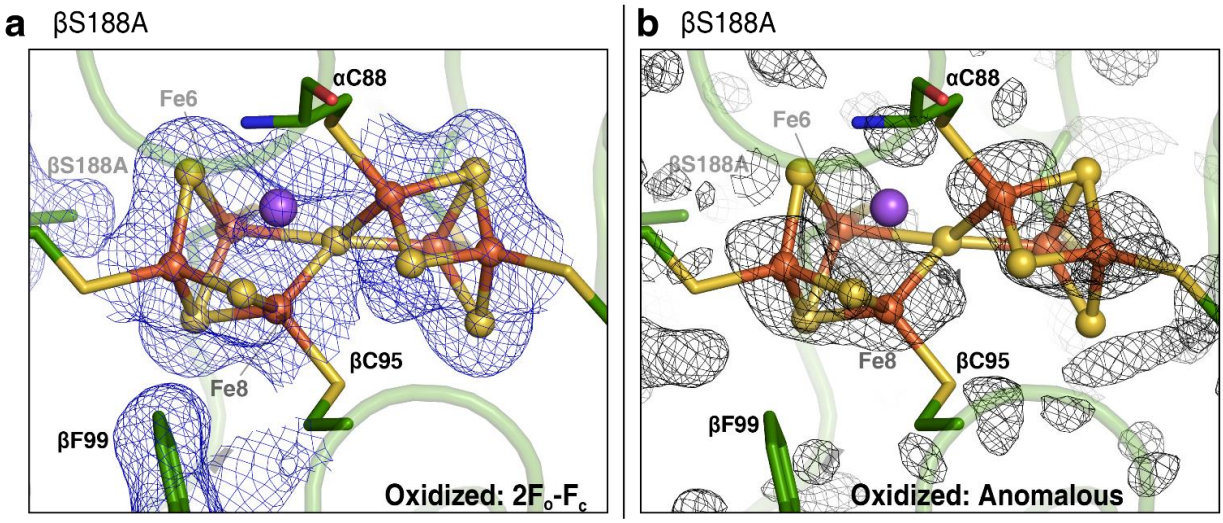


**Figure 2.4** Maps demonstrating complete loss of Fe1 and Fe5 from the IDS-oxidized *Av* βSer188Ala MoFeP P-cluster. (PDB ID: 6O7S) (a) P-cluster of IDS-oxidized *Av* βSer188Ala MoFeP with the $2F_O$-$F_C$ map (blue) contoured at 1.0 σ, revelaing electron density where Fe5 was previously located in the DT-reduced structure. This denisty was tentatively modeled as a Na ion (purple sphere). (b) P-cluster of IDS-oxidized *Av* βSer188Ala MoFeP with the anomalous electron density difference map (black) contoured at a low level, 2.0 σ, at which noise becomes apparent. Even at this noisy contour level, there is no anomalous density where Na (purple sphere) is placed, confirming that Fe5 is not present. (12.0 keV, Fe f" = 1.64)

**Table 2.2** X-ray data collection and refinement statistics. Numbers in parentheses correspond to the highest resolution shell.

| | **Reduced βS188A** | **Oxidized βS188A** | **Re-reduced βS188A** | **Reduced βF99Y/βS188A** |
|---|---|---|---|---|
| PDB ID | 6O7L | 6O7S | 6O7Q | 6O7R |
| **Data collection** | | | | |
| Beamline | ALS 5.0.2 | SSRL 9-2 | ALS 5.0.2 | SSRL 9-2 |
| Wavelength (Å) | 1.73892 | 1.03318 | 1.73892 | 1.73885 |
| Space group | P 1 21 1 | P 1 21 1 | P 1 21 1 | P 1 21 1 |
| Cell dimensions (Å) | 80.56 131.03 107.62 90.00 110.85 90.00 | 76.78 128.05 107.54 90.00 108.97 90.00 | 77.44 130.41 107.75 90.00 109.09 90.00 | 76.61 128.81 107.64 90.00 109.07 90.00 |
| Cell angles (°) | | | | |
| Resolution (Å) | 49.42 – 2.26 | 35.45 – 2.26 | 48.68 - 2.00 | 40.25 - 2.27 |
| No. unique reflections | 97426 | 83474 | 135987 | 82483 |
| Rmerge | 0.178 (1.164) | 0.110 (0.368) | 0.213 (1.099) | 0.114 (0.383) |
| Multiplicity | 6.5 (6.4) | 6.5 (6.8) | 6.4 (6.3) | 5.8 (5.6) |
| CC ½ | 0.992 (0.845) | 0.984 (0.927) | 0.985 (0.709) | 0.984 (0.901) |
| *<I/σ(I)>* | 5.9 (1.2) | 11.9 (4.6) | 5.9 (1.5) | 3.4 (3.8) |
| Completeness (%) | 99.9 (99.9) | 92.2 (97.1) | 92.1 (99.9) | 90.6 (94.9) |
| **Refinement** | | | | |
| Rwork/Rfree | 0.2084 / 0.2541 | 0.1702 / 0.2078 | 0.1863 / 0.2294 | 0.1637 / 0.2077 |
| No. atoms | 31202 | 32424 | 32583 | 32665 |
| Protein | 30830 | 31004 | 31124 | 31228 |
| Ligand/ion | 108 | 106 | 108 | 108 |
| Solvent | 264 | 1314 | 1351 | 1329 |
| B-factors (Å$^2$) | 50.95 | 25.78 | 27.66 | 24.6 |
| Protein | 51.05 | 25.72 | 27.41 | 24.38 |
| Ligand/ion | 46.52 | 24.13 | 21.16 | 23.56 |
| Solvent | 46.51 | 26.53 | 31.07 | 27.27 |
| R.m.s. deviations | | | | |
| Bond lengths (Å) | 0.035 | 0.027 | 0.035 | 0.036 |
| Bond angles (°) | 1.02 | 1.02 | 0.97 | 1.07 |
| Clashscore | 5.72 | 2.76 | 1.82 | 3.13 |
| Ramachandran plot (%) | | | | |
| Favored | 95.45 | 96.68 | 96.16 | 96.38 |
| Outliers | 0.20 | 0.30 | 0.10 | 0.25 |
| Rotamer outliers (%) | 2.53 | 1.20 | 1.48 | 2.49 |

**Table 2.2** X-ray data collection and refinement statistics, continued.

| | **Oxidized βF99Y/βS188A** | **Re-reduced βF99Y/βS188A** | **Reduced βF99Y** | **Oxidized βF99Y** |
|---|---|---|---|---|
| PDB ID | 6O7N | 6O7O | 6O7P | 6O7M |
| **Data collection** | | | | |
| Beamline | SSRL 12-2 | SSRL 12-2 | SSRL 9-2 | SSRL 9-2 |
| Wavelength (Å) | 1.54975 | 1.54975 | 0.95369 | 0.95369 |
| Space group | P 1 21 1 | P 1 21 1 | P 1 21 1 | P 1 21 1 |
| Cell dimensions (Å) | 76.34 127.96 107.51 90.00 109.01 | 76.75 128.68 107.54 90.00 108.94 | 76.85 128.44 107.71 90.00 109.09 | 76.46 127.79 107.54 90.00 109.00 |
| Cell angles (°) | 90.00 | 90.00 | 90.00 | 90.00 |
| Resolution (Å) | 40.10 - 1.75 | 36.75 - 1.89 | 46.65 - 1.70 | 40.11 - 1.40 |
| No. unique reflections | 177299 | 147935 | 189177 | 357803 |
| Rmerge | 0.160 (1.476) | 0.141 (0.867) | 0.237 (1.422) | 0.197 (2.220) |
| Multiplicity | 6.0 (4.6) | 6.3 (6.1) | 6.4 (6.2) | 5.9 (5.8) |
| CC ½ | 0.853 (0.042) | 0.987 (0.695) | 0.987 (0.271) | 0.958 (0.187) |
| $\langle I/\sigma(I) \rangle$ | 6.5 (0.8) | 8.0 (1.8) | 6.4 (1.5) | 6.1 (0.9) |
| Completeness (%) | 90.0 (57.3)) | 94.0 (93.5) | 87.5 (96.6) | 93.7 (89.1) |
| **Refinement** | | | | |
| Rwork/Rfree | 0.1866 / 0.2232 | 0.1486 / 0.1859 | 0.1677 / 0.2013 | 0.1822 / 0.2082 |
| No. atoms | 33866 | 33431 | 34131 | 34304 |
| Protein | 31631 | 31316 | 31491 | 31654 |
| Ligand/ion | 108 | 108 | 108 | 108 |
| Solvent | 2127 | 2007 | 2532 | 2542 |
| B-factors (Å$^2$) | 23.72 | 24.56 | 18.28 | 16.16 |
| Protein | 22.97 | 23.67 | 17.23 | 14.91 |
| Ligand/ion | 18.58 | 18.11 | 11.95 | 9.98 |
| Solvent | 29.60 | 31,9 | 25.15 | 24.2 |
| R.m.s. deviations | | | | |
| Bond lengths (Å) | 0.052 | 0.033 | 0.033 | 0.044 |
| Bond angles (°) | 1.16 | 1.22 | 1.13 | 1.23 |
| Clashscore | 4.66 | 3.41 | 2.41 | 3.24 |
| Ramachandran plot (%) | | | | |
| Favored | 96.53 | 96.69 | 96.88 | 96.43 |
| Outliers | 0.25 | 0.25 | 0.20 | 0.20 |
| Rotamer outliers (%) | 1.33 | 1.71 | 1.46 | 1.16 |

*Av* βPhe99Tyr/βSer188Ala MoFeP has a primary coordination sphere around the P-cluster similar to wt *Gd*. In $P^N$, this P-cluster resembled the structures of wt *Av* and wt *Gd* P-clusters (PDB ID: 6O7R, 2.3Å) (**Fig. 2.5a**). Upon IDS oxidation to $P^{OX}$, a cubane of the *Av* βPhe99Tyr/βSer188Ala P-cluster opened such that Fe8 dissociated from the central sulfide S1 and coordinated to βPhe99Tyr, analogous to wt *Gd* (PDB ID: 6O7N, 1.8 Å) (**Fig. 2.5b**). Superposition of the *Av* βPhe99Tyr/βSer188Ala MoFeP P-cluster with wt *Av* and *Gd* P-clusters in the $P^{OX}$ state clearly demonstrates the structural similarity between this mutant and wt *Gd* (**Fig. 2.6**).[97] However, unlike the wt *Gd* $P^{OX}$,[59] $P^{OX}$ of *Av* βPhe99Tyr/βSer188Ala MoFeP contained three Fe centers that were only partially occupied at ~67% occupancy (Fe1, Fe5, and Fe8 occupancies are 68%, 59%, and 71%, respectively), indicating that each P-cluster in this mutant lost one Fe per P-cluster, on average, upon IDS oxidation. Two of these three Fe sites correspond to the labile sites in *Av* βSer188Ala MoFeP, indicating that the βPhe99Tyr ligand partially stabilizes the P-cluster. The P-cluster can thus be described by a model in which an equilibrium exists between three conformational states, where each state contains only one missing Fe center (Fe1, Fe5, or Fe8) (**Fig. 2.7**). Upon re-reduction with DT, the three labile sites of the *Av* βPhe99Tyr/βSer188Ala P-cluster were fully reconstituted (PDB ID: 6O7O, 1.9 Å) (**Fig. 2.6c**).[97]

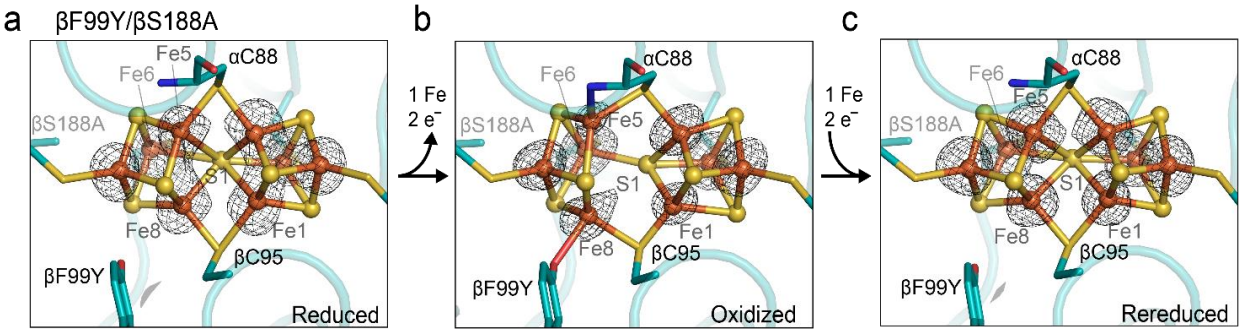


**Figure 2.5** X-ray crystal structures of the P-cluster of *Av* βPhe99Tyr/βSer188Ala MoFeP. Anomalous electron density difference maps determined using X-ray diffraction data collected near the Fe K-edge are shown in black mesh. (a) The DT-reduced state of the βPhe99Tyr/βSer188Ala P-cluster. Map is contoured at 8.0 σ. (7.13 keV, Fe f" = 3.93) (PDB ID: 6O7R) (b) The IDS-oxidized state of the βPhe99Tyr/βSer188Ala P-cluster. Fe1, Fe5, and Fe8 are all only present at partial occupancy of ~0.67 in the IDS-oxidized P-cluster. Map is contoured at 6.0 σ. (8.0 keV, Fe f" = 3.18) (PDB ID: 6O7N) (c) The DT-re-reduced state of the βPhe99Tyr/βSer188Ala P-cluster after one cycle of IDS oxidation. Fe1, Fe5, and Fe8 are present at full occupancy. Map is contoured at 6.0 σ. (8.00 keV, Fe f" = 3.18) (PDB ID: 6O7O)

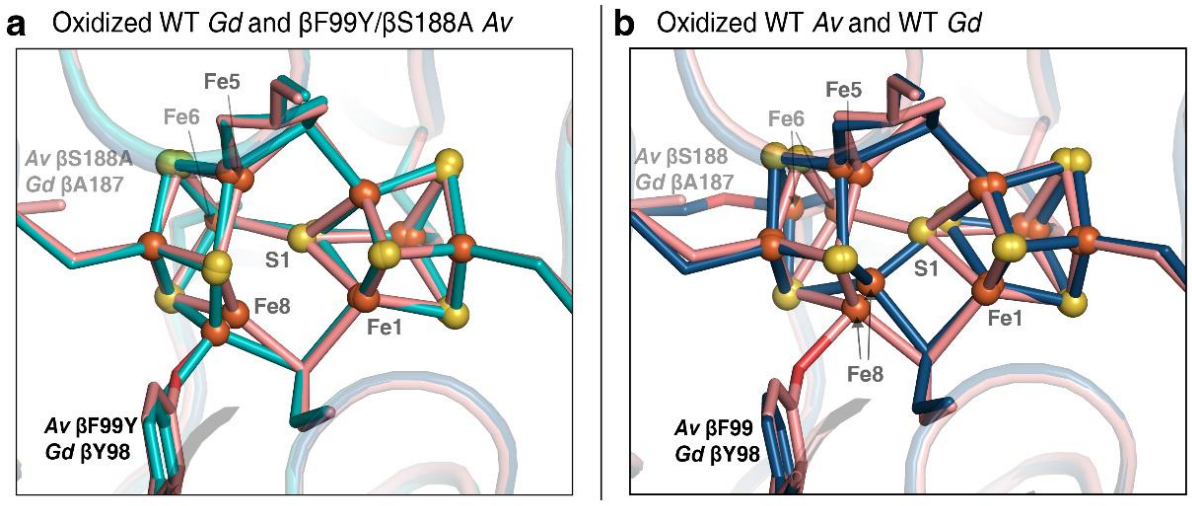


**Figure 2.6** Structural alignment of oxidized P-clusters illustrating that oxidized '*Gd*-like' βPhe99Tyr/βSer188Ala MoFeP (teal, PDB ID: 6O7N) closely resembles wt *Gd* (pink, PDB ID: 5KOJ), while wt *Av* (blue, PDB ID: 2MIN) MoFeP and wt *Gd* (pink) have large differences in the positions of Fe6 and Fe8. Alignments were performed using all atoms within 7 Å of the P-cluster. Fe (orange) and S (yellow) atoms in the cluster are colored by element. (a) Oxidized P-clusters of βPhe99Tyr/βSer188Ala MoFeP (teal) and wt *Gd* MoFeP (pink) are superimposable with an RMS of 0.165 Å for atoms used in the alignment. (b) The aligned oxidized P-clusters of wt *Gd* (pink) and wt *Av* (blue) show differences in ligation schemes (RMS = 0.179 Å for all atoms used in the alignment).

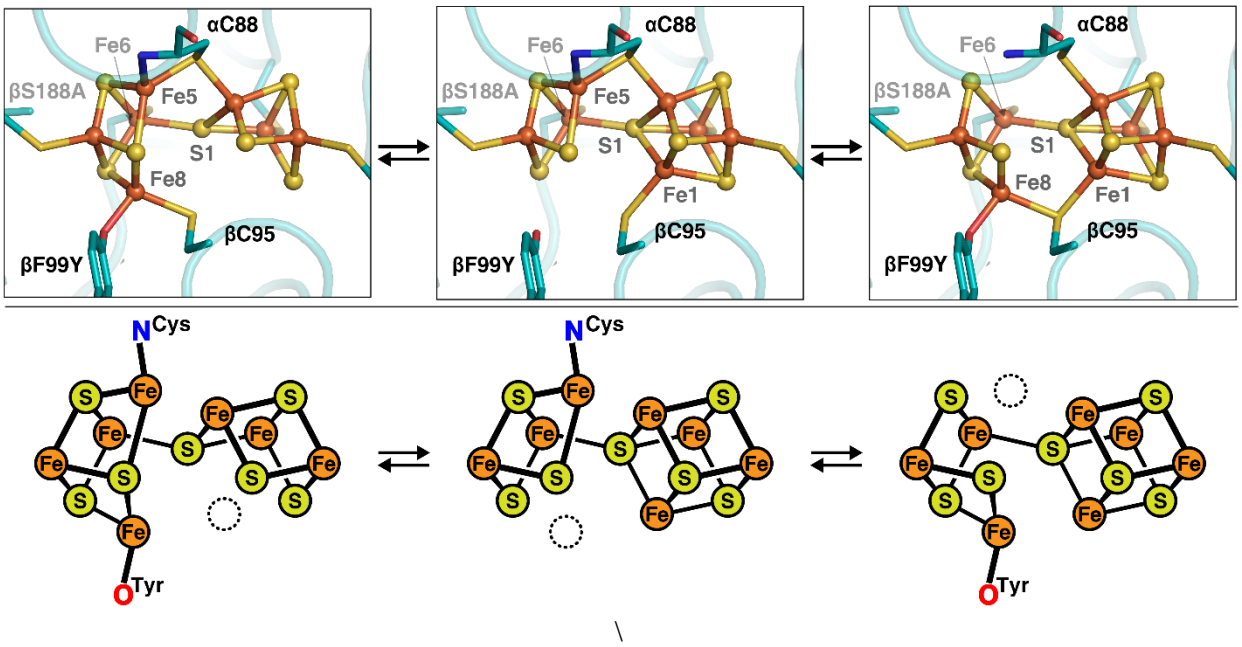


**Figure 2.7** Equilibrium conformational states of the IDS-oxidized [7Fe-7S] P-cluster of *Av* βPhe99Tyr/βSer188Ala MoFeP. The non-native Tyr ligand coordinates the cluster in two of the equilibrium states, and Fe1, Fe5, and Fe8 are redox-labile. In the cartoon (bottom), labile sites are represented with a dashed circle. (Pymol figures are constructed from PDB ID: 6O7N)

Lastly, I structurally characterized the *Av* βPhe99Tyr mutant, which contained both oxygenic ligands (Ser and Tyr). Both $P^N$ and $P^{OX}$ of this mutant resembled the wt *Av* P-cluster (PDB ID: 6O7P, 1.7 Å, and PDB ID: 6O7M, 1.4 Å, respectively) (**Fig. 2.8**). In $P^{OX}$, βSer188 was coordinated to Fe6, and there was no electron density between βPhe99Tyr and Fe8 (**Fig. 2.8b**).[97] Taken together, the compositional instability of the *Av* βPhe99Tyr/βSer188Ala P-cluster upon oxidation and the preference for βSer188 ligation over βPhe99Tyr indicate that *Av* MoFeP evolved to preferentially stabilize $P^{OX}$ with a serinate ligand, and differences in unidentified residues outside of the primary coordination sphere must help stabilize the oxidized *Gd* P-cluster.

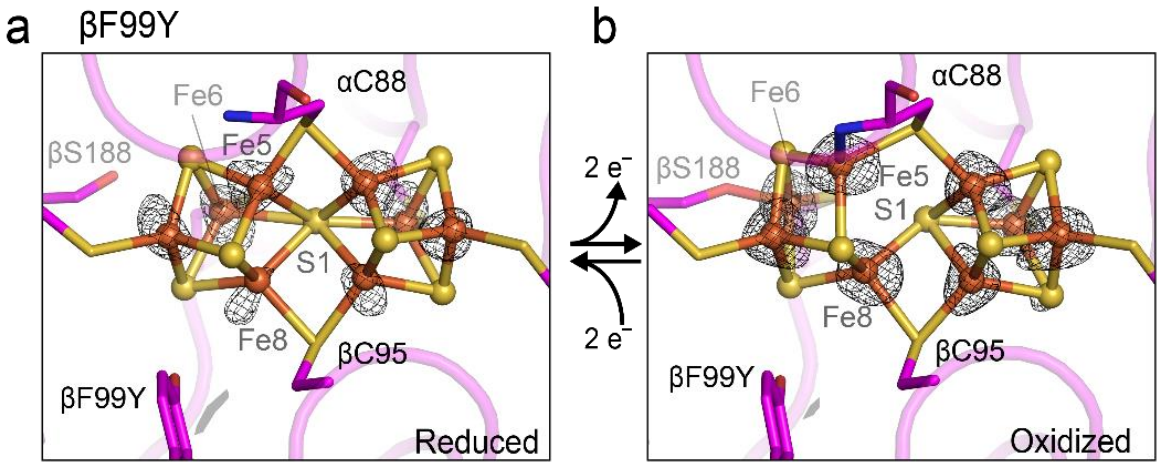


**Figure 2.8** X-ray crystal structures of the P-cluster of *Av* βPhe99Tyr MoFeP. Anomalous electron density difference maps determined using X-ray diffraction data collected near the Fe K-edge are shown in black mesh. (a) The DT-reduced state of the βPhe99Tyr P-cluster. Map is contoured at 3.5 σ. (7.13 keV, Fe f" = 3.93) (PDB ID: 6O7P) (b) The IDS-oxidized state of the βPhe99Tyr P-cluster. The Ser ligand coordinates the P-cluster, but not the Tyr ligand. Map is contoured at 3.5 σ. (13.0 keV, Fe f" = 1.43) (PDB ID: 6O7M)

To validate the density of the P-clusters in each of the crystal structures, omit maps were created in which all atoms of the P-cluster and residues at positions β99 and β188 were omitted (**Fig. 2.9**). In all structures, FeMoco resembled wt DT-reduced FeMoco (**Fig. 2.10**). The re-reduced samples did not contain an exogenous source of Fe, leaving the source of reconstituted Fe unclear. It is possible that the Fe was cannibalized from MoFeP in the crystallization solution, similar to how aconitase can be reconstituted upon re-reduction.[105]

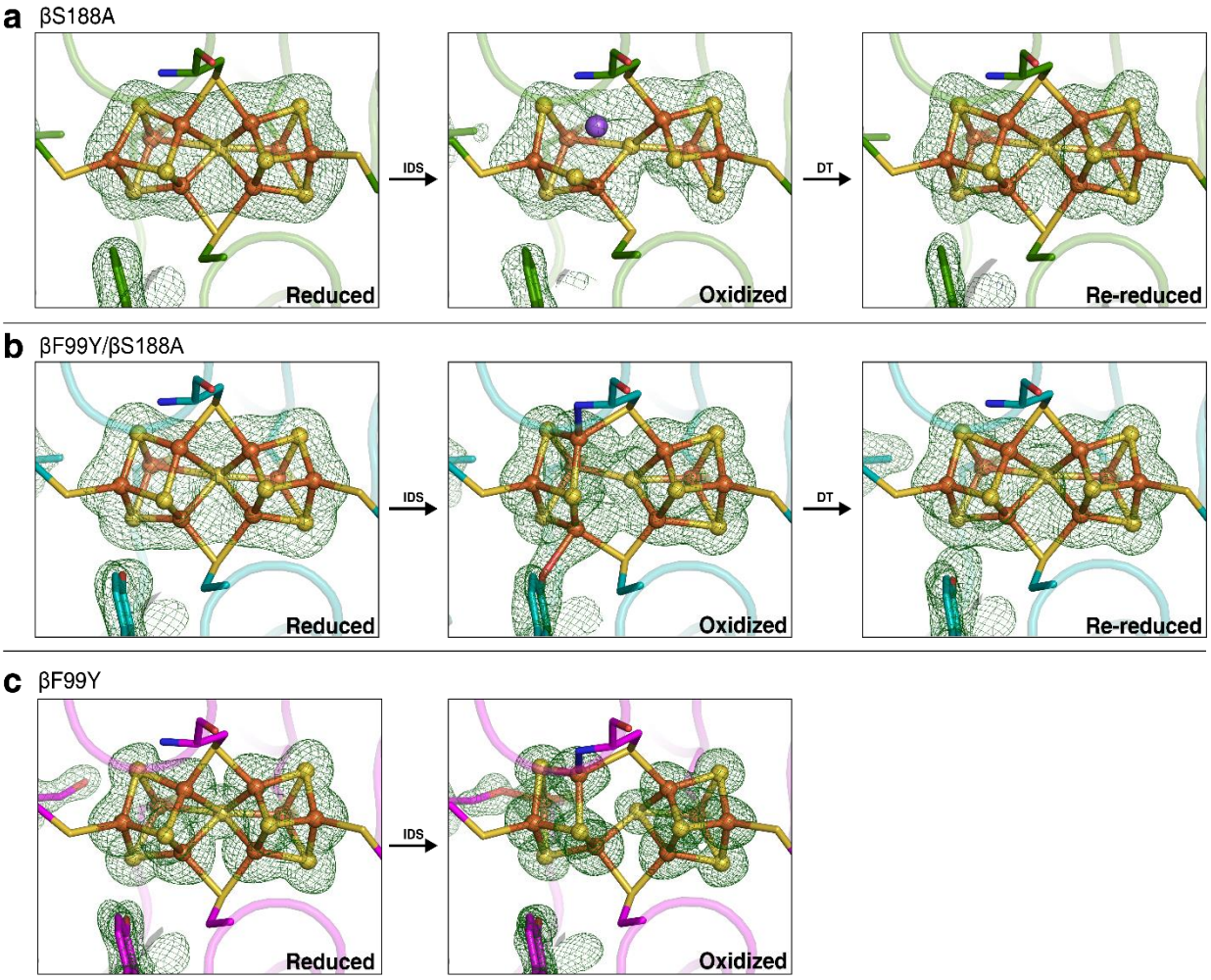


**Figure 2.9** *2F*$_O$*-F*$_C$ omit maps contoured at 5.0 σ corresponding to all atoms in residues β99 and β188 and the P-cluster in (a) βSer188Ala, (b) βPhe99Tyr/βSer188Ala, and (c) βPhe99Tyr *Av* MoFeP. The purple spheres (middle panel in (a)) was tentatively assigned to a Na ion.

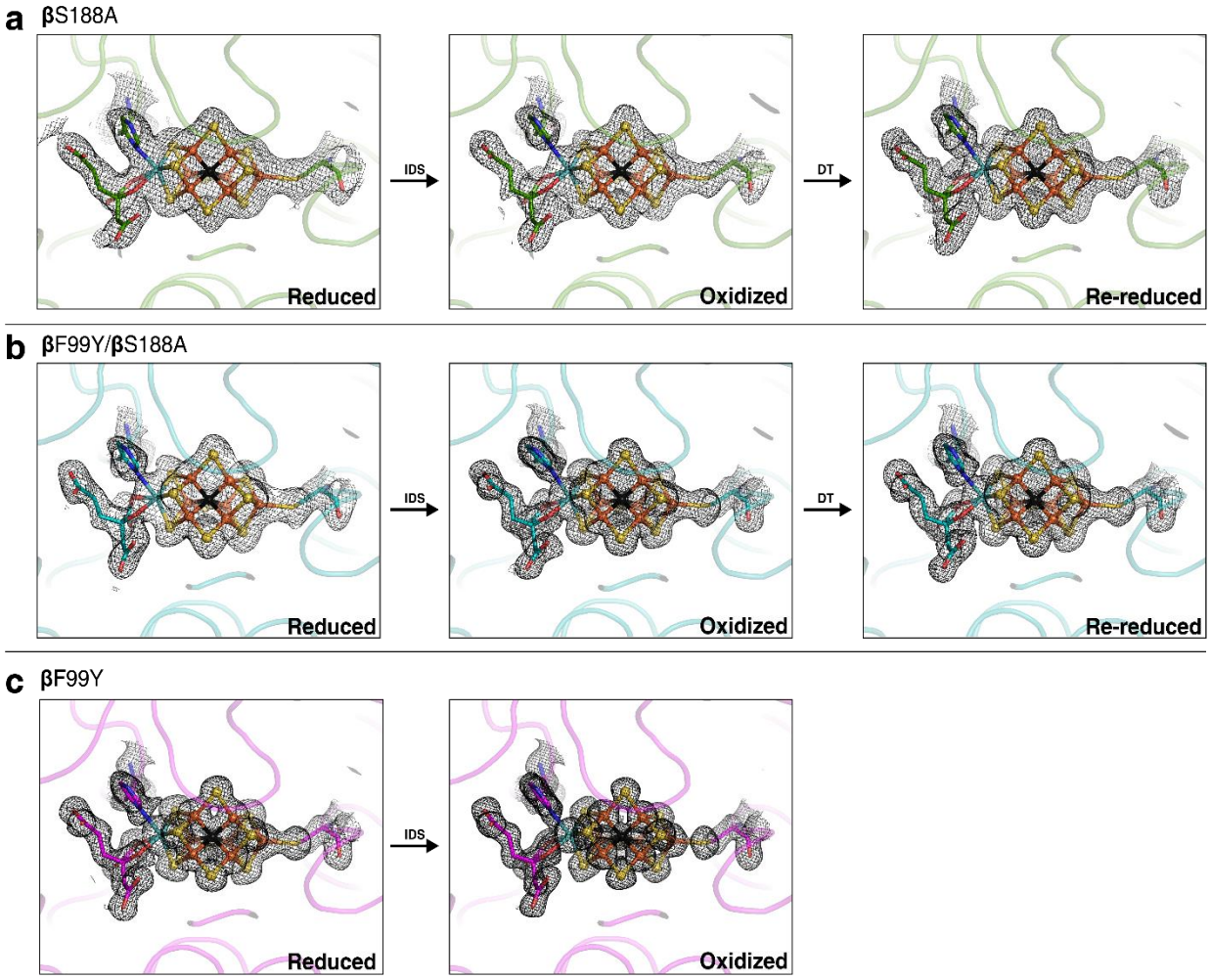


**Figure 2.10** Structures of FeMoco demonstrate proper cluster incorporation into each of the *Av* MoFeP mutants. $2F_O–F_C$ electron density maps are contoured at 1.0 σ. (a) DT-reduced, IDS-oxidized, and DT- re-reduced βSer188Ala MoFeP. (b) DT-reduced, IDS-oxidized, and DT-re-reduced βPhe99Tyr/βSer188Ala MoFeP. (c) DT-reduced and IDS-oxidized βPhe99Tyr MoFeP.

### 2.3.2 Electron paramagnetic resonance (EPR) spectroscopy of *Azotobacter vinelandii* MoFe-protein P-cluster ligand mutants

To probe the electronic states of the P-clusters in the MoFeP variants, X-band EPR spectra were collected on the DT-reduced, IDS-oxidized, and DT-re-reduced (in the case of the labile P-cluster mutants) MoFePs (**Fig. 2.11**).[97] Perpendicular mode spectra of the DT-reduced and DT-re-reduced samples exhibit $S$ = 3/2 signals, typical of resting state FeMoco (**Fig. 2.11a**).[95, 96] The DT-re-reduced samples of *Av* βPhe99Tyr/βSer188Ala and *Av* βSer188Ala contained a new feature in the $g \approx 1.9$ region

that could possibly have arisen from some degraded protein. As expected, no features could be assigned to the all-ferrous P-cluster in the DT-reduced resting state.[97]

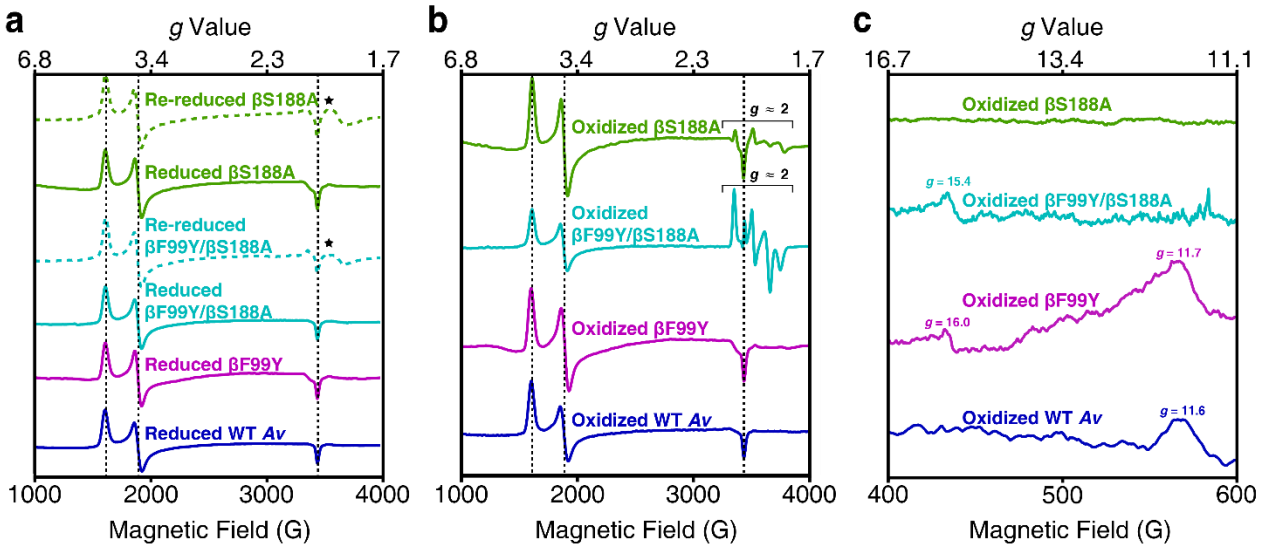


**Figure 2.11** X-band EPR spectra of the *Av* MoFeP variants. All spectra were collected at 5−10 K. Dashed black lines mark the features that arise from the $S = 3/2$ signal associated with FeMoco. (a) Perpendicular-mode EPR spectra of DT-reduced and DT-re-reduced MoFeP. Reduced mutants have the same FeMoco-associated features present in wt *Av*. The spectra of re-reduced βSer188Ala and βPhe99Tyr/βSer188Ala MoFeP display new features in the $g \approx 1.9$ region (*) that may arise from some amount of degraded protein. The data (from top to bottom) were collected at 8, 6, 9, 5, 6, and 8 K. (b) Perpendicular-mode EPR spectra of IDS-oxidized MoFeP. The spectra of βSer188Ala and βPhe99Tyr/βSer188Ala MoFeP have features in the $g \approx 2.0$ region attributed to a population of MoFeP containing only one $Fe^{3+}$ per P-cluster. Data (from top to bottom) were collected at 5, 9, 6, and 8 K. (c) Parallel-mode spectra of the oxidized *Av* MoFeP demonstrate that ligation of the oxygenic ligand to the P-cluster results in an integer spin. Tyr ligation (βPhe99Tyr/βSer188Ala and βPhe99Tyr) results in features at $g \approx 16$, and Ser ligation (βPhe99Tyr and wt) at $g \approx 12$. The data (from top to bottom) were collected at 5, 9, 6, and 8 K

Upon oxidation to $P^{OX}$, wt *Av* and *Gd* MoFeP exhibited solely the $S = 3/2$ signal in perpendicular mode EPR arising from FeMoco. Interestingly, both the labile *Av* P-cluster mutants (*Av* βPhe99Tyr/βSer188Ala and *Av* βSer188Ala) exhibited an additional feature at $g \approx 2$ upon IDS-oxidation (**Fig. 2.11b**). Both of these spectra have peaks at the same $g$ values, although the intensity is much stronger for *Av* βPhe99Tyr/βSer188Ala than *Av* βSer188Ala. This feature arose from changes in the P-cluster and not FeMoco, as evidenced by FeMoco remaining in its resting state conformation in the crystal structures (**Fig. 2.10b,c**), and by wt and βPhe99Tyr MoFePs lacking this feature.[97] This signal

matches the perpendicular mode EPR spectrum of *Av* $P^{1+}$. $P^{1+}$ is very difficult to stably reach in wt due the nearly identical midpoint potentials of the $P^N/P^{1+}$ and $P^{1+}/P^{OX}$ redox couples.[51, 62] In the case of the labile P-cluster mutants, these signals likely arose from a population of P-clusters that contained only one $Fe^{3+}$ ion and are thus in a pseudo $P^{1+}$ state ("pseudo" because these P-clusters would only have seven Fe atoms instead of eight). In the case *Av* βSer188Ala, the population of the pseudo $P^{1+}$ state was very small as evidenced by the complete loss of two Fe in the crystal structure and the low intensity $g \approx 2$ feature. This indicated that the labile Fe centers are $Fe^{3+}$, rather than $Fe^{2+}$, and that a small population of IDS-oxidized *Av* βSer188Ala MoFeP lost only one Fe per P-cluster.

In wt MoFeP, $P^{OX}$ creates an integer spin system ($S \geq 3$) which results in a parallel mode EPR signal at $g \approx 12$ or $g \approx 16$ for *Av* or *Gd* (and also MoFeP from the Tyr-containing organism *Xanthobacter autotrophicus* (*Xa*)), respectively.[51, 59, 95, 96] It has been proposed that the shift in the signal results from the identity of the oxygenic ligand (Ser vs Tyr), although this had not been previously tested.[59] Upon oxidation, *Av* βSer188Ala was silent in parallel mode EPR, in agreement with both labile Fe centers having an oxidation state of +3 (**Fig. 2.11c**). Oxidized *Av* βPhe99Tyr/βSer188Ala had a signal at $g \approx 15$, similar to the signal of *Gd* $P^{OX}$ (**Fig. 2.11c**). The shift of the parallel mode signal from wt *Av* $g \approx 12$ to almost the $g \approx 16$ as seen in wt *Gd* provided evidence that the *g* value was highly influenced by the identity of the oxygenic ligand. Lastly, the $P^{OX}$ parallel mode EPR signal of *Av* βPhe99Tyr exhibited a feature at $g \approx 12$ and $g \approx 16$ (**Fig. 2.11c**). The $g \approx 12$ feature was much more intense than the $g \approx 16$ signal, indicating that Ser and Tyr ligation existed in equilibrium, with the Ser ligation being the preferred state. All DT-reduced MoFeP variants and wt *Av* MoFeP were parallel-mode EPR silent, as expected (**Fig 2.12**).[97]

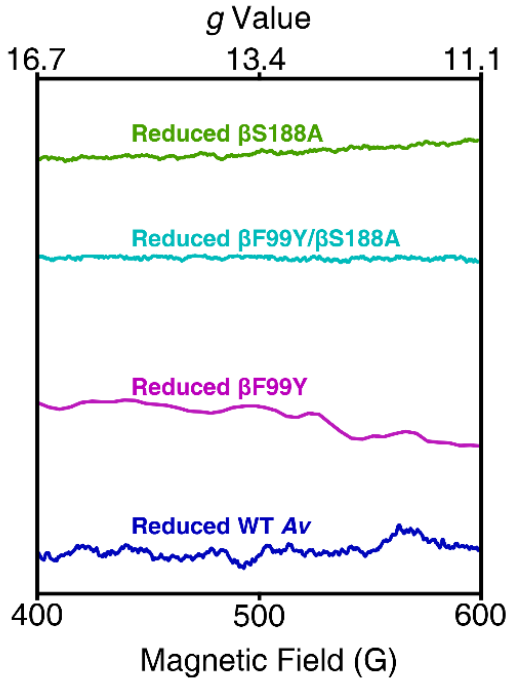


**Figure 2.12** Parallel-mode X-band EPR spectra of the DT-reduced *Av* MoFeP variants collected at 5−10 K. No features are present in any of the spectra.

### 2.3.3 *In vitro* specific activity of *Azotobacter vinelandii* MoFe-protein P-cluster mutants

To assess the functional effects of the mutations to the oxygenic P-cluster ligands, I measured the substrate reduction activities of each MoFeP variant *in vitro* (**Fig. 2.13**). Surprisingly, the activities of the six-electron reduction of $N_2$ and concomitant two-electron reduction of protons ($H^+$) to form hydrogen ($H_2$) were indistinguishable from wt *Av* MoFeP (**Fig. 2.13a,b,c**). Nitrogenase is also capable of reducing many simpler substrates besides $N_2$, including the two-electron reduction of acetylene ($C_2H_2$) to ethylene ($C_2H_4$). The $C_2H_2$ reduction activities (pH 8.0) of *Av* βSer188Ala, *Av* βPhe99Tyr/βSer188Ala, and *Av* βPhe99Tyr relative to wt *Av* MoFeP were 79 ± 3%, 82 ± 4%, and 60 ± 7%, respectively (**Fig. 2.13d**).[97] The similarity of the $N_2/H^+$ reduction activities of the P-cluster mutants and wt could result from (1) the kinetics of Fe loss from the P-cluster being faster than the rate-limiting steps of substrate reduction, (2) the kinetics of reducing the oxidized P-cluster during catalysis being faster than dissociation of Fe from

the oxidized P-cluster, or (3) the structures of the IDS-oxidized P-clusters not being populated during catalysis.

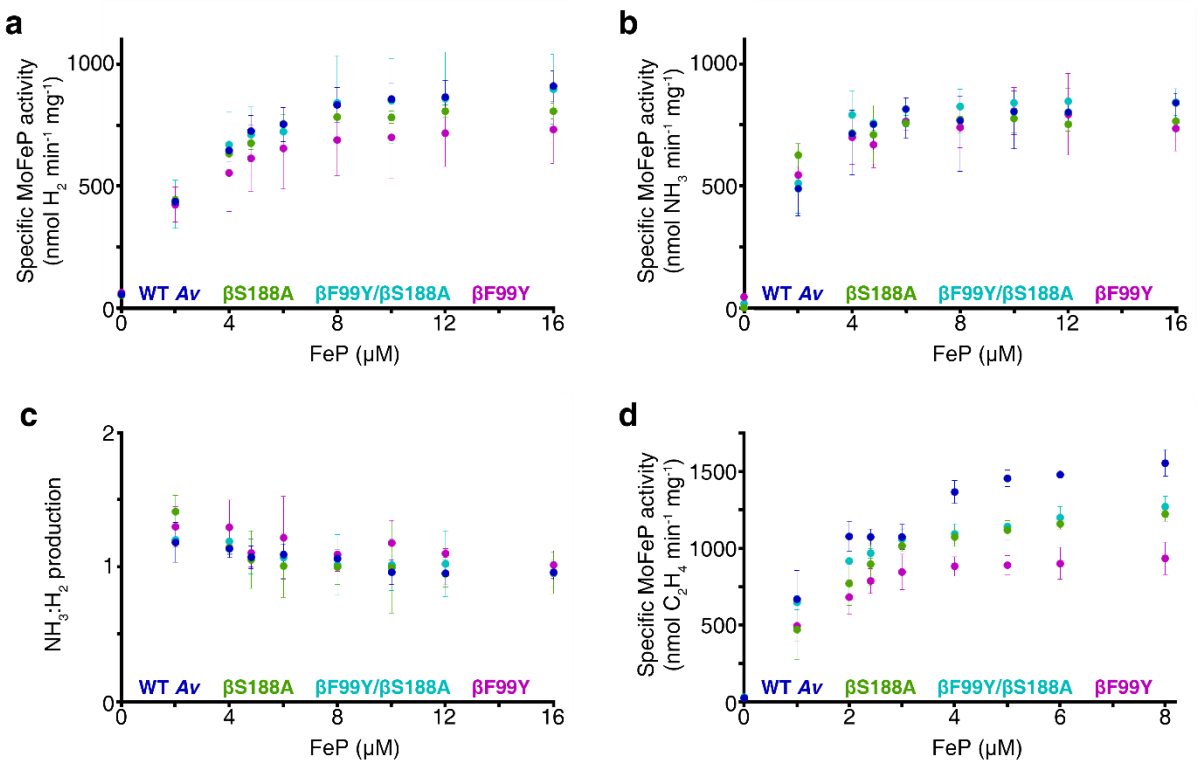


**Figure 2.13** Activity assays for wt, βSer188Ala, βPhe99Tyr/βSer188Ala, and βPhe99Tyr MoFeP. Error bars represent one standard deviation. (a) Nitrogenase reduction of $H^+$ to $H_2$ under $N_2$ atmosphere. (b) Nitrogenase reduction of $N_2$ to $NH_3$ under $N_2$ atmosphere. (c) Ratio of $NH_3$ to $H_2$ production measured in parallel from a single sample under $N_2$ atmosphere. (d) Nitrogenase reduction of $C_2H_2$ to $C_2H_4$ under $Ar/C_2H_2$ atmosphere.

### 2.3.4 Growth rates of *Azotobacter vinelandii* MoFe-protein P-cluster ligand mutant strains

To probe if the P-cluster mutants affected $N_2$ reduction *in vivo*, the growth rates of the *Av* P-cluster mutants and wt *Av* cells were determined under diazotrophic growth conditions (**Fig. 2.14**). The doubling times of the mutants were indistinguishable from the doubling time of wt *Av* cells.[97] Thus, under the growth conditions used, the mutations did not affect the diazotrophic growth rates of the mutant *Av* strains, suggesting that all of the MoFeP variants were possibly as active as wt MoFeP *in vivo*.

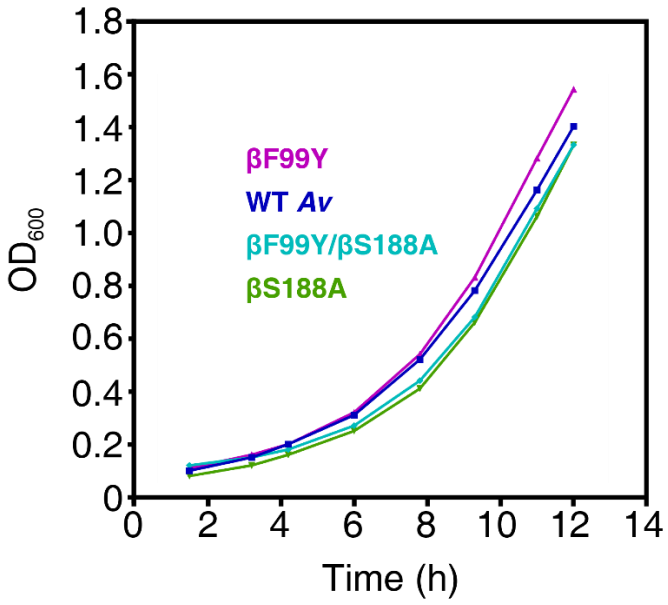


**Figure 2.14** Diazotrophic growth curves of *Av* MoFeP variants and wt *Av*. βSer188Ala and βPhe99Tyr/βSer188Ala strains demonstrate a slightly longer lag time than wt and βPhe99Tyr.

**2.4 Conclusions**

These results indicate that the P-cluster is very dynamic, and that it is also an intrinsically labile Fe-S cluster that rests on the brink of instability. The native, oxygenic ligand (βSer188 in *Av* or βTyr99 in *Gd*) stabilizes $P^{OX}$ and thus controls the redox-metastability. There exist many other systems in nature that contain compositionally dynamic clusters, including the C-cluster in CODH,[103] the [4Fe-3S] cluster in oxygen-tolerant hydrogenases,[106, 107] FeVco in V-nitrogenase,[67] and FeMoco in Mo-nitrognease.[63-66, 104] In all of these examples, the dynamics of the clusters are integral to their function, as is likely the case for the P-cluster. Additionally, *Av* and *Gd* have clearly evolved to stabilize the P-cluster with their native oxygenic ligand, Ser or Tyr, respectively. Factors outside of the primary (and even secondary) coordination spheres of the P-cluster must play a role in stabilizing $P^{OX}$. In nitrogenase, ET from the P-cluster to FeMoco is conformationally gated, and the dynamics of the P-clusters likely play an essential role in the gating mechanism. Elucidating the mechanism of biological nitrogen fixation thus requires a complete understanding of ET in the nitrogenase complex, including how the P-cluster controls ET to FeMoco.

## 2.5 Future directions: Covariance analysis of nitrogenase MoFe-protein sequences

The *Av* βPhe99Tyr/βSer188Ala MoFeP mutant was designed to mimic wt *Gd* MoFeP by replicating the primary coordination sphere of the *Gd* P-cluster. Unexpectedly, this mutant demonstrated reversible, redox-mediated loss of one Fe on average per P-cluster upon chemical oxidation with IDS. In contrast, wt *Gd* MoFeP does not demonstrate any redox-mediated compositional instability, indicating that one or more residues outside of the primary coordination sphere of the P-cluster must provide redox-stability to the *Gd* P-cluster, and such residue(s) are not present in wt *Av* MoFeP.

To search for residues that may provide compositional stability to the *Gd* MoFeP P-cluster, 45 group I MoFeP sequences[98] (both *nifD* and *nifK* genes coding for the α- and β-subunits, respectively) were aligned and analyzed for residues (using the R package bio3d)[108-110] that covary with βSer188 and βPhe99. Of the 45 group I sequences, 18 contain βTyr99- and 25 contain βSer188- as the sole oxygenic ligand, and 2 contain both βTyr99 and βSer188. As expected, the covariance analysis output the known covariances of βPhe99 with βSer188 as (i.e., *Av*) and βTyr99 with βAla188 (i.e., *Gd*) (**Table 2.3**). In addition to the known covarying residues, the analysis identified 25 more residues that strictly covary with βTyr99, of which 8 are located in *nifD* and 17 in *nifK*. Of these residues, only one is within the vicinity of the P-cluster, βHis102 (~11 Å from Cα to P-cluster) (**Fig. 2.15**). It is possible that *Gd* βHis102 undergoes conformational changes during catalysis, moving close enough to stabilize the deprotonated *Gd* βTyr99 via H-bonding network. In all 18 sequences containing βTyr99, position β102 was a His residues. In the 25 sequences containing βSer188 as the sole P-cluster oxygenic ligand, the identity of the residue at position β102 varied (Tyr, His, Thr, Cys). In *Av* MoFeP, position β102 contains a Tyr residue (**Fig. 2.15**).

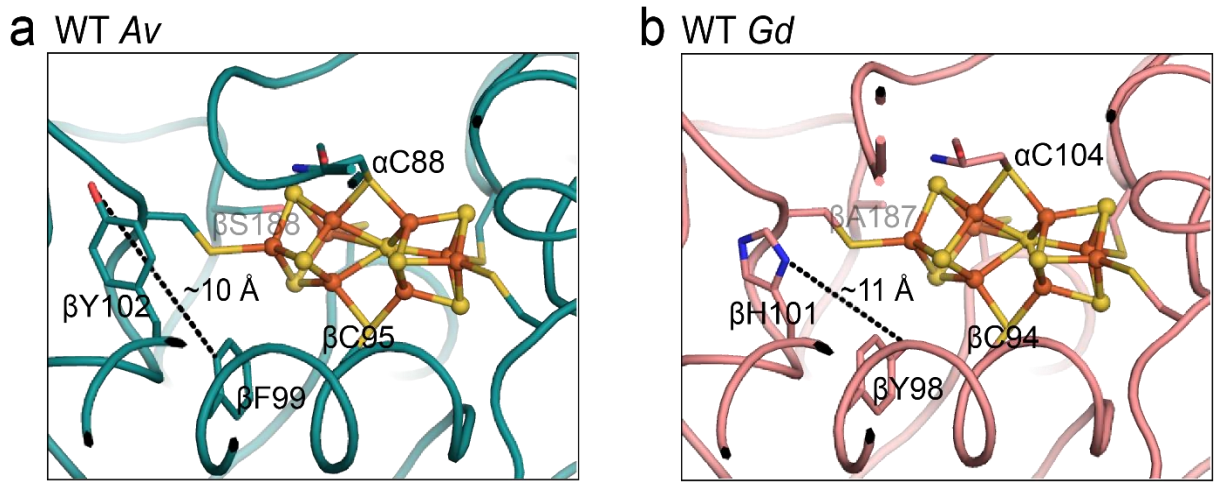


**Figure 2.15** Wt *Av* and *Gd* P-clusters with covarying residue (βTyr102 or βHis 101, respectively) shown as sticks. (a) Wt *Av* contains a Tyr residue in position β102 that is ~10 Å from βPhe99 and ~11 Å from the P-cluster. (PDB ID: 2MIN) (b) Wt *Gd* contains a His residue in position β101 that is ~11 Å from the oxygen atom of βTyr98 and ~11 Å from the P-cluster. (PDB ID: 5KOH)

For the oxygenic ligand (Ser or Tyr) to ligate the P-cluster, it must be in the deprotonated state (serinate or tyrosinate). The hydroxyl groups on Ser and Tyr have a $pK_a$ of ~13 and ~10 in their free amino acid form, indicating that the protein environment around the oxygenic ligand must help to stabilize the ionic form. I hypothesize that βHis102 stabilizes the native, anionic βTyr99 in *Gd*. In future experiments to test this hypothesis, an *Av* βPhe99Tyr/βTyr101His/βSer188Ala mutant should be expressed and characterized. If βHis101 indeed stabilizes *Gd* $P^{OX}$, this mutant will not contain any redox-labile Fe in the P-cluster.

**Table 2.3** Group I MoFeP covariance analysis by identity of residues. Sequences are sorted into groups based on the oxygenic ligand (only βTyr99, only βSer188, or both βTyr99 *and* βSer188).

| Gene | Residue number (*Av* numbering) | Residue(s) present βSer188 group | Residue(s) present βTyr99 group | Residue(s) present βTyr99/βSer188 |
|---|---|---|---|---|
| *nifD* | 59 | I/T/A/Q/V | I | A |
| *nifD* | 240 | I/M/K/R/L | I | A/K |
| *nifD* | 260 | S/H/A/N/T/E/V | A | D/E |
| *nifD* | 263 | E/M/F/I/K/Q/V/T | E | A |
| *nifD* | 268 | V/A/S | A | V |
| *nifD* | 297 | Y/F | Y | F |
| *nifD* | 392 | K/H/Q/G/P/A/E | H | P/E |
| *nifD* | 414 | K/S/E/N/D | E | H/K |
| *nifK* | 10 | A/D/P/-/S/T | D | P/K |
| *nifK* | 18 | Q/D/P/-/E/S | P | - |
| *nifK* | 99 | F | Y | Y |
| *nifK* | 101 | Y/H/T/C | H | T/A |
| *nifK* | 116 | D/S | S | D |
| *nifK* | 188 | S | A | S |
| *nifK* | 208 | F/L | F | L |
| *nifK* | 209 | T/A/S | W | T/A |
| *nifK* | 232 | T(2P) | G | A |
| *nifK* | 234 | L/V/HHP/S/I | V | T |
| *nifK* | 263 | T/S/A/M | T | S |
| *nifK* | 266 | D/M/N/T/L/Y/- | D | D |
| *nifK* | 270 | R/N/E/D/K/Q | R | R |
| *nifK* | 396 | H/S/N/T | T | S |
| *nifK* | 402 | W/F | W | L/V |
| *nifK* | 450 | F/Y/R/A/E | Y | F |
| *nifK* | 483 | T/A/S/P | P | P |
| *nifK* | 498 | V/A/L | L | C/A |
| *nifK* | 499 | N | D | N |
| *nifK* | 502 | L/M/I/F | F | L |

## 2.6 Materials and methods

### 2.6.1 Site-directed mutagenesis, expression, and purification of *Azotobacter vinelandii* MoFe-protein mutants

Burke's media ($BM^+$) was used for all *Av* culture growths, unless otherwise noted. $BM^+$ media contained 0.9 mM $CaCl_2$, 1.67 mM $MgSO_4$, 0.035 mM $FeSO_4$, 0.002 mM $Na_2Mo_2O_4$, 181 mM (or 2.0%) sucrose ($C_{12}H_{22}O_{11}$), 10 mM $K_3PO_4$ pH 7.5, and 10 mM $NH_4Cl$. Diazotrophic growths used Burke's media lacking a fixed source of nitrogen ($NH_4Cl$ was omitted, $BM^-$). Burke's agar additionally contained 23 g/L agar. Cultures were grown at 30 ˚C and shaken at 200 rpm. Cell lysis, purification, and experiments with purified proteins were carried out on a Schlenk line under ultra-high purity Ar (or $N_2$ in the case of nitrogen reduction assays), or in a Coy anaerobic chamber (90% Ar/ 10% $H_2$). All buffers and columns used for assays and purification were prepared under anaerobic conditions.

All MoFeP variants were expressed from the native organism, *Av*. Mutagenesis of the *Av* genome was carried out using a previously established two-step process.[111-113] First, a deletion (Δ) strain was generated in which the location of the mutations and at least the surrounding 50 nucleotides were removed from the genome and replaced with an antibiotic resistance cassette. Here, the deletion strain used was DJ200 (kindly gifted by the Dean lab at Virginia Tech), a Δ*nifDK* strain (deleted region: αGlu476 – βLeu293) containing a kanamycin resistance cassette. This strain was deficient for nitrogen fixation (nif-) and was kanamycin resistant (up to 5 μg/mL kanamycin).

The second step was to transform the deletion strain with a rescue plasmid containing the gene of interest and the desired mutation(s). The gene was incorporated into the genome of the deletion strain via double homologous recombination, replacing the kanamycin resistance cassette. Thus, the transformants were no longer kanamycin resistant, and nitrogen fixation ability had been rescued (nif+). The rescue plasmid used was a pGEM-T Easy plasmid containing the C-terminal region of *nifD* and the complete

*nifK*. Mutations were incorporated into the plasmid via site PCR site-directed mutagenesis with the following primers followed by amplification of the plasmid with *E. coli* XL1-Blue cells:

βSer188Ala forward primer: 5′-ATACCCCGGCCTTCGTGGGC-3′

βSer188Ala reverse primer: 5′-GCCCACGAAGGCCGGGGTAT-3′

βPhe99Tyr forward primer: 5′-TGCGTCGCCTACTACCGCTCCTACTTCAAC-3′

βPhe99Tyr reverse primer: 5′-GTTGAAGTAGGAGCGGTAGTAGGCGACGCA-3′

To transform the DJ200 *Av* cells with the rescue plasmid, cultures were grown in modified $BM^+$ media ($FeSO_4$ was omitted and only 0.09 mM $CaCl_2$) while shaking at 150 rpm to $OD_{600}$ ~0.5. Cultures were fluorescent green from siderophores released due to Fe-limitation. 50 µL of the cells was transformed by adding 50 µL transformation buffer (20 mM MOPS, pH 7.5, 20 mM $MgSO_4$) and 1-5 µg of the purified rescue plasmid. Transformants were screened for both restoration of nitrogen fixation ability on $BM^-$ agar and for loss of kanamycin resistance. Many passes on $BM^-$ agar were required in order to obtain a clean sequencing result due to the large number of copies of the chromosome that each *Av* cell contains. All mutants were confirmed by sequencing after carrying out colony PCR (**Fig 2.16**).

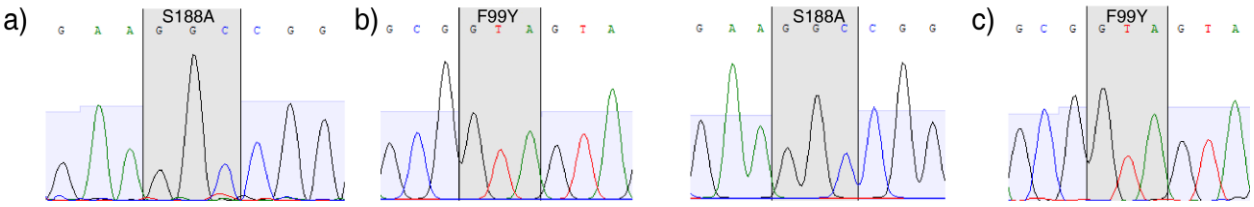


**Figure 2.16** *NifK* sequencing results of mutations to *Av* chromosomal DNA. Codons are shown as reverse complements because sequencing was completed using reverse primers. Highlighted regions are the codons of interest. (a) βSer188Ala mutation (GCC) (b) βPhe99Tyr/βSer188Ala mutations (TAC and GCC, respectively) and (c) βPhe99Tyr mutation (TAC).

Protein expression was carried out using a 60 L New Brunswick Scientific fermenter. First, a 100 mL $BM^-$ starter culture in a 500 mL flask was inoculated and grown to $OD_{600}$ >1.5. Next, a 1.0 L $BM^-$ starter culture in a 2.8 L flask was inoculated with 10-25 mL of the first starter culture. 400 mL of the

starter culture was used to inoculate 50 L of modified $BM^+$ media (only 3 mM $NH_4Cl$) in the fermenter. Derepression of the *nif* genes (and thus nitrogenase expression) was indicated by a spike in the dissolved oxygen content of the culture. Cells were harvested ~4 h after derepression occurred, followed by concentration to < 6 L with a Pellicon 2 Tangential flow membrane and centrifugation at 5000 rpm and 4 ˚C. Cell pellets (ranging from 120-210 g) were stored at -80 ˚C until purification.

Cells were resuspended in buffer Eq (50 mM TRIS, pH 7.75, 200 mM NaCl, 5 mM DT, 0.1 mg/mL DNase I). The resuspended cells were lysed under a bed of Ar using a microfluidizer at 16,000 psi $N_2$. The dark brown lysate was centrifuged under Ar at 12,000 rpm for 75 min, and the supernatant was anaerobically transferred into a pear-shaped flask. Supernatant was loaded onto a DEAE Sepharose column, followed by an overnight wash with 1.5 L of buffer Eq (omitting the DNase). A linear gradient (200 to 500 mM NaCl at 2.5 mL/min for 1.0 L) was used to elute both FeP and MoFeP (proteins eluted at conductivities of ~30 and ~25 mS/cm, respectively). Sodium dodecyl sulfate polyacrylamide gel electrophoresis (SDS-PAGE) was used to identify fractions containing the proteins of interest, which were then combined and diluted ~2-fold with salt-free buffer (50 mM TRIS, pH 7.75). FeP and MoFeP were concentrated individually on a small DEAE column, eluting with high-salt buffer (50 mM TRIS, pH 7.75, 500 mM NaCl, 5 mM DT). An orthogonal purification step was then carried out with gel filtration on a Sepharose 200 column (50 mM TRIS, pH 8.0, 500 mM NaCl, 5 mM DT). Fractions containing pure proteins were identified with SDS-PAGE (**Fig. 2.17**) and concentrated using a 10 kDa Amicon concentrator under ~15 psi 90% Ar/10% $H_2$. Concentrated, purified proteins were aliquoted and stored in cryovials in liquid nitrogen. Protein concentrations were determined using a bpy-Fe-chelation assay (6.2 M guanidine-HCl, 2 mM 2,2-bipyridine, 10% glacial acetic acid) at 522 nm using an extinction coefficient of 8650 $M^{-1}$ $cm^{-1}$.[97]

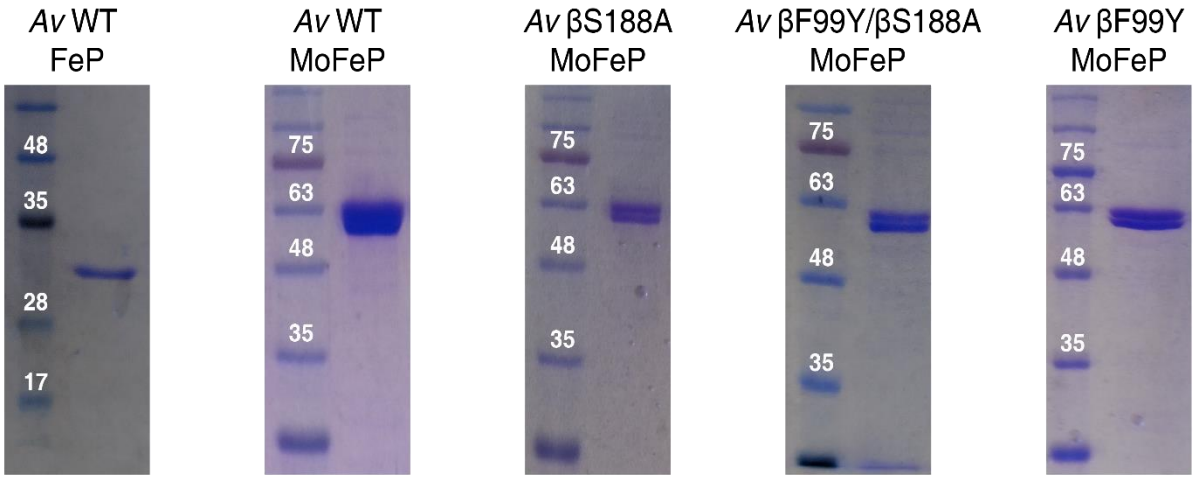


**Figure 2.17** SDS-PAGE of various proteins studied in this work (molecular weight protein ladder is included in each gel as the first lane). MoFeP has characteristic double band due to slight difference in molecular weight of the α- and β-subunits.

### 2.6.2 Crystallography of MoFe-protein

MoFeP crystals were prepared using the sitting drop vapor diffusion method. All crystals were grown, harvested, cryoprotected, and frozen in a Coy anaerobic chamber (90% Ar/ 10% $H_2$) at room temperature (freezing took place in liquid nitrogen). Crystal growth was carried out using 500 μL of precipitation solution and 2 + 2 μL drops of protein solution (125 μM) and precipitation solution. Crystals matured over the course of 3 days to 2 weeks and ranged in size from ~50 μm to ~200 μm along the longest axis. Crystallization solutions are provided in the PDB. Crystals were cryoprotected in perfluoropolyether.[97]

Data were collected with multiwavelength synchrotron radiation at either SSRL beamline 9-2 or ALS beamline 5.0.2. Data collected from ALS were indexed, integrated and scaled using XDS.[114] Data collected from SSRL were indexed, integrated, and scaled using iMosflm and Aimless.[115] Structures were determined using molecular replacement (search model PDB ID: 2MIN) with Phaser-MR of the PHENIX suite, followed by refinement with phenix.refine and Coot.[116] Structure refinement used riding hydrogens that were added to the model with phenix.reduce.[116]

### 2.6.3 Electron paramagnetic resonance spectroscopy of MoFe-protein

EPR samples were prepared in a Coy anaerobic chamber under 90% Ar/ 10% $H_2$. Proteins were prepared for EPR by buffer exchanging into 50 mM TRIS, pH 8.0, 500 mM NaCl with 10 kDa cutoff Microcon filters to remove DT, followed by concentrating to 50 μM. Samples were either reduced or oxidized with 10 mM DT or 5 mM IDS, respectively. Re-reduced samples were prepared by running the oxidized sample over a 10-DG desalting column to remove IDS, concentrating to 50 μM, then re-reducing with 10 mM DT.

Data were collected on X-band Bruker EMX spectrometer with a liquid helium cryostat at 5-10 K. Spectra were recorded with a modulation frequency of 100.0 kHz and modulation amplitude of 9.8 G. Perpendicular and parallel mode spectra were collected with microwave frequencies of ~9.62 and ~9.39 GHz and microwave power of 6 and 127 mW, respectively.[97] Perpendicular mode spectra were background subtracted using the EasySpin software package.[117]

### 2.6.4 *In vitro* MoFe-protein $NH_3$, $H_2$, and $C_2H_4$ activity assays

All substrate reduction assays were replicated at least three times. Assays were carried out in 10 mL vials on a Schlenk line under ultra-high purity gas (Ar or $N_2$). $NH_3$ and $H_2$ were measured from the same sample vial. 1.0 mL of an ATP regeneration system (50 mM buffer: HEPES for $NH_3$ and $H_2$ assays, TRIS for $C_2H_4$ assays, pH 8.0, and 10 mM $MgCl_2$, 0.125 mg/mL creatine kinase, 5 mM $Na_2ATP$, 30 mM phosphocreatine) was used for each sample. Reaction vials and solutions (excluding protein components) were degassed prior to use. Each reaction contained 13 mM DT. For $NH_3$ and $H_2$ assays, proteins were buffer exchanged with 10-DG desalting columns from TRIS to HEPES buffer (50 mM HEPES, pH 8.0, 500 mM NaCl). FeP was used at a final concentration of 0-16 μM or 0-8 μM for $NH_3/H_2$ or $C_2H_4$ assays, respectively. MoFeP was used at a final concentration of 0.4 μM or 0.2 μM for $NH_3/H_2$ or $C_2H_4$ assays, respectively.

$H_2$ and $C_2H_4$ production were quantified using gas chromatography with a 5A 80/100 molecular sieve column with a TCD and with a HayeSep N packed column with an FID, respectively. $H_2$ and $C_2H_4$ calibration curves were prepared with each experiment daily using injections of the gas of interest diluted in ultra-high purity Ar or $N_2$, respectively.

After completing the $H_2$ injections, $NH_3$ was quantified from the same reaction vial using a modified *o*-phthaladehyde (OPA) fluorescence detection method with a HORIBA Jobin Yvon fluorimeter. All steps of the OPA sample preparation were completed in the dark. Proteins were removed from the reactions via filtering 500 μL of the reaction liquid with a 10 kDa cutoff Microcon filtration device. The flow-through was diluted 10-fold with milli-Q water, followed by transferring a 200 μL portion of the diluted solution to 1.8 mL the freshly prepared OPA solution (50 mM $PO_4^{3-}$, 5mM OPA, 3 $Na_2SO_3$, and 12.5% MeOH). The reactions were allowed to react for 2 h before measurements were taken. Fluorescence was measured at excitation of 365 nm and emission of 422 nm. Calibration curves were prepared daily using $NH_4Cl$ standards that were prepared in parallel to the reaction samples. [97]

### 2.6.5 Covariance analysis of nitrogenase MoFe-protein sequences

Covariance analysis was carried out with R using the bio3d package.[108-110] All 45 group I MoFeP sequences[98] were included in the analysis (**Table 2.1**). Sequences (both *nifD* and *nifK*) were aligned using Multiple Sequence Comparison by Log-Expectation (MUSCLE). Each set of aligned sequences (one set for *nifD* and one set for *nifK*) were split into 3 groups: a group that contained βTyr99 as the only oxygenic ligand (18 sequences), a group that contained βSer188 as the only oxygenic ligand (25 sequences), and a group that contained both βTyr99 and βSer188 (2 sequences). Sequence conservation was then analyzed based on identity (pairwise scoring where identical residues have score of 1 and all other have score of 0) and normalized. Similarity scoring (using BLOSUM 62 scoring matrix) yielded similar results to identity scoring, and the remaining analysis only used identity scoring.

Identity scoring was used to determine residues that were highly invariant in each of the three groups (βTyr99, βSer188, and βTyr99/βSer188). The conserved residues in the βTyr99 and βSer188 groups were then compared. Conserved residues that differed (in identity or existence of the conservation) between the two aforementioned groups were then determined to be residues that covaried with the oxygenic P-cluster ligand. The identified residues were then cross-referenced to protein structures in order to form hypotheses regarding which residues play a role in stabilizing the oxidized *Gd* P-cluster.

### 2.7 Acknowledgments

This work was supported by the National Institutes of Health (Grant GM099813 to F.A.T) and by the Molecular Biophysics Training Grant (NIH Grant T32 GM008326). Crystallographic data were collected at either Stanford Radiation Lightsource (SSRL) or the Lawrence Berkeley Natural Laboratory Advanced Light Source (ALS) on behalf of the Department of Energy.

I would like to thank Prof. M. Green (UC Irvine) for the use of EPR instrumentation, Dr. R. Subramanian, and Dr. R. Alberstein for helpful discussions, Prof. C. Morrison and Dr. J. Bailey for help with anaerobic crystallography and structure refinement, and Dr. V. Cash and Prof. D. Dean (Va. Tech) for generously providing the DJ200 *Av* strain.

Chapter 2 is reproduced, in part, with permission from H. Rutledge, J. Rittle, L. M. Williamson, W. A. Xu, D. M. Gagnon, and F. A. Tezcan. Redox-Dependent Metastability of the Nitrogenase P-Cluster, *Journal of the American Chemical Society* **2019**, *141,* 10091-10098. The dissertation author is the primary author on all reprinted materials.

## Chapter 3: Probing the role of βSer188 in *Azotobacter vinelandii* MoFe-protein

### 3.1 Abstract

Nitrogenase catalyzes the multi-electron reduction of dinitrogen to ammonia. Electron transfer in the catalytic protein (MoFeP) proceeds through a unique [8Fe-7S] cluster (P-cluster) to the active site (FeMoco). In the reduced, all-ferrous ($P^N$) state, the P-cluster is coordinated by six cysteine residues. Upon two-electron oxidation to $P^{OX}$, the P-cluster undergoes conformational changes in which a highly conserved oxygenic residue (Ser or Tyr) and a backbone amidate additionally ligate the cluster. Previous studies of *Av* MoFeP in Chapter 2 revealed that when the oxygenic residue, βSer188, was mutated to a non-ligating residue, Ala, the P-cluster became redox-labile and reversibly lost two of its eight Fe centers. Surprisingly, this *Av* strain, βSer188Ala, could still grow and fix nitrogen as quickly as wild-type *Av*, calling into question the necessity of this conserved oxygenic ligand for nitrogenase function. Based on these observations, I hypothesized that βSer188 protects the P-cluster from oxidative stress and metal loss during catalysis under physiologically relevant conditions. Here, I investigated the protective role of βSer188 both *in vivo* and *in vitro*. I measured the ability of the *Av* βSer188Ala to grow under suboptimal conditions (high oxidative stress or Fe-limitation). My results demonstrated that βSer188 (1) increased *Av* cell survival upon exposure to oxidative stress in the form of hydrogen peroxide, (2) was necessary for efficient *Av* diazotrophic growth under Fe-limiting conditions, and (3) protected the P-cluster from metal exchange *in vitro*. Taken together, these findings suggest a structural adaptation of nitrogenase to protect the P-cluster via Ser-ligation, which is a previously unidentified functional role of Ser residues in proteins.

### 3.2 Introduction

#### 3.2.1 Comparing canonical electron transfer Fe-S clusters to the P-cluster

The P-cluster is a unique [8Fe-7S] cluster that serves as an electron relay site, delivering electrons to FeMoco.[8, 57, 118] The evolution of a super-Fe-S-cluster as an electron relay provides evidence, although

circumstantial, that the P-cluster is not a typical, *passive* ET cluster. Canonical Fe-S clusters in ET chains (such as [2Fe-2S], [3Fe-4S], or [4Fe-4S] clusters) are smaller than the P-cluster. The P-cluster is ligated by four terminal and two bridging Cys residues in the $P^N$ state,[21] and it is coordinated by two additional residues (a backbone amidate and a serinate/tyrosinate residue) upon two-electron oxidation to $P^{OX}$ (**Figs 2.1, 2.2**).[21, 58, 59] In contrast, each Fe atom in canonical ET-chain Fe-S clusters is ligated by a terminal side chain residue.[119] Understanding how the P-cluster functions as a *dynamic* electron relay requires understanding the role of P-cluster's unique properties, including the atypical, redox-switchable ligand.

Sequence alignment of 95 MoFeP sequences revealed that the oxygenic ligand (βTyr99 or βSer188) is highly conserved (92 sequences contain one of the oxygenic ligands, 2 of the sequences contain both, and only one contains neither) (**Table 2.1**).[97] The conservation of the oxygenic ligand implies that it serves an important role in nitrogenase function. In chapter 2, I investigated the role of the oxygenic P-cluster ligand by creating three *Av* P-cluster variants: βSer188Ala (no oxygenic ligand), βPhe99Tyr/βSer188Ala (*Gd*-like variant containing only the Tyr ligand), and βPhe99Tyr (contains both oxygenic ligands). Removing or replacing the native βSer188 with Tyr resulted in a compositionally unstable P-cluster that contained up to two redox-labile Fe centers per P-cluster (**Figs 2.3, 2.5**). Despite the redox-instability of these P-cluster variants, the mutant MoFePs retained wt levels of $N_2$ reduction activity *in vitro* (**Fig 2.13b**), and the mutant *Av* strains exhibited identical diazotrophic growth rates as wt *Av* (**Fig 2.14**).[97]

### 3.2.2 Naturally occurring, interconverting [4Fe-4S] clusters and their unique properties

The structural dynamics of $P^N$ and $P^{OX}$ of *Av* βSer188Ala MoFeP resembles interconversion between a pair of [4Fe-4S] clusters and a pair of [3Fe-4S] clusters. Similar cluster interconversions have been seen in naturally occurring clusters including some ferredoxins (*Pyrococcus furiosus* Fd, *Desulfovibrio africanus* Fd I, and *Desulfovibrio africanus* Fd III)[120] and in a class of enzymes containing a catalytic cluster that acts as a Lewis acid. This latter group of clusters includes dihydroxy-acid dehydratase,[121] fumarases A and B,[122] and aconitases.[100, 105] In all of the naturally interconverting clusters,

three of the four Fe atoms are ligated by Cys, while the fourth Fe atom is coordinated by a non-Cys residue (Asp in the case of the ferredoxins)[120] or a an aqua ligand (in the case of the Lewis acidic catalytic clusters).[123]

Like *Av* βSer188Ala, these interconverting clusters reversibly lose an Fe atom from the cubane upon oxidation, resulting in deactivation of the cluster.[120, 122, 124-128] Additionally, the cluster can be demetallated when the cellular labile iron pool (LIP) is low[129] and can be mismetallated *in vitro* in the presence of exogenous metal ions.[120, 130-135] The similarities (redox-lability and conversion between [4Fe-4S] and [3Fe-4S] cubane geometries) between the naturally occurring, interconverting Fe-S clusters and the *Av* βSer188Ala P-cluster suggest that the stabilizing role of the oxygenic ligand (βSer188 in *Av* MoFeP) may serve to protect the P-cluster from oxidative damage and mismetallation, which would not have been evident under the ideal, Fe-replete conditions previously used to measure βSer188Ala's *Av* diazotrophic growth rate and *in vitro* catalytic activity.[97] Such a role may not have been evident in the experiments in Chapter 2 due to the highly reducing environment present during the activity assays and the large excess of Fe used in the growth media. To this end, I investigated the role of βSer188 in protecting the *Av* nitrogenase P-cluster *in vivo* by measuring *Av* βSer188Ala's response to oxidative stress and determining the diazotrophic growth curves under Fe-limiting conditions. Additionally, I have investigated the ability of the βSer188Ala MoFeP P-cluster to be heterometallated *in vitro*.

### 3.3 Results and discussion

#### 3.3.1 *Azotobacter vinelandii* βSer188 protects the P-cluster from oxidative stress *in vivo*

Naturally occurring, interconverting [4Fe-4S] ↔ [3Fe-4S] clusters are prone to oxidative stress, similar to the redox-lability of the *Av* βSer188Ala P-cluster. If βSer188 does indeed protect the wt *Av* P-cluster during *in vivo* $N_2$ reduction, then wt *Av* cells would be less prone to oxidative stress when grown diazotrophically compared to *Av* βSer188Ala which may release Fe from the P-cluster. To investigate if βSer188 protected the P-cluster during oxidative stress *in vivo*, I conducted an oxidative stress test using a

previously reported procedure[136, 137] on both *Av* wt and *Av* βSer188Ala cells by measuring cell survival after exposure to 5 mM hydrogen peroxide ($H_2O_2$), a potent oxidant, for 30 minutes (**Fig. 3.1**).

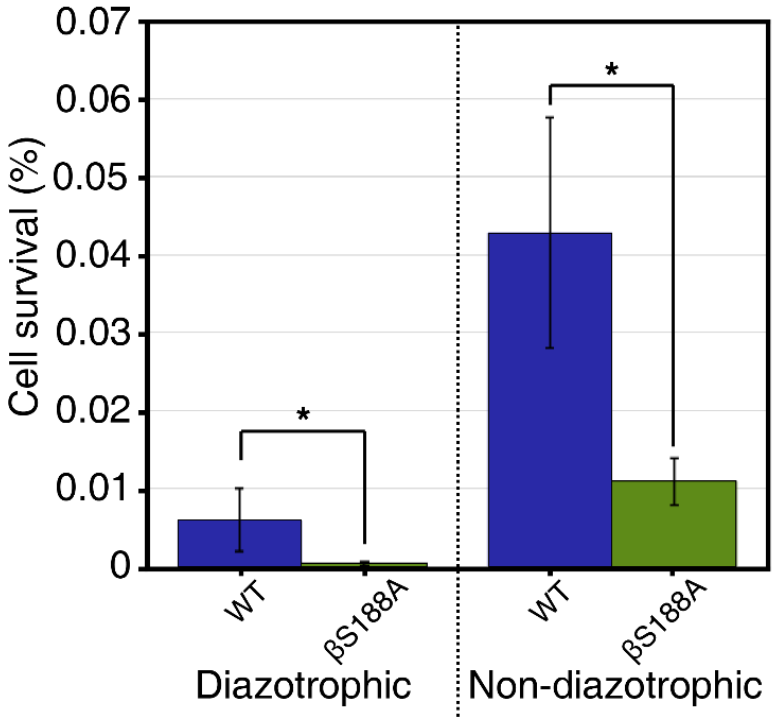


**Figure 3.1** Oxidative stress test of wt and βSer188Ala *Av* cells represented as cell survival. Cell survival was measured by counting colony forming units (CFUs) before and after 30 min exposure to 5 mM $H_2O_2$. Error bars represent standard deviation of experiment carried out in triplicate. Statistical significance is represented by "ns" (not significant) or * (p-value <0.05). Left- culture media contained no fixed source of nitrogen (diazotrophic growth conditions). Right- culture media contained a fixed source of nitrogen (non-diazotrophic).

When exposed to oxidative stress during diazotrophic growth conditions, wt and βSer188Ala *Av* cells had survival rates of $6x10^{-3} \pm 4x10^{-3}$% and $4x10^{-4} \pm 2x10^{-4}$%, respectively. *Av* βSer188Ala's survival rate was only 7% of wt *Av* cells. As expected, the wt *Av* cells exhibited better resilience to the oxidative stress, potentially due to *Av* βSer188Ala losing Fe from its P-cluster. The experiment was also carried out under non-diazotrophic growth conditions, Surprisingly, wt *Av* had a survival rate of $4x10^{-2} \pm 1x10^{-2}$% and *Av* βSer188Ala had a survival rate of $1.1x10^{-2} \pm 3x10^{-3}$%. The survival rate of *Av* βSer188Ala was only 8% that of wt under non-diazotrophic growth conditions. Thus, *Av* βSer188Ala cells were more prone to oxidative stress than wt even in the presence of a fixed source of nitrogen. It has been

demonstrated that *Av* has some expression of MoFeP under non-diazotrophic growth conditions, although the expression levels are much lower than under diazotrophic conditions.[138] It is possible that *Av* βSer188Ala cells may undergo changes in the size of its LIP during non-diazotrophic oxidative stress, potentially leading to changes in Fe metabolism and slowing down growth or limiting cell survival.

### 3.3.2 *Azotobacter vinelandii* βSer188 is required for optimal diazotrophic growth of cells under Fe-limiting conditions

In Chapter 2, the diazotrophic growth curves of the *Av* P-cluster mutants were virtually indistinguishable from wt *Av* (**Fig. 2.14**). The growth medium used for these growth curves is Fe-rich, containing 35 μM Fe (hereafter referred to as 100% Fe). Nutrient rich media is typically used to grow *Av* cells in the lab to ensure fast growth and high expression levels of nitrogenase.[139] The high concentration of Fe would ensure that the cells maintain a large LIP. Although I have been unable to directly probe whether βSer188Ala contains a labile P-cluster *during catalysis* (either *in vivo* or *in vitro*), valuable insights may be gained by indirect observations. If the βSer188Ala P-cluster loses Fe atoms during *in vivo* catalysis, a large LIP could enable growth rates equal to that of wt *Av* by either (1) fast reconstitution of the P-cluster such that Fe-reconstitution is not the rate-limiting step or (2) providing enough Fe to overexpress βSer188Ala MoFeP. To this end, I measured the growth rates of wt and βSer188Ala *Av* cells under diazotrophic growth conditions with varying concentrations of Fe (**Fig. 3.2**).

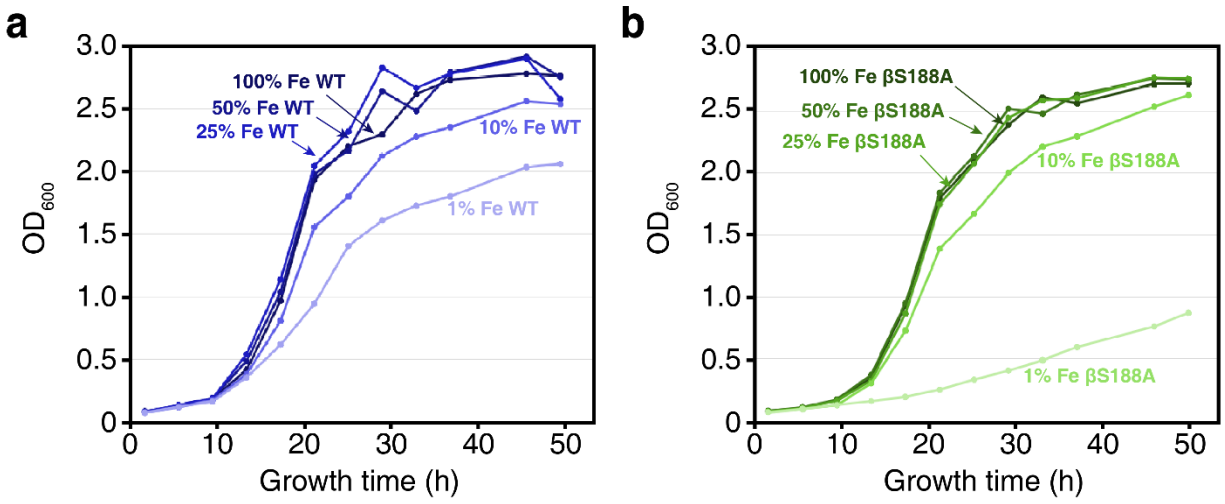


**Figure 3.2** Diazotrophic growth curves of wt and βSer188Ala *Av* cells under varying concentrations of Fe in the medium. Typical Burke's medium contains 35 μM Fe, denoted 100% Fe. (a) Diazotrophic growth curves of wt *Av* have doubling times of 3.9, 4.0, 4.0, 4.2, and 6.3 h at 100%, 50%, 25%, 10%, and 1% Fe, respectively. (b) Diazotrophic growth curves of βSer188Ala *Av* had doubling times of 3.9, 3.9, 3.8, 4.1, and 12.7 h at 100%, 50%, 25%, 10%, and 1% Fe, respectively.

When grown diazotrophically with 10-100% Fe (3.5 – 35 μM Fe), wt and βSer188Ala *Av* cells exhibited identical growth rates. Under 100% Fe, the doubling time of both *Av* strains was 3.9 h. Reducing the Fe concentration to 1% (0.4 μM) decreased the growth rates of both wt and βSer188Ala *Av* to doubling times of 6.3 and 12.7 h, respectively. It is noteworthy that βSer188Ala *Av* was affected to a larger extent than wt *Av*. These results demonstrated that the oxygenic ligand, βSer188, plays a functional role in nitrogenase catalysis *in vivo*. However, the growth rates themselves do not shed light on how βSer188Ala *Av* cells compensate for their lesser-functioning, mutant MoFeP in media containing high Fe concentrations. To probe what causes the different growth rates under different concentrations of Fe, the relative *in vivo* MoFeP activities and expression rates needed to be measured.

### 3.3.3 RT-qPCR of *nifK* gene expression and activity of MoFe-protein *in vivo*

Quantitative reverse transcription polymerase chain reaction (RT-qPCR) was used to determine the relative *nifK* transcript levels, with results normalized to reference gene *rho*, a transcription termination factor that is constitutively expressed and has been used previously for *Av* RT-qPCR normalization (**Fig. 3.3**).[140] As a negative control, *nifK* transcript levels were measured under

non-diazotrophic growth conditions, and unsurprisingly, MoFeP was downregulated in both *Av* strains. When grown under 100% Fe, wt and βSer188Ala *Av* have the same expression rates. Taken together, the observations that both the MoFeP expression rates and the doubling times are identical signifies that their MoFeP *in vivo* activity must be similar under these conditions, even if βSer188Ala MoFeP loses Fe from its P-cluster during catalysis.

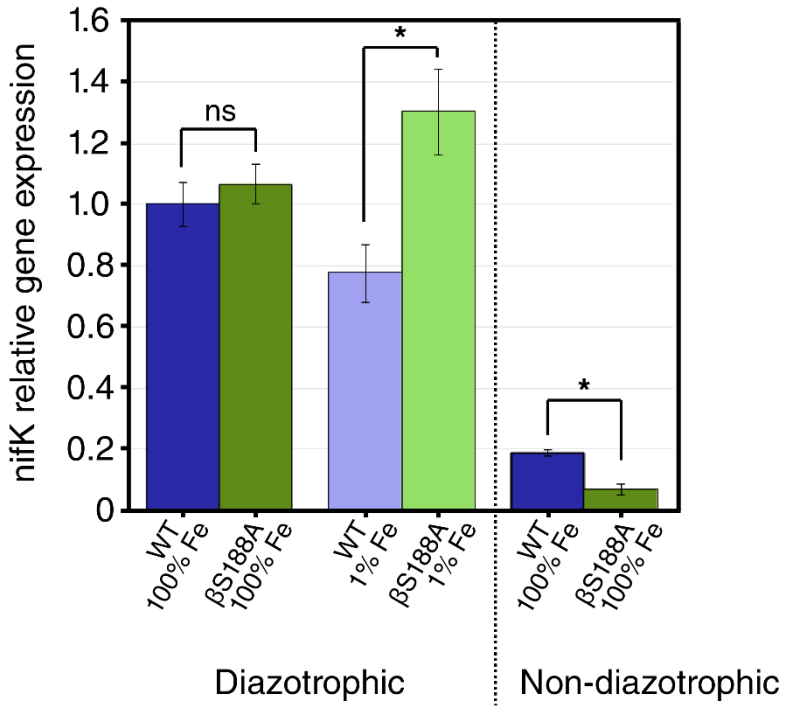


**Figure 3.3** Relative diazotrophic *niK* expression rates determined using RT-qPCR. *nifK* gene expression of wt and βSer188Ala *Av* grown diazotrophically (left) and non-diazotrophically (right) with varying %Fe. Expression levels were normalized to the expression level of reference gene *rho*, and the presented data is relative to wt *Av* cells grown diazotrophically with 100% Fe. Experiment was carried out in technical triplicate of biological triplicates. Error bars represent standard deviation. Statistical significance is represented by "ns" (not significant) or * (p-value <0.05).

In contrast, the expression levels of *nifK* differed under 1% Fe growth conditions: Wt and βSer188Ala *nifK* transcripts were measured at 78% and 130% relative to 100% Fe wt, respectively. This relative increase in βSer188Ala's *nifK* expression suggests that βSer188Ala MoFeP is not functioning at full efficiency under Fe-limited conditions, and thus the cells are compensating via upregulation. The

change in efficiency could result from βSer188Ala having slower P-cluster reconstitution at 1% Fe than at 100% Fe (and thus P-cluster reconstitution may become the rate-limiting step of nitrogen fixation).

*In vivo* efficiencies of wt and βSer188Ala MoFeP were probed by measuring whole cell acetylene ($C_2H_2$) reduction activity. The quantity of ethylene ($C_2H_4$) produced was normalized to the amount of *nifK* transcripts and the $OD_{600}$ of the diazotrophically-grown cells (**Fig. 3.4**). Three of the four efficiencies measured were within error of each other: wt at 1% and 100% Fe, and βSer188Ala at 100% Fe. In contrast, βSer188Ala at 1% Fe exhibited <50% of the activity of wt at 100% Fe. The lowered efficiency of βSer188Ala at 1% Fe suggested that this variant MoFeP was operating much less efficiently under Fe-limited conditions. Thus, βSer188Ala *Av* required a larger LIP than wt to operate efficiently under physiological conditions, implying that βSer188Ala may indeed have a labile P-cluster during physiological catalysis.

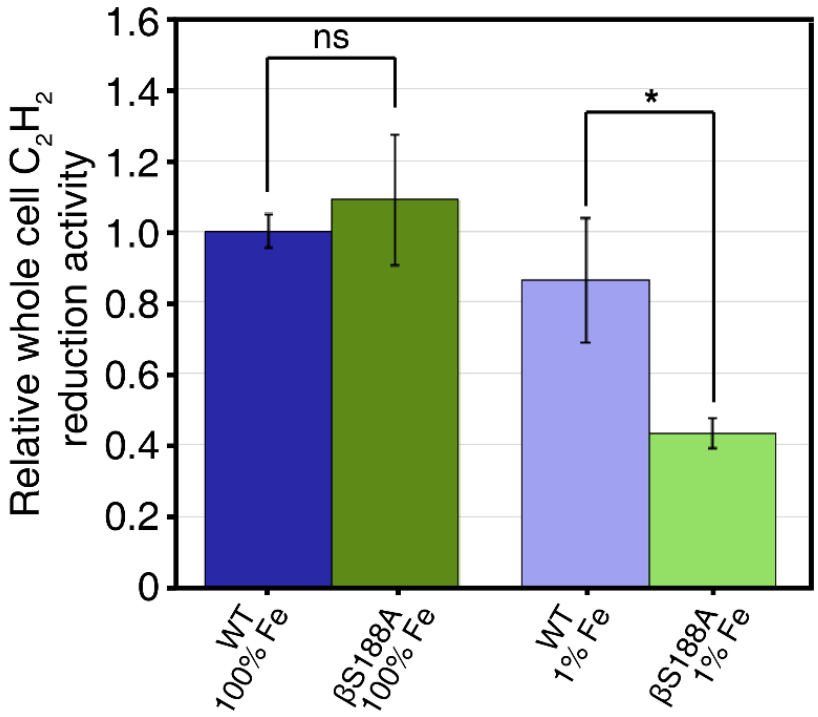


**Figure 3.4** Whole-cell $C_2H_2$ reduction assay using the cultures used for RT-qPCR in Figure 3.3. Error bars represent standard deviation of experiment carried out in biological triplicate. Statistical significance is represented by "ns" (not significant) or * (p-value <0.05).

### 3.3.4 Mössbauer spectroscopy of *Azotobacter vinelandii* $^{57}$Fe-reconstituted βSer188Ala P-cluster

Having determined the role of βerS188 in maintaining the structural and functional integrity of the P-cluster *in vivo*, I next investigated if the absence of this Ser ligand could also lead to dynamic metal exchange with the environment. Heterometallation of the P-cluster is of interest for two reasons: 1) site-specific labeling of the P-cluster could perturb the electronic properties as has been demonstrated with FeMoco,[141, 142] and 2) heterometallation of the βerS188Ala P-cluster would indicate that the Ser ligand may protect the P-cluster from mismetallation *in vivo*. To establish that the [6Fe-7S] βSer188Ala P-cluster could be reconstituted from metal added directly to the solution, βSer188Ala was reconstituted with $^{57}Fe^{2+}$, and a Mössbauer spectrum was collected (**Fig. 3.5 green**). The spectrum collected was best fit by three quadrupole doublets (**Table 3.1**). Comparison of this spectrum with MoFeP from *Klebsiella pneumoniae* (*Kp*) with $^{57}$Fe labeled $P^N$-clusters[143] and that with and that of MoFeP from *Av* with $^{57}$Fe[144] labeled FeMoco demonstrated that the signals arose from the P-clusters, *not* FeMoco. McLean et al. termed the spectral components D, $Fe^{2+}$, and S, and determined that they accounted for a ratio of 10:4:2 Fe sites (4.2 K), respectively.[143] The D-components closely match those of *Kp* with only minor deviations in their isomer shifts and quadrupole splitting that could be due to slight differences in the P-cluster environments. However, not all *Kp* P-cluster features are observed in this spectrum: the S and $Fe^{2+}$ sites are not present. In addition, the βSer188Ala spectrum included a new feature, hereafter referred to as the βSer188Ala-specific feature (however it is possible that this feature arises from octahedral Fe in the form of free $Fe^{2+}(H_2O)_6$ or the 16$^{th}$ Fe-site). Taken together, this Mössbauer experiment indicates that $^{57}Fe^{2+}$ can be taken up from solution into the βSer188Ala P-cluster, but not all sites become occupied by the isotopic label. However, these experiments neither confirm nor rule out the possibility of shuffling of the metals into more than just the two labile sites upon reconstitution.

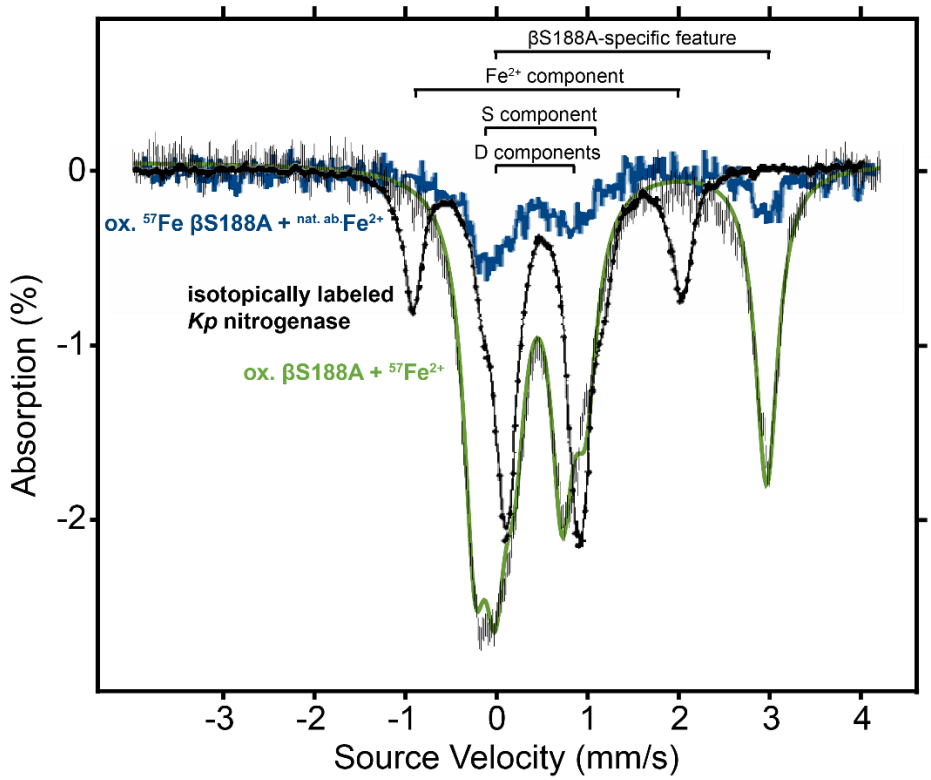


**Figure 3.5** Mössbauer spectra of βSer188Ala after reconstitution with $^{57}Fe^{2+}$ and after subsequent reconstitution with natural abundance $Fe^{2+}$. The [6Fe-7S] P-cluster of oxidized βSer188Ala was reconstituted with $^{57}Fe^{2+}$ (blue). This same sample was oxidized, then reconstituted with natural abundance $Fe^{2+}$ (green). The D-component agrees with the *Kp* P-cluster Mössbauer D-component. The atypical P-cluster component only present in this sample is labeled the βS188A-specific feature, but may arise from adventitious Fe.

**Table 3.1** Best fit resolution of Mössbauer spectra of $^{57}Fe^{2+}$-reconstituted βSer188Ala MoFeP.

| Feature | $\Delta E_Q$ (mm/s) | Δ (mm/s) | Relative area (%) |
|---|---|---|---|
| $D_1$ | 0.779 | 0.589 | 23.8 |
| $D_2$ | 0.735 | 0.352 | 39.6 |
| βSer188Ala-specific feature | 3.203 | 1.363 | 36.6 |

In order to determine whether the Fe-loss and Fe-uptake occurs completely with each redox cycle of MoFeP, the initial Mössbauer sample was re-oxidized with IDS, followed by reconstitution with

natural abundance $Fe^{2+}$. If complete labilization of the same sites occurs with each redox cycle, the expected spectrum would be featureless. However, if incomplete labilization occurs, or if there is shuffling of Fe within the P-cluster upon reconstitution, the previously observed features should remain, albeit at a weaker intensity. The resulting spectrum (**Fig. 3.5 blue**) did indeed contain the same features at lower intensities. Thus, there was either incomplete loss of Fe1 and Fe5 during each redox cycle, or there was shuffling of metals upon reconstitution.

### 3.3.5 Structural characterization of mismetallated *Azotobacter vinelandii* βSer188Ala P-clusters

After establishing that the βSer188Ala P-cluster can uptake $Fe^{2+}$ from solution, I investigated the ability of the cluster to uptake non-Fe metal ions (i.e., heterometals). After oxidizing βSer188Ala MoFeP, the protein was soaked with heterometal ($Ga^{3+}$, $Ni^{2+}$, and $Co^{2+}$), followed by multiple buffer exchanges to remove any excess (unbound) metal ions from solution. The heterometal-reconstituted MoFeP was then crystallized in the presence of DT (**Fig. 3.6**, **Table 3.2**).[97] In Section 2.3.1, crystallization of DT-re-reduced βSer188Ala resulted in full reconstitution (i.e., 8.0 Fe atoms per P-cluster) without any metal ions added to solution (**Fig 2.3c**). Thus, if the heterometal does not incorporate into the oxidized P-cluster, I would expect to see the fully occupied [8Fe-7S] P-cluster with full occupancy of Fe atoms in each of the eight metal-binding sites, which was not the case (**Fig 3.6**). In contrast, each of the heterometallated P-clusters contained a total metal occupancy of 6.0 to 6.9 (integrated over the entire P-cluster) (**Table 3.3**). The labile sites in βSer188Ala were M1 and M5 (where M refers to the site possibly containing either metal ion). Here they showed partial occupancy in the crystal structures, although not full (1.0) occupancy. These differences in occupancy alone suggest that the P-clusters were indeed heterometallated.

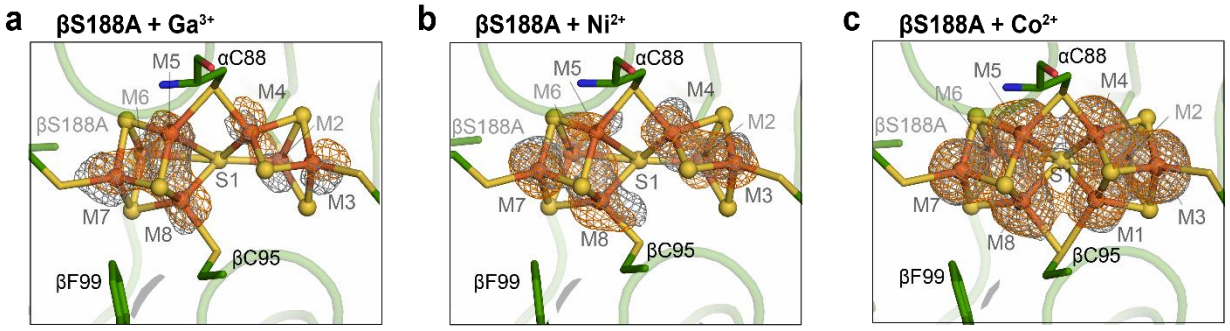


**Figure 3.6** Crystal structures of *Av* βSer188Ala P-clusters with heterometals. Anomalous electron density difference maps determined using X-ray diffraction data collected above and below the heterometal K-edge are shown in orange and gray mesh, respectively. Inorganic sulfides are depicted as yellow spheres and metals as orange spheres (modelled as Fe). (a) 2.2 Å structure of *Av* βSer188Ala P-cluster reconstituted with $Ga^{3+}$ contoured at 4.0 σ. (Above Ga K-edge: 10379 eV, Fe f" = 2.1, Ga f" = 3.9; below Ga K-edge: 10357 eV, Fe f" = 2.1, Ga f" = 0.5) (b) 2.0 Å structure of *Av* βSer188Ala P-cluster reconstituted with $Ni^{2+}$ contoured at 4.5 σ. (Above Ni K-edge: 8350 eV, Fe f" = 3.0, Ni f" = 3.9; below Ni K-edge: 8228 eV, Fe f" = 3.1, Ni f" = 0.5) (c) 2.0 Å structure of *Av* βS188A P-cluster reconstituted with $Co^{2+}$ contoured at 4.5 σ. (Above Co K-edge: 7730 eV, Fe f" = 3.4, Co f" = 3.9; below Co K-edge: 7690 eV, Fe f" = 3.4, Co f" = 0.5)

Anomalous density maps above and below the K-edge of the heterometal (Ga K-edge = 10367 eV, Ni K-edge = 8332 eV, Co K-edge = 7709 eV, Fe K-edge = 7112, note that the Fe K-edge is lower than any heterometal K-edge) did not clearly depict any single site as being solely occupied by one type of metal (Fe or the heterometal) (**Fig. 3.6**), nor were all the non-labile sites (all M sites excluding M1 and M5) fully occupied (**Table 3.3**). These maps indicate that the occupied labile sites (M1 and M5) likely contain a mixture of Fe and heterometal, and that it is possible that the heterometal may shuffle into the non-labile sites as well. By collecting data both above and below the K-edge of the heterometal, I hoped to quantify the occupancy of each metal type at each site. However, I was unable to determine the absolute or relative occupancies of Fe or the heterometal at these positions, even after integrating over the anomalous maps at each metal site using MAPMAN software, due to the confounding factors (total occupancy of the M site being less than unity and the site being partially occupied by two different metals). Total occupancy at each site was determined by refinement of metal at each site after refining B-factors, whereby B-factors were held constant at values comparable to the inorganic sulfides.

**Table 3.2**. X-ray data collection and refinement statistics. Numbers in parentheses correspond to the highest resolution shell.

| | **βS188A + $Ni^{2+}$** | **βS188A + $Ga^{3+}$** | **βS188A + $Co^{2+}$** |
|---|---|---|---|
| PDB ID | To be deposited | To be deposited | To be deposited |
| **Data collection** | | | |
| Beamline | ALS 5.0.2 | SSRL 9-2 | SSRL 9-2 |
| Wavelength (Å) | 1.48484 | 1.19453 | 1.60388 |
| Space group | P 1 21 1 | P 1 21 1 | P 1 21 1 |
| Cell dimensions (Å) | 77.259 129.009 107.76 | 76.607 127.968 107.269 | 77.127 130.039 107.76 |
| Cell angles (°) | 90 109.22 90 | 90 108.85 90 | 90 109.12 90 |
| Resolution (Å) | 71.47 - 1.99 | 54.13 - 2.20 | 50.91 - 2.00 |
| No. unique reflections | 136062 | 87122 | 127536 |
| $R_{merge}$ | 0.1972 (2.178) | 0.07269 (0.3819) | 0.05611 (0.2755) |
| $\langle I/\sigma(I) \rangle$ | 3.44 (0.53) | 6.33 (1.99) | 9.00 (2.91) |
| Completeness (%) | 99.00 (97.03) | 87.86 (65.85) | 94.26 (93.17) |
| **Refinement** | | | |
| $R_{work}/R_{free}$ | 0.2080 / 0.2510 | 0.2170 / 0.2505 | 0.1652 / 0.2005 |
| No. atoms[1] | 16876 | 16880 | 17534 |
| Protein | 15700 | 15780 | 15803 |
| Ligand/ion | 108 | 108 | 108 |
| Solvent | 1080 | 1003 | 1635 |
| B-factors ($Å^2$) | 35.70 | 28.89 | 28.36 |
| Protein | 35.68 | 28.91 | 28.07 |
| Ligand/ion | 32.92 | 28.95 | 22.47 |
| Solvent | 36.27 | 28.70 | 31.45 |
| R.m.s. deviations | | | |
| Bond lengths (Å) | 0.009 | 0.007 | 0.013 |
| Bond angles (°) | 1.36 | 1.07 | 2.05 |
| Clashscore | 8.64 | 9.89 | 9.05 |
| Ramachandran plot (%) | | | |
| Favored | 96.01 | 95.32 | 95.88 |
| Outliers | 0.56 | 0.75 | 0.85 |
| Rotamer outliers (%) | 1.50 | 1.31 | 1.25 |

[1]Riding-hydrogens not included

Furthermore, inductively coupled plasma mass spectrometry (ICP-MS) analysis of both the heterometallated and $^{57}Fe^{2+}$ reconstituted βSer188Ala MoFeP confirmed the presence of added metal ions, but not after reconstitution of reduced βSer188Ala, nor any wt reconstituted samples, oxidized or reduced. However, there were large, sample-dependent variations in the amount of incorporated heterometal, which I interpret as further evidence for the highly dynamic nature of the oxidized βSer188Ala P-cluster.

The composition of the heterometallated P-clusters differed based on the identity of the heterometal. Reconstitution with either $Ga^{3+}$ or $Ni^{2+}$ resulted in only seven of the eight P-cluster metal sites (**Fig 3.6a,b, Table 3.3**). In contrast, all eight of the sites were occupied when reconstituted with $Co^{2+}$ (**Fig 3.6c, Table 3.3**). $Co^{2+}$ may have a higher propensity to remetallate the P-cluster due to its similarity to $Fe^{2+}$ in terms of ionic radius and propensity to form tetrathiolate complexes with tetrahedral geometry.[145] The structures obtained suggested that site M5 had a higher affinity for heterometallation than site M1. This may be due to the backbone amidate of αCys88 providing additional stability to the M5 site.

**Table 3.3** Crystallographic occupancies of each metal site in the re-reduced and heterometallated βSer188Ala P-clusters.

| Metal site | DT-re-reduced βS188A | βS188A + $Ga^{3+}$ | βS188A + $Ni^{2+}$ | βS188A + $Co^{2+}$ |
|---|---|---|---|---|
| M1 | 1.00 | 0.00 | 0.00 | 0.61 |
| M2 | 1.00 | 0.84 | 0.75 | 0.84 |
| M3 | 1.00 | 0.97 | 0.87 | 0.89 |
| M4 | 1.00 | 0.93 | 0.74 | 0.93 |
| M5 | 1.00 | 0.68 | 0.74 | 0.87 |
| M6 | 1.00 | 1.00 | 0.98 | 0.89 |
| M7 | 1.00 | 0.99 | 1.00 | 0.93 |
| M8 | 1.00 | 1.00 | 0.89 | 0.92 |
| *Total* | *8.00* | *6.41* | *5.97* | *6.88* |

### 3.3.6 Electron paramagnetic resonance spectroscopy of mismetallated *Azotobacter vinelandii* βSer188Ala MoFe-protein

To further characterize the mismetallated βSer188Ala P-clusters, I collected EPR spectra after soaking with $^{57}Fe^{2+}$ or heterometals ($Ga^{3+}$, $Ni^{2+}$, and $Co^{2+}$) (**Fig. 3.7**). The samples were buffer exchanged after soaking to remove any free metal ions from solution. Spectra were collected on both wt and βSer188Ala *Av* MoFeP after IDS-oxidation and DT-reduction. All samples exhibited the previous established $S = 3/2$ signal ($g \approx 4.3$, 3.7, and 2.0) arising from resting state FeMoco. Because wt MoFeP does not contain a redox-labile P-cluster, I expected it to be unable to remetallate with heterometals under either DT-reduced or IDS-oxidized conditions, in agreement with the EPR spectra (**Fig. 3.7a,c**). Reconstitution of oxidized βSer188Ala with $^{57}Fe^{2+}$, $Co^{2+}$, and $Ni^{2+}$ resulted in near identical features in the $g \approx 5$ region (**Fig 3.7b**) which were not detected in the wt samples (**Fig 3.7a,c**), nor in reduced βSer188Ala (**Fig 3.7d**). Similar features have been observed in Cd[132] and Ni[133]-metallated *Pyrococcus furiosus* Fd, consistent with the association of heterometals with βSer188Ala MoFeP (likely at the P-cluster and not FeMoco). The possibility that heterometals associated with FeMoco rather than the

P-cluster was eliminated by the fact that this process did *not* give rise to similar $g \approx 5$ EPR signals in the spectra for wt protein (**Fig 3.7a**).

The $g \approx 2$ features in the heterometallated βSer188Ala strongly resembled the oxidized βSer188Ala MoFeP (**Fig. 3.7b**),[97] with slight differences in peak intensities and broadening. Of note, these features were weakest in the samples reconstituted with $^{57}Fe^{2+}$ and $Co^{2+}$, perhaps due to their ability to occupy all eight P-cluster metal sites. The high symmetry of the fully occupied P-cluster generated a more electronically isotropic spin system. In contrast, the $Ni^{2+}$ and $Ga^{3+}$ reconstituted βSer188Ala contained vacancies at M1 (**Fig. 3.6**), reducing the overall symmetry of the cluster that manifested in a more anisotropic EPR spectrum.

The similarity of the signals that arises in the IDS-oxidized βSer188Ala samples (regardless of the transition metal used for reconstitution) is unexpected. I tentatively attributed this signal to rearrangement of the many close, low energy electronic states of the P-cluster[146] or changes in the population of clusters in a previously established $S = 5/2$ excited state.[95] Reconstitution of βSer188Ala with $Ga^{3+}$ did not produce the $g \approx 5$ signals, which I rationalized by its frontier orbitals having much more p and less d character than the transition metals used, resulting in vastly different electronic properties from the other heterometallic P-clusters. The $g \approx 5$ signal thus may be an indicator of a degree of covalency in the interaction between the heterometal and the P-cluster.

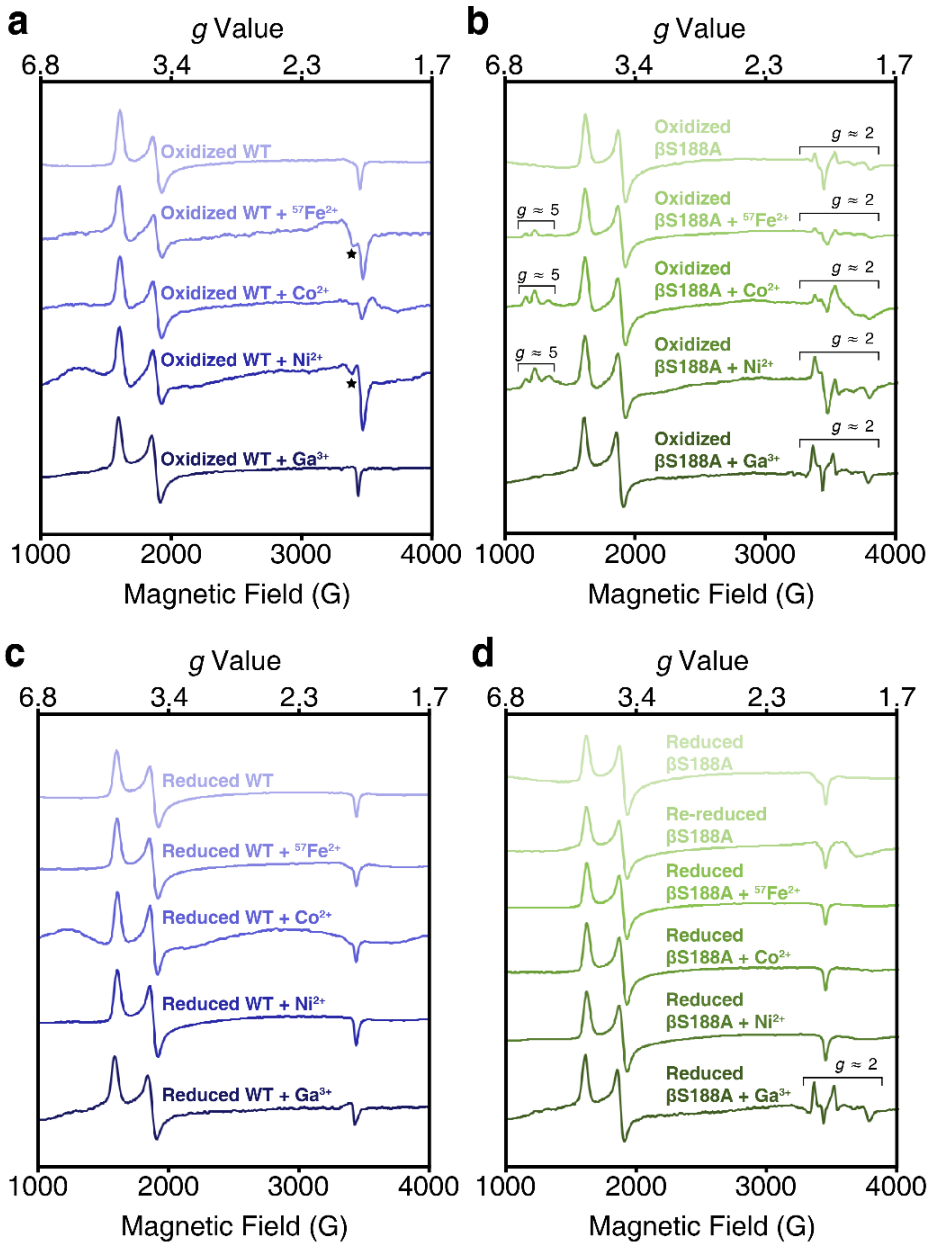


**Figure 3.7** X-band EPR spectra (4 K) of wt and βSer188Ala MoFeP after isotope labeling ($^{57}Fe^{2+}$) or soaking with heterometals ($Ga^{3+}$, $Ni^{2+}$, and $Co^{2+}$). (a) IDS-oxidized wt MoFeP soaked with various metals. From top to bottom: no metal, $^{57}Fe^{2+}$, $Co^{2+}$, $Ni^{2+}$, and $Ga^{3+}$. The feature marked with * is of unknown origin. (b) IDS-oxidized βSer188Ala MoFeP soaked with various metals. From top to bottom: no metal, $^{57}Fe^{2+}$, $Co^{2+}$, $Ni^{2+}$, and $Ga^{3+}$. Reconstitution with $^{57}Fe^{2+}$, $Co^{2+}$, and $Ni^{2+}$ resulted in new features in the $g \approx 5$ region. All βSer188Ala had features in the $g \approx 2$ region that closely resembled oxidized βSer188Ala, but the features varied in intensity. (c) DT-reduced wt MoFeP soaked with various metals. From top to bottom: no metal, $^{57}Fe^{2+}$, $Co^{2+}$, $Ni^{2+}$, and $Ga^{3+}$. (d) DT-reduced βSer188Ala MoFeP soaked with various metals. From top to bottom: no metal, $^{57}Fe^{2+}$, $Co^{2+}$, $Ni^{2+}$, and $Ga^{3+}$. DT-reduced βSer188Ala soaked with $Ga^{3+}$ contained features in the $g \approx 2$ region resembling IDS-oxidized βSer188Ala MoFeP.

### 3.3.7 *Azotobacter vinelandii* βSer188Ala ΔnifB P-cluster behaves differently than its holo counterpart

Next, I attempted to deconvolute the EPR spectra in the $g \approx 2$ region by creating an *Av* βSer188Ala MoFeP variant lacking FeMoco (apo βSer188Ala) by deleting a portion of *nifB*. The *nifB* gene product is part of the FeMoco maturation pathway, and deletion of this gene in wt *Av* resulted in MoFeP containing an intact P-cluster, but lacking FeMoco.[147] However, apo βSer188Ala MoFeP behaved differently from holo βSer188Ala MoFeP upon reconstitution, preventing me from deconvoluting the spectra (**Fig. 3.8**). In the $P^N$ state, the P-cluster was expected to be all ferrous and EPR silent. In the absence of FeMoco, this would have resulted in a featureless spectrum. In practice, there has been a very minor feature reported for apo wt MoFeP in the $g \approx 2$ region which has been attributed to P-cluster precursors. A feature existed in the DT-reduced spectrum of apo βSer188Ala (**Fig. 2.8a, top**) with similar *g* values, but much greater intensity than previously reported. Furthermore, IDS-oxidation of apo βSer188Ala followed by reconstitution with heterometals (**Fig. 3.8 b**) did not result in the same features seen in the EPR spectra of reconstituted holo βSer188Ala (**Fig. 3.7 b**).

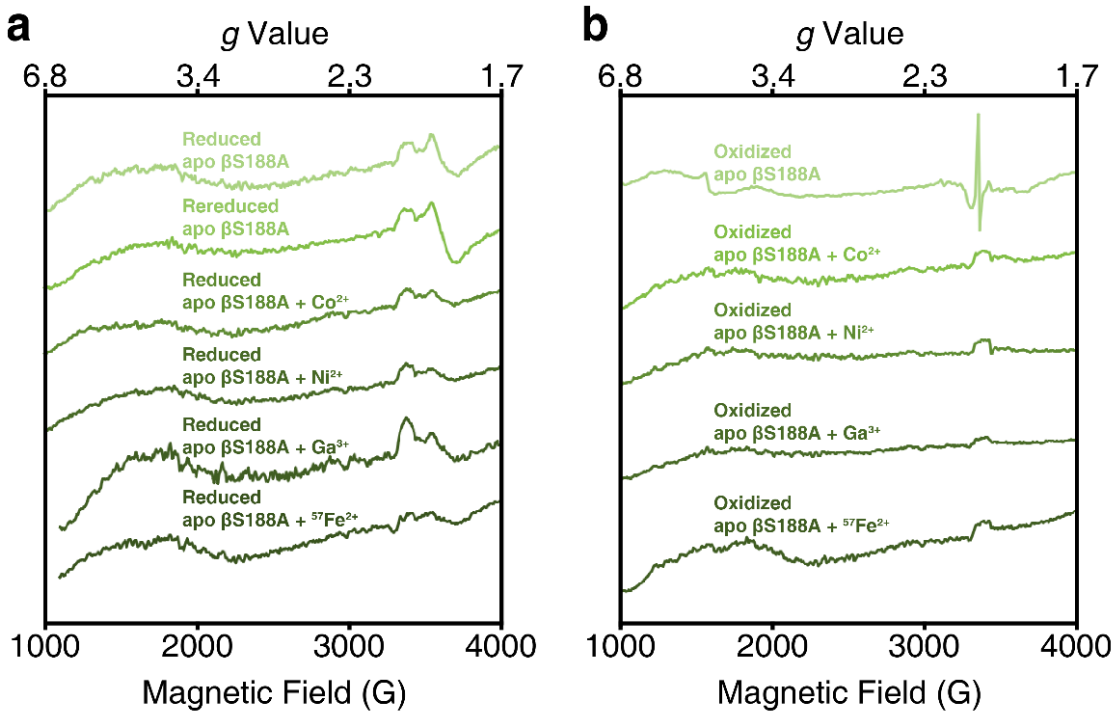


**Figure 3.8** X-band EPR spectra collected of DT-reduced apo βSer188Ala MoFeP and IDS-oxidized apo βSer188Ala MoFeP soaked with various metals ($^{57}Fe^{2+}$, $Co^{2+}$, $Ni^{2+}$, $Ga^{3+}$) at 4 K. (a) Reduced apo βSer188Ala MoFeP soaked with heterometals. (b) Oxidized apo βSer188Ala MoFeP soaked with heterometals.

Taken together, these results indicated that the electronics and structure of the apo βSer188Ala P-cluster are quite different from the holo βSer188Ala P-cluster, for reasons that I could only speculate: The P-cluster bridges the α- and β-subunits of MoFeP, and the α-subunit in apo wt MoFeP is much less compacted than its holo-counterpart.[147] Thus, differences in reconstitution behavior of the holo and apo βSer188Ala proteins could possibly be attributed to the increased flexibility of the α-subunit affecting the P-cluster, possibly even leading to splitting of the dicubane structure upon IDS-oxidation. Whatever the differences are, they resulted in apo βSer188Ala being a poor choice for deconvoluting the holo βSer188Ala reconstituted EPR spectra.

### 3.4 Conclusions

Taken together, my results provide evidence that the serine ligand, βSer188, protects the P-cluster in *Av* nitrogenase. Due to nitrogenase's sensitivity to oxygen and inhibition by various small molecules,

diazotrophs have evolved numerous mechanisms to protect the enzyme.[52, 148-150] Here, I have expanded upon known protective mechanisms by demonstrating that βSer188 prevented mismetallation of the P-cluster *in vitro*, protected *Av* cells against oxidative stress *in vivo*, and permitted optimal diazotrophic growth of *Av* cell cultures under Fe-limiting conditions. It is reasonable to predict that tyrosine (βTyr99) performs analogous functional roles in the nitrogenases lacking serine, such as in the previously characterized MoFeP from *Gd*.

Interestingly, there is only one known diazotroph that contains neither a serine nor a tyrosine P-cluster ligand, *Methanococcus aeolicus Nankai-3*.[59] This archaeon is a strict anaerobe that was isolated from marine sediments near the Nankai Trough,[151] an environment with high Fe availability,[152] which may explain why it is able to thrive without the protection of an oxygenic (serine or tyrosine) P-cluster ligand. Nonetheless, the conservation of an oxygenic P-cluster ligand clearly emphasizes its role in stabilizing the P-cluster during the required redox cycling that occurs during nitrogen fixation. The work in this Chapter provides critical insights into how the unique coordination chemistry of the P-cluster provides protection to the cluster, and furthermore, I established a new functional role of serine (and possibly tyrosine) residues in protecting Fe-S clusters from oxidative stress and mismetallation.

## 3.5 Materials and methods

### 3.5.1 Site-directed mutagenesis, expression, and purification of *Azotobacter vinelandii* MoFeP protein mutants

βSer188Ala was created, grown, and purified as described in Section 2.6.1. The wt Δ*nifB* strain (DJ1018) was kindly provided by the Dean lab (Va. Tech). βSer188Ala Δ*nifB* was generated, grown, and purified using the same methods as βSer188Ala, with the following exceptions: βSer188Ala cells were transformed with plasmid PDB218 (kindly provided by the Dean lab of Va. Tech), which contained a kanamycin resistance cassette flanked by the beginning and end of *nifB*, creating a strain of βSer188Ala that was nif- because it lacked FeMoco. Screening for transformants was carried out on $BM^+$ agar

containing 5 μg/mL kanamycin. The final transformant was verified with sequencing of the *nifB* region of the genome. All subsequent growths of βSer188Ala Δ*nifB* were carried out in $BM^+$ agar containing 5 μg/mL kanamycin, except for the fermenter growth which contained only 3 mM $NH_4Cl$. All proteins used were purified using the same methods described in Section 2.6.1.

### 3.5.2 Oxidative stress test of *Azotobacter vinelandii* cells

*Av* cell cultures (wt and βSer188Ala) were grown in both $BM^+$ and $BM^-$ media (200 rpm, 30 °C) in biological triplicate until $OD_{600}$ reached ~ 0.8. Cells were plated in a dilution series on solid $BM^+$ or $BM^-$ media (same as liquid growth conditions) to determine colony forming units (CFUs) present in the cultures prior to 5 mM $H_2O_2$ exposure. Cultures were centrifuged (5,000 rpm, 4 °C) to pellet cells, followed by resuspension in fresh media ($BM^+$ and $BM^-$ media corresponding to initial growth conditions) containing 5 mM Suprapur $H_2O_2$ (EMD Millipore) and shaken at 200 rpm and 30 °C for 30 min. Cells were pelleted again via centrifugation (5,000 rpm, 4 °C), then resuspended in fresh media ($BM^+$ and $BM^-$ media corresponding to initial growth conditions) without $H_2O_2$. Cells were plated in a dilution series to determine CFUs present after oxidative stress by $H_2O_2$. Colonies were manually counted 3-5 days after plating. The plates used for colony counting contained between 30-500 colonies.

### 3.5.3 Growth curves of *Azotobacter vinelandii* cells with different iron concentrations

All glassware used for growth curves was acid-washed with nitric acid. 25 mL $BM^-$ cultures (varying % Fe, 125 mL flasks) were shaken at 200 rpm, 30 °C. All media and growths were prepared in parallel. Cultures were inoculated with cells ($OD_{600(\text{starter culture})} > 0.10$) that had undergone extensive Fe-starvation under non-diazotrophic conditions: four passes on 0% Fe $BM^+$ agar followed by one liquid growth in 0% Fe $BM^+$. The % Fe in the media ranged from 1%, 10%, 25%, 50%, and 100. Time points of absorption at 600 nm (path length 0.6 cm) were takes approximately every four h over the course of 50 h by sterilely removing a 200 μL aliquot.

### 3.5.4 RT-qPCR of *nifK* gene

*Av* cells (wt and βSer188Ala) were grown in biological triplicate to $OD_{600}$ ~ 1.0 in 25 mL 100% and 1% Fe $BM^{-}$ media at 200 rpm and 30 °C. 3 mL of cells was removed and added to 6 mL of RNAprotect Bacteria Reagent (Qiagen), then immediately vortexed for 5 sec and incubated at room temperature for 5 min. Cells were centrifuged (5,000 g) for 10 min at room temperature resulting in a small, white pellet. The supernatant was removed, and pellets were frozen at −80 °C until RNA purification (total time frozen < 1 week).

Total RNA purification was carried out using the RNeasy Mini Kit (Qiagen) using the included protocols for enzymatic lysis of bacteria and purification of total RNA from bacterial lysate. Successful extraction of RNA was confirmed by visualizing rRNA bands with a 1% RNA agarose gel and was quantified with UV-Vis. Reverse transcription (RT) was carried out with Superscript III Reverse Transcriptase, random 9-mer primers, and 1 μg total RNA. cDNA products were confirmed via a smear on a 1% DNA agarose gel (**Fig. 3.9**). qPCR of the cDNA products was carried out using 10 ng of cDNA, Sybr dye, and Phusion HF polymerase in 20 μL total reaction volume in a Stratagene Mx3000 qPCR thermalcycler. qPCR reactions were carried out in technical triplicate of the biological replicates. Two housekeeping genes, *gyrA* and *rho*, were amplified as internal controls. However, *gyrA* provided inconsistent results. Data was thus normalized to the *rho* reference gene. The following primers were used with an annealing temperature of 54 °C, resulting in amplicons with lengths of ~100 base pairs:

Forward *nifK* primer: CGAGACCTACCTGGGCAAC

Reverse *nifK* primer: CACTTCTTCCGGATCGGAGA

Forward *rho* primer: GGAAATGGCCGAACAGATGG

Reverse *rho* primer: GATTTCCTCGCCGCTTTTCG

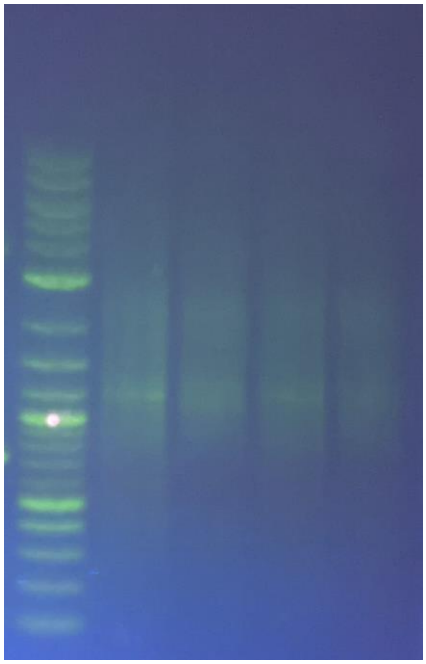

**Figure 3.9** 1% DNA agarose gel showing representative cDNA samples. Results were a smear as expected. Leftmost lane is a ladder, following four lanes are representative cDNA samples.

### 3.5.5 Whole cell $C_2H_2$ reduction activity assays

Whole cell activity assays were conducted with the same *Av* cell cultures that were used for total RNA extraction and RT-qPCR analysis. Immediately after removing a portion of cells for RNA extraction, 1.0 mL of whole cells was removed and placed in a 10 mL vial under air and sealed with a septum. 1.0 mL of $C_2H_2$ (room temperature, atmospheric pressure) was transferred into the headspace of the vial via gastight Hamilton syringe. Vials were shaken in 30 °C water bath for 95 min. $C_2H_4$ production was measured as described in Section 2.6.4. *In vivo* relative specific activity of MoFeP was calculated using the relative quantities of *nifK* mRNA transcripts determined from RT-qPCR.

### 3.5.6 Preparation of reconstituted *Azotobacter vinelandii* βSer188Ala MoFe-protein P-cluster with different metals

All handling of MoFeP in this section was carried out in a Coy anaerobic chamber under 90-95% Ar / 5-10% $H_2$. DT was removed from MoFeP solution by desalting over a 10DG gravity-flow column with 500 mM TRIS, pH 8.0, 500 mM NaCl. MoFeP was concentrated to 50 μM using 30 kDa Microcon

centrifugal filters. Concentrated MoFeP was oxidized with 2.5 mM IDS for one hour, followed by desalting over another 10DG to remove IDS, followed by Microcon concentration to 50 μM. Proteins were aliquoted for addition of metal. 1 mM of metal (M = $NiSO_4$, $CoCl_2$, $GaCl_3$, or $^{57}FeSO_4$) was added to the protein solution and allowed to rest for one hour. Excess metal was removed by buffer exchanging the protein into fresh buffer (50 mM TRIS, pH 8.0, 500 mM NaCl) with 30 kDa Microcon filters. Proteins were concentrated to 50 μM as confirmed by Bradford protein assay.

### 3.5.7 Mössbauer spectroscopy of *Azotobacter vinelandii* βSer188Ala MoFe-protein

The initial Mössbauer sample was prepared as described in the above section, 3.5.5, followed by concentration to 1 mM (400 μL final volume), as confirmed with Fe-chelation assay (assuming 30 Fe/MoFeP) as described in Section 2.6.1. After collecting the initial spectrum, the sample was diluted to 125 μM, remetallated with natural abundance $Fe^{2+}$ according to the same method. The sample was then concentrated back down to 1 mM (400 μL final volume). Both Mössbauer samples were prepared and flash frozen in liquid nitrogen in a Coy anaerobic chamber.

Mössbauer spectra were recorded on a SEE Co. spectrometer in constant acceleration mode and transmission geometry at 80 K. A Janis SVT-300T dewar was used with a 54 mT magnetic field applied parallel to the propagation of the γ-beam. Isomer shifts were determined relative to the centroid of a metallic foil of a α-Fe at room temperature.

### 3.5.8 Crystallization of mismetallated βSer188Ala MoFe-protein

Mismetallated βSer188Ala was prepared as described in Section 3.5.5. The heterometallated protein was crystallized as described in Section 2.6.2, in the presence of DT. Ni- and Co-substituted βS188A crystals were grown from the same samples used in the EPR experiments. The Ga-substituted crystal used a sample prepared separately from the EPR samples. All proteins were crystallized in the presence of 10 mM DT in the crystallization solution.

### 3.5.9 Electron paramagnetic resonance spectroscopy of MoFe-protein

Samples were prepared as described in Section 3.5.5, followed by concentration to 50 μM in 30 kDa Microcon filters. All data were collected on a Bruker EMX spectrometer. A helium cryostat was used to maintain temperatures in the range of 5−10 K. The modulation frequency was 100.0 kHz, and the modulation amplitude was 9.8 G when recording spectra. The microwave frequency used was ~9.62 GHz. All spectra in figures were background subtracted using the EasySpin software package.[117]

### 3.6 Acknowledgements

This work was supported by the National Institutes of Health (Grant GM099813 to F.A.T) and by the Molecular Biophysics Training Grant (NIH Grant T32 GM008326). Crystallographic data were collected at either Stanford Radiation Lightsource (SSRL) or the Lawrence Berkeley Natural Laboratory Advanced Light Source (ALS) on behalf of the Department of Energy.

I would like to thank Prof. C. Owens (Chapman U), Dr. J. Zhu, Dr. C. J. Yu, Dr. N. Avakyan, A. Kakkis, and R. Yu for critical discussions, Dr. V. Cash and Prof. D. Dean. (Va. Tech) for generously providing *Av* strains and plasmids (DJ200, DJ1018, and PDB 218), and E. Lavorando for RT-qPCR assistance.

Chapter 3 is reproduced, in part, with permission from H. Rutledge, M. J. Field, J. Rittle, M. T. Green, and F. A. Tezcan. The Role of Serine Coordination in the Structural and Functional Protection of the Nitrogenase P-cluster. The dissertation author is the primary author on all reprinted materials.

## Chapter 4: CryoEM structures of the nitrogenase complex during catalytic turnover

### 4.1 Abstract

The enzyme nitrogenase couples adenosine triphosphate (ATP) hydrolysis to the multi-electron reduction of atmospheric dinitrogen into ammonia. Despite extensive research, the mechanistic details of ATP-dependent energy transduction and dinitrogen reduction by nitrogenase are not well understood, requiring new strategies to monitor its structural dynamics during catalytic action. Here I report the cryogenic electron microscopic interrogation of the nitrogenase complex under enzymatic turnover conditions, which have enabled the structural characterization of the nitrogenase reaction intermediates at high resolution for the first time. These structures show that asymmetry governs all aspects of nitrogenase mechanism including ATP hydrolysis, protein-protein interactions, and catalysis. Furthermore, they reveal several previously unobserved, mechanistically relevant conformational changes near the catalytic iron-molybdenum cofactor that are correlated with the nucleotide-hydrolysis state of the enzyme.

### 4.2 Introduction

#### 4.2.1 Structures of nitrogenase under non-resting state conditions

Elucidating the mechanism of biological $N_2$ reduction requires understanding how nitrogenase orchestrates the many electron- and proton-transfers to the active site during catalysis. As described in Section 1.3, nitrogenase is an extremely dynamic system with many states populated on the reaction coordinate diagram including DGs 1-3, $E_{0\text{-}8}$, ADP pre- and post- $P_i$ release, etc. While the complex has been crystallized under varying conditions,[54-56, 153, 154] the static nature of crystallography precludes the determination of any structures of the nitrogenase assembly during turnover, and thus only provides snapshots that may or may not be catalytically relevant. It is necessary to find a method to structurally characterize nitrogenase during $N_2$ reduction in order to provide insights into many key components of the mechanism including (1) the role of ATP hydrolysis, (2) conformational changes involved in gating of ET, (3) the role, if any, of cooperativity between the two halves of the nitrogenase complex, and (4)

conformational dynamics of the active site during catalysis. Crystal structures have been able to provide many insights, albeit static (and highly debated in the literature), that contribute to the understanding of nitrogenase. In addition to the structures of the complexes described in Section 1.3.2 (**Fig 1.5**), many recent structures investigating the dynamics of the active site have been published.[63-68, 104]

The first structural evidence that the active site, FeMoco, may be dynamic during catalysis came from the high resolution MoFeP crystal structure of CO-bound FeMoco.[63] CO is a noncompetitive inhibitor of $N_2$ reduction.[155, 156] In order to prepare inhibitor-bound MoFeP for crystallization, Spatzal et al. had to first obtain MoFeP from a dynamic assay mixture, then rapidly crystallize the protein, all in the presence of CO. The structure revealed the diatomic CO ligand bound to FeMoco, which can be described by CO bound to Fe2 and Fe6 in a $\mu_2$-bridinging mode, displacing the belt sulfide S2B (**Fig 4.1**). The displacement of S2B was confirmed by the anomalous density map (7100 eV). Furthermore, the process was reversible, as evidenced by reactivation.[63]

Recently, a CO-bound structure of FeVco (the active site in the vanadium (V)-nitrogenase) was determined.[157] Unlike FeMoco, FeVco contains a trigonal planar ligand (hypothesized to be carbonate, $CO_3^2$) in the as-isolated, resting state in place of belt sulfide S3A.[158] Under low pressures of CO, similar to the conditions used in obtaining crystals of CO-bound FeMoco, CO bound to the active site in the same binding mode as FeMoco (**Fig 4.2**), replacing belt sulfide S2B. Under higher pressures of CO, a second molecule of CO bound to Fe6 of VFeco in a linear fashion.[157]

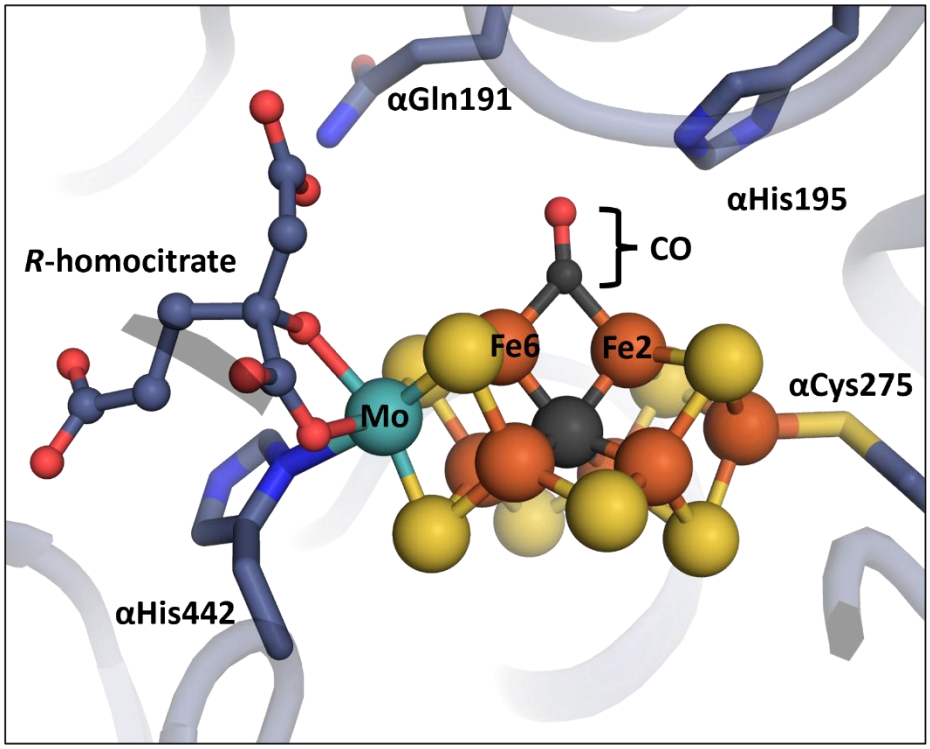


**Figure 4.1** Carbon monoxide (CO)-bound FeMoco (PDB ID: 4TKV). CO displaces the belt sulfide S2B and is bound as a $\mu_2$-bridging ligand to Fe2 and Fe6.

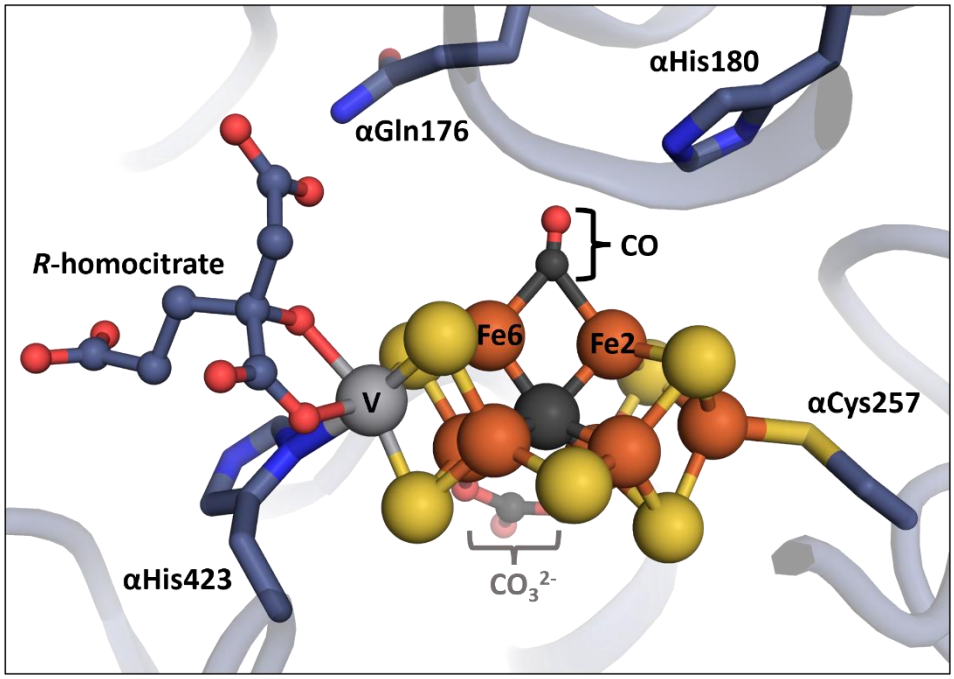


**Figure 4.2** Carbon monoxide (CO)-bound FeVco (PDB ID: 7ADR). CO displaces the belt sulfide S2B and is bound as a $\mu_2$-bridging ligand to Fe2 and Fe6, similar to the structure of CO-bound FeMoco. FeVco contains a bridging ligand (likely a carbonate) in place of belt sulfide S3A.[158]

Structural investigations of nitrogenase seeking to probe events post-catalysis (as opposed to structurally characterizing as-isolated, resting state nitrogenase proteins) were carried out on MoFeP following reduction of selenocyanate ($SeCN^-$),[104] an alternative substrate and inhibitor of $N_2$ reduction,[159] under an acetylene ($C_2H_2$) atmosphere. Anomalous density maps (12,662 eV) revealed that Se atoms were incorporated into FeMoco, replacing the belt sulfides. All three belt sulfide positions (S3A, S2B, S5A) were at least partially occupied by Se, with position S2B containing the highest occupancy of Se.[104] Taken together with the CO-bound FeMoco structure, it is highly likely that FeMoco is dynamic during $N_2$ reduction, with a possible $\mu_2$-bridging $N_2$ binding mode between Fe2 and Fe6 that displaces belt sulfide S2B. However, it is possible that $N_2$ binds in a different mode or location on FeMoco than the alternative substrates and inhibitors.

Recently, structural studies have aimed to capture a nitrogen-species bound to the nitrogenase active site. To capture such an intermediate species, the catalytic nitrogenase protein (MoFeP or VFeP) was isolated from cells using either a reduced amount of reductant (DT) in the case of VFeP,[64] or in the absence of reductant for MoFeP, capturing a potential "turnover" state.[67] The "turnover" state of VFeP contains a protonated N-species bound to FeVco in a $\mu_2$-bridinging mode (**Fig 4.3**), displacing S2B, similar to the CO-bound structures (**Fig 4.1, 4.2**).[67] Much of the protein environment surrounding the active sites in MoFeP and VFeP is conserved, including coordinating residues (αCys275 and αHis442 in *Av* MoFeP; αCys257 and αHis423 in *Av* VFeP) and residues thought to play a key role in catalysis (αGln191 and αHis195 in *Av* MoFeP; αGln176 and αHis180 in *Av* VFeP). These key residues were superimposable in all of the CO-bound and resting-state structures.[63, 157] In contrast, VFeco bound to the protonated N-species revealed conformational changes such that the side chain of αGln176 flipped toward FeVco, placing it within H-bonding distance of the N-species and breaking its H-bonds to homocitrate.[67] Additionally, there was anomalous density (7000 eV) for sulfur in the location of the resting state position of αGln176, providing a potential site for the displaced S2B.[67] However, the relevance of this structure to

the mechanism of biological $N_2$ reduction has been called into question after Cao et al. found that a bridging hydroxy group fit the density better than a protonated N-species based on quantum mechanics/molecular mechanics (QM/MM) calculations.[68] Similarly, the structure of $N_2$-species-bound FeMoco is highly contested. Kang et al. determined the structure and reported asymmetric FeMocos, in which one FeMoco was bound to a side-on $N_2$-species displacing S2B and bridging Fe2 and Fe6, and the other FeMoco was bound to two $N_2$-species, displacing S3A and S5A (**Fig 4.4**). [64] However, the diffraction data did not allow for confident assignment, such that it was possible that both the FeMocos were the as-isolated, resting state, without any substrate bound.[65, 66]

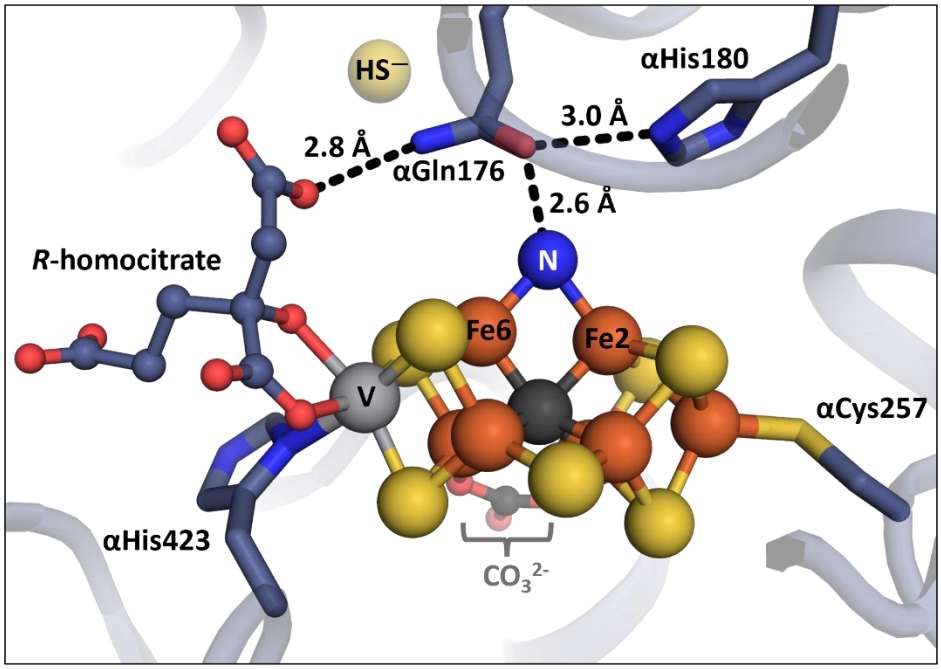


**Figure 4.3** FeVco bound to a reaction intermediate, proposed to be a protonated N-species. (PDB ID: 6FEA). Belt sulfide S2B was replaced by the N-species. QM/MM analysis disputed the identity of this species, proposing that it was $OH^-$.[68] FeVco contained a bridging ligand (likely a carbonate) in place of belt sulfide S3A.[158]

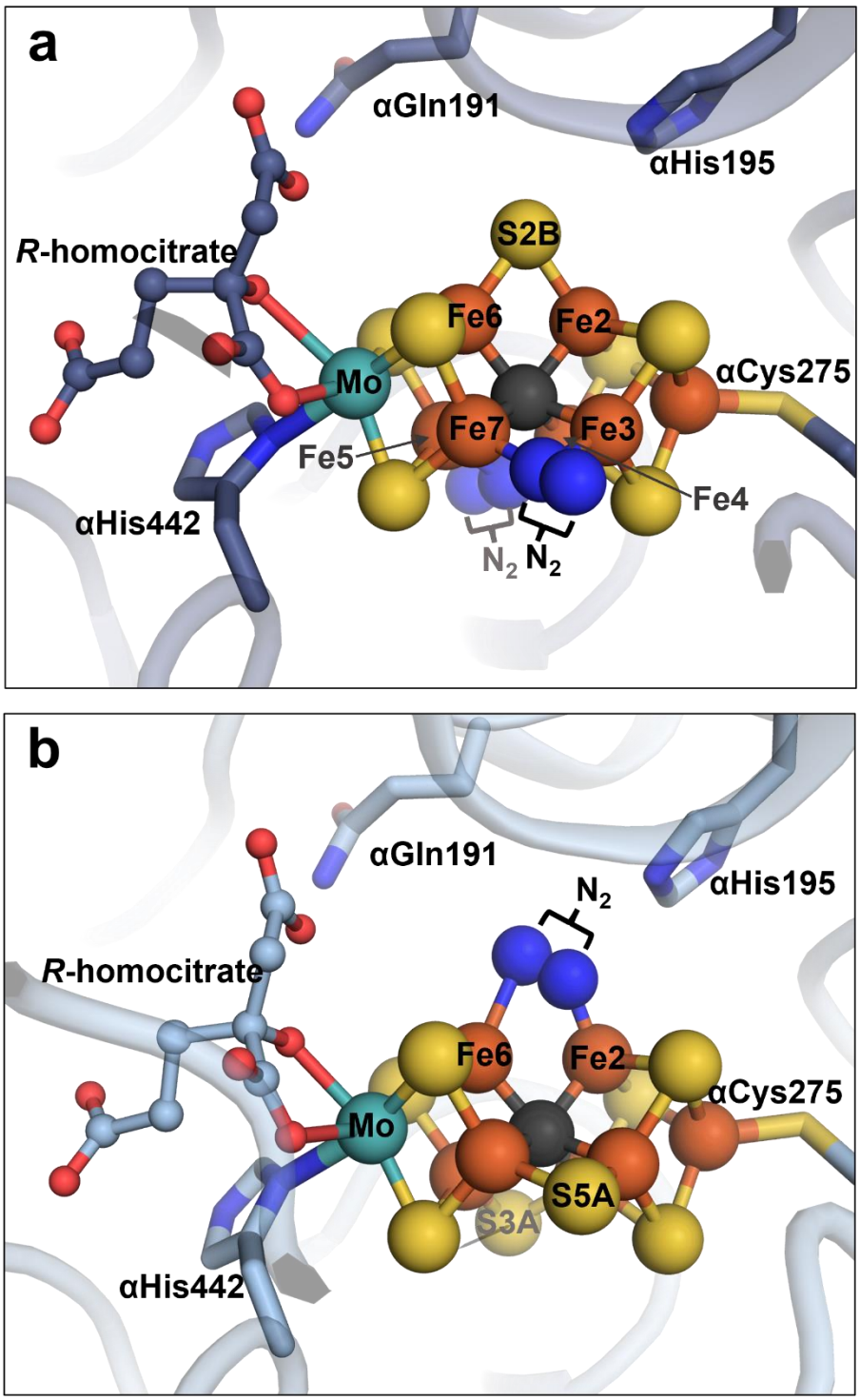


**Figure 4.4** $N_2$-species bound FeMoco (PDB ID: 6UG0). This accuracy of this structure has been questioned in the literature due to the low-quality diffraction data.[65, 66] (a) FeMoco in chain A was modelled with two $N_2$-species bound in a linear fashion, displacing belt sulfides S3A and S5A. (b) FeMoco in chain B was modelled with $N_2$-species bound in a side-on manner displacing belt sulfide $S_2B$.

### 4.2.2 Nitrogenase has not previously been structurally characterized during catalytic turnover

As demonstrated in the previous Section, structurally characterizing nitrogenase in its non-resting state poses considerable challenges. Furthermore, the intrinsic limitations of crystallography (providing only static snapshots, long timescale for crystallization, etc.) make it impossible to crystallize the entire complex during catalysis. Reduced FeP and continuous ATP hydrolysis are required for capturing nitrogenase in a substrate- or inhibitor-bound state [8, 82] because nitrogenase is an inherent hydrogenase and will thus revert back to resting state upon termination of ATP hydrolysis via hydrogen evolution. The complicated ensemble nature of nitrogenase during turnover makes it difficult to isolate single species along the reaction pathway for characterization, and the timescale required for protein crystallization (hours to weeks) results in characterization of stable states formed only after catalysis has concluded. These shortcomings prevent key catalytic steps from being observed, and furthermore, the published non-resting state structures have been difficult to model with confidence, calling into question both their accuracy and relevance to the catalytic mechanism.

To overcome these obstacles and characterize the ATP-dependent FeP-MoFeP interactions and structural dynamics within each protein, the nitrogenase complex in its entirety must be structurally characterized *during* catalytic turnover. The only method currently available to carry out such characterization is single-particle cryogenic electron microscopy (cryoEM). Although cryoEM was suitable for this task, there were still significant challenges due to the dynamics, heterogeneity, and low symmetry of nitrogenase during catalysis. Here, I present the first structures of the nitrogenase complex *during catalysis*, along with structures of free MoFeP and $BeF_x$-inhibited nitrogenase, which were obtained using novel cryoEM protocols and techniques for sample preparation and data analysis. These high-resolution structures provide critical insights into the mechanism of biological $N_2$ fixation.

## 4.3 Results and discussion

### 4.3.1 CryoEM of the nitrogenase complex reveals an asymmetric 1:1 FeP:MoFeP complex

We prepared cryoEM samples of *Av* nitrogenase under high-electron flux turnover conditions to maximize $NH_3$ production. The optimized samples contained a 10-fold molar excess of FeP over MoFeP and low ionic strength (≤25 mM NaCl) to favor the formation of electrostatically driven FeP-MoFeP complexes. We included moderately high MgATP and reductant (DT) concentrations (both 5 mM) to ensure that they were not depleted during turnover while minimizing background electron scattering. Samples were prepared anaerobically under a $N_2$ atmosphere and immediately flash frozen in liquid $N_2$ following initiation of turnover. The 30-s sample preparation period was sufficiently long to ensure that steady-state catalytic conditions were reached but short enough such that there was still excess reductant in solution and no significant MgADP build-up. We collected a large cryoEM dataset (>15K movies) which yielded >4.5 million usable particles (**Fig. 4.5-4.7, Table 4.1**). Through exhaustive 2- and 3-D classification and refinement, we isolated free MoFeP (~60%) and FeP particles (~5%) as well as FeP-MoFeP nitrogenase assemblies (~35%) from this heterogeneous mixture (**Fig. 4.7**). We determined the structures of two conformationally distinct 1:1 FeP:MoFeP complexes under turnover, designated "$^{t/o}$Complex-1" and "$^{t/o}$Complex-2", at ~2.4 Å resolution (**Fig. 4.5**). As a reference, we also obtained a ~1.8-Å resolution cryoEM structure of resting-state MoFeP, termed "$^{rs}$MoFeP", using the same turnover conditions but in the absence of FeP (**Fig. 4.5, 4.8, Table 4.2**).

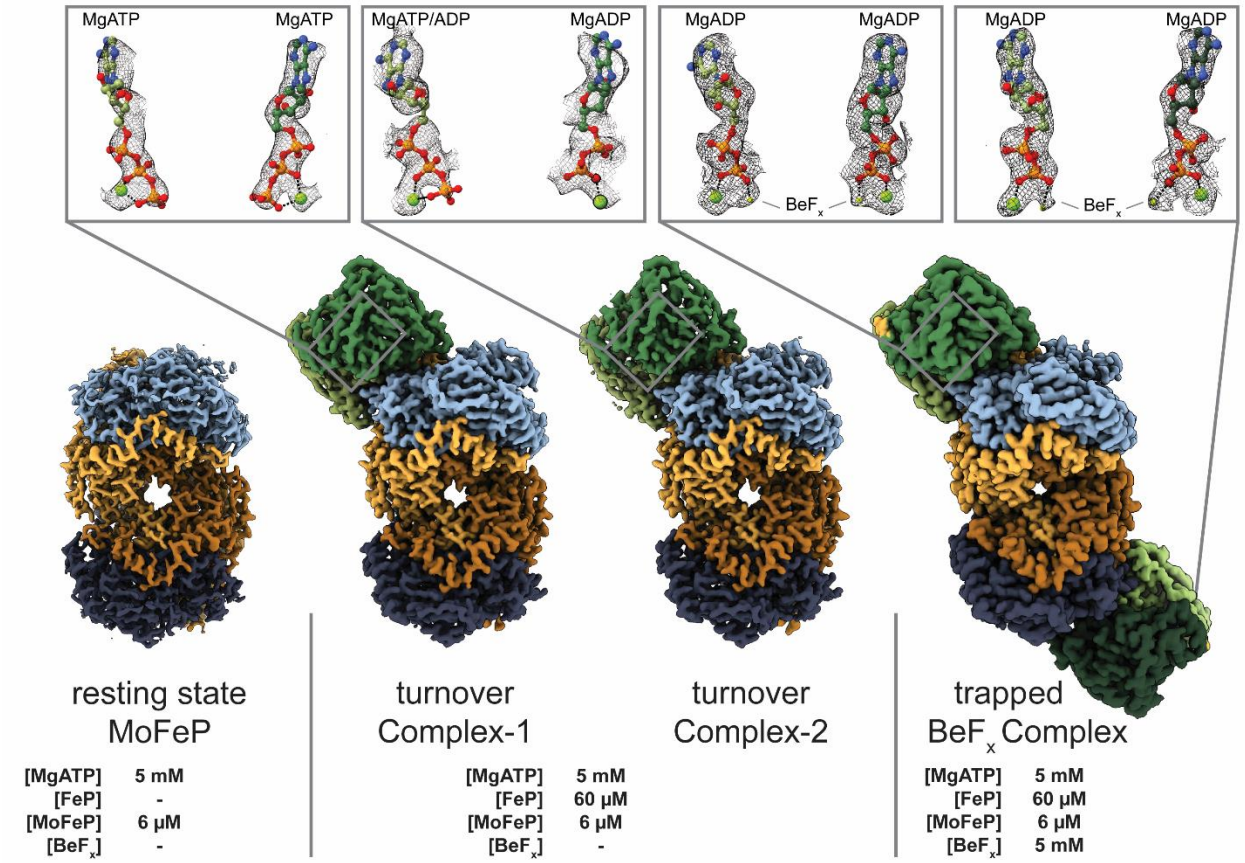


**Figure 4.5** CryoEM maps of *Av* nitrogenase. CryoEM map of resting state MoFeP obtained in the absence of FeP, the 1:1 FeP:MoFeP complexes determined from a single sample of a nitrogenase during catalytic $N_2$ reduction, and the 2:1 FeP:MoFeP $BeF_x$ nitrogenase complex trapped during $N_2$ reduction. Maps of the nucleotides are shown in boxes. α-, β-, and γ- subunits are shown in shades of blue, orange, and green, respectively.

**Figure 4.6** Data processing flowchart for the single-particle cryoEM analysis of nitrogenase complexes formed under turnover. (a) Representative motion-corrected micrograph of vitrified nitrogenase collected at ~1.5 µm underfocus. 19,711,170 particles were identified from dose-weighted micrographs by crYOLO trained using resting state MoFeP. These particles were extracted and downsampled 8 x 8 in RELION, randomly split into ~1M particle sets, and subjected to iterative rounds of reference-free 2-D classification in RELION. Representative 2-D class averages are shown for each iterative step. The best nitrogenase classes were set aside (green arrows) while the remaining classes were randomly split into 10 subsets and subjected to another round of 2-D classification (orange arrows). The best classes were then combined and 3-D auto-refined to 6.82 Å. Particles were then imported into cryoSPARC and subjected to a 5-class heterogenous refinement. The best class for the 1:1 nitrogenase complex was selected (green box) and two iterative rounds of two class heterogenous refinements were performed. 1:1 FeP:MoFeP complex particles were isolated and re-extracted in RELION and imported into cryoSPARC for 3-D variability analysis. The cluster with the strongest FeP density in the 1:1 FeP:MoFeP complex was selected (green box) and non-uniform refined before a final round of 3-D variability analysis. The two clusters with density for both proteins were re-centered and re-extracted in RELION without downsampling, 3-D auto-refined, and subjected to Bayesian particle polishing. After polishing, the particles were imported into cryoSPARC and locally refined. The half maps were combined, resulting in the $^{t/o}$Complex-1 and $^{t/o}$Complex-2 resolving to 2.28 Å and 2.29 Å, respectively. Histogram and directional 3-D FSC plots generated from the independent composite half maps contributing to the ~2.28 Å and 2.29 Å resolution (b) $^{t/o}$Complex-1 and (c) $^{t/o}$Complex-2 structures, respectively. (d) EM density of $^{t/o}$Complex-1 colored by local resolution. The left image corresponds to the surface of $^{t/o}$Complex-1, and the right image is a cross-section of the complex. (e) EM density of $^{t/o}$Complex-2 colored by local resolution. The left image corresponds to the surface of $^{t/o}$Complex-2, and the right image is a cross-section of the complex. (f) Histogram and directional 3-D FSC plots generated from the independent composite half maps contributing to the ~2.59 Å resolution MoFeP (*C2* symmetry) map. (g) EM density of MoFeP ($C_2$ symmetry) colored by local resolution. The left image is surface view of MoFeP, and the right image is a cross-section of the protein.

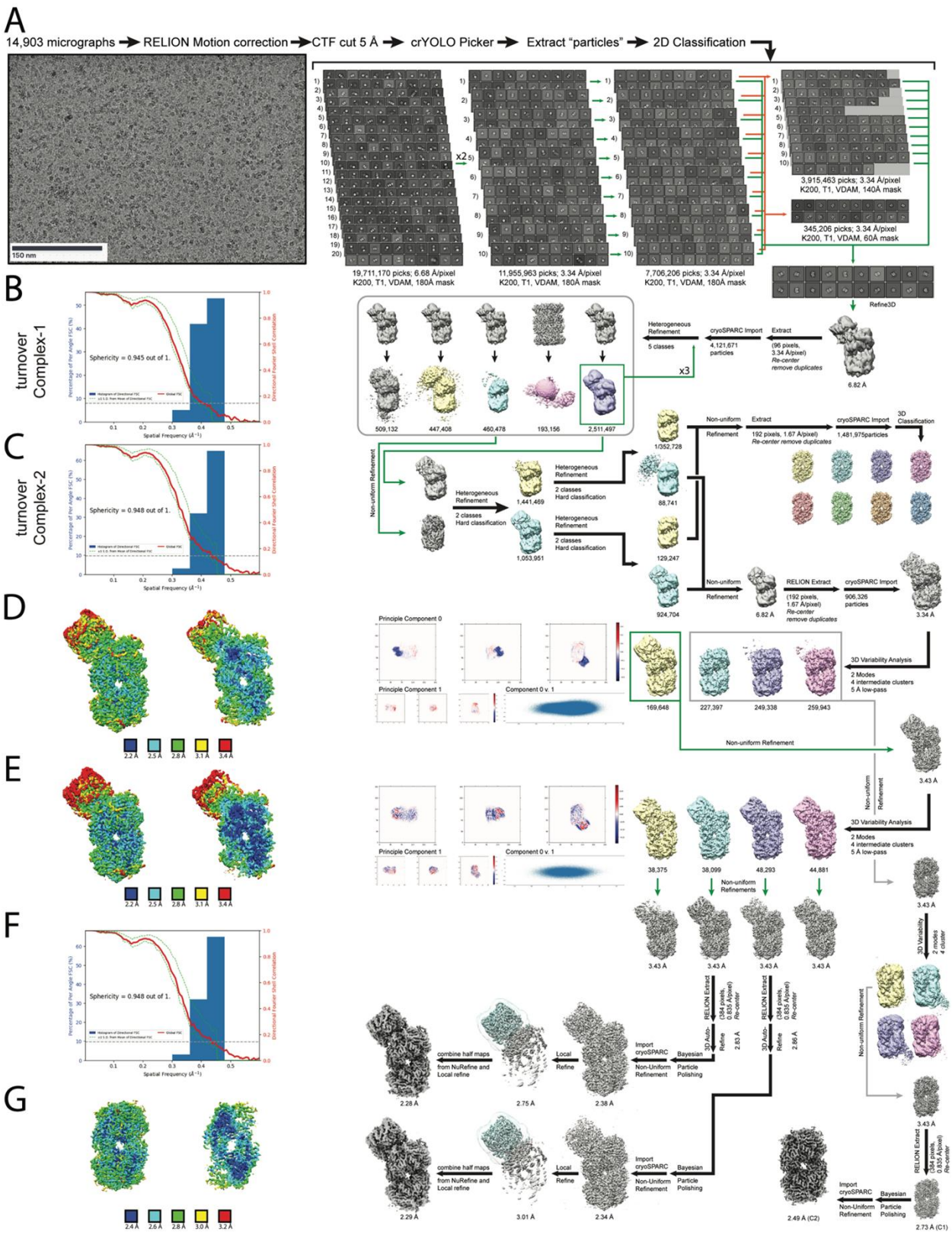
A
14,903 micrographs
RELION Motion correction
CTF cut 5 Å
crYOLO Picker
Extract "particles"
2D Classification
150 nm
19,711,170 picks; 6.68 Å/pixel
K200, T1, VDAM, 180Å mask
11,955,963 picks; 3.34 Å/pixel
K200, T1, VDAM, 180Å mask
7,706,206 picks; 3.34 Å/pixel
K200, T1, VDAM, 180Å mask
3,915,463 picks; 3.34 Å/pixel
K200, T1, VDAM, 140Å mask
345,206 picks; 3.34 Å/pixel
K200, T1, VDAM, 60Å mask
Refine3D
B
turnover
Complex-1
Sphericity = 0.945 out of 1.
C
turnover
Complex-2
Sphericity = 0.948 out of 1.
D
E
F
Sphericity = 0.948 out of 1.
G
Heterogeneous Refinement
5 classes
cryoSPARC Import
4,121,671 particles
Extract
(96 pixels, 3.34 A/pixel)
Re-center
remove duplicates
x3
6.82 Å
509,132
447,408
460,478
193,156
2,511,497
Non-uniform Refinement
Heterogeneous Refinement
2 classes
Hard classification
1,441,469
1,053,951
1/352,728
88,741
129,247
924,704
Non-uniform Refinement
Extract
192 pixels, 1.67 A/pixel)
Re-center remove duplicates
cryoSPARC Import
1,481,975particles
3D Classification
RELION Extract
(192 pixels, 1.67 A/pixel)
Re-center
remove duplicates
cryoSPARC Import
906,326 particles
6.82 Å
3.34 Å
Principle Component 0
Principle Component 1
Component 0 v. 1
169,648
227,397
249,338
259,943
3D Variability Analysis
2 Modes
4 intermediate clusters
5 Å low-pass
Non-uniform Refinement
3.43 Å
38,375
38,099
48,293
44,881
Non-uniform Refinements
3D Variability
2 modes
4 cluster
RELION Extract
(384 pixels, 0.834 A/pixel)
Re-center
3D Auto-Refine
2.83 Å
2.86 Å
Import cryoSPARC Non-Uniform Refinement
Bayesian Particle Polishing
Local Refine
combine half maps from NuRefine and Local refine
2.28 Å
2.75 Å
2.38 Å
2.29 Å
3.01 Å
2.34 Å
2.49 Å (C2)
2.73 Å (C1)

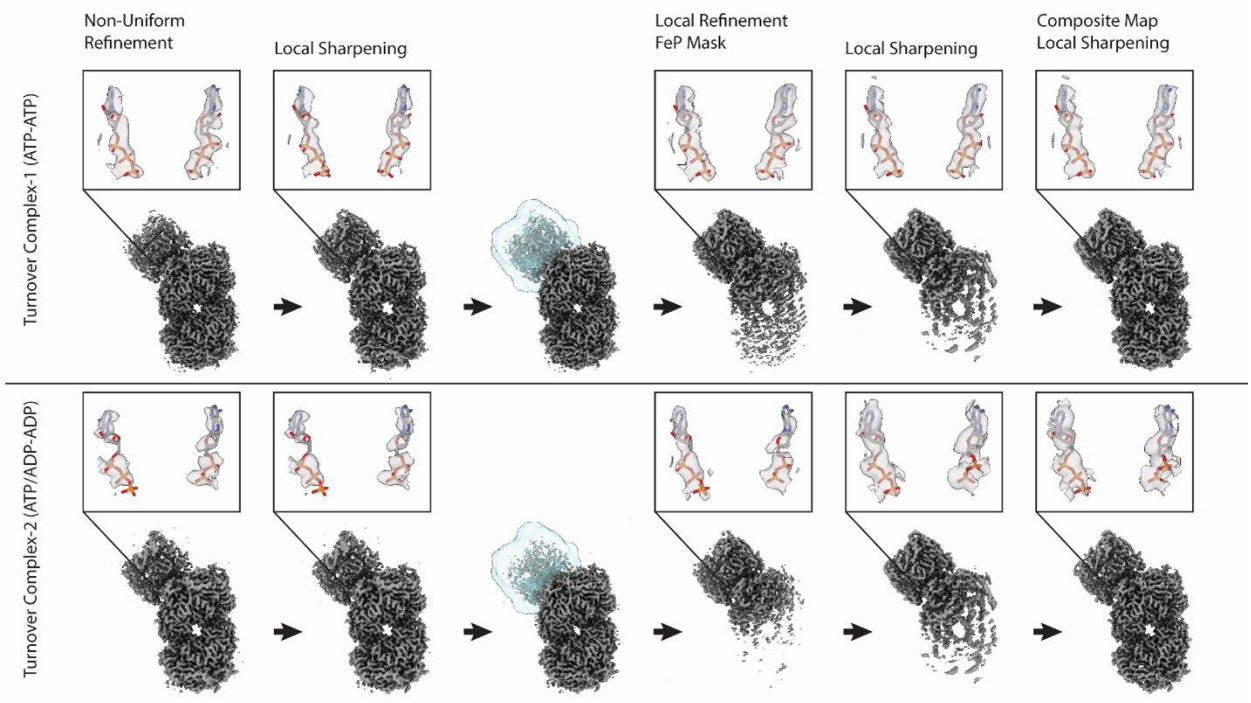


**Figure 4.7** Improvements in map quality for the 1:1 FeP:MoFeP complexes formed under turnover. (left to right) Non-uniform refinements of the $^{t/o}$Complex-1 (top) and $^{t/o}$Complex-2 (bottom) yielded ~2.4 Å resolution maps with lower resolution regions for the FeP subunits. Local noise estimates and sharpening using deepEMhancer were used to improve the quality of the FeP density. Local refinement of each particle set using a soft FeP protein mask and subsequent local sharpening improved the EM density quality for the FeP subunits with lower quality density for the MoFeP subunits. Maximal voxel values for the non-uniform and local refinements were taken to generate composite half maps that were then used for resolution estimation, local noise estimates and sharpening.

**Figure 4.8** Data processing flowchart for the single-particle cryo-EM analysis of free MoFeP ($^{rs}$MoFeP) (a) Representative motion-corrected micrographs of vitrified MoFeP collected at ~1.5 µm underfocus. ~1.5M particles were identified using RELION's automated template based Autopicking, downsampled 8 x 8, and subjected to iterative rounds of reference free 2-D classification. Classes with strong secondary structural detail were isolated (green boxes/arrows), while poorly aligning classes were subjected to a final round of 2-D classification (orange boxes/arrows). All good classes were combined for an initial round of 3-D auto-refinement that refined to 6.73 Å resolution. Particles were then split into their respective sessions and processed in parallel. The refined coordinates were used to re-center and re-extract particles without binning and subjected to 3-D auto-refinement, CTF refinement, and 3-D auto-refinement before Bayesian particle polishing in RELION. No alignment 3-D classification was performed, and the best classes were selected (boxed). After iterative rounds of refinement, the sessions were combined, imported into cryoSPARC for non-uniform refinement in $C_1$ or $C_2$ symmetries using defocus and aberration refinement to yield 1.91 Å ($C_1$) and 1.81 Å ($C_2$) resolution structures. (b) Representative 2-D CTF fit for the data. (c) Histogram and directional 3-D FSC [160]plots generated from the independent half maps contributing to the ~1.81 Å $C_2$ structure. (d) EM density of the $C_2$-refined structure colored by local resolution. The top image corresponds to the surface of MoFeP and the bottom image corresponds to a cross-section of the protein, highlighting core regions.

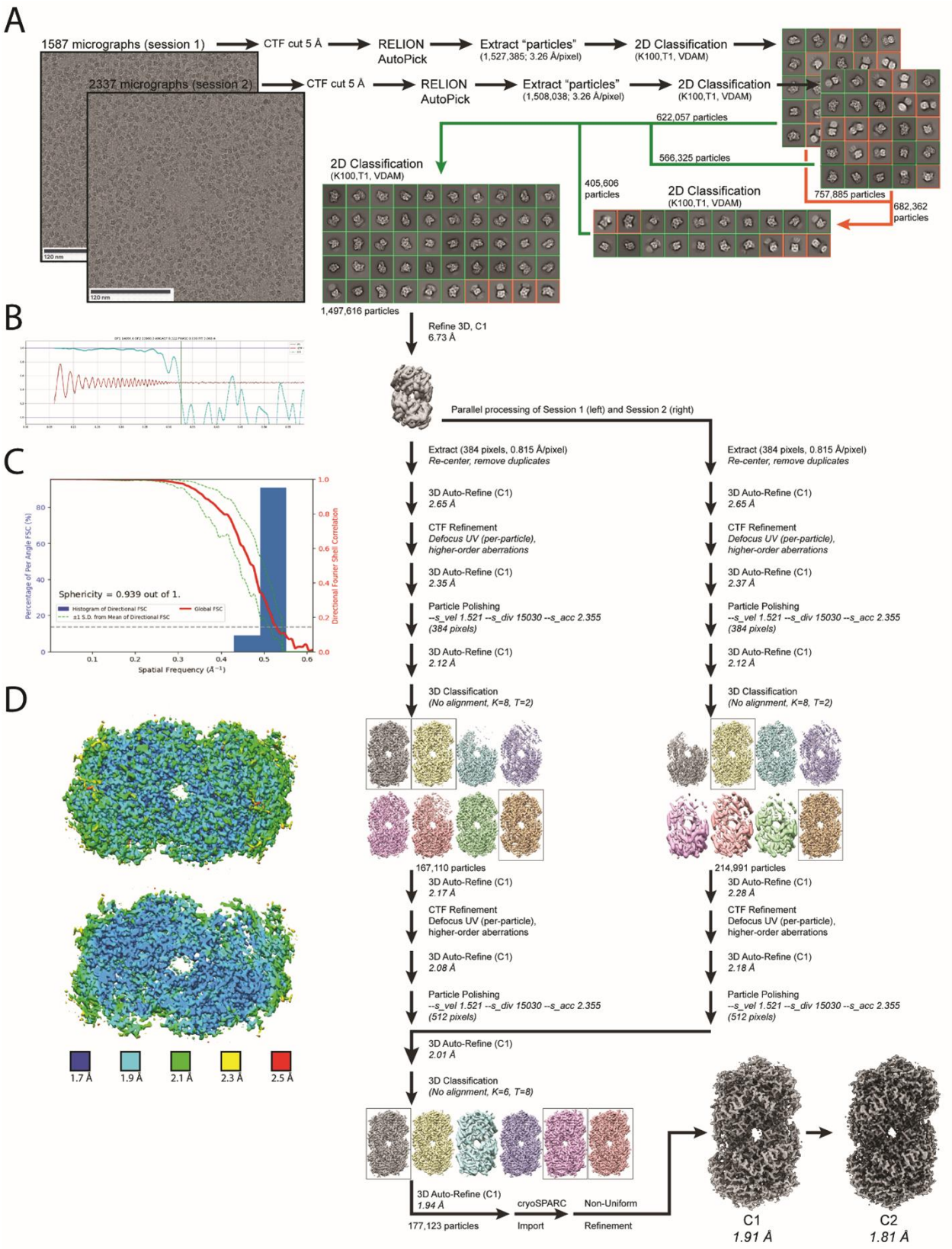
A
1587 micrographs (session 1)
CTF cut 5 Å
RELION AutoPick
Extract "particles" (1,527,385; 3.26 Å/pixel)
2D Classification (K100,T1, VDAM)
2337 micrographs (session 2)
CTF cut 5 Å
RELION AutoPick
Extract "particles" (1,508,038; 3.26 Å/pixel)
2D Classification (K100,T1, VDAM)
622,057 particles
566,325 particles
757,885 particles
682,362 particles
405,606 particles
2D Classification (K100,T1, VDAM)
2D Classification (K100,T1, VDAM)
1,497,616 particles
B
Refine 3D, C1 6.73 Å
C
Sphericity = 0.939 out of 1.
Histogram of Directional FSC
Global FSC
±1 S.D. from Mean of Directional FSC
Percentage of Per Angle FSC (%)
Directional Fourier Shell Correlation
Spatial Frequency (Å⁻¹)
Parallel processing of Session 1 (left) and Session 2 (right)
Extract (384 pixels, 0.815 Å/pixel)
Re-center, remove duplicates
3D Auto-Refine (C1)
2.65 Å
CTF Refinement
Defocus UV (per-particle), higher-order aberrations
3D Auto-Refine (C1)
2.35 Å
Particle Polishing
--s_vel 1.521 --s_div 15030 --s_acc 2.355
(384 pixels)
3D Auto-Refine (C1)
2.12 Å
3D Classification
(No alignment, K=8, T=2)
167,110 particles
214,991 particles
3D Auto-Refine (C1)
2.17 Å
2.28 Å
CTF Refinement
Defocus UV (per-particle), higher-order aberrations
3D Auto-Refine (C1)
2.08 Å
2.18 Å
Particle Polishing
--s_vel 1.521 --s_div 15030 --s_acc 2.355
(512 pixels)
3D Auto-Refine (C1)
2.01 Å
3D Classification
(No alignment, K=6, T=8)
3D Auto-Refine (C1)
1.94 Å
177,123 particles
cryoSPARC Import
Non-Uniform Refinement
C1
1.91 Å
C2
1.81 Å
D
1.7 Å
1.9 Å
2.1 Å
2.3 Å
2.5 Å

**Table 4.1** CryoEM data collection and refinement statistics of *Azotobacter vinelandii* $^{t/o}$Complex-1 and $^{t/o}$Complex-2.

| | **$^{t/o}$Complex-1 (EMDB-26760) (PDB-7UT8)** | **$^{t/o}$Complex-2 (EMDB-26763) (PDB-7UT9)** |
|---|---|---|
| **Data Collection** | Titan Krios G3i K3 BioQuantum | |
| Magnification | 130kx | |
| Voltage (kV) | 300 | |
| Spherical Aberration (mm) | 2.7 | |
| Electron Exposure ($e^-/Å^2$) | 65 | |
| Defocus range (μm) | -1.1 to -2 | |
| Pixel size (Å, Physical/Digital) | 0.835 | |
| Energy Filter Slit Width (eV) | 20 | |
| Movies | 2580 | |
| **Map Statistics and Post-Processing** | **$^{t/o}$Complex-1** | **$^{t/o}$Complex-2** |
| Symmetry imposed | $C_1$ | $C_1$ |
| Map Resolution (Å) | 2.28 | 2.29 |
| Local resolution range for 75% of voxels | 2.731 | 2.577 |
| Local resolution range (model) | 1.897 - 21.602 | 1.843 - 22.574 |
| Map sharpening *B* factor ($Å^2$) | 47.5 | 47.3 |
| Map sharpening method | DeepEMhancer | DeepEMhancer |
| 3D FSC values<br>X<br>Y<br>Z | <br>2.78<br>2.78<br>2.78 | <br>2.66<br>3.28<br>2.66 |
| **Model Statistics and Validation** | **$^{t/o}$Complex-1** | **$^{t/o}$Complex-2** |
| Model composition<br>Non-hydrogen atoms<br>Protein residues<br>Nucleic acids<br>Ligands | <br>20194<br>20026<br>0<br>168 | <br>20182<br>20018<br>0<br>164 |
| *B*-factors ($Å^2$)<br>Protein/Nucleic acid atoms<br>Ligands/non-protein atoms | <br>58.63<br>68.84 | <br>63.87<br>79.58 |

**Table 4.1** CryoEM data collection and refinement statistics of *Azotobacter vinelandii* $^{t/o}$Complex-1 and $^{t/o}$Complex-2, continued.

| | | |
|---|---|---|
| R.M.S deviations<br>Bond lengths (Å)<br>Bond angles (°) | <br>0.006<br>1.475 | <br>0.006<br>1.496 |
| MolProbity Score | 1.81 | 2.04 |
| MolProbity Clashscore | 7.80 | 9.36 |
| CaBLAM (% outliers) | 1.79 | 1.95 |
| Rotamer outliers (#,%) | 1.48 | 2.27 |
| Cis peptides (#, %) | 8, 0.3% | 8.1, 0.3% |
| Ramachandran Plot<br>Favored (%)<br>Allowed (%)<br>Disallowed (%) | <br>96.28<br>3.48<br>0.24 | <br>96.00<br>3.76<br>0.24 |
| EM Ringer score | 4.03 | 3.98 |
| Map/Model FSC (0.5) | 2.95 | 2.84 |

**Table 4.2** CryoEM data collection and refinement statistics of *Azotobacter vinelandii* $^{rs}$MoFeP.

| | **$^{rs}$MoFe $C_1$ (EMDB-26756) (PDB-7UT6)** | **$^{rs}$MoFe $C_2$ (EMDB-26757) (PDB-7UT7)** |
|---|---|---|
| **Data Collection** | Titan Krios G3 K2 BioContinuum | |
| Magnification | 165kx | |
| Voltage (kV) | 300 | |
| Spherical Aberration (mm) | 2.7 | |
| Electron Exposure ($e^-/Å^2$) | 65 | |
| Defocus range (μm) | -0.5 to -1.5 | |
| Pixel size (Å, Physical/Digital) | 0.815 | |
| Energy Filter Slit Width (eV) | 10 | |
| Movies | 1460 (session 1)<br>2313 (session 2) | |
| **Map Statistics and Post-Processing** | **$^{rs}$MoFe $C_1$** | **$^{rs}$MoFe $C_2$** |
| Symmetry imposed | $C_1$ | $C_2$ |
| Map Resolution (Å) | 1.91 | 1.81 |
| Local resolution range for 75% of voxels | 5.299 | 2.883 |
| Local resolution range (model) | 1.826 - 30.347 | 1.826- 29.563 |
| Map sharpening *B* factor ($Å^2$) | 37.9 | 39.8 |
| Map sharpening method | DeepEMhancer | DeepEMhancer |
| 3D FSC values<br>X<br>Y<br>Z | <br>2.47<br>2.78<br>2.37 | <br>1.93<br>1.94<br>1.84 |
| **Model Statistics and Validation** | **$^{rs}$MoFe $C_1$** | **$^{rs}$MoFe $C_2$** |
| Model composition<br>Non-hydrogen atoms<br>Protein residues<br>Nucleic acids<br>Ligands | <br>20194<br>20026<br>0<br>168 | <br>20182<br>20018<br>0<br>164 |
| *B*-factors ($Å^2$)<br>Protein/Nucleic acid atoms<br>Ligands/non-protein atoms | <br>58.63<br>68.84 | <br>63.87<br>79.58 |

**Table 4.2** CryoEM data collection and refinement statistics of *Azotobacter vinelandii* $^{rs}$MoFeP, continued.

| | | |
|---|---|---|
| R.M.S deviations<br>Bond lengths (Å)<br>Bond angles (°) | <br>0.006<br>1.475 | <br>0.006<br>1.496 |
| MolProbity Score | 1.81 | 2.04 |
| MolProbity Clashscore | 7.80 | 9.36 |
| CaBLAM (% outliers) | 1.79 | 1.95 |
| Rotamer outliers (#,%) | 1.48 | 2.27 |
| Cis peptides (#, %) | 8, 0.3% | 8.1, 0.3% |
| Ramachandran Plot<br>Favored (%)<br>Allowed (%)<br>Disallowed (%) | <br>96.28<br>3.48<br>0.24 | <br>96.00<br>3.76<br>0.24 |
| EM Ringer score | 4.03 | 3.98 |
| Map/Model FSC (0.5) | 2.95 | 2.84 |

Given the $C_2$ symmetry of MoFeP and the large separation (>65 Å) between the nearest clusters from the symmetry-related αβ-subunits, it has long been assumed that the two αβ-halves of MoFeP function independently from one another.[8, 88] In support of this assumption, the crystal structures of various FeP-MoFeP complexes in different nucleotide-bound states largely possess a 2:1 FeP:MoFeP stoichiometry.[54, 55, 153] Unexpectedly, our turnover samples did not contain any particles that could be assigned to a 2:1 FeP:MoFeP complex (**Figs. 4.5, 4.6**). We considered the possibility that the exclusive observation of 1:1 complexes in our turnover samples could arise from an experimental artifact such as protein degradation or increase in ionic strength during cryoEM grid preparation. Therefore, we prepared a second set of turnover samples as above that also included 5 mM beryllium fluoride ($BeF_x$), which is known to arrest ATP hydrolysis in a transition-like state to yield quasi-irreversible, solution-stable 2:1 and 1:1 FeP-MoFeP complexes.[161] Accordingly, our cryoEM samples contained a large fraction of 2:1 FeP:MoFeP complexes alongside 1:1 species, but no free MoFeP particles (**Fig. 4.9, 4.10, Table 4.3**). We determined the structure of the MgADP.$BeF_x$-bound 2:1 FeP:MoFeP at ~2.4 Å resolution and found it to be isostructural to the crystal structure of the related MgADP.$AlF_x$-bound 2:1 FeP:MoFeP complex (**Fig. 4.10**). These observations affirm that our cryoEM samples contain intact proteins and operate under native turnover conditions, in turn indicating that the 1:1 FeP:MoFeP stoichiometry is the predominant nitrogenase assembly state during catalysis.

**Figure 4.9** Data processing flowchart for the single-particle cryo-EM analysis of the BeFx-trapped nitrogenase complex. (a) Representative motion-corrected micrograph for each of the datasets for vitrified $BeF_x$-trapped nitrogenase complexes collected at ~1.5 μm underfocus. A total of 1,117,055 particles identified from dose-weighted micrographs using RELION auto-pick with resting state MoFeP as a template. Particles were extracted from each dataset downsampled 4 x 4 and subjected to iterative rounds of 2-D classification in parallel before being combined for additional 2-D classification and 3-D auto-refinement. Particles were then re-centered and re-extracted unbinned and subjected to iterative rounds of 3-D auto- and CTF refinement, followed by a no alignment 3-D classification. The best classes were combined and subjected to additional rounds of no-alignment classification using a soft mask for the FeP subunits. 1:1 and 2:1 FeP:MoFeP complexes were separated and processed in parallel. After iterative rounds of 3-D auto- and CTF refinement, Bayesian particle polishing, ~2.69 Å and ~2.40 Å resolution structures were obtained for the 1:1 and 2:1 complexes, respectively. (b) Representative 2-D CTF fit for the data. (c-d) Histogram and directional 3-D FSC plots [160] generated from the independent half maps contributing to the structures of the (c) 1:1 and (d) 2:1 complexes (e) EM density for the 2:1 $BeF_x$-trapped FeP:MoFeP complex colored by local resolution. The left image shows the surface of the complex and the right image is a volume cross-section highlighting core regions. Data processing of *Av* nitrogenase complex trapped $BeF_x$ during catalytic turnover.

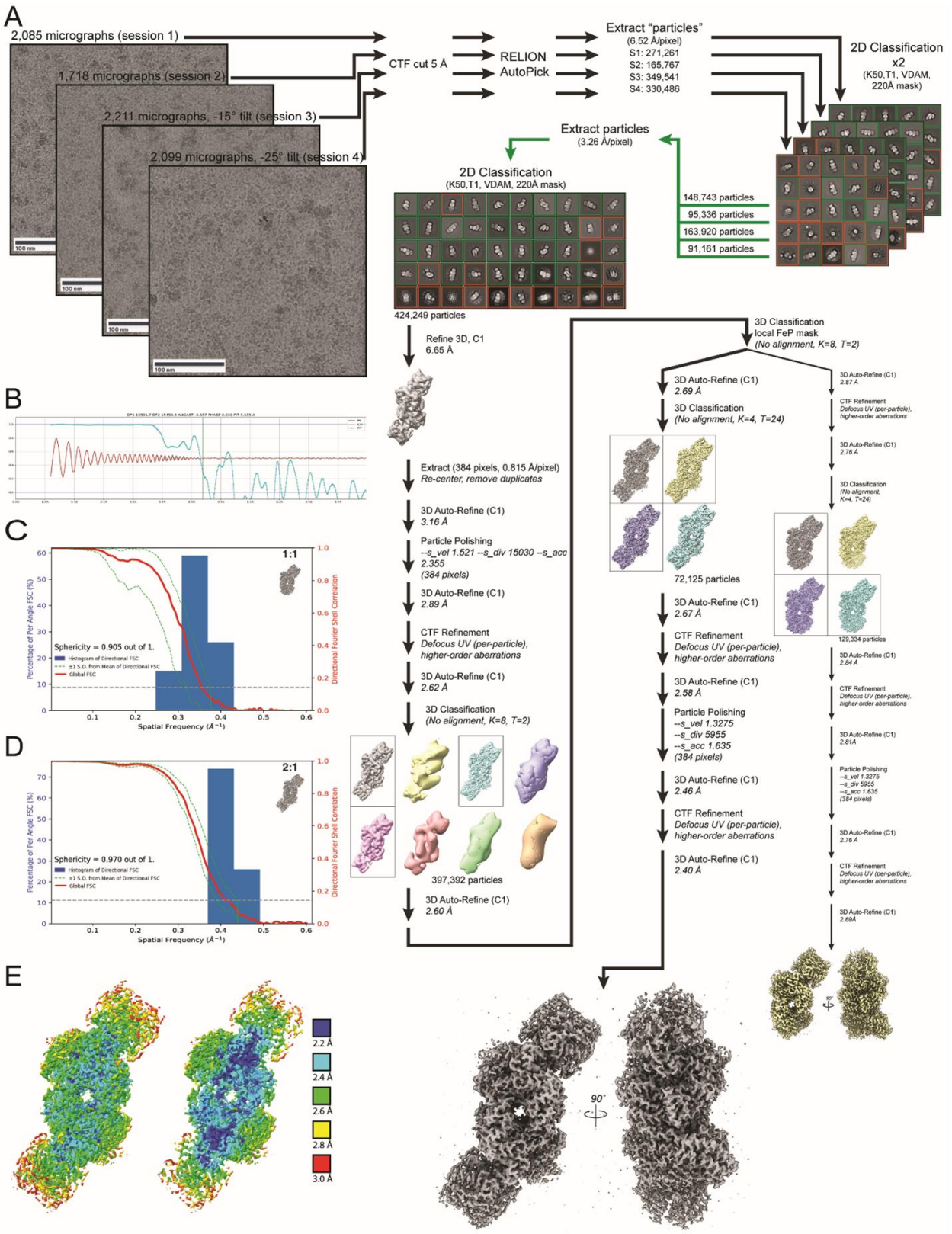
A
2,085 micrographs (session 1)
1,718 micrographs (session 2)
2,211 micrographs, -15° tilt (session 3)
2,099 micrographs, -25° tilt (session 4)
CTF cut 5 Å
RELION AutoPick
Extract "particles"
(6.52 Å/pixel)
S1: 271,261
S2: 165,767
S3: 349,541
S4: 330,486
2D Classification x2
(K50,T1, VDAM, 220Å mask)
Extract particles
(3.26 Å/pixel)
2D Classification
(K50,T1, VDAM, 220Å mask)
148,743 particles
95,336 particles
163,920 particles
91,161 particles
424,249 particles
Refine 3D, C1
6.65 Å
B
C
D
E
Extract (384 pixels, 0.815 Å/pixel)
Re-center, remove duplicates
3D Auto-Refine (C1)
3.16 Å
Particle Polishing
--s_vel 1.521 --s_div 15030 --s_acc 2.355
(384 pixels)
3D Auto-Refine (C1)
2.89 Å
CTF Refinement
Defocus UV (per-particle), higher-order aberrations
3D Auto-Refine (C1)
2.62 Å
3D Classification
(No alignment, K=8, T=2)
397,392 particles
3D Auto-Refine (C1)
2.60 Å
3D Classification
local FeP mask
(No alignment, K=8, T=2)
3D Auto-Refine (C1)
2.69 Å
3D Classification
(No alignment, K=4, T=24)
72,125 particles
3D Auto-Refine (C1)
2.67 Å
CTF Refinement
Defocus UV (per-particle), higher-order aberrations
3D Auto-Refine (C1)
2.58 Å
Particle Polishing
--s_vel 1.3275
--s_div 5955
--s_acc 1.635
(384 pixels)
3D Auto-Refine (C1)
2.46 Å
CTF Refinement
Defocus UV (per-particle), higher-order aberrations
3D Auto-Refine (C1)
2.40 Å
3D Auto-Refine (C1)
2.87 Å
CTF Refinement
Defocus UV (per-particle), higher-order aberrations
3D Auto-Refine (C1)
2.76 Å
3D Classification
(No alignment, K=4, T=24)
129,334 particles
3D Auto-Refine (C1)
2.84 Å
CTF Refinement
Defocus UV (per-particle), higher-order aberrations
3D Auto-Refine (C1)
2.81Å
Particle Polishing
--s_vel 1.3275
--s_div 5955
--s_acc 1.635
(384 pixels)
3D Auto-Refine (C1)
2.76 Å
CTF Refinement
Defocus UV (per-particle), higher-order aberrations
3D Auto-Refine (C1)
2.69Å
1:1
Sphericity = 0.905 out of 1.
Histogram of Directional FSC
±1 S.D. from Mean of Directional FSC
Global FSC
Percentage of Per Angle FSC (%)
Directional Fourier Shell Correlation
Spatial Frequency (Å⁻¹)
2:1
Sphericity = 0.970 out of 1.
2.2 Å
2.4 Å
2.6 Å
2.8 Å
3.0 Å
90°

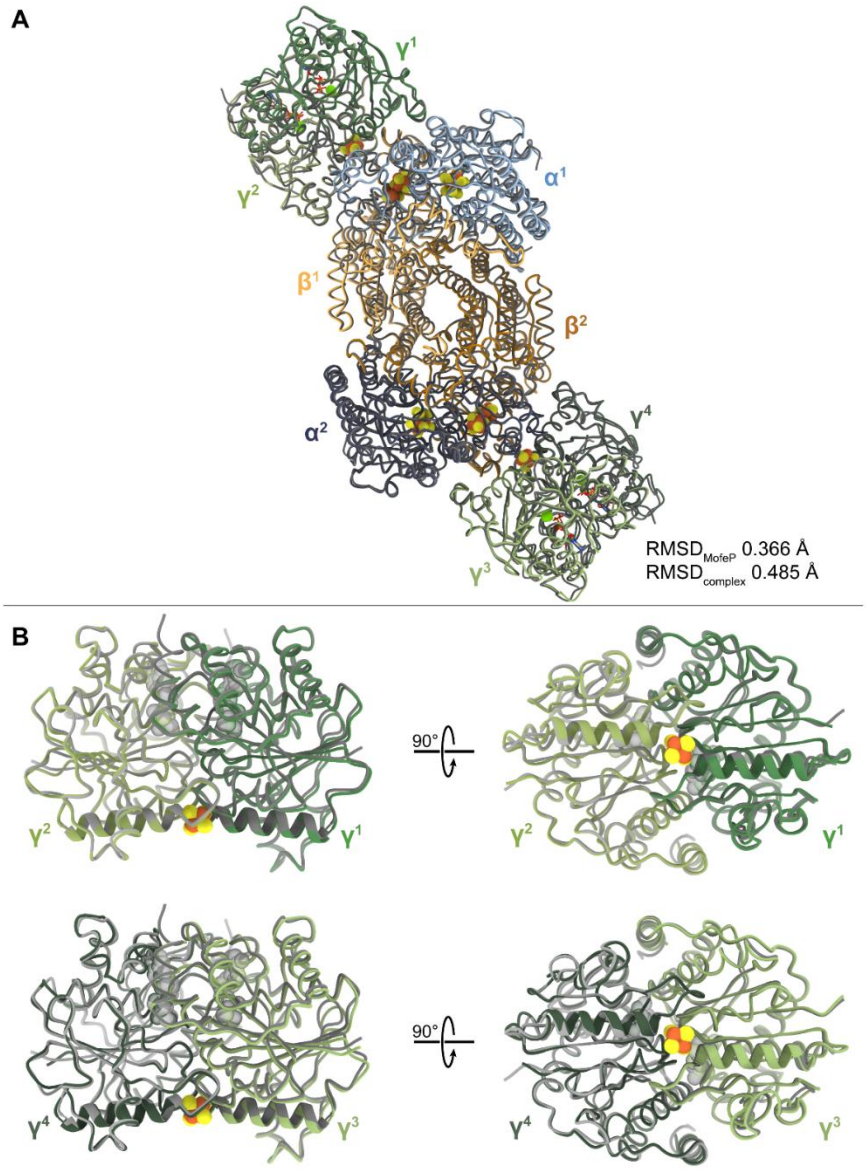


**Figure 4.10** Comparison of $BeF_X$-bound cryoEM structure with $AlF_X$ crystal structure. (**A**) Overlay of $BeF_X$-bound structure (green, orange, and blue) with the $AlF_X$ crystal structure (PDB ID: 1M34) highlighting the overall similarity in the inhibited structures. RMSDs of MoFeP and entire complex alignments are 0.366 Å and 0.485 Å, respectively. (**B**) Structural overlay of the FeP components ($\gamma^1$ and $\gamma^2$ top, ($\gamma^3$ and $\gamma^4$ bottom) in $BeF_X$ and $AlF_X$ structures in which the left subunit ($\gamma^2$ or $\gamma^4$) has been aligned. The g100's helices are depicted as thick cartoons.

**Table 4.3** CryoEM data collection and refinement statistics of *Azotobacter vinelandii* nitrogenase complex inhibited by $BeF_x$.

| | **$BeF_x$ trapped complex (EMDB-26764) (PDB-7UTA)** | |
|---|---|---|
| **Data Collection** | Titan Krios G3 K2 BioContinuum | |
| Magnification | 165kx | |
| Voltage (kV) | 300 | |
| Spherical Aberration (mm) | 2.7 | |
| Electron Exposure ($e^-/Å^2$) | 65 | |
| Defocus range (μm) | -0.5 to -1.5 | |
| Pixel size (Å, Physical/Digital) | 0.815 | |
| Energy Filter Slit Width (eV) | 10 | |
| Movies (Tilt (°)) | 1460 | 0 |
| | 2313 | 0 |
| | 2211 | -15 |
| | 2099 | -25 |
| **Map Statistics and Post-Processing** | **$BeF_x$ trapped complex** | |
| Symmetry imposed | $C_1$ | |
| Map Resolution (Å) | 2.40 | |
| Local resolution range for 75% of voxels | 2.883 | |
| Local resolution range (model) | 1.826- 29.563 | |
| Map sharpening *B* factor ($Å^2$) | 39.8 | |
| Map sharpening method | DeepEMhancer | |
| 3D FSC values<br>X<br>Y<br>Z | <br>3.17<br>2.84<br>2.95 | |

**Table 4.3** CryoEM data collection and refinement statistics of *Azotobacter vinelandii* nitrogenase complex inhibited by $BeF_x$, continued.

| **Model Statistics and Validation** | **$BeF_x$ trapped complex** |
|---|---|
| Model composition | |
| Non-hydrogen atoms | 24304 |
| Protein residues | 24077 |
| Nucleic acids | 0 |
| Ligands | 227 |
| *B*-factors (Å$^2$) | |
| Protein/Nucleic acid atoms | 47.27 |
| Ligands/non-protein atoms | 58.79 |
| R.M.S deviations | |
| Bond lengths (Å) | 0.011 |
| Bond angles (°) | 1.137 |
| MolProbity Score | 3.20 |
| MolProbity Clashscore | 18.38 |
| CaBLAM (% outliers) | 0.59 |
| Rotamer outliers (#,%) | 13.95 |
| Cis peptides (#, %) | 8, 0.3% |
| Ramachandran Plot | |
| Favored (%) | 89.53 |
| Allowed (%) | 8.11 |
| Disallowed (%) | 2.36 |
| EM Ringer score | 3.67 |
| Map/Model FSC (0.5) | 2.87 |

Prior work using pre-steady-state kinetics measurements revealed that the extents of interprotein ET and ATP hydrolysis were approximately half of what would be expected if there were two independent FeP binding sites on MoFeP.[81] Originally, such half-reactivity was attributed to either partial inactivity of FeP molecules[81] or to the possible existence of an alternative interaction mode between FeP and MoFeP.[162] Recent studies instead favored a model of negative cooperativity within a 2:1 FeP:MoFeP complex, whereby one of the bound FeP molecules suppresses ATP hydrolysis by the other bound FeP

and the redox activity of the distal αβ-half.[163, 164] Our structural finding that MoFeP only binds one FeP at a time during turnover provides a clear basis for negative cooperativity whereby FeP binding to one αβ-half of MoFeP disfavors FeP association with the other αβ-half.

### 4.3.2 Asymmetric nucleotide hydrolysis and MoFeP residue conformations in $^{t/o}$Complex-1 and $^{t/o}$Complex-2

Because $^{t/o}$Complex-1 and $^{t/o}$Complex-2 were distinguished during cryoEM data processing based exclusively on the structural variability of the FeP components, we first examined whether these differences are associated with the ATP-hydrolysis state of the two complexes. Earlier crystal structures identified at least three nucleotide-state-dependent FeP-MoFeP docking geometries (DG1, DG2 and DG3) and led to the hypothesis that FeP moves in a unidirectional fashion across the MoFeP surface during turnover (**Fig. 4.11a**).[8, 55] The DG1 state predominates in the absence of nucleotides but is also populated in the presence of ATP,[86] and corresponds to an electrostatically guided encounter complex wherein FeP largely interacts with the β-subunit of MoFeP. DG2 is the activated nitrogenase complex in which ATP hydrolysis is coupled to interprotein ET, with FeP occupying the quasi-symmetric surface of MoFeP shared between α- and β-subunits (**Figs. 1.5, 4.11a**).[54, 55] Finally, DG3 is formed by ADP-bound FeP and primarily utilizes the α-subunit surface of MoFeP.[55] The cryoEM analysis of our turnover samples revealed that $^{t/o}$Complex-1 and $^{t/o}$Complex-2 were exclusively in DG2 (**Fig. 4.11a**), implying that this configuration has a higher stability and/or longer residence time relative to DG1 and DG3. Characteristic of a DG2 configuration, both complexes feature extensive interactions between FeP and MoFeP (buried surface areas >3600 Å$^2$) and a short [4Fe:4S]-to-P-cluster edge-to-edge distance of ~15 Å, primed for rapid interprotein ET (**Fig. 4.11b**).

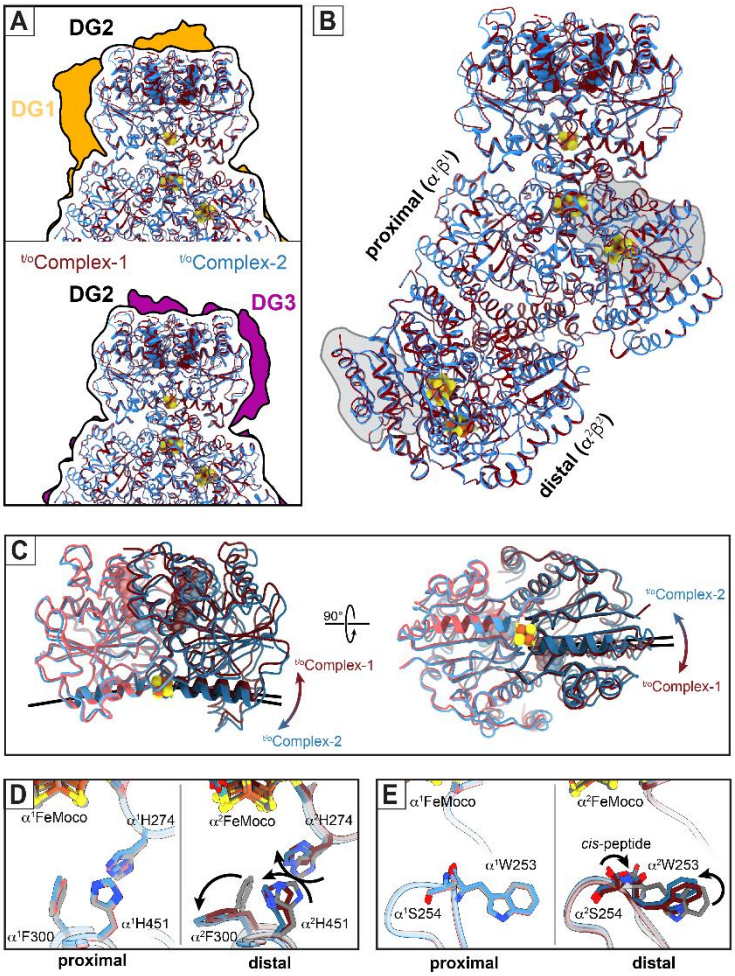


**Figure 4.11** Structural details of nitrogenase complexes characterized under turnover conditions. (**A**) Comparison of the FeP:MoFeP docking geometry (DG) in $^{t/o}$Complex-1 (maroon) and $^{t/o}$Complex-2 (blue) observed in the DG2 configuration (black outline) compared to DG1 (gold; PDB ID:2AFH) and DG3 (purple; PDB ID: 2AFI) configurations characterized by X-ray crystallography. (**B**) Structural overlay of $^{t/o}$Complex-1 and $^{t/o}$Complex-2, indicating that the only large-scale conformational changes are observed in FeP. "Proximal" and "distal" refer to the $\alpha^1\beta^1$ and $\alpha^2\beta^2$ halves of MoFeP bound and not bound to FeP, respectively. The αIII domains of MoFeP are outlined in gray. (**C**) Structural overlay of the FeP components in $^{t/o}$Complex-1 and $^{t/o}$Complex-2, highlighting the nucleotide-dependent conformational differences (hinging – left, twisting - right) motions of the $\gamma^1$ and $\gamma^2$ subunits relative to one another during ATP hydrolysis. The axes of the γ100's helices that radiate from [4Fe:4S] cluster are shown as black lines to illustrate these conformational differences. (**D,E**) Residues in the vicinity of FeMoco (**D**, αHis274, αPhe300, αHis451; **E**, αTrp253) that have undergone conformational changes in the distal subunit ($\alpha^2$) of MoFeP during turnover. Side chain movements between the resting-state ($^{rs}$MoFeP) (gray) and the turnover structures (maroon and blue) are indicated with arrows.

In $^{t/o}$Complex-1, both FeP γ-subunits ($\gamma^1$ and $\gamma^2$) are occupied by ATP molecules with clear densities for the γ-phosphate groups and associated $Mg^{2+}$ ions (**Fig. 4.5**). By contrast, the $\gamma^1$ subunit of $^{t/o}$Complex-2 features an ATP molecule with weak density for the γ-phosphate, whereas the $\gamma^2$ subunit is ADP-bound and the γ-phosphate is completely absent from the nucleotide binding pocket, indicative of asymmetry in ATP hydrolysis (**Fig. 4.5**). This observation is consistent with the crystal structure of a mixed-nucleotide FeP-MoFeP complex, in which AMPPCP (a non-hydrolyzable ATP analog) and ADP were selectively bound to the $\gamma^1$ and $\gamma^2$-subunits, respectively.[56] The differences in the nucleotide occupancies of $^{t/o}$Complex-1 and $^{t/o}$Complex-2 are reflected in their distinct FeP conformations (**Fig. 4.11c**), which is further corroborated by a principal component analysis of all available FeP structures (**Fig. 4.12**). Collectively, these observations indicate that (1) our cryoEM samples represent active turnover conditions, (2) the hydrolysis of two ATP molecules in each FeP cycle occurs in a stepwise fashion, and (3) $^{t/o}$Complex-1 and $^{t/o}$Complex-2 correspond, respectively, to pre- and mid-ATP hydrolysis states of the nitrogenase complex that are populated along the catalytic reaction coordinate.

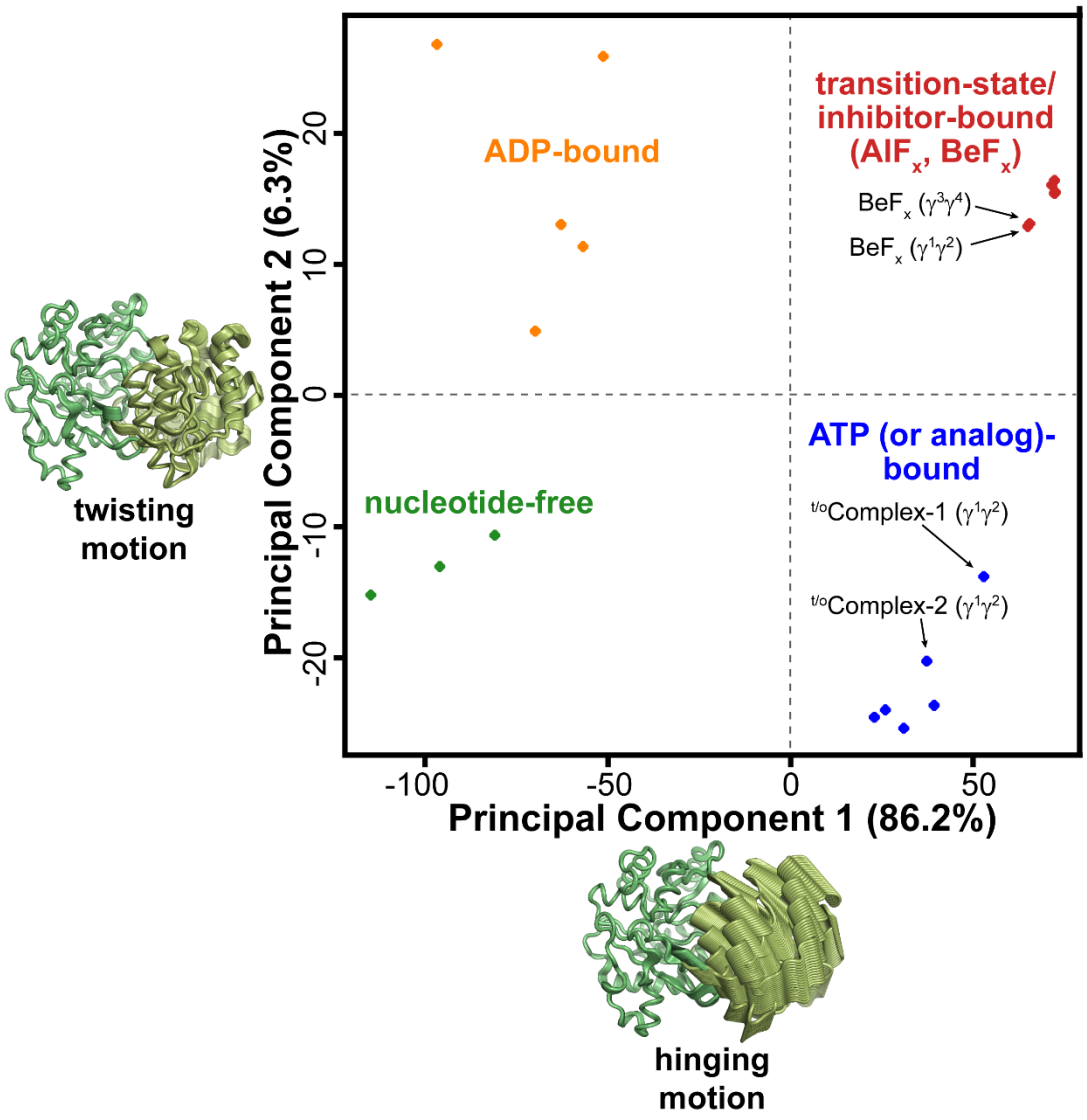


**Figure 4.12** Principal component analysis (PCA) of FeP. PCA of FeP was generated from 20 free- or MoFeP-complexed FeP structures. The first two principal components (PC) account for 92.5% of the variance. PC1 and PC2 are described by hinging/rotation and twisting motions, respectively. FeP conformations clustered into four nucleotide-state-dependent classes. FeP structures from the cryoEM structures are labeled.

The asymmetry present both in ATP hydrolysis and FeP-MoFeP interactions has important implications for the timing of ET events during catalysis. Compared to a concerted process, stepwise nucleotide hydrolysis by FeP would be expected to increase the lifetime of the activated DG2 complex and provide additional conformational states for orchestrating the multistep redox reactions that occur at FeMoco and the P-cluster.[8, 56] Similarly, an alternating docking mechanism between FeP and MoFeP (as

imposed by negative cooperativity between the αβ-halves) would effectively slow down successive ET steps to a given αβ-subunit, providing sufficient time for anticipated protein and metallocluster rearrangements during $N_2$ reduction. This is consistent with the suggestion of Thorneley and Lowe that the slow kinetics of nitrogenase ($k_{turnover} \approx 1\ s^{-1}$) governed by FeP-MoFeP interactions may be a mechanistic imperative to favor $N_2$ fixation over the competing but less demanding $H^+$ reduction. [77]

Having established $^{t/o}$Complex-1 and $^{t/o}$Complex-2 as two distinct intermediates along the FeP cycle, we next investigated if they exhibited any conformational changes in their MoFeP components that may be correlated with the ATP hydrolysis state. In both $^{t/o}$Complex-1 and $^{t/o}$Complex-2, the P-clusters are in their fully reduced, all-ferrous ($P^N$) forms, and the protein backbone arrangements of MoFePs in both complexes are essentially indistinguishable from one another as well as from those in $^{rs}$MoFeP and previously determined MoFeP crystal structures (Cα RMSD: 0.2 Å) (**Figs. 4.11b, 4.13, 4.14, Table 4.4**). We observed no large-scale conformational changes that could account for mechanical coupling and negative cooperativity between symmetry-related FeP docking surfaces on MoFeP, implicating the involvement of a dynamic allosteric mechanism (e.g., FeP-induced changes in MoFeP conformational entropy).[165] Furthermore, no conformational differences in key residues residing between the metalloclusters were observed (**Fig. 4.14**). Yet, a detailed inspection of the structures revealed that the FeP-free (i.e., "distal") $\alpha^2\beta^2$-half in both $^{t/o}$Complex-1 and $^{t/o}$Complex-2 possessed several features that distinguish it from the FeP-bound (i.e., "distal") $\alpha^1\beta^1$-half and $^{rs}$MoFeP.

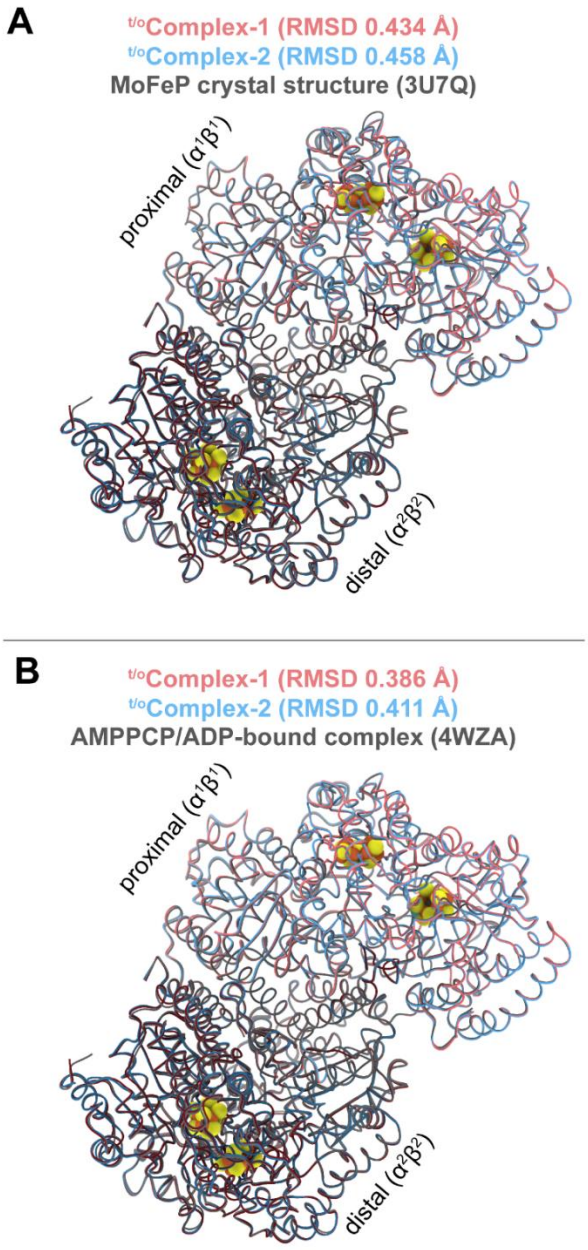


**Figure 4.13** Structural comparison of MoFeP from the turnover complexes with MoFeP from crystal structures. The backbone of MoFeP is superimposable in the cryoEM turnover complexes and published crystal structures as demonstrated by the overlay of $^{t/o}$Complex-1 (maroon) and $^{t/o}$Complex-2 (blue) with (a) a crystal structure of MoFeP (gray, PDB ID: 3U7Q), and (b) MoFeP from the AMPPCP/ADP bound FeP-MoFeP complex crystal structure (gray, PDB ID: 4WZA chains A,B,C,D).

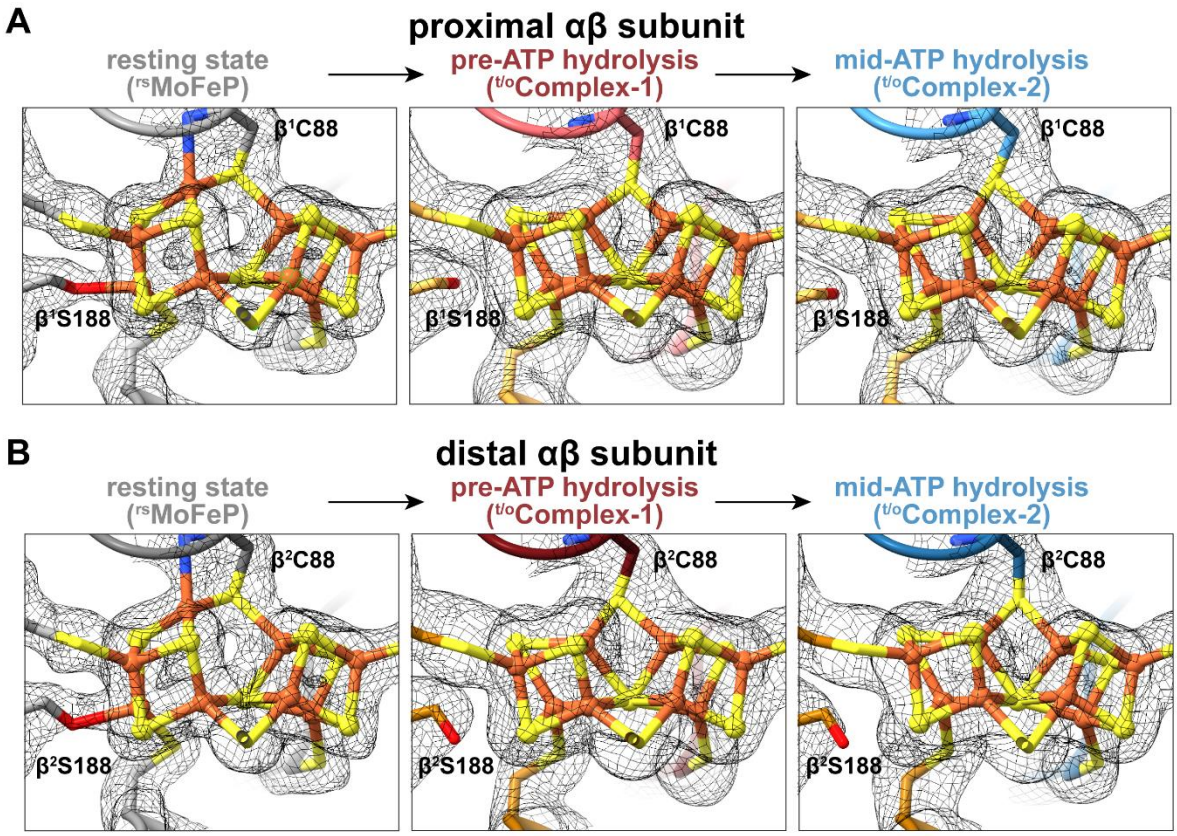


**Figure 4.14** P-clusters of $^{rs}$MoFeP, $^{t/o}$Complex-1, and $^{t/o}$Complex-2. (a,b) Views of the P-cluster and P-cluster ligands in the proximal (a) and distal (b) αβ halves of MoFeP in $^{rs}$MoFeP (gray), $^{t/o}$Complex-1 (maroon), and $^{t/o}$Complex-2 (blue) structures. CryoEM maps for each individual structure are contoured at the same level.

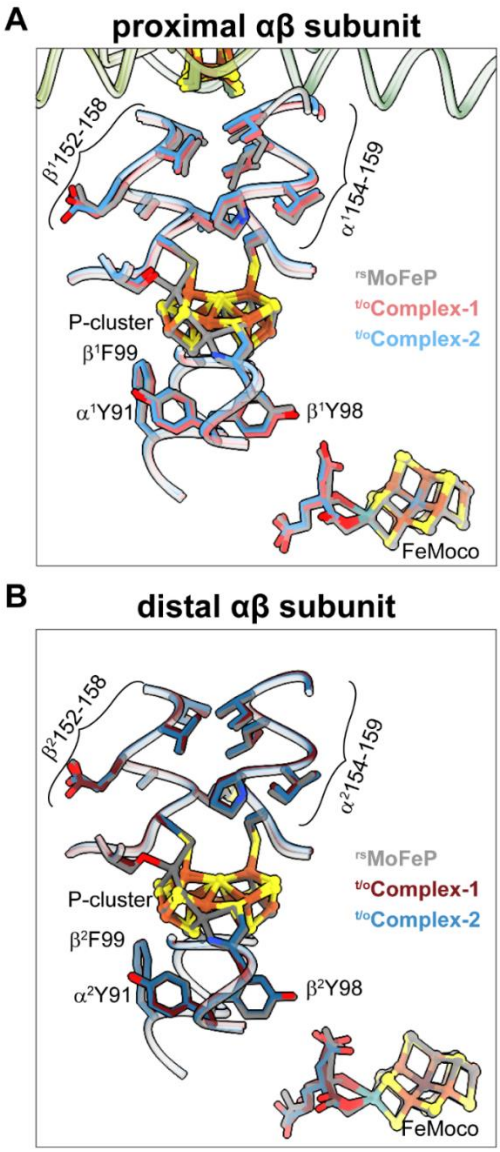


**Figure 4.15** Overlay of important residues between the P-cluster and FeMoco. (a,b) Overlay key residues residing between the [4Fe-4S] cluster and the P-cluster, and between the P-cluster and FeMoco in $^{rs}$MoFeP (gray), $^{t/o}$Complex-1 (maroon), and $^{t/o}$Complex-2 (blue) structures. The proximal (a) and distal (b) αβ halves of MoFeP are shown. γ100's helices are shown in green.

**Table 4.4** RMSDs of MoFeP alignments

| structure | MoFeP (3u7q) | nucleotide-free complex (2afh) | AMPPCP-bound (4wzb) | ADP-bound (2afi) | AMPPCP/ADP-bound (4wza) | ADP.AlF$_x$ (1m34) | N-species-bound MoFeP (6ug0) | CO-bound MoFeP (4tkv) | $^{rs}$MoFeP | $^{t/o}$Complex-1 | $^{t/o}$Complex-2 |
|---|---|---|---|---|---|---|---|---|---|---|---|
| nucleotide-free complex (2afh) | 0.365 | | | | | | | | | | |
| AMPPCP-bound (4wzb) | 0.323 | 0.291 | | | | | | | | | |
| ADP-bound (2afi) | 0.386 | 0.329 | 0.374 | | | | | | | | |
| AMPPCP/ADP-bound (4wza) | 0.241 | 0.246 | 0.196 | 0.337 | | | | | | | |
| ADP.AlFx (1m34) | 0.396 | 0.319 | 0.318 | 0.401 | 0.318 | | | | | | |
| N-species-bound MoFeP (6ug0) | 0.232 | 0.324 | 0.283 | 0.328 | 0.283 | 0.378 | | | | | |
| CO-bound MoFeP (4tkv) | 0.106 | 0.329 | 0.224 | 0.361 | 0.224 | 0.385 | 0.224 | | | | |
| $^{rs}$MoFeP | 0.324 | 0.313 | 0.311 | 0.320 | 0.302 | 0.322 | 0.310 | 0.321 | | | |
| $^{t/o}$Complex-1 | 0.434 | 0.397 | 0.359 | 0.412 | 0.386 | 0.348 | 0.410 | 0.444 | 0.233 | | |
| $^{t/o}$Complex-2 | 0.458 | 0.416 | 0.385 | 0.420 | 0.411 | 0.375 | 0.436 | 0.465 | 0.246 | 0.170 | |
| BeF$_x$-bound | 0.437 | 0.399 | 0.382 | 0.429 | 0.404 | 0.366 | 0.433 | 0.444 | 0.261 | 0.246 | 0.252 |

First, there are several, highly conserved residues ($\alpha^2$Trp253, $\alpha^2$His274, $\alpha^2$Phe300, $\alpha^2$His451) (26)[98] in the vicinity of the distal FeMoco which adopt non-resting-state conformations (**Fig. 4.11d,e**). αTrp253 is particular in its *cis*-peptide bond to αSer254 and its position in a proposed substrate access channel from the protein surface to FeMoco.[166, 167] The observed conformational flip in $\alpha^2$Trp253 leads to the diversion of this putative channel to an alternate face of FeMoco (**Figs. 4.11e, 4.16**). $\alpha^2$His274, $\alpha^2$Phe300 and $\alpha^2$His451 sidechains appear to have undergone a concerted motion compared to their resting state (**Fig. 4.11d**), whereby $\alpha^2$His274 and $\alpha^2$Phe300 assume a similar configuration as that seen in the low-pH crystal structure of MoFeP (**Fig 4.17**).[168] This αHis274 configuration was proposed to form a water-bridged H-bond to a protonated belt sulfur (S5A) of FeMoco.[168] Along these lines, the observed rearrangement of the $\alpha^2$His274 sidechain in the turnover complexes could be envisioned to stabilize a protonated FeMoco intermediate and/or to increase the reduction potential of the cofactor, thus promoting its reduction by the P-cluster.

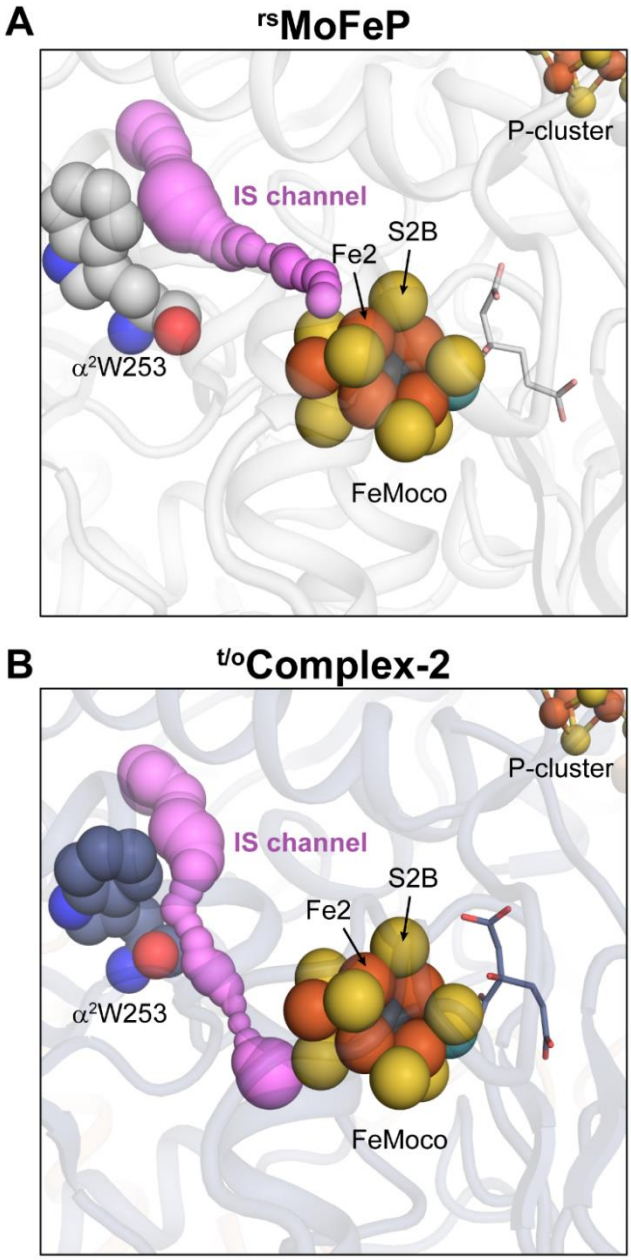


**Figure 4.16** Diversion of the IS channel during turnover. (a,b) The proposed substrate pathway, termed the IS channel after the authors,[166] is shown in pink and was calculated using the software CAVER[169]. (a) In $^{rs}$MoFeP, the IS channel leads from the surface of MoFeP to the proposed catalytic face of FeMoco. (b) Conformational changes during catalysis, as shown with $^{t/o}$Complex-2 divert the IS channel to a different face FeMoco.

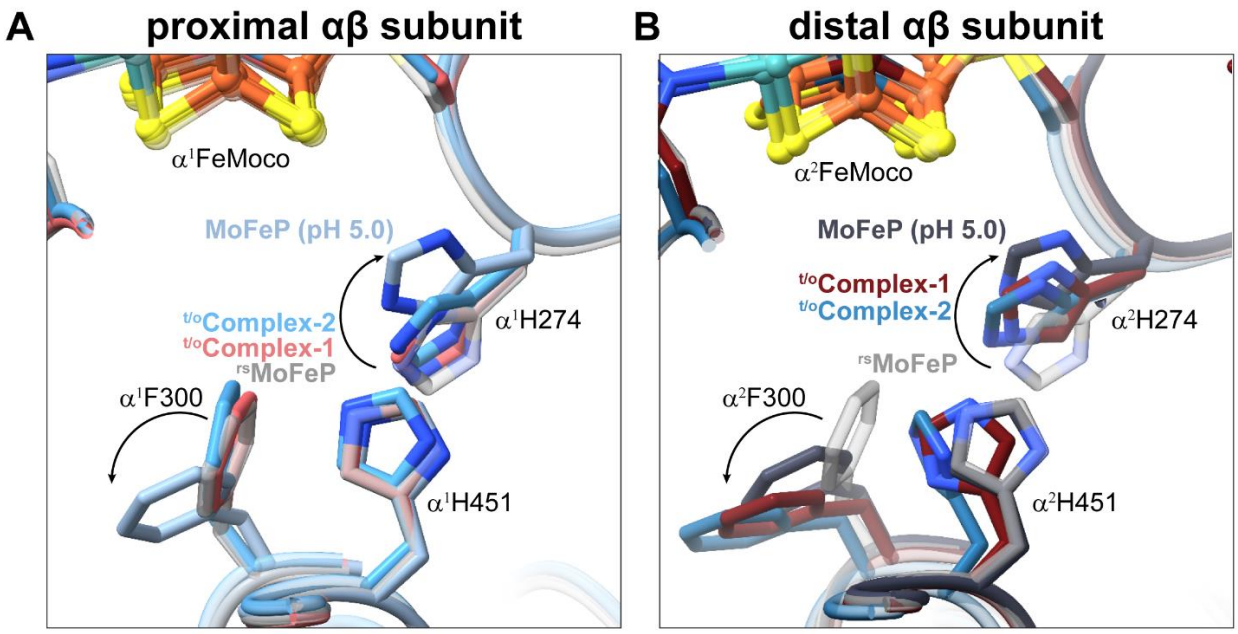


**Figure 4.17** Overlay of αHis274, αPhe300 and αHis451 from pH 5.0 MoFeP crystal structure and cryoEM structures. (a,b) Overlay of the conformationally altered tried in $^{rs}$MoFeP (transparent gray), $^{t/o}$Complex-1 (maroon), $^{t/o}$Complex-2 (blue), and the crystal structure of MoFeP at pH 5.0 (sky blue/slate PDB ID: 5VQ4) structures in both the proximal (a) and distal (b) αβ-halves of MoFeP.

Second, the cryoEM densities surrounding the $\alpha^2$His442 and homocitrate ligands to the Mo center of the distal FeMoco are considerably less well defined compared to their counterparts in the proximal αβ-half and the residues in the vicinity (**Fig. 4.18**), and they cannot be unambiguously modeled with the resting-state configurations of these ligands (**Fig. 4.19**). The reduction in map density is particularly pronounced for $^{t/o}$Complex-2 (i.e., mid-ATP-hydrolysis) compared to $^{t/o}$Complex-1 (i.e., pre-ATP-hydrolysis). These observations suggest that $\alpha^2$His442 and homocitrate are mobile during turnover and that Mo undergoes changes in inner-sphere coordination in a way that is correlated with the nucleotide hydrolysis state of FeP bound to the opposing αβ-half of MoFeP. The substitution of Mo with V or Fe in alternative nitrogenases, the replacement of homocitrate with citrate, and alterations in H-bonding to homocitrate have been shown to substantially diminish $N_2$ reduction activity and alter substrate specificity.[9, 88, 170, 171] Indeed, the direct involvement of the Mo center in $N_2$ reduction has been proposed early on,[88, 172] although recent experimental findings have shifted the focus to the central Fe centers of

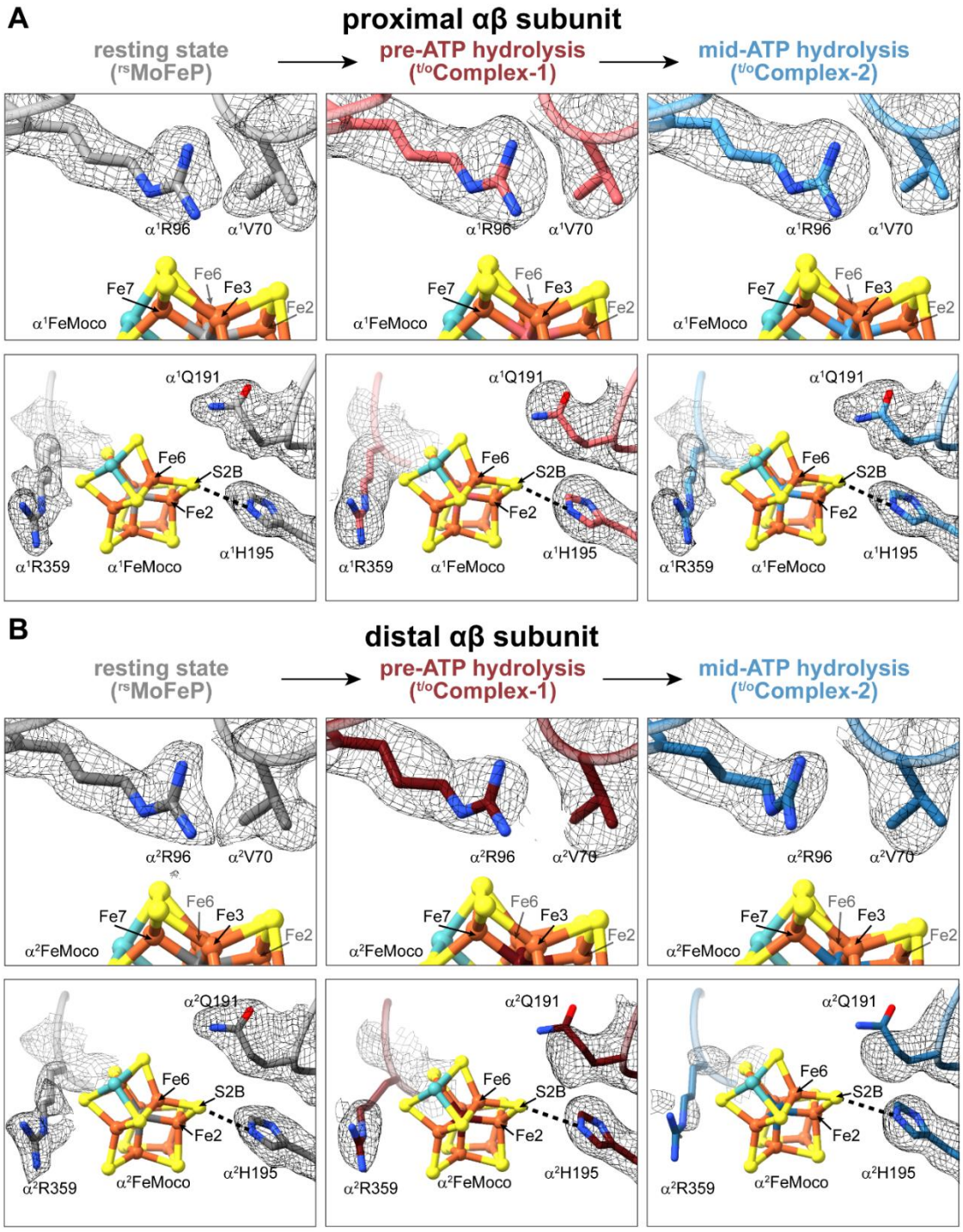


**Figure 4.18** The FeMoco environment in the cryoEM structures. (a,b) Views of FeMoco and the nearby residues αVal70, αArg96, αGln191, αHis195, and αArg359 in the proximal (a) and distal (b) αβ-halves of MoFeP in $^{rs}$MoFeP (gray), $^{t/o}$Complex-1 (maroon), and $^{t/o}$Complex-2 (blue) structures. CryoEM maps for each individual structure are contoured at the same level.

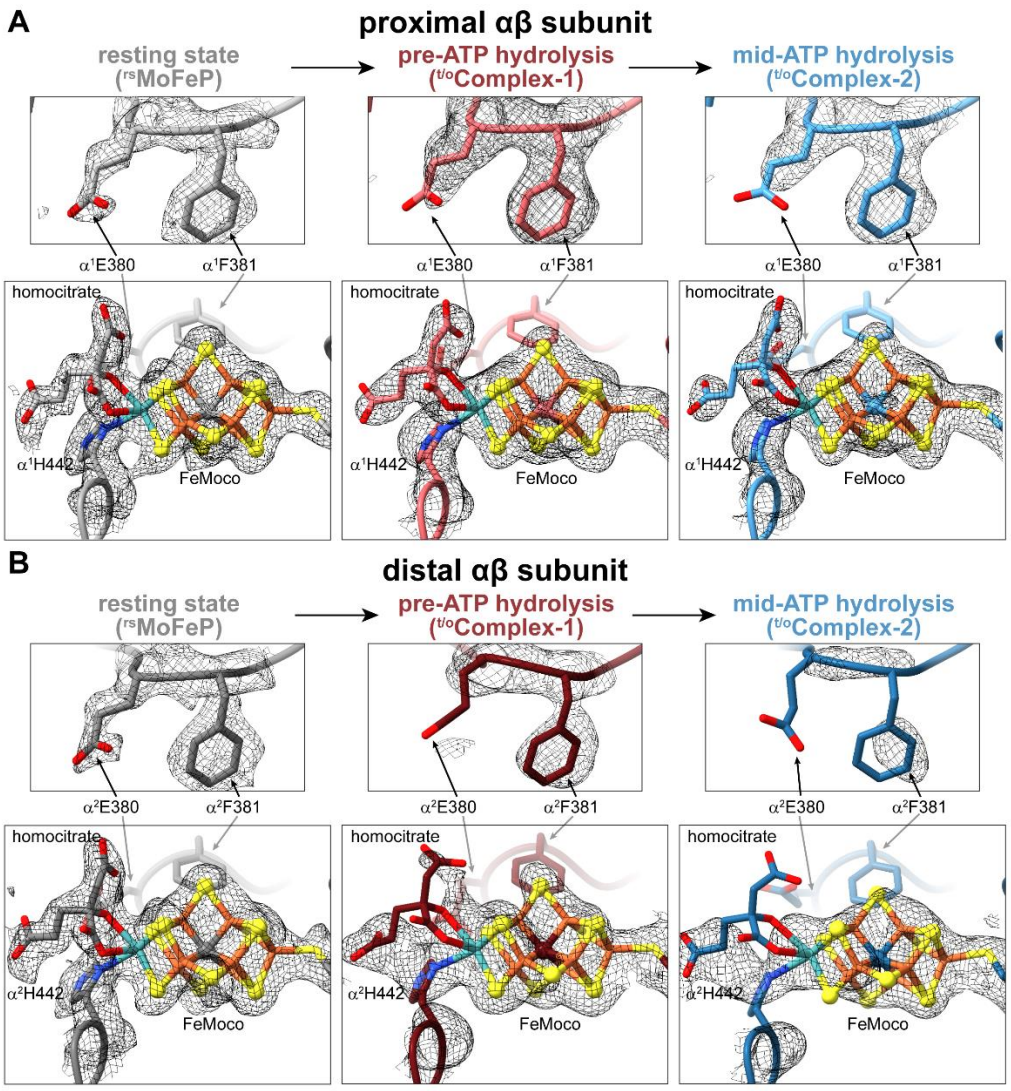


**Figure 4.19** Changes in the FeMoco environment observed during catalytic turnover. (a,b) Views of FeMoco and the nearby residues αGlu380 and αPhe381 in the proximal (a) and distal (b) αβ-halves of MoFeP in $^{rs}$MoFeP (gray), $^{t/o}$Complex-1 (maroon), and $^{t/o}$Complex-2 (blue) structures. CryoEM maps for each individual structure are contoured at the same level.

FeMoco as being the primary sites for substrate activation.[84, 173] Our cryo-EM observations provide evidence that Mo–or the corresponding apical Fe/V sites in alternative nitrogenases–also directly participates in substrate binding and reduction, enabled by the labilization of homocitrate or αHis442 ligands upon cofactor reduction to furnish a coordinatively unsaturated Mo center.

Third, portions of a large domain in the distal αβ-subunit comprising residues α25-48 and α2378-403 (particularly in $^{t/o}$Complex-2) possess increased mobility compared to the rest of the MoFeP (**Fig. 4.20**. This so-called αIII domain forms a lid above FeMoco and includes residues αGlu380 and αPhe381 that form close contacts with FeMoco (**Figs. 4.11b, 4.19**). In resting state MoFeP, αIII is well-ordered, αGlu380 forms water-bridged H-bonds to the Mo-ligated αHis442 sidechain and homocitrate, and αPhe381 is in van der Waals contact with the labile belt sulfide S2B of FeMoco (**Figs. 4.19a, 4.20**). By contrast, in the distal $\alpha^2\beta^2$-halves of $^{t/o}$Complex-1 and $^{t/o}$Complex-2, the cryoEM densities for αIII and sidechains of $\alpha^2$Glu380 and $\alpha^2$Phe381 sidechains are either diffuse or entirely missing, consistent with their movement during turnover (**Figs. 4.19b, 4.20**). This movement is likely coupled to the dynamics of the Mo ligands and FeMoco as a whole. αIII has also been shown to undergo major structural rearrangements associated with the insertion of FeMoco into MoFeP (34). Furthermore, αIII displays some of the highest temperature factors in most MoFeP crystal structures and is positioned away from lattice contacts (**Table 4.5**),[18, 54-56, 168] implying that it is inherently more flexible than other parts of MoFeP. Combined with this observation, $^{t/o}$Complex-1 and $^{t/o}$Complex-2 structures point to a possible role of αIII mobility in nitrogenase catalysis. Notably, αIII abuts the docking surface of MoFeP for MgADP-bound FeP in DG3 and may lie in the trajectory of FeP moving directionally across the MoFeP surface during ATP hydrolysis.[55] Thus, a dynamic αIII domain could also provide a direct mechanical conduit between FeP and the proximal FeMoco, further linking the timing of nucleotide-dependent FeP-MoFeP interactions to redox transformations at FeMoco.

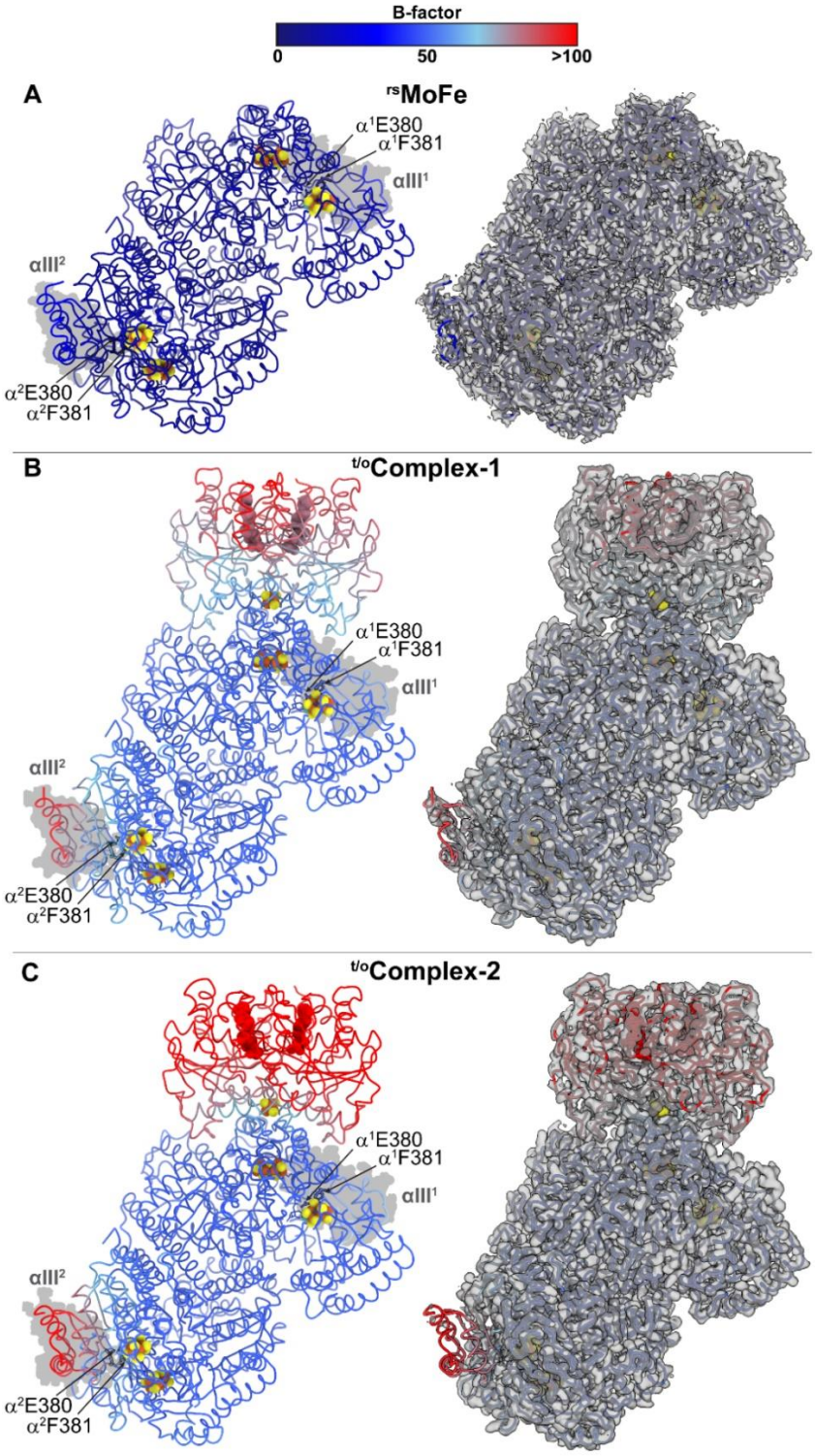


**Figure 4.20** $^{t/o}$Complex-1, and $^{t/o}$Complex-2 colored by B-factor and comparison of αIII density. $^{rs}$MoFeP (a), $^{t/o}$Complex-1 (b), and $^{t/o}$Complex-2 (c) colored by B-factor (left) and comparison of αIII density (right).

**Table 4.5** Average B-factors for the MoFeP components and the αIII domains in various nitrogenase X-ray crystal structures.

| **Structure (resolution / PDB ID)** | **average B for the entire MoFeP component (Å$^2$)** | **average B for αIII (chain A) (Å$^2$)** | **average B for αIII (chain C) (Å$^2$)** |
|---|---|---|---|
| MoFeP with oxidized P-cluster (2.03 Å / 2 MIN) | 24.13 | 34.70 | 34.14 |
| MoFeP at pH 5.0 (2.30 Å / 5VQ4) | 24.65 | 45.58 | 42.73 |
| Ultra-high resolution MoFeP (1.0 Å / 3U7Q) | 10.58 | 11.37 | 13.13 |
| F99YMoFeP with oxidized P-cluster (1.4 Å / 6O7M) | 17.08 | 22.62 | 23.09 |
| Nucleotide-free FeP-MoFeP complex (2.1 Å / 2AFH) | 22.58 | 32.58 | 32.49 |
| MgADP-bound FeP-MoFeP complex - molecule 1 in asymmetric unit (3.1 Å / 2AFI) | 32.42 | 45.70 | 45.67 |
| MgADP-bound FeP-MoFeP complex - molecule 2 in asymmetric unit (3.1 Å / 2AFI)) | 33.44 | 46.89 | 46.53 |
| MgAMPPCP/MgADP-bound FeP-MoFeP complex (1.9 Å / 4WZA) | 23.93 | 37.40 | 31.48 |
| MgAMPPCP-bound FeP-MoFeP complex (2.3 Å / 4WZB) | 27.35 | 45.01 | 37.91 |
| Crosslinked FeP-MoFeP complex (3.2 Å / 1M1Y) | 52.60 | 57.09 | 68.55 |
| MgADP.$AlF_x$ -stabilized MoFeP-FeP complex – molecule 1 in asymmetric unit (2.30 Å / 1M34) | 33.45 | 44.61 | 48.94 |
| MgADP.$AlF_x$ -stabilized MoFeP-FeP complex – molecule 2 in asymmetric unit (2.30 Å / 1M34) | 33.55 | 44.62 | 49.50 |

### 4.4 Conclusions

In conclusion, the cryoEM structures of FeP-MoFeP complexes formed during catalysis reveal that MoFeP is highly dynamic, opposing the existing view of its structural rigidity derived from crystallographic studies. ATP-driven asymmetry and directionality in FeP and MoFeP interactions emerge as pervasive elements in nitrogenase function, which may be critical for the timing of successive electron and proton transfers to FeMoco optimize $N_2$ reduction and avoid unproductive $H_2$ evolution. Importantly, under turnover conditions, MoFeP displays several unforeseen structural features such as conformational changes in specific residues near FeMoco (**Fig. 4.11d,e**), mobility in Mo ligands (**Fig. 4.19**) and increased αIII domain motions (**Fig. 4.20**), which are correlated with the nucleotide-state of a distally-bound FeP and can reasonably be linked to redox gating and catalytic events. Based on the available structures, it is not obvious how FeP-MoFeP interactions induce these conformational changes over a distance of ≥80 Å or which states of the MoFeP cycle (i.e., $E_0$-$E_8$) the observed nitrogenase complexes correspond to. It is safe to assume, however, that all copies of FeMoco in these complexes represent the more stable or longer-lived of all catalytic intermediates present in the turnover solution. The density maps for the proximal FeMocos are essentially identical to those for the resting-state cofactors (**Fig. 4.19**). Thus, an assignment of $E_0$ for these cofactors is plausible, although $E_1$-$E_4$ are also reasonable as these states have been proposed as hydride-bound FeMoco intermediates,[84, 173] which may be structurally indistinguishable from $E_0$ at the current cryoEM resolution of 2.4 Å. At the same time, the obvious deviations between the densities of distal and proximal FeMocos suggest that the distal cofactors in $^{t/o}$Complex-1 and $^{t/o}$Complex-2 represent an $E_x$ state or a mixture of $E_x$ states that are different and likely more advanced in the catalytic cycle (i.e., ≥$E_1$) than the proximal FeMocos, and involve the participation of the Mo center. In light of the asymmetry between the FeMocos in the two αβ-halves, it is tempting to propose a "ping-pong"-like mechanism in which the cofactors proceed through each of the eight catalytic steps in an alternating fashion. This scenario would assign a dual role to FeP: (1) to deliver an electron to one αβ-subunit of MoFeP and (2) to suppress FeP binding to the opposite αβ-subunit while

priming it for catalytic transformations through long-distance activation of electron, $H^+$ and/or substrate access pathways to the distal FeMoco. Although the examination of such a mechanism will require future studies, our current work illustrates that it is finally possible to characterize *bona fide* intermediates of nitrogenase catalysis at near-atomic resolution via cryoEM, which represents a critical step toward understanding the mechanism of this enigmatic enzyme in full structural detail.

## 4.5 Future directions

### 4.5.1 CryoEM of the nitrogenase complex under turnover with non-natural substrates

The structures of the nitrogenase complex during catalytic turnover presented in Section 4.3. have provided many insights into the mechanism of $N_2$ reduction, but many questions remain regarding the binding mode of $N_2$ to the active site, FeMoco. In crystallography, the wavelength of the X-ray used for data collection can be chosen to help identify the type of atom by choosing an energy slightly higher than the K-edge of the element of interest. There is not an analogous method to determine atom identity in cryoEM, which makes assigning ambiguous density and thus the potential site of $N_2$ binding to FeMoco difficult. To better identify the site of substrate binding, cryoEM structures of the nitrogenase complex under turnover with alternative, triatomic substrates will be determined. To this end, I have prepared cryoEM samples of nitrogenase under high electron-flux turnover with the alternative substrates and inhibitors of $N_2$ reduction: azide ($N_3^-$) and thiocyanate ($SCN^-$). Because these substrates are triatomic, the Coulombic density maps may provide unambiguous density demonstrating their binding modes to FeMoco during catalysis, which may be relevant to $N_2$ reduction. These samples will be further characterized by other students in the lab.

### 4.5.2 Investigating the nitrogenase complex during low electron-flux $N_2$ catalytic turnover with cryoEM

As shown in the MoFeP cycle of the TL model (**Fig 1.4b**), MoFeP populates many states during catalysis. Nitrogenase catalysis under low electron-flux conditions (such as low FeP:MoFeP ratio) favors

population of earlier $E_n$ states. To this end, I have conducted preliminary cryoEM characterization of the nitrogenase complex during turnover under high salt conditions (75 mM) yielding a structure of 1:1 FeP:MoFeP stoichiometry at ~2.7 Å resolution. FeP-MoFeP association is mediated by many electrostatic interactions between the proteins, and increasing the salt concentration effectively increases the FeP dissociation constant, giving rise to a low electron-flux system. Interestingly, FeMoco in $\alpha^1$ has a displaced Fe-atom that is flipped out of the cluster and is stabilized by the backbone amidate of $\alpha^2$His442 (**Fig 4.21**). In contrast, Fe5 in the $\alpha^2$ FeMoco is in the typical position. However, more data needs to be collected at low flux to unambiguously model these atypical FeMoco density and to verify that this conformation is mechanistically relevant.

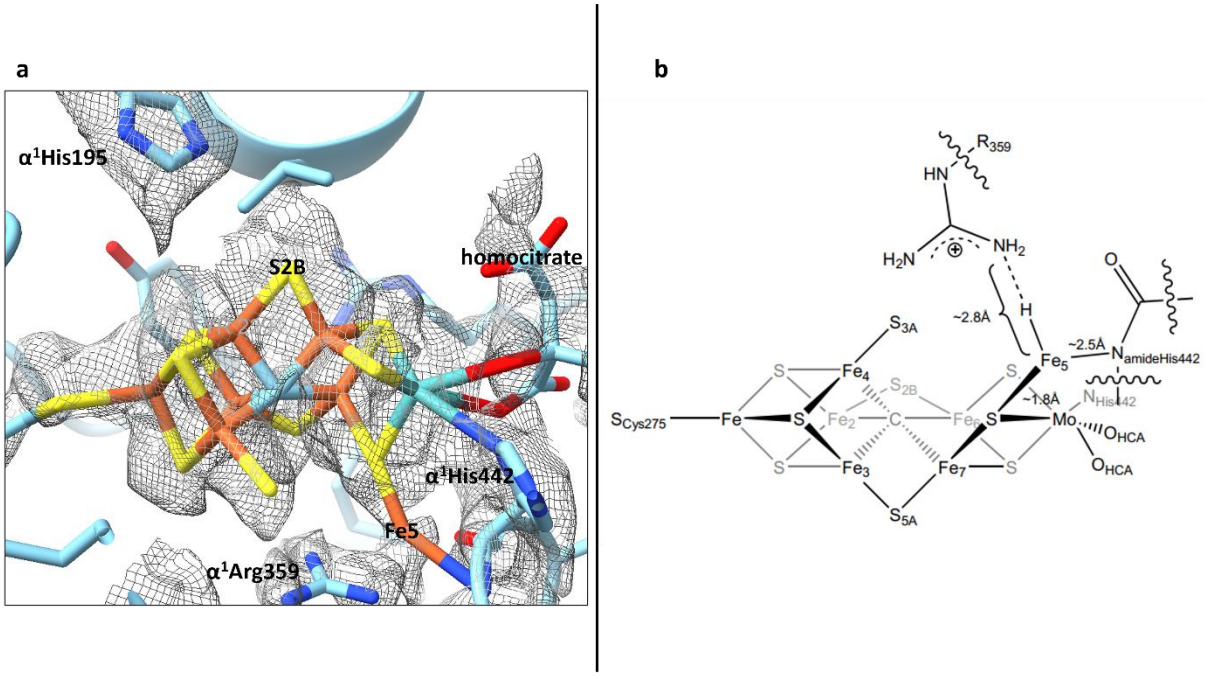


**Figure 4.21** Low electron flux (i.e., high salt) turnover cryoEM structure of $\alpha^1$ FeMoco. (a) Structural model shows Fe5 flipped out of FeMoco, breaking the bonds to the central carbide and belt sulfide S3A. Fe5 is stabilized by $\alpha^1$Arg359 and the backbone amidate of $\alpha^1$His442. (b) Cartoon of non-resting-state FeMoco.

## 4.6 Materials and methods

### 4.6.1 Protein expression and purification

Wild-type, untagged FeP and MoFeP were expressed in their native organism, *Azotobacter vinelandii* (*Av*) cells (strain DJ) using previously established protocols [97]. Briefly, *Av* cultures were grown aerobically in Burk's media (181 mM sucrose, 0.9 mM $CaCl_2$, 1.7 mM $MgSO_4$, 35 μM $FeSO_4$, 2 μM $Na_2Mo_2O_4$, 0.2 mM citric acid, 10 mM $K_3PO_4$ pH 7.5, 3 mM $NH_4Cl$) in a 60 L fermenter at 30°C, 200 rpm. Cells were harvested and pelleted ~4 h after derepression of nitrogenase, as indicated by a spike in dissolved oxygen content. Cell pellets were stored at −80 °C until purification.

Cell lysis and protein purification were carried out under ultrahigh-purity Ar on a Schlenk line, or under a 95% Ar/5% $H_2$ mixture in a Coy Lab anaerobic chamber using previously established protocols [97]. All buffers used were purged of air and stored under Ar. Cell pellets were resuspended in ~200 mL equilibration buffer (50 mM Tris pH 7.75, 200 mM NaCl, 5 mM sodium dithionite (NaDT), 0.1 mg/mL DNase I) prior to lysis with a microfluidizer at 16,000 psi Ar. The lysate was centrifuged at 12,000 rpm for 75 min. Both nitrogenase component proteins were purified from the supernatant by separation on a DEAE Sepharose column with a NaCl gradient (200 to 500 mM NaCl in 50 mM Tris pH 7.75, 5 mM NaDT). MoFeP eluted at ~25 mS/cm, and FeP eluted at ~30 mS/cm. Fractions containing nitrogenase proteins were brown in color and were verified by sodium dodecyl sulfate polyacrylamide gel electrophoresis (SDS-PAGE). Fractions containing FeP or MoFeP proteins were pooled and diluted two-fold with salt-free buffer (50 mM Tris, pH 7.75), then concentrated using a second, smaller DEAE Sepharose column by eluting with high salt buffer (500 mM NaCl, 50 mM Tris, pH 7.75, 5 mM NaDT). MoFeP and FeP were further purified with a Sepharose 200 gel filtration column (500 mM NaCl, 50 mM Tris, pH 8.0, 5 mM NaDT). Fractions containing pure protein were identified with SDS-PAGE. Purified protein was concentrated using an Amicon concentrator at 20 psi 95% Ar/5% $H_2$ using a 30 kDa and 100 kDa cutoff membrane for FeP and MoFeP, respectively. Purified proteins were syringe filtered through a 0.2 μm filter membrane. Protein concentrations were determined using Bradford assay and verified with

an Fe chelation assay (6.2 M guanidine-HCl, 2 mM 2,2'-bipyridine, 10% glacial acetic acid) by measuring absorption at 522 nm and using an extinction coefficient of 8650 $M^{-1}$ $cm^{-1}$, using 4 Fe per FeP and 30 Fe per MoFeP in stoichiometric calculations. Purified proteins were determined to be fully active for $C_2H_2$ and $N_2$ reduction assays that were performed as previously described [97]. Purified proteins were stored under liquid $N_2$ and underwent only one freeze-thaw cycle before use.

### 4.6.2 Sample preparation for EM analysis

All EM samples were prepared under ultra-high-purity $N_2$. FeP and MoFeP were buffer exchanged into reaction buffer (20 mM Tris, pH 8.0, 25 mM NaCl, anaerobic) and concentrated using 30 kDa and 100 kDa Microcon centrifugal filters, respectively. Protein concentrations were measured using an Fe chelation assay. All EM samples contained a final concentration of 6 μM MoFeP, 60 μM FeP (except for the MoFeP control sample, which did not contain FeP), 5 mM $MgCl_2$, 5 mM $Na_2ATP$, 5 mM NaDT, 20 mM Tris, pH 8.0, and 25 mM NaCl. All reaction component stock solutions were made, degassed, and syringe filtered (0.2 μm filter) immediately prior to use. In addition, the $BeF_x$-inhibited sample contained 25 mM NaF and 5 mM $BeSO_4$. Proteins were transferred into sealed reaction vials using Hamilton gas-tight syringes after reaction components had been mixed. Catalysis was initiated in the turnover and $BeF_x$-inhibited sample by addition of FeP after all other components had been mixed. 10 μL of each EM sample was transferred to a 200 μL thin-wall tube under nitrogen and immediately flash frozen in liquid nitrogen 15 seconds after reaction was initiated (or after last component was added in the case of MoFeP control). Flash frozen EM samples were stored under liquid $N_2$ until grid preparation.

All samples were prepared on UltraAuFoil 1.2/1.3, 300 mesh grids that had been freshly plasma-cleaned using a Gatan Solarus II plasma cleaner (10 s, 15 Watts, 75% Ar/25% $O_2$ atmosphere). To minimize exposure to air and reaction time between thawing frozen samples and freezing grids, all grids were prepared using a custom manual plunge freezer designed by the Herzik Lab located in a humidified ($\geq$95% relative humidity) cold room (4 ˚C). Immediately after thawing, 3 μL of the sample was applied to the grid surface followed by manual blotting for ~5 to 6 s using Whatman No. 1 filter paper before

vitrifying in an 50% ethane/ 50% propane liquid mixture cooled by liquid $N_2$.[174] The time that each sample spent outside of liquid $N_2$ was less than 15 sec. Grids were stored under liquid $N_2$ until data collection.

### 4.6.3 EM data acquisition and image processing

**$^{rs}$MoFeP:** Data acquisition for the free MoFeP ($^{rs}$MoFeP) was carried out at UCSD's CryoEM Facility on a Titan Krios G3 (Thermo Fisher Scientific) operating at 300 keV equipped with a Gatan BioContinuum energy filter. Images were collected at a magnification of 165,000x in EF-TEM mode (0.815 Å calibrated pixel size) on a Gatan K2 detector using a 20-eV slit width and a cumulative electron exposure of ~65 electrons/Å$^2$ (50 frames). Data were collected automatically using EPU with aberration free image shift using a defocus range of -0.5 – -2.5 µm. Motion correction was performed using the MotionCor2 frame alignment program implemented within RELION [175] 4.0-beta1 using 7x7 tiled frames with a B-factor of 250. Dose-weighted images were used for preliminary processing and CTF estimation using CTFFind4 within RELION (1024-pixel box size, 0.1 amplitude contrast, 30 Å minimum resolution, 3 Å maximum resolution).[175, 176] Aligned images with a CTF-estimated resolution below 5 Å or with a cumulative total motion exceeding 60 Å were excluded. For free MoFeP, initial particle picks were obtained using cryoSPARC Live's blob picker (50 – 120 Å circular and elliptical blobs) and an *ab initio* model was generated using optimal 2-D classes.[177] This initial model was then used to generate 2-D templates for automated template-based particle picking using RELION 4.0-beta2.[175] A total of (1,527,385+1,508,038) particle picks were extracted from (1,587+2,337) micrographs collected across two different sessions from two different grids, downsampled 4 x 4 (3.26 Å/pixel, 64 pixel box size) and subjected to iterative rounds of reference-free 2-D classification (100 classes, tau_fudge=1, VDAM, ignore first CTF peak, 140 Å mask). Particles were subjected to four iterative rounds of 2-D classification and those 2-D class averages containing the strongest secondary structural details were isolated (1,497,616 particles in total) for 3-D auto-refinement using $C_1$ symmetry.[178] Each session was then processed in parallel. The refined coordinates were used to re-center and re-extract particles unbinned

(0.815 Å/pixel, 384 pixel box size). These particles were refined against a scaled version of the previously refined map followed by CTF refinement (per-particle defocus UV, per-micrograph astigmatism, anti-symmetrical and symmetrical higher-order aberrations). Following an iterative rounds of 3-D and CTF refinement, particles were subjected to RELION's Bayesian particle polishing using parameters trained against the data (--s_vel 1.52100 --s_div 15030.00000 --s_acc 2.35500).[175] Following particle polishing, 3-D auto-refinement, and CTF-refinement, a 2.12 Å structure was obtained. These particles were then subjected to a no-alignment 3-D classification (8 classes, tau_fudge=2) and the best classes (167,110 and 214,991 particles) were selected for iterative rounds of 3-D and CTF refinement followed by particle polishing using the same parameters but 512-pixel extraction box size. Both sessions were then combined and a 3-D auto-refinement led to a to ~2.01 Å refinement. Another round of no-alignment 3-D classification was performed (6 classes, tau_fudge=8) and particles comprising the highest-quality classes (177,123 particles) were combined 3-D auto-refined and then imported into cryoSPARC for a non-uniform refinement using $C_1$ symmetry (1.91 Å resolution) or $C_2$ symmetry (1.81 Å resolution).[177]

**$^{t/o}$Complex-1 and $^{t/o}$Complex-2:** Data for the nitrogenase turnover sample were collected at the $S^2C^2$ Stanford-SLAC CryoEM Center on TEM Gamma (Titan Krios G3i (Thermo Fisher Scientific) equipped with a Gatan K3 direct electron detector) operating at 300 keV. Images were collected at a magnification of 135,000x (0.835 Å/pixel) on a K3 detector with an electron exposure of ~65 electrons/Å$^2$ (66 frames) with a nominal defocus range of -1.2 – -2.0 μm. Motion correction was performed using the MotionCor2 frame alignment program implemented within RELION 4.0-beta1 using 10x14 tiled frames with a B-factor of 250.[175, 176] Dose-weighted images were used for preliminary processing and CTF estimation using CTFFind4 within RELION (1024-pixel box size, 0.1 amplitude contrast, 30 Å minimum resolution, 3 Å maximum resolution).[175, 179] Aligned images with a CTF-estimated resolution below 5 Å or with a cumulative total motion exceeding 60 Å were excluded. The resting state MoFeP structure was used to template pick ~50 movies and the top picks were used to train crYOLO for picking against the entire data set.[180] 19,711,170 picks were obtained from 14,903 micrographs and extracted in RELION

4.0-beta2 downsampled 8 x 8 (6.68 Å/pixel, 64 pixel box size), randomly split into ~1M particle sets, and each subjected to iterative rounds of reference-free 2-D classification (200 classes, tau_fudge=1, VDAM, ignore first CTF peak, 180 Å mask) where only obvious false classes were eliminated.[175] 11,955,963 particles were then re-centered and re-extracted, downsampled 4 x 4 (3.34 Å/pixel, 96 pixel box size), randomly split into ~1M particle sets and each subjected to iterative rounds of reference-free 2-D classification (200 classes, tau_fudge=1, VDAM, ignore first CTF peak, 180 Å mask) where only obvious false classes were eliminated. 7,708,206 particles from the best classes were combined, randomly split into 10 subsets, and subjected to another round of 2-D classification. The best nitrogenase classes were then set aside and the remaining classes were re-ran through 2-D classification. The best nitrogenase classes were then combined with the previous run and subjected to 3-D auto-refine. These particles were then re-centered and re-extracted downsampled 4 x 4 (3.34 Å/pixel, 96 pixel box size) with duplicates removed. 4,121,671 particles were imported into cryoSPARC v3.3.2 and subjected to a heterogeneous refinement using four nitrogenase 1:1 classes and one 20S proteasome class (EMDB-8741).[177] The best 1:1 nitrogenase class comprising 2,511,497 particles was then subjected to a 2-class heterogenous refinement using 1:1 nitrogenase and MoFeP volumes as initial models. 1:1 complexes and MoFeP particles were then re-ran through this 2-class heterogenous refinement two times before combining all the 1:1 complexes and MoFeP particles separately and subjected to a non-uniform Refinement. These particles were then re-centered and re-extracted in RELION downsampled 2 x 2 (1.67 Å/pixel, 192 pixel box size) with duplicates removed.[175] 906,326 1:1 complex particles were subjected to a non-uniform refinement in cryoSPARC yielding a Nyquist-limited 3.43 Å resolution map with high-quality FeP density. These particles were then subjected to a 3-D variability analysis (two modes, four intermediate clusters, 5 Å low-pass, no overlap).[181] The best 1:1 nitrogenase class was then subjected to another round of non-uniform refinement and 3-D variability analysis (two modes, four intermediate clusters, 5 Å low-pass filter).[181] Each cluster was then independently subjected to non-uniform refinement and the best two classes with FeP density for both subunits were re-centered, re-extracted in RELION without downsampling (0.835 Å/pixel, 384 pixel box size) and 3-D auto-refined followed by Bayesian particle

polishing using parameters trained against the data (--s_vel 0.9225 --s_div 6570.00000 --s_acc 2.65500).[175] These particles were then imported into cryoSPARC for a non-uniform refinement, yielding 2.38 Å and 2.34 Å resolution maps for the ATP-ATP and ATP/ADP-ADP structures, respectively.[177] A soft mask for FeP was then used for a local refinement (4-Å deviation over priors, 4-degree search, 4-Å shift search) yielding 2.75 Å and 3.01 Å maps for the ATP-ATP and ATP/ADP-ADP structures, respectively. The composite half maps from each independent half set from full and locally refined were assembled (maximum voxel value) and subjected to deepEMhancer[182] (high-resolution model; version 0.13). The FSC estimated resolution for the composite maps 2.28 Å and 2.29 Å ATP-ATP and ATP/ADP-ADP structures, respectively.

**BeFx-trapped nitrogenase complex:** Data for the $BeF_x$-trapped complex were collected at UCSD's CryoEM Facility on a Titan Krios G3 (Thermo Fisher Scientific) operating at 300 keV equipped with a Gatan BioContinuum energy filter. Images were collected at a magnification of 165,000x in EF-TEM mode (0.815 Å calibrated pixel size) on a Gatan K2 detector using a 20-eV slit width and a cumulative electron exposure of ~65 electrons/$Å^2$ (50 frames). Data were collected automatically using EPU with aberration free image shift using a defocus range of -0.5 – -2.5 µm. 4 separate data sets were collected using 0˚, 15˚ or 25˚ specimen tilt. Motion correction was performed using the MotionCor2 frame alignment program implemented within RELION 4.0-beta1 using 7x7 tiled frames with a B-factor of 250.[176] Dose-weighted images were used for preliminary processing and CTF estimation using CTFFind4 within RELION (1024-pixel box size, 0.1 amplitude contrast, 30 Å minimum resolution, 3 Å maximum resolution).[175] Aligned images with a CTF-estimated resolution below 5 Å or with a cumulative total motion exceeding 60 Å were excluded. Initial particle picks were obtained using RELION's template picker using free MoFeP as a template.[175] A total of (271,261+165,767+349+541+330,486) particle picks were extracted from (2,085+1,718+2,211+2,099) micrographs collected across four different sessions from two different grids, downsampled 8 x 8 (6.52 Å/pixel, 48 pixel box size). Each data set was subjected to two rounds of reference-free 2-D classification (50 classes, tau_fudge=1,

VDAM, ignore first CTF peak, 220 Å mask). Particles from 2-D class averages containing the strongest secondary structural details (148,743+95,336+163,920+91,161 particles) were combined and subjected to another round of 2-D classification (50 classes, tau_fudge=1, VDAM, ignore first CTF peak, 220 Å mask). 424,249 particles were 3-D auto-refined ($C_1$ symmetry), re-centered and re-extracted (removing duplicates) without downsampling (0.815 Å/pixel, 384 pixel box size). The particles were then 3-D auto-refined and subjected to Bayesian particle polishing using parameters determined from the free MoFeP data set. These particles then underwent 3-D auto-refinement, CTF refinement (defocus UVA and aberrations), and a 3-D auto-refinement before a no-alignment 3-D classification (8 classes, tau_fudge=8). The best classes (397,392 particles) were then refined followed by local FeP masked 3-D classification (8 classes, tau_fudge=2). 2:1 complex particles were separated and 3-D refined followed by a subsequent no-alignment 3-D classification (4 classes, tau_fudge=24). The three best classes, representing 72,125 particles, were then subjected to 3-D autorefinement, CTF refinement, and a 3-D auto-refinement particles were subjected to Bayesian particle polishing using parameters determined from this data set (--s_vel 1.3275 --s_div 5955.00000 --s_acc 1.63500). A final series of 3-D auto-refinement, CTF refinement, and 3-D auto-refinement yielded a 2.40 Å resolution structure for the 2:1 $BeF_x$-trapped FeP:MoFeP complex.

Local resolution estimates were performed using cryoSPARC.[177] 3-D FSC calculations were performed using the 3-DFSC server. Visualization was performed using UCSF's Chimera and ChimeraX. Particle meta data manipulation was performed using csparc2star.py and in-house developed Python scripts.

### 4.7 Acknowledgements

We thank K. Corbett, S. Narehood, J. Figueroa, and R. Subramanian for critical discussions, and members of the Tezcan and Herzik Labs for their assistance. Molecular graphics and analyses were performed with UCSF ChimeraX, developed by the Resource for Biocomputing, Visualization, and Informatics at the University of California, San Francisco, with support from National Institutes of Health

grant R01-GM129325 and the Office of Cyber Infrastructure and Computational Biology, National Institute of Allergy and Infectious Diseases. We also think members of UCSD's CryoEM facility, the Stanford-Slac Cryo-EM Center ($S^2C^2$), and UCSD's Physics Computing Facility for help in data collection, data processing, and computational support. I would like to thank Prof. M. Herzik for collaborating with me on this project and Dr. R. Subramanian for helpful discussions.

Chapter 4 is reproduced, in part, with permission from H. Rutledge, B. Cook, H. Nguyen, M. Herzik, and F. A. Tezcan. CryoEM structures of the nitrogenase complex during catalytic turnover. The dissertation author is the primary author on all reprinted materials.

## Chapter 5: Conclusions

### 5.1 Introduction

Biological nitrogen fixation is arguably one of the most essential and complex catalytic tasks carried out in the biosphere. The enzyme that carries out this reaction, nitrogenase, is extremely dynamic and utilizes unique proteins and superclusters to accomplish binding, activating, and reduction of the incredibly stable and kinetically inert $N_2$ triple bond (:N≡N:). Despite extensive studies over the course of many decades, much of the catalytic mechanism has remained enigmatic. Key questions that remain regarding the enzyme include: How do the unique metalloclusters (P-cluster and FeMoco) function, and why are they needed for $N_2$ reduction? How are ATP hydrolysis, and by extension FeP—MoFeP interactions, coupled to ET and catalysis? Significant research efforts have gone into understanding the mechanism using a variety of methods including spectroscopies, X-ray crystallography, and ATP-independent systems (i.e. light-activated reduction and electrochemical reduction of MoFeP).[8, 84, 183] In this work, I have contributed to the current understanding of the nitrogenase mechanism by probing the catalytically-relevant dynamics of Mo-nitrogenase in the context of (1) small (Å-scale), redox-mediated conformational changes of the P-cluster, and (2) larger (nm-scale) dynamics of the entire nitrogenase complex during catalysis.

### 5.2 Redox-mediated dynamics and stabilization of the nitrogenase P-cluster

Initial redox-dependent conformational changes of the P-cluster were discovered via X-ray crystallography of the nitrogenase MoFeP from *Av*. Upon two-electron oxidation to $P^{OX}$, one of the cubanes opens as two of the Fe-centers become coordinated to the backbone amidate of bridging αCys88 and to the serinate from βSer188 (**Fig 2.1**).[21] However, the necessity of the serinate ligation was called into question at the time due to the variance of residues that occur at position β188 (Ala commonly resides in this position, which cannot coordinate an Fe-center) (**Table 2.1**). Furthermore, mutagenesis of *Av* βSer188 to Gly did not completely abolish nitrogenase activity.[184] Owens et al. structurally

characterized MoFeP from an organism lacking βSer188, *Gd*, and discovered that βTyr99 performed a similar role, ligating an Fe-center of the P-cluster in $P^{OX}$. Further analysis revealed that the Ser and Tyr residues were covariant (**Table 2.1**), renewing interest in the redox-switchable coordination of the P-cluster by a hard, O-based ligand.

I investigated the role of *Av* βSer188 by generating, purifying, and characterizing three *Av* MoFeP mutants in which there was (1) no oxygenic ligand (βSer188Ala), (2) only Tyr (βPhe99Tyr/βSer188Ala), and (3) both Ser and Tyr (βPhe99Tyr). These studies revealed that in the absence of the oxygenic ligand, the P-cluster became compositionally labile upon oxidation, reversibly losing two Fe-centers. Furthermore, swapping the Ser ligand for Tyr in the *Av* βPhe99Tyr/βSer188Ala mutant resulted in redox-instability, unlike *Gd* which natively contains βTyr99, suggesting that structural control of these ligands must extend past the primary and secondary coordination spheres of the P-cluster. Surprisingly, these mutants retained wt levels of *in vitro* $N_2$ reduction activity (**Fig 2.13b**) and diazotrophic growth rates using standard growth medium (**Fig 2.14**).[97]

The redox-labile βSer188Ala P-cluster was reminiscent of coordinatively unsaturated [4Fe-4S] clusters that naturally occur in many proteins and are also prone to oxidative damage.[100, 105, 120-122] Upon oxidation, the clusters lose one Fe-center and reversibly convert from a [4Fe-4S] cluster to a [3Fe-4S] cluster.[120, 122, 124-128] Furthermore, these clusters can be demetallated *in vivo* when the cellular LIP is low,[129] and they can be heterometallated *in vitro*. [120, 130-135] Thus, I hypothesized that the stabilizing role of the oxygenic ligand (βSer188 in *Av* MoFeP) protect the P-cluster during from oxidative damage and mismetallation, which would not have been evident under the ideal, Fe-replete conditions previously used. To this end, I measured *Av* βSer188Ala's cell survival after oxidative stress, growth rate under Fe-limiting conditions, and ability to become heterometallated. I investigated the role of βSer188 in protecting the *Av* nitrogenase P-cluster *in vivo* and observed that *Av* βSer188Ala was more prone to environmental duress (oxidative stress and Fe-limitation) than wt *Av*. I also probed the ability of βSer188 to protect the P-cluster from heterometallation *in vitro*¸ finding that the oxidized βSer188Ala P-cluster

can be reconstituted with various metals, unlike wt. Taken together, these results established a new functional role of serine (and possibly tyrosine) residues in protecting Fe-S clusters from oxidative stress and mismetallation.

### 5.3 Dynamics of the nitrogenase complex during catalytic reduction of $N_2$

X-tray crystallography has provided valuable structures of the nitrogenase proteins, elucidating the structure of their metalloclusters and the path of electron flow (**Fig 1.2**). Furthermore, published crystal structures have demonstrated that the clusters themselves are very dynamic (**Fig 2.1, 2.2, 4.1-4.4**), and that FeP-MoFeP interactions are nucleotide-dependent (**Fig 1.5**). However, the static nature of crystallography has prevented the determination of any structures of the nitrogenase complex *during* catalysis, providing only resting-state, inhibitor-bound, or post-catalytic states of nitrogenase. Furthermore, spectroscopic studies of nitrogenase during catalysis has been limited to EPR-active redox states which are hard to obtain in homogeneity, leaving an incomplete picture of electronic states of the active-site.

To overcome these obstacles, I structurally characterized the nitrogenase complex *during catalytic $N_2$ reduction* with cryoEM at high-resolution. These structures represent the first (1) structurally characterized nitrogenase complex during turnover, (2) ATP-bound wt FeP, and (2) structures of the nitrogenase complex not limited by the intrinsic static nature of crystallography. I structurally characterized two states of the nitrogenase complex during catalysis (2.4 Å), one structure of free, resting-state MoFeP (1.8 Å), and the structures of the $BeF_3^-$-inhibited complex during $N_2$ reduction (2.4 Å) (**Fig 4.5**).

The following observations of turnover structures were of particular interest: (1) the structures are 1:1 FeP:MoFeP stoichiometry, (2) the complexes are in DG2, (3) density of the terminal ATP phosphate group is weaker in the $\gamma^1$ subunit than the $\gamma^2$ subunit, and (4) there are asymmetric structural changes in MoFeP. Taken together, these results suggested negative cooperativity (such that binding of one FeP to

MoFeP prevents binding of a second FeP) is a mechanistic imperative, requiring reevaluation of the long-standing assumption that each half of the nitrogenase complex operates independently.[185, 186] Negative cooperativity has been previously postulated, in corroboration with these results.[163] Further, they implied that the rate-limiting step of biological $N_2$ reduction is en route to DG3. The rate-limiting step has been controversial in the literature whereby it could either be release of $P_i$ from FeP or dissociation of FeP from MoFeP.[76, 87, 187, 188] These structures were in DG2, suggesting that the rate-limiting step *is not* dissociation of FeP from MoFeP in DG3, but rather resides along the pathway from DG2 to DG3. Lastly, the observation of asymmetric amino acid conformations around the $\alpha^1$ and $\alpha^2$ FeMocos indicated that FeP binding to one half of MoFeP transduces conformational changes over large (> 100 Å) distances. I hypothesize that these features of biological $N_2$ reduction function to slow down catalysis, serving as a kinetic control to limit diversion of electrons to $H^+$ reduction, as previously predicted.[77] Such a mechanistic imperative explain why nitrogenase evolved to be such a complex, dynamic, and slow enzyme.

**References**


1. Smith, B. E., Nitrogenase reveals its inner secrets. *Science* **2002,** *297* (5587), 1654-1655.

2. Smil, V., Global population and the nitrogen cycle. *Scientific American* **1997,** *277* (1), 76-81.

3. Simpson, F. B.; Burris, R. H., A nitrogen pressure of 50 atmospheres does not prevent evolution of hydrogen by nitrogenase. *Science* **1984,** *224* (4653), 1095-7.

4. Winter, H. C.; Burris, R. H., Stoichiometry of the adenosine triphosphate requirement for $N_2$ fixation and $H_2$ evolution by a partially purified preparation of *Clostridium pasteurianum*. *Journal of Biological Chemistry* **1968,** *243* (5), 940-4.

5. Kennedy, I. R.; Morris, J. A.; Mortenson, L. E., $N_2$ fixation by purified components of the $N_2$-fixing system of *Clostridium pasteurianum*. *Biochimica et Biophysica Acta* **1968,** *153* (4), 777-86.

6. Hadfield, K. L.; Bulen, W. A., Adenosine triphosphate requirement of nitrogenase from *Azotobacter vinelandii*. *Biochemistry* **1969,** *8* (12), 5103-8.

7. Watt, G. D.; Bulen, W. A.; Burns, A.; Hadfield, K. L., Stoichiometry, ATP/2e values, and energy requirements for reactions catalyzed by nitrogenase from *Azotobacter vinelandii*. *Biochemistry* **1975,** *14* (19), 4266-72.

8. Rutledge, H. L.; Tezcan, F. A., Electron Transfer in Nitrogenase. *Chemical Reviews* **2020,** *120* (12), 5158-5193.

9. Eady, R. R., Structure-Function Relationships of Alternative Nitrogenases. *Chemical Reviews* **1996,** *96* (7), 3013-3030.

10. Einsle, O.; Rees, D. C., Structural Enzymology of Nitrogenase Enzymes. *Chemical Reviews* **2020,** *120* (12), 4969-5004.

11. Eady, R. R., Current status of structure function relationships of vanadium nitrogenase. *Coord. Chem. Rev.* **2003,** *237* (1-2), 23-30.

12. Harris, D. F.; Lukoyanov, D. A.; Shaw, S.; Compton, P.; Tokmina-Lukaszewska, M.; Bothner, B.; Kelleher, N.; Dean, D. R.; Hoffman, B. M.; Seefeldt, L. C., Mechanism of $N_2$ Reduction Catalyzed by Fe-Nitrogenase Involves Reductive Elimination of $H_2$. *Biochemistry* **2018,** *57* (5), 701-710.

13. Hales, B. J., Vanadium Nitrogenase. In *Catalysts for Nitrogen Fixation: Origins, Applications, and Research Progress*, Smith, B. E.; Richards, R. L.; Newton, W. E., Eds. Springer, Dordrecht: 2004; Vol. 1.

14. Schneider, K.; Müller, A., Iron-Only Nitrogenase: Exceptional Catalytic, Structural and Spectroscopic Features. In *Catalysts for Nitrogen Fixation: Nitrogenases, Relevant Chemical Models and Commercial Processes*, Smith, B. E.; Richards, R. L.; Newton, W. E., Eds. Springer Netherlands: Dordrecht, 2004; pp 281-307.

15. Georgiadis, M. M.; Komiya, H.; Chakrabarti, P.; Woo, D.; Kornuc, J. J.; Rees, D. C., Crystallographic structure of the nitrogenase iron protein from *Azotobacter vinelandii*. *Science* **1992,** *257* (5077), 1653-9.

16. Raymond, J.; Siefert, J. L.; Staples, C. R.; Blankenship, R. E., The natural history of nitrogen fixation. *Molecular Biology and Evolution* **2004,** *21* (3), 541-54.

17. Kim, J.; Rees, D. C., Crystallographic structure and functional implications of the nitrogenase molybdenum-iron protein from *Azotobacter vinelandii*. *Nature* **1992,** *360* (6404), 553-60.

18. Einsle, O.; Tezcan, F. A.; Andrade, S. L. A.; Schmid, B.; Yoshida, M.; Howard, J. B.; Rees, D. C., Nitrogenase MoFe-protein at 1.16 angstrom resolution: A central ligand in the FeMo-cofactor. *Science* **2002,** *297* (5587), 1696-1700.

19. Spatzal, T.; Aksoyoglu, M.; Zhang, L. M.; Andrade, S. L. A.; Schleicher, E.; Weber, S.; Rees, D. C.; Einsle, O., Evidence for Interstitial Carbon in Nitrogenase FeMo Cofactor. *Science* **2011,** *334* (6058), 940-940.

20. Lancaster, K. M.; Roemelt, M.; Ettenhuber, P.; Hu, Y. L.; Ribbe, M. W.; Neese, F.; Bergmann, U.; DeBeer, S., X-ray Emission Spectroscopy Evidences a Central Carbon in the Nitrogenase Iron-Molybdenum Cofactor. *Science* **2011,** *334* (6058), 974-977.

21. Peters, J. W.; Stowell, M. H.; Soltis, S. M.; Finnegan, M. G.; Johnson, M. K.; Rees, D. C., Redox-dependent structural changes in the nitrogenase P-cluster. *Biochemistry* **1997,** *36* (6), 1181-7.

22. Jasniewski, A. J.; Sickerman, N. S.; Hu, Y.; Ribbe, M. W., The Fe Protein: An Unsung Hero of Nitrogenase. *Inorganics* **2018,** *6* (1), 25.

23. Howard, J. B.; Rees, D. C., Structural basis of biological nitrogen fixation. *Chemical Reviews* **1996,** *96* (7), 2965-2982.

24. Walker, J. E.; Saraste, M.; Runswick, M. J.; Gay, N. J., Distantly related sequences in the alpha- and beta-subunits of ATP synthase, myosin, kinases and other ATP-requiring enzymes and a common nucleotide binding fold. *The EMBO Journal* **1982,** *1* (8), 945-951.

25. Saraste, M.; Sibbald, P. R.; Wittinghofer, A., The P-loop — a common motif in ATP- and GTP-binding proteins. *Trends in Biochemical Sciences* **1990,** *15* (11), 430-434.

26. Ryle, M. J.; Seefeldt, L. C., Elucidation of a MgATP signal transduction pathway in the nitrogenase iron protein: formation of a conformation resembling the MgATP-bound state by protein engineering. *Biochemistry* **1996,** *35* (15), 4766-75.

27. Jang, S. B.; Seefeldt, L. C.; Peters, J. W., Insights into nucleotide signal transduction in nitrogenase: structure of an iron protein with MgADP bound. *Biochemistry* **2000,** *39* (48), 14745-52.

28. Walker, G. A.; Mortenson, L. E., An effect of magnesium adenosine 5'-triphosphate on the structure of azoferredoxin from *Clostridium pasteurianum*. *Biochemical and Biophysical Research Communications* **1973,** *53* (3), 904-9.

29. Walker, G. A.; Mortenson, L. E., Effect of magnesium adenosine 5'-triphosphate on the accessibility of the iron of clostridial azoferredoxin, a component of nitrogenase. *Biochemistry* **1974,** *13* (11), 2382-2388.

30. Lanzilotta, W. N.; Ryle, M. J.; Seefeldt, L. C., Nucleotide hydrolysis and protein conformational changes in *Azotobacter vinelandii* nitrogenase iron protein: defining the function of aspartate 129. *Biochemistry* **1995,** *34* (34), 10713-23.

31. Ljones, T.; Burris, R. H., Nitrogenase: the reaction between the Fe protein and bathophenanthrolinedisulfonate as a probe for interactions with MgATP. *Biochemistry* **1978,** *17* (10), 1866-72.

32. Deits, T. L.; Howard, J. B., Kinetics of MgATP-dependent iron chelation from the Fe-protein of the *Azotobacter vinelandii* nitrogenase complex. *Journal of Biological Chemistry* **1989,** *264* (12), 6619-28.

33. Mortenson, L. E.; Walker, M. N.; Walker, G. A. In *Effect of Magnesium Di- and Triphosphates on the Structure and Electron Transport Function of the Components of Clostridial Nitrogenase*, Proceedings of the 1st International Symposium on Nitrogen Fixation, Newton, W. E.; Nyman, C. J., Eds. Washington State University Press, Pullman: 1975; p 117.

34. Buckel, W.; Hetzel, M.; Kim, J., ATP-driven electron transfer in enzymatic radical reactions. *Current Opinion in Chemical Biology* **2004,** *8* (5), 462-7.

35. Kim, J.; Hetzel, M.; Boiangiu, C. D.; Buckel, W., Dehydration of (*R*)-2-hydroxyacyl-CoA to enoyl-CoA in the fermentation of α-amino acids by anaerobic bacteria. *FEMS Microbiology Reviews* **2004,** *28* (4), 455-68.

36. Hans, M.; Buckel, W.; Bill, E., Spectroscopic evidence for an all-ferrous $[4Fe\text{-}4S]^0$ cluster in the superreduced activator of 2-hydroxyglutaryl-CoA dehydratase from *Acidaminococcus fermentans*. *J Biol Inorg Chem* **2008,** *13* (4), 563-74.

37. Holm, R. H.; Kennepohl, P.; Solomon, E. I., Structural and Functional Aspects of Metal Sites in Biology. *Chemical Reviews* **1996,** *96* (7), 2239-2314.

38. Noodleman, L.; Pique, M. E.; Roberts, V. A., Iron-Sulfur Clusters: Properties and Functions. In *Wiley Encyclopedia of Chemical Biology*, Begley, T., Ed. 2008; pp 1-11.

39. Watt, G. D.; Reddy, K. R. N., Formation of an all Ferrous $Fe_4S_4$ Cluster in the Iron Protein Component of *Azotobacter vinelandii* Nitrogenase. *Journal of Inorganic Biochemistry* **1994,** *53* (4), 281-294.

40. Angove, H. C.; Yoo, S. J.; Burgess, B. K.; Munck, E., Mossbauer and EPR Evidence for an All-Ferrous $Fe_4S_4$ Cluster with S = 4 in the Fe Protein of Nitrogenase. *Journal of the American Chemical Society* **1997,** *119* (37), 8730-8731.

41. Musgrave, K. B.; Angove, H. C.; Burgess, B. K.; Hedman, B.; Hodgson, K. O., All-ferrous titanium(III) citrate reduced Fe protein of nitrogenase: An XAS study of electronic and metrical structure. *Journal of the American Chemical Society* **1998,** *120* (21), 5325-5326.

42. Jacobs, D.; Watt, G. D., Nucleotide-assisted $[Fe_4S_4]$ redox state interconversions of the *Azotobacter vinelandii* Fe protein and their relevance to nitrogenase catalysis. *Biochemistry* **2013,** *52* (28), 4791-9.

43. Strop, P.; Takahara, P. M.; Chiu, H.; Angove, H. C.; Burgess, B. K.; Rees, D. C., Crystal structure of the all-ferrous $[4Fe\text{-}4S]^0$ form of the nitrogenase iron protein from *Azotobacter vinelandii*. *Biochemistry* **2001,** *40* (3), 651-6.

44. Rupnik, K.; Lee, C. C.; Wiig, J. A.; Hu, Y. L.; Ribbe, M. W.; Hales, B. J., Nonenzymatic Synthesis of the P-Cluster in the Nitrogenase MoFe Protein: Evidence of the Involvement of All-Ferrous $[Fe_4S_4]^0$ Intermediates. *Biochemistry* **2014,** *53* (7), 1108-1116.

45. Scott, T. A.; Berlinguette, C. P.; Holm, R. H.; Zhou, H. C., Initial synthesis and structure of an all-ferrous analogue of the fully reduced $[Fe_4S_4]^0$ cluster of the nitrogenase iron protein. *Proc. Natl. Acad. Sci. U. S. A.* **2005,** *102* (28), 9741-9744.

46. Zanello, P., The competition between chemistry and biology in assembling iron-sulfur derivatives. Molecular structures and electrochemistry. Part V. {[$Fe_4S_4$]($S\text{-}_{Cys}$)$_4$} proteins. *Coord. Chem. Rev.* **2017,** *335*, 172-227.

47. Watt, G. D.; Wang, Z.-C.; Knotts, R. R., Redox Reactions of and Nucleotide Binding to the Iron Protein of *Azotobacter vinelandii*. *Biochemistry* **1986,** *25*, 8156-8162.

48. Morgan, T. V.; Prince, R. C.; Mortenson, L. E., Electrochemical titration of the S = 3/2 and S = ½ states of the iron protein of nitrogenase. *FEBS Letters* **1986,** *206* (1), 4-8.

49. Guo, M.; Sulc, F.; Ribbe, M. W.; Farmer, P. J.; Burgess, B. K., Direct assessment of the reduction potential of the $[4Fe\text{-}4S]^{1+/0}$ couple of the Fe protein from *Azotobacter vinelandii*. *Journal of the American Chemical Society* **2002,** *124* (41), 12100-1.

50. Braaksma, A.; Haaker, H.; Grande, H. J.; Veeger, C., The effect of the redox potential on the activity of the nitrogenase and on the Fe-protein of *Azotobacter vinelandii*. *European Journal of Biochemistry* **1982,** *121* (3), 483-91.

51. Lanzilotta, W. N.; Seefeldt, L. C., Changes in the midpoint potentials of the nitrogenase metal centers as a result of iron protein molybdenum-iron protein complex formation. *Biochemistry* **1997,** *36* (42), 12976-12983.

52. Mus, F.; Colman, D. R.; Peters, J. W.; Boyd, E. S., Geobiological feedbacks, oxygen, and the evolution of nitrogenase. *Free Radical Biology and Medicine* **2019,** *140*, 250-259.

53. Kim, J.; Woo, D.; Rees, D. C., X-ray crystal structure of the nitrogenase molybdenum-iron protein from *Clostridium pasteurianum* at 3.0-A resolution. *Biochemistry* **1993,** *32* (28), 7104-15.

54. Schindelin, H.; Kisker, C.; Schlessman, J. L.; Howard, J. B.; Rees, D. C., Structure of ADP·$AlF_4^-$-stabilized nitrogenase complex and its implications for signal transduction. *Nature* **1997,** *387* (6631), 370-6.

55. Tezcan, F. A.; Kaiser, J. T.; Mustafi, D.; Walton, M. Y.; Howard, J. B.; Rees, D. C., Nitrogenase complexes: multiple docking sites for a nucleotide switch protein. *Science* **2005,** *309* (5739), 1377-80.

56. Tezcan, F. A.; Kaiser, J. T.; Howard, J. B.; Rees, D. C., Structural evidence for asymmetrical nucleotide interactions in nitrogenase. *Journal of the American Chemical Society* **2015,** *137* (1), 146-9.

57. Peters, J. W.; Fisher, K.; Newton, W. E.; Dean, D. R., Involvement of the P-cluster in intramolecular electron transfer within the nitrogenase MoFe protein. *Journal of Biological Chemistry* **1995,** *270* (45), 27007-13.

58. Keable, S. M.; Zadvornyy, O. A.; Johnson, L. E.; Ginovska, B.; Rasmussen, A. J.; Danyal, K.; Eilers, B. J.; Prussia, G. A.; LeVan, A. X.; Raugei, S.; Seefeldt, L. C.; Peters, J. W., Structural characterization of the $P^{1+}$ intermediate state of the P-cluster of nitrogenase. *Journal of Biological Chemistry* **2018,** *293* (25), 9629-9635.

59. Owens, C. P.; Katz, F. E.; Carter, C. H.; Oswald, V. F.; Tezcan, F. A., Tyrosine-Coordinated P-Cluster in *G. diazotrophicus* Nitrogenase: Evidence for the Importance of O-Based Ligands in Conformationally Gated Electron Transfer. *Journal of the American Chemical Society* **2016,** *138* (32), 10124-7.

60. Pierik, A. J.; Wassink, H.; Haaker, H.; Hagen, W. R., Redox properties and EPR spectroscopy of the P clusters of *Azotobacter vinelandii* MoFe protein. *European Journal of Biochemistry* **1993,** *212* (1), 51-61.

61. Watt, G. D.; Burns, A.; Lough, S.; Tennent, D. L., Redox and spectroscopic properties of oxidized MoFe protein from *Azotobacter vinelandii*. *Biochemistry* **1980,** *19* (21), 4926-32.

62. Lanzilotta, W. N.; Christiansen, J.; Dean, D. R.; Seefeldt, L. C., Evidence for coupled electron and proton transfer in the [8Fe-7S] cluster of nitrogenase. *Biochemistry* **1998,** *37* (32), 11376-11384.

63. Spatzal, T.; Perez, K. A.; Einsle, O.; Howard, J. B.; Rees, D. C., Ligand binding to the FeMo-cofactor: Structures of CO-bound and reactivated nitrogenase. *Science* **2014,** *345* (6204), 1620-1623.

64. Kang, W.; Lee, C. C.; Jasniewski, A. J.; Ribbe, M. W.; Hu, Y., Structural evidence for a dynamic metallocofactor during N2 reduction by Mo-nitrogenase. *Science* **2020,** *368* (6497), 1381-1385.

65. Wonchull, K.; Chi Chung, L.; Andrew, J. J.; Markus, W. R.; Yilin, H., Response to Comment on "Structural evidence for a dynamic metallocofactor during N2 reduction by Mo-nitrogenase". *Science* **2021,** *371* (6530), eabe5856.

66. John, W. P.; Oliver, E.; Dennis, R. D.; Serena, D.; Brian, M. H.; Patrick, L. H.; Lance, C. S., Comment on "Structural evidence for a dynamic metallocofactor during N2 reduction by Mo-nitrogenase". *Science* **2021,** *371* (6530), eabe5481.

67. Sippel, D.; Rohde, M.; Netzer, J.; Trncik, C.; Gies, J.; Grunau, K.; Djurdjevic, I.; Decamps, L.; Andrade, S. L. A.; Einsle, O., A bound reaction intermediate sheds light on the mechanism of nitrogenase. *Science* **2018,** *359* (6383), 1484-+.

68. Cao, L.; Caldararu, O.; Ryde, U., Does the crystal structure of vanadium nitrogenase contain a reaction intermediate? Evidence from quantum refinement. *JBIC Journal of Biological Inorganic Chemistry* **2020,** *25* (6), 847-861.

69. Eady, R. R.; Lowe, D. J.; Thorneley, R. N., Nitrogenase of *Klebsiella pneumoniae*: a pre-steady state burst of ATP hydrolysis is coupled to electron transfer between the component proteins. *FEBS Letters* **1978,** *95* (2), 211-3.

70. Thorneley, R. N.; Lowe, D. J.; Eday, R. R.; Miller, R. W., The coupling of electron transfer in nitrogenase to the hydrolysis of magnesium adenosine triphosphate. *Biochemical Society Transactions* **1979,** *7* (4), 633-6.

71. Thorneley, R. N.; Deistung, J., Electron-transfer studies involving flavodoxin and a natural redox partner, the iron protein of nitrogenase. Conformational constraints on protein-protein interactions and the kinetics of electron transfer within the protein complex. *Biochemical Journal* **1988,** *253* (2), 587-95.

72. Yates, M. G.; Thorneley, R. N.; Lowe, D. J., Nitrogenase of *Azotobacter chroococcum*: inhibition of ADP of the reduction of oxidised Fe protein by sodium dithionite. *FEBS Letters* **1975,** *60* (1), 89-93.

73. Thorneley, R. N., Nitrogenase of *Klebsiella pneumoniae*. A stopped-flow study of magnesium-adenosine triphosphate-induce electron transfer between the compeonent proteins. *Biochemical Journal* **1975,** *145* (2), 391-6.

74. Thorneley, R. N.; Cornish-Bowden, A., Kinetics of nitrogenase of *Klebsiella pneumoniae*. Heterotropic interactions between magnesium-adenosine 5'-diphosphate and magnesium-adenosine 5'-triphosphate. *Biochemical Journal* **1977,** *165* (2), 255-62.

75. Smith, B. E.; Lowe, D. J.; Chen, G. X.; O'Donnell, M. J.; Hawkes, T. R., Evidence on intramolecular electron transfer in the MoFe protein of nitrogenase from *Klebsiella pneumoniae* from rapid-freeze electron-paramagnetic-resonance studies of its oxidation by ferricyanide. *The Biochemical journal* **1983,** *209* (1), 207-213.

76. Thorneley, R. N.; Lowe, D. J., Nitrogenase of *Klebsiella pneumoniae*. Kinetics of the dissociation of oxidized iron protein from molybdenum-iron protein: identification of the rate-limiting step for substrate reduction. *Biochemical Journal* **1983,** *215* (2), 393-403.

77. Lowe, D. J.; Thorneley, R. N., The mechanism of *Klebsiella pneumoniae* nitrogenase action. Pre-steady-state kinetics of $H_2$ formation. *Biochemical Journal* **1984,** *224* (3), 877-86.

78. Lowe, D. J.; Thorneley, R. N., The mechanism of *Klebsiella pneumoniae* nitrogenase action. The determination of rate constants required for the simulation of the kinetics of $N_2$ reduction and $H_2$ evolution. *Biochemical Journal* **1984,** *224* (3), 895-901.

79. Thorneley, R. N. F.; Lowe, D. J., Kinetics and Mechanism of the Nitrogenase Enzyme System. In *Molybdenum Enzymes*, Spiro, T. G., Ed. Wiley-Interscience: New York, 1985; pp 221-284.

80. Thorneley, R. N.; Ashby, G.; Howarth, J. V.; Millar, N. C.; Gutfreund, H., A transient-kinetic study of the nitrogenase of *Klebsiella pneumoniae* by stopped-flow calorimetry. Comparison with the myosin ATPase. *Biochemical Journal* **1989,** *264* (3), 657-61.

81. Ashby, G. A.; Thorneley, R. N., Nitrogenase of *Klebsiella pneumoniae*. Kinetic Studies on the Fe Protein Involving Reduction by Sodium Dithionite, the binding of MgADP and a conformation change that alters the reactivity of the 4Fe-4S centre. *Biochemical Journal* **1987,** *246* (2), 455-65.

82. Seefeldt, L. C.; Hoffman, B. M.; Peters, J. W.; Raugei, S.; Beratan, D. N.; Antony, E.; Dean, D. R., Energy Transduction in Nitrogenase. *Acc Chem Res* **2018,** *51* (9), 2179-2186.

83. Thorneley, R. N.; Lowe, D. J., *Molybdenum Enzymes*. Wiley: New York, 1985.

84. Seefeldt, L. C.; Yang, Z. Y.; Lukoyanov, D. A.; Harris, D. F.; Dean, D. R.; Raugei, S.; Hoffman, B. M., Reduction of Substrates by Nitrogenases. *Chemical Reviews* **2020,** *120* (12), 5082-5106.

85. Hoffman, B. M.; Lukoyanov, D.; Dean, D. R.; Seefeldt, L. C., Nitrogenase: a draft mechanism. *Acc Chem Res* **2013,** *46* (2), 587-95.

86. Owens, C. P.; Katz, F. E.; Carter, C. H.; Luca, M. A.; Tezcan, F. A., Evidence for Functionally Relevant Encounter Complexes in Nitrogenase Catalysis. *Journal of the American Chemical Society* **2015,** *137* (39), 12704-12.

87. Danyal, K.; Mayweather, D.; Dean, D. R.; Seefeldt, L. C.; Hoffman, B. M., Conformational Gating of Electron Transfer from the Nitrogenase Fe Protein to MoFe Protein. *Journal of the American Chemical Society* **2010,** *132* (20), 6894-+.

88. Burgess, B. K.; Lowe, D. J., Mechanism of molybdenum nitrogenase. *Chemical Reviews* **1996,** *96* (7), 2983-3011.

89. Renner, K. A.; Howard, J. B., Aluminum fluoride inhibition of nitrogenase: stabilization of a nucleotide Fe-protein MoFe-protein complex. *Biochemistry* **1996,** *35* (17), 5353-5358.

90. Duyvis, M. G.; Wassink, H.; Haaker, H., Formation and characterization of a transition state complex of *Azotobacter vinelandii* nitrogenase. *FEBS Letters* **1996,** *380* (3), 233-6.

91. Danyal, K.; Dean, D. R.; Hoffman, B. M.; Seefeldt, L. C., Electron Transfer within Nitrogenase: Evidence for a Deficit-Spending Mechanism. *Biochemistry* **2011,** *50* (43), 9255-9263.

92. Lanzilotta, W. N.; Parker, V. D.; Seefeldt, L. C., Electron transfer in nitrogenase analyzed by Marcus theory: evidence for gating by MgATP. *Biochemistry* **1998,** *37* (1), 399-407.

93. Muraki, N.; Nomata, J.; Ebata, K.; Mizoguchi, T.; Shiba, T.; Tamiaki, H.; Kurisu, G.; Fujita, Y., X-ray crystal structure of the light-independent protochlorophyllide reductase. *Nature* **2010,** *465* (7294), 110-U124.

94. Hu, Y. L.; Ribbe, M. W., Nitrogenase and homologs. *J. Biol. Inorg. Chem.* **2015,** *20* (2), 435-445.

95. Tittsworth, R. C.; Hales, B. J., Detection of EPR Signals Assigned to the 1-Equiv-Oxidized P-Clusters of the Nitrogenase MoFe-Protein from *Azotobacter vinelandii*. *Journal of the American Chemical Society* **1993,** *115* (21), 9763-9767.

96. Surerus, K. K.; Hendrich, M. P.; Christie, P. D.; Rottgardt, D.; Ormejohnson, W. H.; Munck, E., Mossbauer and Integer-Spin EPR of the Oxidized P-Clusters of Nitrogenase - $P^{ox}$ Is a Non-Kramers System with a Nearly Degenerate Ground Doublet. *Journal of the American Chemical Society* **1992,** *114* (22), 8579-8590.

97. Rutledge, H. L.; Rittle, J.; Williamson, L. M.; Xu, W. A.; Gagnon, D. M.; Tezcan, F. A., Redox-Dependent Metastability of the Nitrogenase P-Cluster. *Journal of the American Chemical Society* **2019,** *141* (25), 10091-10098.

98. Howard, J. B.; Kechris, K. J.; Rees, D. C.; Glazer, A. N., Multiple amino acid sequence alignment nitrogenase component 1: insights into phylogenetics and structure-function relationships. *PLoS One* **2013,** *8* (9), e72751.

99. Zheng, K. Y.; Ngo, P. D.; Owens, V. L.; Yang, X. P.; Mansoorabadi, S. O., The biosynthetic pathway of coenzyme F430 in methanogenic and methanotrophic archaea. *Science* **2016,** *354* (6310), 339-342.

100. Robbins, A. H.; Stout, C. D., Structure of Activated Aconitase - Formation of the [4Fe-4S] Cluster in the Crystal. *Proc. Natl. Acad. Sci. U. S. A.* **1989,** *86* (10), 3639-3643.

101. Berkovitch, F.; Nicolet, Y.; Wan, J. T.; Jarrett, J. T.; Drennan, C. L., Crystal structure of biotin synthase, an S-adenosylmethionine-dependent radical enzyme. *Science* **2004,** *303* (5654), 76-79.

102. McLaughlin, M. I.; Lanz, N. D.; Goldman, P. J.; Lee, K. H.; Booker, S. J.; Drennan, C. L., Crystallographic snapshots of sulfur insertion by lipoyl synthase. *Proc. Natl. Acad. Sci. U. S. A.* **2016,** *113* (34), 9446-9450.

103. Wittenborn, E. C.; Merrouch, M.; Ueda, C.; Fradale, L.; Leger, C.; Fourmond, V.; Pandelia, M. E.; Dementin, S.; Drennan, C. L., Redox-dependent rearrangements of the NiFeS cluster of carbon monoxide dehydrogenase. *Elife* **2018,** *7*.

104. Spatzal, T.; Perez, K. A.; Howard, J. B.; Rees, D. C., Catalysis-dependent selenium incorporation and migration in the nitrogenase active site iron-molybdenum cofactor. *Elife* **2015,** *4*, e11620.

105. Beinert, H.; Kennedy, M. C.; Stout, C. D., Aconitase as iron-sulfur protein, enzyme, and iron-regulatory protein. *Chemical Reviews* **1996,** *96* (7), 2335-2373.

106. Fritsch, J.; Scheerer, P.; Frielingsdorf, S.; Kroschinsky, S.; Friedrich, B.; Lenz, O.; Spahn, C. M. T., The crystal structure of an oxygen-tolerant hydrogenase uncovers a novel iron-sulphur centre. *Nature* **2011,** *479* (7372), 249-253.

107. Noor, N. D. M.; Matsuura, H.; Nishikawa, K.; Tai, H. L.; Hirota, S.; Kim, J.; Kang, J. Y.; Tateno, M.; Yoon, K. S.; Ogo, S.; Kubota, S.; Shomura, Y.; Higuchi, Y., Redox- dependent conformational changes of a proximal [4Fe-4S] cluster in Hyb-type [NiFe]-hydrogenase to protect the active site from $O_2$. *Chem. Commun.* **2018,** *54* (87), 12385-12388.

108. Grant, B. J.; Rodrigues, A. P.; ElSawy, K. M.; McCammon, J. A.; Caves, L. S., Bio3d: an R package for the comparative analysis of protein structures. *Bioinformatics* **2006,** *22* (21), 2695-6.

109. Skjaerven, L.; Yao, X. Q.; Scarabelli, G.; Grant, B. J., Integrating protein structural dynamics and evolutionary analysis with Bio3D. *BMC Bioinformatics* **2014,** *15*, 399.

110. Grant, B. J.; Skjaerven, L.; Yao, X. Q., The Bio3D packages for structural bioinformatics. *Protein Sci.* **2021,** *30* (1), 20-30.

111. Glick, B. R.; Brooks, H. E.; Pasternak, J. J., Transformation of *Azotobacter vinelandii* with plasmid DNA. *Journal of Bacteriology* **1985,** *162* (1), 276-9.

112. Page, W. J.; Von T 'igerstrom, M., Optimal Conditions for Transformation of *Azotobacter vinelandii*. *Journal of bacteriology* **1979,** *139* (3), 1058-1061.

113. Roth, L. E.; Tezcan, F. A., ATP-Uncoupled, Six-Electron Photoreduction of Hydrogen Cyanide to Methane by the Molybdenum-Iron Protein. *Journal of the American Chemical Society* **2012,** *134* (20), 8416-8419.

114. Kabsch, W., Integration, scaling, space-group assignment and post-refinement. *Acta Crystallogr D Biol Crystallogr* **2010,** *66* (Pt 2), 133-44.

115. The CCP4 Suite: Programs for Protein Crystallography. *Acta Crystallogr D Biol Crystallogr* **1994,** *50* (Pt 5), 760-3.

116. Adams, P. D.; Afonine, P. V.; Bunkoczi, G.; Chen, V. B.; Davis, I. W.; Echols, N.; Headd, J. J.; Hung, L. W.; Kapral, G. J.; Grosse-Kunstleve, R. W.; McCoy, A. J.; Moriarty, N. W.; Oeffner, R.; Read, R. J.; Richardson, D. C.; Richardson, J. S.; Terwilliger, T. C.; Zwart, P. H., PHENIX: a Comprehensive Python-Based System for Macromolecular Structure Solution. *Acta Crystallogr D Biol Crystallogr* **2010,** *66* (Pt 2), 213-21.

117. Stoll, S.; Schweiger, A., EasySpin, a comprehensive software package for spectral simulation and analysis in EPR. *J. Magn. Reson.* **2009,** *178* (1), 42-55.

118. Chan, J. M.; Christiansen, J.; Dean, D. R.; Seefeldt, L. C., Spectroscopic evidence for changes in the redox state of the nitrogenase P-cluster during turnover. *Biochemistry* **1999,** *38* (18), 5779-5785.

119. Liu, J.; Chakraborty, S.; Hosseinzadeh, P.; Yu, Y.; Tian, S.; Petrik, I.; Bhagi, A.; Lu, Y., Metalloproteins containing cytochrome, iron-sulfur, or copper redox centers. *Chemical Reviews* **2014,** *114* (8), 4366-469.

120. Holm, R. H., Trinuclear Cuboidal and Heterometallic Cubane-Type Iron-Sulfur Clusters - New Structural and Reactivity Themes in Chemistry and Biology. *Adv. Inorg. Chem.* **1992,** *38*, 1-71.

121. Babu, B. N.; Brown, O. R., Quantitative effects of redox-cycling chemicals on the oxidant-sensitive enzyme dihydroxy-acid dehydratase. *Microbios* **1995,** *82* (332), 157-70.

122. Flint, D. H.; Emptage, M. H.; Guest, J. R., Fumarase-a from Escherichia-Coli - Purification and Characterization as an Iron Sulfur Cluster Containing Enzyme. *Biochemistry* **1992,** *31* (42), 10331-10337.

123. Lauble, H.; Kennedy, M. C.; Beinert, H.; Stout, C. D., Crystal structures of aconitase with isocitrate and nitroisocitrate bound. *Biochemistry* **1992,** *31* (10), 2735-48.

124. Flint, D. H.; Tuminello, J. F.; Emptage, M. H., The Inactivation of Fe-S Cluster Containing Hydro-Lyases by Superoxide. *Journal of Biological Chemistry* **1993,** *268* (30), 22369-22376.

125. Imlay, J. A., Iron-sulphur clusters and the problem with oxygen. *Molecular Microbiology* **2006,** *59* (4), 1073-1082.

126. Imlay, J. A., Cellular defenses against superoxide and hydrogen peroxide. *Annual Review of Biochemistry* **2008,** *77*, 755-76.

127. Imlay, J. A., The molecular mechanisms and physiological consequences of oxidative stress: lessons from a model bacterium. *Nat Rev Microbiol* **2013,** *11* (7), 443-454.

128. Kuo, C. F.; Mashino, T.; Fridovich, I., Alpha,Beta-Dihydroxyisovalerate Dehydratase - a Superoxide-Sensitive Enzyme. *Journal of Biological Chemistry* **1987,** *262* (10), 4724-4727.

129. Varghese, S.; Tang, Y.; Imlay, J. A., Contrasting sensitivities of Escherichia coli aconitases A and B to oxidation and iron depletion. *Journal of Bacteriology* **2003,** *185* (1), 221-230.

130. Martic, M.; Jakab-Simon, I. N.; Haahr, L. T.; Hagen, W. R.; Christensen, H. E. M., Heterometallic [AgFe3S4] ferredoxin variants: synthesis, characterization, and the first crystal structure of an engineered heterometallic iron-sulfur protein. *J. Biol. Inorg. Chem.* **2013,** *18* (2), 261-276.

131. Finnegan, M. G.; Conover, R. C.; Park, J. B.; Zhou, Z. H.; Adams, M. W. W.; Johnson, M. K., Electronic, Magnetic, Redox, and Ligand-Binding Properties of [Mfe(3)S(4)] Clusters (M=Zn, CO, Mn) in Pyrococcus-Furiosus Ferredoxin. *Inorg. Chem.* **1995,** *34* (21), 5358-5369.

132. Staples, C. R.; Dhawan, I. K.; Finnegan, M. G.; Dwinell, D. A.; Zhou, Z. H.; Huang, H. S.; Verhagen, M. F. J. M.; Adams, M. W. W.; Johnson, M. K., Electronic, magnetic, and redox properties of [MFe3S4] clusters (M = Cd, Cu, Cr) in Pyrococcus furiosus ferredoxin. *Inorg. Chem.* **1997,** *36* (25), 5740-5749.

133. Conover, R. C.; Park, J. B.; Adams, M. W. W.; Johnson, M. K., Formation and Properties of a Nife3s4 Cluster in Pyrococcus-Furiosus Ferredoxin. *Journal of the American Chemical Society* **1990,** *112* (11), 4562-4564.

134. Fu, W. G.; Telser, J.; Hoffman, B. M.; Smith, E. T.; Adams, M. W. W.; Finnegan, M. G.; Conover, R. C.; Johnson, M. K., Interaction of Tl+ and Cs+ with the [Fe3s4] Cluster of Pyrococcus-Furiosus Ferredoxin - Investigation by Resonance Raman, MCD, EPR, and Endor Spectroscopy. *Journal of the American Chemical Society* **1994,** *116* (13), 5722-5729.

135. Faridoon, K. Y.; Zhuang, H. Y.; Sykes, A. G., Kinetic Studies on the Reaction of M2+ Ions with Aconitase Fe3S40 To Give Fe3MS42+ Clusters (M = Fe, Mn, Co). *Inorg. Chem.* **1994,** *33* (10), 2209-2212.

136. Sandercock, J. R.; Page, W. J., RpoS expression and the general stress response in Azotobacter vinelandii during carbon and nitrogen diauxic shifts. *J. Bacteriol.* **2008,** *190* (3), 946-53.

137. Rodriguez-Rojas, A.; Kim, J. J.; Johnston, P. R.; Makarova, O.; Eravci, M.; Weise, C.; Hengge, R.; Rolff, J., Non-lethal exposure to H2O2 boosts bacterial survival and evolvability against oxidative stress. *PLoS Genet.* **2020,** *16* (3).

138. Barney, B. M.; Plunkett, M. H.; Natarajan, V.; Mus, F.; Knutson, C. M.; Peters, J. W., Transcriptional Analysis of an Ammonium-Excreting Strain of Azotobacter vinelandii Deregulated for Nitrogen Fixation. *Applied and Environmental Microbiology* **2017,** *83* (20).

139. Page, W. J.; Huyer, M., Derepression of the Azotobacter-Vinelandii Siderophore System, Using Iron-Containing Minerals to Limit Iron Repletion. *Journal of Bacteriology* **1984,** *158* (2), 496-502.

140. Noguez, R.; Segura, D.; Moreno, S.; Hernandez, A.; Juarez, K.; Espin, G., Enzyme I NPr, NPr and IIA Ntr are involved in regulation of the poly-beta-hydroxybutyrate biosynthetic genes in Azotobacter vinelandii. *J Mol Microbiol Biotechnol* **2008,** *15* (4), 244-54.

141. Srisantitham, S.; Badding, E. D.; Suess, D. L. M., Postbiosynthetic modification of a precursor to the nitrogenase iron-molybdenum cofactor. *Proc. Natl. Acad. Sci. U. S. A.* **2021,** *118* (11).

142. Badding, E.; Srisantitham, S.; Lukoyanov, D.; Hoffman, B. M.; Suess, D., Connecting the Geometric and Electronic Structures of the Nitrogenase Iron–Molybdenum Cofactor through Site-Selective Labeling. *ChemRxiv* **2022**.

143. McLean, P. A.; Papaefthymiou, V.; Orme-Johnson, W. H.; Munck, E., Isotopic hybrids of nitrogenase. Mossbauer study of MoFe protein with selective $^{57}$Fe enrichment of the P-cluster. *Journal of Biological Chemistry* **1987,** *262* (27), 12900-3.

144. Yoo, S. J.; Angove, H. C.; Papaefthymiou, V.; Burgess, B. K.; Münck, E., Mössbauer Study of the MoFe Protein of Nitrogenase from Azotobacter vinelandii Using Selective 57Fe Enrichment of the M-Centers. *Journal of the American Chemical Society* **2000,** *122* (20), 4926-4936.

145. Vasak, M.; Kagi, J. H., Metal thiolate clusters in cobalt(II)-metallothionein. *Proc. Natl. Acad. Sci. U. S. A.* **1981,** *78* (11), 6709-13.

146. Li, Z.; Guo, S.; Sun, Q.; Chan, G. K., Electronic landscape of the P-cluster of nitrogenase as revealed through many-electron quantum wavefunction simulations. *Nat Chem* **2019**.

147. Schmid, B.; Ribbe, M. W.; Einsle, O.; Yoshida, M.; Thomas, L. M.; Dean, D. R.; Rees, D. C.; Burgess, B. K., Structure of a cofactor-deficient nitrogenase MoFe protein. *Science* **2002,** *296* (5566), 352-6.

148. Schlesier, J.; Rohde, M.; Gerhardt, S.; Einsle, O., A Conformational Switch Triggers Nitrogenase Protection from Oxygen Damage by Shethna Protein II (FeSII). *Journal of the American Chemical Society* **2016,** *138* (1), 239-47.

149. Medina, M. S.; Bretzing, K. O.; Aviles, R. A.; Chong, K.; Espinoza, A.; Garcia, C. N. G.; Katz, B. B.; Kharwa, R. N.; Hernandez, A.; Lee, J. L.; Lee, T. M.; Strul, M. W.; Lo Verde, C.; Wong, E. Y.; Owens, C. P., CowN sustains nitrogenase turnover in the presence of the inhibitor carbon monoxide. *Journal of Biological Chemistry* **2021**, 100501.

150. Varghese, F.; Kabasakal, B. V.; Cotton, C. A. R.; Schumacher, J.; Rutherford, A. W.; Fantuzzi, A.; Murray, J. W., A low-potential terminal oxidase associated with the iron-only nitrogenase from the nitrogen-fixing bacterium Azotobacter vinelandii. *Journal of Biological Chemistry* **2019,** *294* (24), 9367-9376.

151. Kendall, M. M.; Liu, Y.; Sieprawska-Lupa, M.; Stetter, K. O.; Whitman, W. B.; Boone, D. R., Methanococcus aeolicus sp. nov., a mesophilic, methanogenic archaeon from shallow and deep marine sediments. *Int J Syst Evol Microbiol* **2006,** *56* (Pt 7), 1525-1529.

152. Torres, M. E.; Cox, T.; Hong, W.-L.; McManus, J.; Sample, J. C.; Destrigneville, C.; Gan, H. M.; Gan, H. Y.; Moreau, J. W., Crustal fluid and ash alteration impacts on the biosphere of Shikoku Basin sediments, Nankai Trough, Japan. *Geobiology* **2015,** *13* (6), 562-580.

153. Chiu, H. J.; Peters, J. W.; Lanzilotta, W. N.; Ryle, M. J.; Seefeldt, L. C.; Howard, J. B.; Rees, D. C., MgATP-bound and nucleotide-free structures of a nitrogenase protein complex between the Leu 127 Delta-Fe-protein and the MoFe-protein. *Biochemistry* **2001,** *40* (3), 641-650.

154. Schmid, B.; Einsle, O.; Chiu, H. J.; Willing, A.; Yoshida, M.; Howard, J. B.; Rees, D. C., Biochemical and structural characterization of the cross-linked complex of nitrogenase: comparison to the ADP·$AlF_4^-$-stabilized structure. *Biochemistry* **2002,** *41* (52), 15557-65.

155. Hwang, J. C.; Chen, C. H.; Burris, R. H., Inhibition of nitrogenase-catalyzed reductions. *Biochim. Biophys. Acta* **1973,** *292* (1), 256-70.

156. Cameron, L. M.; Hales, B. J., Investigation of CO binding and release from Mo-nitrogenase during catalytic turnover. *Biochemistry* **1998,** *37* (26), 9449-56.

157. Rohde, M.; Laun, K.; Zebger, I.; Stripp, S. T.; Einsle, O., Two ligand-binding sites in CO-reducing V nitrogenase reveal a general mechanistic principle. *Science Advances* **2021,** *7* (22), eabg4474.

158. Sippel, D.; Einsle, O., The structure of vanadium nitrogenase reveals an unusual bridging ligand. *Nat. Chem. Biol.* **2017,** *13* (9), 956-+.

159. Rasche, M. E.; Seefeldt, L. C., Reduction of thiocyanate, cyanate, and carbon disulfide by nitrogenase: kinetic characterization and EPR spectroscopic analysis. *Biochemistry* **1997,** *36* (28), 8574-85.

160. Tan, Y. Z.; Baldwin, P. R.; Davis, J. H.; Williamson, J. R.; Potter, C. S.; Carragher, B.; Lyumkis, D., Addressing preferred specimen orientation in single-particle cryo-EM through tilting. *Nat Methods* **2017,** *14* (8), 793-796.

161. Clarke, T. A.; Yousafzai, F. K.; Eady, R. R., Klebsiella pneumoniae nitrogenase: formation and stability of putative beryllium fluoride-ADP transition state complexes. *Biochemistry* **1999,** *38* (31), 9906-13.

162. Clarke, Thomas A.; Fairhurst, S.; Lowe, David J.; Watmough, Nicholas J.; Eady, Robert R., Electron transfer and half-reactivity in nitrogenase. *Biochemical Society Transactions* **2011,** *39* (1), 201-206.

163. Danyal, K.; Shaw, S.; Page, T. R.; Duval, S.; Horitani, M.; Marts, A. R.; Lukoyanov, D.; Dean, D. R.; Raugei, S.; Hoffman, B. M.; Seefeldt, L. C.; Antony, E., Negative cooperativity in the nitrogenase Fe protein electron delivery cycle. *Proc. Natl. Acad. Sci. U. S. A.* **2016,** *113* (40), E5783-E5791.

164. Huang, Q.; Tokmina-Lukaszewska, M.; Johnson, L. E.; Kallas, H.; Ginovska, B.; Peters, J. W.; Seefeldt, L. C.; Bothner, B.; Raugei, S., Mechanical coupling in the nitrogenase complex. *PLoS Comp. Biol.* **2021,** *17* (3), e1008719.

165. Motlagh, H. N.; Wrabl, J. O.; Li, J.; Hilser, V. J., The ensemble nature of allostery. *Nature* **2014,** *508* (7496), 331-9.

166. Igarashi, R. Y.; Seefeldt, L. C., Nitrogen fixation: the mechanism of the Mo-dependent nitrogenase. *Crit. Rev. Biochem. Mol. Biol.* **2003,** *38* (4), 351-84.

167. Morrison, C. N.; Hoy, J. A.; Zhang, L.; Einsle, O.; Rees, D. C., Substrate pathways in the nitrogenase MoFe protein by experimental identification of small molecule binding sites. *Biochemistry* **2015,** *54* (11), 2052-60.

168. Morrison, C. N.; Spatzal, T.; Rees, D. C., Reversible Protonated Resting State of the Nitrogenase Active Site. *J. Am. Chem. Soc.* **2017,** *139* (31), 10856-10862.

169. Chovancova, E.; Pavelka, A.; Benes, P.; Strnad, O.; Brezovsky, J.; Kozlikova, B.; Gora, A.; Sustr, V.; Klvana, M.; Medek, P.; Biedermannova, L.; Sochor, J.; Damborsky, J., CAVER 3.0: a tool for the analysis of transport pathways in dynamic protein structures. *PLoS Comput Biol* **2012,** *8* (10), e1002708.

170. McLean, P. A.; Dixon, R. A., Requirement of nifV gene for production of wild-type nitrogenase enzyme in Klebsiella pneumoniae. *Nature* **1981,** *292* (5824), 655-6.

171. Durrant, M. C.; Francis, A.; Lowe, D. J.; Newton, W. E.; Fisher, K., Evidence for a dynamic role for homocitrate during nitrogen fixation: the effect of substitution at the alpha-Lys426 position in MoFe-protein of Azotobacter vinelandii. *Biochem. J.* **2006,** *397* (2), 261-70.

172. Pickett, C. J., The Chatt cycle and the mechanism of enzymic reduction of molecular nitrogen. *JBIC Journal of Biological Inorganic Chemistry* **1996,** *1* (6), 601-606.

173. Hoffman, B. M.; Lukoyanov, D.; Yang, Z. Y.; Dean, D. R.; Seefeldt, L. C., Mechanism of Nitrogen Fixation by Nitrogenase: The Next Stage. *Chemical Reviews* **2014,** *114* (8), 4041-4062.

174. Nguyen, H. P. M.; McGuire, K. L.; Cook, B. D.; Herzik, M. A., Jr., Manual Blot-and-Plunge Freezing of Biological Specimens for Single-Particle Cryogenic Electron Microscopy. *J Vis Exp* **2022,** (180).

175. Kimanius, D.; Dong, L.; Sharov, G.; Nakane, T.; Scheres, S. H. W., New tools for automated cryo-EM single-particle analysis in RELION-4.0. *Biochem. J.* **2021,** *478* (24), 4169-4185.

176. Zheng, S. Q.; Palovcak, E.; Armache, J. P.; Verba, K. A.; Cheng, Y.; Agard, D. A., MotionCor2: anisotropic correction of beam-induced motion for improved cryo-electron microscopy. *Nat Methods* **2017,** *14* (4), 331-332.

177. Punjani, A.; Rubinstein, J. L.; Fleet, D. J.; Brubaker, M. A., cryoSPARC: algorithms for rapid unsupervised cryo-EM structure determination. *Nat Methods* **2017,** *14* (3), 290-296.

178. Zivanov, J.; Nakane, T.; Scheres, S. H. W., Estimation of high-order aberrations and anisotropic magnification from cryo-EM data sets in RELION-3.1. *IUCrJ* **2020,** *7* (Pt 2), 253-267.

179. Rohou, A.; Grigorieff, N., CTFFIND4: Fast and accurate defocus estimation from electron micrographs. *J. Struct. Biol.* **2015,** *192* (2), 216-21.

180. Wagner, T.; Merino, F.; Stabrin, M.; Moriya, T.; Antoni, C.; Apelbaum, A.; Hagel, P.; Sitsel, O.; Raisch, T.; Prumbaum, D.; Quentin, D.; Roderer, D.; Tacke, S.; Siebolds, B.; Schubert, E.;

Shaikh, T. R.; Lill, P.; Gatsogiannis, C.; Raunser, S., SPHIRE-crYOLO is a fast and accurate fully automated particle picker for cryo-EM. *Commun Biol* **2019,** *2*, 218.

181. Punjani, A.; Fleet, D. J., 3D variability analysis: Resolving continuous flexibility and discrete heterogeneity from single particle cryo-EM. *J. Struct. Biol.* **2021,** *213* (2), 107702.

182. Sanchez-Garcia, R.; Gomez-Blanco, J.; Cuervo, A.; Carazo, J. M.; Sorzano, C. O. S.; Vargas, J., DeepEMhancer: a deep learning solution for cryo-EM volume post-processing. *Commun Biol* **2021,** *4* (1), 874.

183. Van Stappen, C.; Decamps, L.; Cutsail, G. E., 3rd; Bjornsson, R.; Henthorn, J. T.; Birrell, J. A.; DeBeer, S., The Spectroscopy of Nitrogenases. *Chemical Reviews* **2020,** *120* (12), 5005-5081.

184. Peters, J. W.; Fisher, K.; Dean, D. R., Nitrogenase structure and function: a biochemical-genetic perspective. *Annual Review of Microbiology* **1995,** *49*, 335-66.

185. Thorneley, R. N.; Lowe, D. J., The mechanism of Klebsiella pneumoniae nitrogenase action. Pre-steady-state kinetics of an enzyme-bound intermediate in N2 reduction and of NH3 formation. *Biochem. J.* **1984,** *224* (3), 887-94.

186. Wilson, P. E.; Nyborg, A. C.; Watt, G. D., Duplication and extension of the Thorneley and Lowe kinetic model for Klebsiella pneumoniae nitrogenase catalysis using a MATHEMATICA software platform. *Biophys. Chem.* **2001,** *91* (3), 281-304.

187. Yang, Z. Y.; Ledbetter, R.; Shaw, S.; Pence, N.; Tokmina-Lukaszewska, M.; Eilers, B.; Guo, Q.; Pokhrel, N.; Cash, V. L.; Dean, D. R.; Antony, E.; Bothner, B.; Peters, J. W.; Seefeldt, L. C., Evidence That the $P_i$ Release Event Is the Rate-Limiting Step in the Nitrogenase Catalytic Cycle. *Biochemistry* **2016,** *55* (26), 3625-35.

188. Duval, S.; Danyal, K.; Shaw, S.; Lytle, A. K.; Dean, D. R.; Hoffman, B. M.; Antony, E.; Seefeldt, L. C., Electron transfer precedes ATP hydrolysis during nitrogenase catalysis. *Proc. Natl. Acad. Sci. U. S. A.* **2013,** *110* (41), 16414-9.